Distinction of degradation mechanisms in perovskites solar cells through statistical approaches on large simulated datasets

Arthur Julien

INSTITUT POLYTECHNIQUE DE PARIS

ÉCOLE POLYTECHNIQUE

IP PARIS

NNT : 2020IPPA0000

Thèse de doctorat

Distinction of degradation mechanisms in perovskites solar cells through statistical approaches on large simulated datasets

Thèse de doctorat de l'Institut Polytechnique de Paris
préparée à l'IPVF

École doctorale n°626 Ecole Doctorale de l'Institut Polytechnique de Paris (EDIPP)
Spécialité de doctorat: Sciences et technologies industrielles

Thèse présentée et soutenue à Palaiseau, le 24 octobre 2023, par

Arthur JULIEN

Composition du Jury :

Muriel Matheron Ingénieure-chercheure, CEA (Liten)	Rapportrice
Anne Migan Dubois Professeure, Université Paris-Saclay (GeePs)	Rapportrice
Jacky Even Professeur, INSA Rennes (FOTON)	Examinateur
Ian Marius Peters Docteur, Forschungszentrum Jülich (HIERN)	Examinateur
Wolfgang Tress Professeur, ZHAW School of Engineering (ICP)	Examinateur
Jean-François Guillemoles Directeur de recherche, CNRS (UMR IPVF)	Directeur de thèse
Jean-Baptiste Puel Ingénieur-chercheur EDF R&D (IPVF)	Encadrant

Abstract

Perovskite solar cells have attracted a lot of attention in the past years, due to high power conversion efficiencies and low cost of fabrication. Material and interface properties in these devices have been intensely studied, allowing to significantly improve performances. However, the expected lifetime remain short, because of numerous potential degradation mechanisms, triggered by various environmental factors.

This work aims at helping the understanding of these degradation processes and supporting the development of stable perovskite solar cells. Precisely, modelling methods have been developed to distinguish and identify the mechanisms responsible for performance degradation under given aging experiments.

Current voltage curves and photoluminescence spectra measurements, performed periodically over the course of aging experiments have been investigated. The associated evolutions of optoelectrical parameters over time were at the core of the approach developed here.

In order to investigate the photovoltaic behavior of perovskite solar cells, optical (transfer matrices) and electrical (drift diffusion) modeling have been coupled. Furthermore, a statistical approach has been developed, because of some unwell known input parameters. A genetic algorithm has been designed, providing numerous sets of inputs that reproduce the initial performances of a given sample. These sets were the basis to simulate various hypothetical unitary degradation mechanisms.

Importantly, pathways are obtained by considering the correlated evolution of optoelectrical parameters. They constitute characteristic footprints of the processes responsible for the performance degradation, and simulated and experimental pathways can be directly compared. As a result, compatible mechanisms can be proposed, and others excluded when pathways differ. The causality between performance losses and degradation mechanisms is here directly tackled.

After applying this approach to experimental measurements reported in literature, making possible to compare results to authors analyses and demonstrate the validity of the approach, aging experiments performed at IPVF were investigated. A first set of samples prepared with four variations in the deposition method of the perovskite layer. Results showed that the perovskite could be excluded as a cause for degradation in most cases, except for a specific method, also having the least stable samples.

A second set, containing devices having different hole and electron transport layers was investigated through coupled current-voltage and photoluminescence measurements. Interestingly, hole transport layer degradation could be attributed to several samples, and a protective role of the electron transport could be envisaged. Also, coupling characterization techniques helped to distinguish pathways through new complementary planes.

Finally, the last part of this work took advantage of the numerous simulations performed to investigate degradation. It aimed at simplifying the design of drift diffusion simulations by reducing the number of necessary inputs and identifying the most important ones. Meta-parameters candidates have been proposed by considering relevant quantities in an analytical model. Moreover, their validity to define a solar cell performance was assessed through their correlation with its optoelectrical outputs. Finally, principal components analyses were also employed on subsets selected according to solar cells performances, to point out the most important parameters or provide new simple phenomenological models.

This work shows how modelling can support experimental development of stable perovskite solar cells. Notably, insights on the causes of degradation of various samples have been proposed. Finally, this also demonstrates that statistical approaches can support the solar cell modeling research field, by being less dependent on the knowledge of given parameters.

List of symbols and acronyms

Symbols

α	Absorption coefficient
N_A	Acceptor density
E_A	Activation energy
E_G	Bandgap energy
k_B	Boltzmann constant
V_{bi}	Built in potential
σ	Capture cross section
n_0 / p_0	Dark, equilibrium density of electrons / holes
D_n / D_p	Diffusion coefficient of electrons / holes
L_n / L_p	Diffusion lengths of electrons / holes
N_t	Density of defects
$N_{t-ETL/pvk}$	Density of defects at perovskite / ETL interface
$N_{t-HTL/pvk}$	Density of defects at perovskite / HTL interface
N_D	Donor density
N_C	Effective density of states in conduction band
N_V	Effective density of states in valence band
q	Elementary charge
E	Electrical field
Φ	Electrical potential
χ	Electron affinity
n	Electron density
E_C	Energy level of conduction band
E_V	Energy level of valence band
R_S	External series resistance
R_{Sh}	External shunt resistance
E_F	Fermi level
E_{F-n} / E_{F-p}	Quasi-Fermi level for electrons / holes
ΔE_F	Quasi-Fermi levels splitting
FF	Fill factor

ν	Frequency
p	Hole density
n_i	Intrinsic carrier concentration
τ	Lifetime
Jmpp	Maximum power point current
Vmpp	Maximum power point voltage
μ_n / μ_p	Mobility of electrons / holes
Voc	Open circuit voltage
ϵ	Permittivity
Emax	Photon energy at max of photoluminescence emission peak
ϕ	Photon flux
h / $\hbar$	Planck constant / reduced Planck constant
B	Radiative recombination coefficient
Jsc	Short circuit current
c	Speed of light
S_n / S_p	Surface recombination velocity for electrons / holes
T	Temperature
v_{th}	Thermal velocity
λ	Wavelength

Acronyms

FA	Formamidinium
JV	Current voltage characteristic
ETL	Electron Transport Layer
HTL	Hole Transport Layer
MA	Methylammonium
PL	Photoluminescence
PV	Photovoltaic
PCA	Principal Component Analysis
TCO	Transparent Conductive Oxide
SRH	Shockley-Read-Hall recombination

Table of contents

Introduction

Table of contents

Challenges of energy supply in the context of global ecological crisis

Energy supply, through its nature, availability and cost are main challenges for several aspects of society. In the past, the quantity of available energy has been for instance at the core of economical and societal development, by allowing to expand production means and accelerate transport over longer distances.

Now, the environmental impact of energy sources is also a main concern, in the context of global warming, climate change and ecological crisis. As illustrated in Figure 1, its major part comes from fossil fuels, which also have the highest CO_2 emission rates. As a result consumption of fossil fuels is a main cause of greenhouse gas emissions, being at the source of global warming and climate change [1].

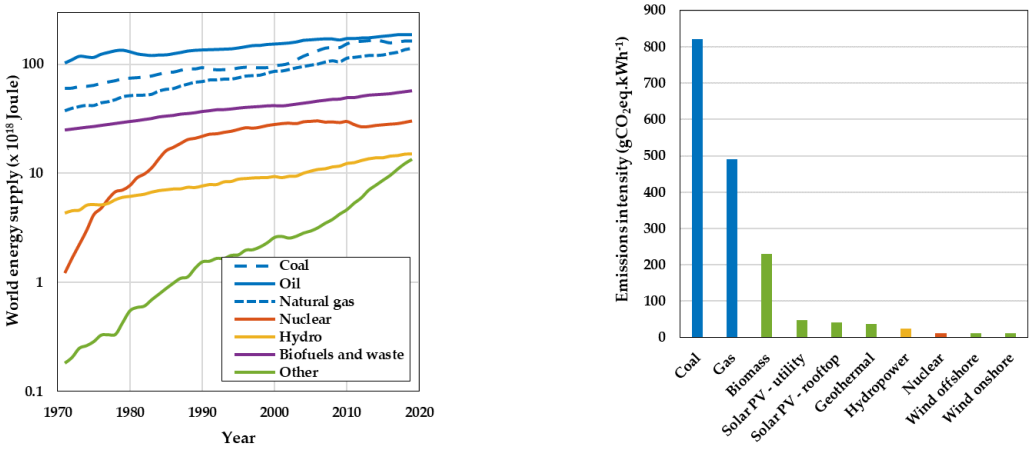

Figure 1. *Left: world energy supply, by source. Other includes geothermal, solar, wind, tide/wave/ocean, heat and other sources. Source: IEA* [2]. *Right: lifetime emission intensity in CO_2 equivalent. Source: IPCC* [1].

In this context, renewable energies such as photovoltaics provide a useful alternative to fossil fuels, through low greenhouse gas emissions but also highly available and infinite stock, being the solar irradiance.

However, the quantity of materials necessary to fabricate photovoltaic energy production systems is also a key point. The vast majority of solar cells fabricated today is based on silicon, an abundant material. However, the total system also necessitates aluminum, coper, tin, silver, some polymers and glass. Even if comparatively low quantities are employed, the environmental impact of extracting and processing these materials has to be considered. Notably, projections show that the annual demand of indium (employed in transparent conductive oxides) in a scenario of 700 GW annual capacity growth, would necessitate to employ the total current indium production (for all industries). Silver, aluminum and copper could also face supply issues [3].

The supply of associated raw material could become major issues for the society (even more that currently) coupled with the environmental risks associated to mining and extraction.

Opportunities proposed by perovskite solar cells and challenges

The need of high energy quantities and low material intensive production are core motivations for the photovoltaic research today to propose solar cells with high power conversion efficiency and low material costs. In fact, such devices is crucial to be able to tackle global warming by replacing fossil fuels, without worsening the environmental crisis through raw materials extraction.

For these reasons, perovskite solar cells have been intensely studied over the past ten years. They are mostly based on lead-halide perovskite materials, characterized by their composition of the type ABX_3 (A is a cation, B a metal and X an anion). These materials have demonstrated suitable semi-conductor properties to fabricate highly efficient solar cells. For instance, they absorb well light due to their direct bandgap and allow efficient charge carrier extraction through relatively high mobilities, long diffusion lengths and low recombination.

In the most studied compositions, the A site cation is usually an organic molecule, the B site metal lead (or tin) and the C site an anion such as iodide or bromide. Moreover they are usually employed with at least two other layers, responsible for selective charge carrier extraction, usually fabricated with polymers or metal oxides.

Importantly, these solar cells are in the form of thin films, needing low quantity of materials. They can even be deposited through low temperature solution based processes, making fabrication costs very low. These aspects constitute significant assets that motivate intense research work to understand better the properties of these materials and their interfaces when included in a solar cell, in order to propose the most suitable combination. As a result record power conversion efficiencies have increased a lot in the past years and attained 24.8 % [4]. They have even been combined to silicon solar cells in tandem structures, reaching 32.5 % [5].

However, a main challenge for perovskite solar cells is now their stability. Most record devices show lifetimes (usually the elapsed time to reach 80 % of initial power conversion efficiency) in the order of thousands of hours, when exposed to continuous illuminations and ambient lab conditions (usually encapsulated samples) [6]. This is a main issue for perovskite solar cells to fulfill the objectives mentioned above: if their lifetime is too low, energy production is not low material intensive anymore.

Therefore, intense work is now focused on investigating stability of these solar cells, and a first important aspect is the high number of possible degradation mechanisms, triggered by several environmental factors. For instance, water can penetrate the perovskite layer, disturb its crystal structure and even react with it's A site organic cation. Oxygen combined with illumination have been reported to oxidize constituents of the perovskite. Moreover, transport layers can also degrade, for instance through temperature instability of organic hole transport materials, or photooxidation of oxides employed as electron transport layer. As a result, it is often difficult to tell the cause of instability for a given sample.

Objectives of this work and outline

These instability aspects are the main motivation for this work, which aims at helping to distinguish and identify mechanisms causing degradation. More specifically, it aims at analyzing experimental aging measurements, and providing insights on the degradation cause for each considered sample.

To do so, specific modelling methods have been developed, with a statistical approach to specifically tackle the challenges of simulating the performance of perovskite solar cells. In fact, this work considers several methods to be less dependent on the knowledge of some input parameters: exploration of the input space with a genetic algorithm and investigation of parameters statistics with principal components analyses.

The first chapter of this manuscript exposes first useful concepts of semi-conductor physics and important properties of perovskite solar cells. Also, a review of degradation mechanisms, together with associated investigation techniques, is proposed to expose in detail the motivation of this work. Finally, recent modeling studies of the degradation of perovskite solar cells are reported.

The second chapter exposes the methods employed in this work. Coupled optical and electrical modeling have been employed, allowing to reproduce experimental characterizations considered in this work: current voltage characteristics and photoluminescence spectra. The samples and associated aging studies analyzed in this work are also exposed. They were gathered from literature, or from experiments performed at IPVF by the dedicated stability team. Notably, such measurements (recording characteristics periodically over time) are commonly performed, but their dynamics rarely investigated to study degradation processes.

In the third chapter, the statistical approach employed here is exposed. First the input space, associated to parameters for which uncertainty has been considered, is presented. Then, it has been explored with a genetic algorithm, allowing to obtain sets of inputs, compatible with any given sample. Finally, these sets were the basis to simulate the impact of various hypothetical unitary degradation mechanisms on the given sample.

The fourths chapter is dedicated to the main results of this work. Degradation pathways are presented, being time independent representations of degrading optoelectrical parameters. They allow to directly compare experimental results and associated simulated mechanisms, without implementing kinetical or environmental activation models. As a result, compatible mechanisms can be proposed, and others excluded when pathways differ. Results obtained in a first step on experimental measurements reported in literature could be compared to authors analyses and demonstrated the validity of the approach. Moreover, aging experiments performed at IPVF were investigated. From a first set of samples, variations of the deposition technique and its impact on the stability of the perovskite layer could be addressed and distinguished from the degradation of other layers. A second set, containing devices having different hole and electron transport materials was investigated. Here

degradation of the first layer has been found, with a possible influence of the second. Importantly, coupling current-voltage and photoluminescence characterizations helped to distinguish pathways through information on new complementary aspects, allowing to consider pathways from further perspectives.

Finally, the fifth chapter reports work that takes advantage of the numerous simulations performed to investigate degradation. It aimed at simplifying the design of drift diffusion simulations through meta-parameters, assessed by their correlation with the optoelectrical outputs. Moreover, principal components analyses were also employed on specifically designed subsets, to point out the most important parameters or provide new simple phenomenological models. This finally supports the understanding of the role of the material parameters and their impact on solar cells performances.

In this work, modelling methods have been employed to help the understanding of perovskite solar cells degradation mechanisms. Moreover, it illustrates how theory based simulation studies can take advantage of the several statistical aspects considered here. As a result, this work aims at supporting the photovoltaic research community in developing efficient, stable, cost effective and low material intensive perovskite solar cells.

References

[1] IPCC, "AR5 Climate Change 2014: Mitigation of Climate Change," 2014.

[2] IEA, "World total energy supply by source, 1971-2019," *IEA, Paris*, 2023. https://www.iea.org/data-and-statistics/charts/world-total-energy-supply-by-source-1971-2019 (accessed Jul. 23, 2023).

[3] IRENA, "Critical materials for the energy transition," 2021.

[4] M. Jeong *et al.*, "Stable perovskite solar cells with efficiency exceeding 24.8% and 0.3-V voltage loss," *Science (1979)*, vol. 369, no. 6511, pp. 1615–1620, 2020, doi: 10.1126/science.abb7167.

[5] S. Mariotti *et al.*, "Interface engineering for high-performance, triple-halide perovskite-silicon tandem solar cells," *Science (1979)*, vol. 381, no. 6653, pp. 63–69, 2023, doi: 10.1126/science.adf5872.

[6] T. A. Chowdhury, M. A. Bin Zafar, M. Sajjad-Ul Islam, M. Shahinuzzaman, M. A. Islam, and M. U. Khandaker, "Stability of perovskite solar cells: issues and prospects," *RSC Adv*, vol. 13, no. 3, pp. 1787–1810, 2023, doi: 10.1039/d2ra05903g.

Chapter 1: State of the art

Table of content

Chapter introduction

In this chapter, the aspects necessary to understand what is at stake when investigating the stability of perovskite solar cells are exposed.

First, useful concepts of semiconductors physics, defining the optoelectrical performances of a solar cell, are exposed in Section 1.1.

In Section 1.2, characteristics of perovskite materials explaining their capability to provide highly efficient devices are reported. Moreover, materials employed as electron and hole transporting layers are also described.

Importantly, numerous degradation mechanisms can be responsible for performance losses. This constitutes the motivation of the work presented here. The various processes reported in literature are summarized in Section 1.3.

Finally, the several modeling approaches employed to examine the impact of degradation on solar cells optoelectrical performances are reported in Section 1.4.

Chapter key points:

- Important semiconductors properties to make an efficient solar cell: absorption coefficient, carrier mobility, defect densities in bulk and at interfaces, doping level and charge carrier selectivity at interfaces.
- Perovskite materials have high absorption coefficient, good carrier mobilities and long diffusion lengths despite high defect densities.
- Films employed to fabricate perovskite solar cells have properties that depend significantly on fabrication processes.
- Degradation processes in perovskite solar cells can be triggered by temperature, humidity, light, oxygen and applied bias.
- Most materials and interfaces can degrade.
- Reversible and irreversible processes have been reported.
- Drift diffusion simulation approaches have now been developed to couple ionic and electronic transport, but the link with long term degradation is still unclear.

1.1 Physics of solar cells

The fundamentals principles of semiconductor physics necessary to understand the key aspects of perovskite solar cells are summarized in this section. The concepts exposed here allow to understand what the optoelectrical performances of a solar cell are. Furthermore, it exposes how degradation of the materials can impact its behavior and performances.

1.1.1 Useful concepts of semiconductor physics

Semiconductor materials are at the basis of photovoltaic electricity production. They are employed to fabricate solar cells and their characteristics define the response to illumination and energy production [1], [2].

Semi-conductors are defined by their bandgap energy. In fact, the available energy states for electrons in the crystal of such material are not continuously distributed. The position of these states arises from interactions of the atomic orbitals, and their interaction in the crystal. There exist a range of inaccessible energy levels, and they constitute the bandgap. Also, the (almost) continuums of available states bellow and above this range are respectively called valence and conduction bands.

In practice, the valance band is almost full of electrons, and the conduction band almost empty. Notably, holes are hypothetical particles denoting the absence of an electron in the valence band. They are subjected to the same processes as electrons and carry a positive electrical charge. Therefore, the behavior of a semiconductor material is usually analyzed in terms of electron and holes densities, mobilities and currents.

In fact, the energetic distribution of electrons (across available states) is described in the dark and at thermal equilibrium by a Fermi-Dirac distribution. This allows to express the electron density (noted n) and hole density (noted p) in the conduction and valence band respectively through the Fermi level (noted E_F):

$$n = N_C \, e^{-\frac{E_C - E_F}{k_B T}} \quad (1)$$

$$p = N_V \, e^{-\frac{E_F - E_V}{k_B T}} \quad (2)$$

N_C and N_V are the effective density of states in the conduction and valence band respectively and E_C and E_V are the energy level of their respective minimum and maximum.

This shows the importance of the position of the Fermi level in the bandgap to describe both carriers' densities. The closer it is to the conduction band, the higher the density of electrons and the lower the density of holes. Inversely if the Fermi level lies close to the valence band.

Notably extrinsic doping is commonly employed to arbitrarily modify the density of carriers. Adding atoms with more valence electrons than the semiconductor will increase the electron density in the conduction band. This is named n doping. Importantly, the Fermi level is displaced accordingly, and the density of holes

lowered. The reverse principle occurs when atoms with less valence electrons are included in the crystal, resulting in p doping.

Importantly, another major factor can cause an increase of electrons and holes density: illumination. The precise mechanism is exposed in the next sub-section. The simultaneous increase of electrons and holes when light is absorbed causes the semiconductor to be at quasi-equilibrium. The new carriers rapidly attain similar energy levels as the other carriers in the crystal (they thermalize) and their energy distribution can be described by a Fermi-Dirac distribution. However, they are not at equilibrium with each-other as it was in the dark.

As a result, two Fermi-Dirac distributions are employed to describe their energy distribution and density, with two quasi-Fermi levels. Importantly, the difference between both quasi-Fermi levels is a crucial quantity to describe the charge carriers' densities. For instance, the product $n \cdot h$ is related to its value in the intrinsic non doped case (noted n_i^2) through the expression:

$$n \cdot p = N_C \, e^{-\frac{E_C - E_{F-n}}{k_B T}} N_V \, e^{-\frac{E_{F-p} - E_V}{k_B T}} \quad (3)$$

$$= N_C N_V \, e^{-\frac{E_C - E_V}{k_B T}} \, e^{-\frac{E_{F-p} - E_{F-n}}{k_B T}} \quad (4)$$

$$= n_i^2 e^{-\frac{\Delta E_F}{k_B T}} \quad (5)$$

Finally, the Fermi level can be interpreted as an electrochemical potential of the electrons. Therefore, the quasi-Fermi levels splitting is usually related to the maximum electrical potential that can be obtained by contacting the semiconductor and perfectly collecting holes and electrons.

1.1.2 Generation, transport and recombination processes

The densities of electrons and holes and their associated quasi-Fermi levels have been exposed in the previous subsection. Now the processes impacting these quantities are presented: generation, transport and recombination [1], [2].

Generation:

Electron – hole pair generation occurs when a photon is absorbed, and its energy is passed to an electron from the valence band to reach the conduction band. The associated bandgap energy threshold explains that only part of the light spectrum with photon energies higher than the bandgap can be absorbed. The capacity of a material to absorb a photon is quantified by its absorption coefficient, noted α, and described by Beers' law:

$$\frac{d\phi(h\nu, x)}{dx} = -\alpha(h\nu)\, \phi(h\nu, x) = G(h\nu, x) \quad (6)$$

$\phi(h\nu, x)$ is the flux of photons with energy $h\nu$ in the material at a depth x. $G(h\nu, x)$ is the photogeneration rate. It is to note that in practice, reflections and refractions occur at interfaces, making the photon flux mor complex to compute across

a device depth. This subject is treated in detail in Section 2.1.1. Finally, a greater absorption coefficient is usually beneficial for a solar cell, as it allows more electron-holes pairs to be generated over a thinner material depth.

Transport:

The role of a solar cell is to collect the photogenerated electrons and holes, in order to produce a current and electrical power. This is possible through drift and diffusion of the charge carriers.

Drift is due to the presence of electrical field, and will drive electrons to lower electrical potential areas, whereas holes will flow towards higher potential. The mobility of the carriers is the characteristic of the material that quantifies the ability of the carriers to move in the material when subjected to an electrical field.

Diffusion is due to a gradient of carrier density, making carriers flow towards areas with lower densities. Here the diffusion coefficient characterize the current flow. Notably both mobilities (μ) and diffusion coefficient (D) are related through Einstein's relation:

$$D = \frac{\mu k_B T}{q} \quad (7)$$

Finally, it is to note that a higher charge carrier mobility will enhance the optoelectrical performances of a solar cells, by facilitating the charge currents. This material characteristic is usually influence by the presence of defects in the crystal, and by the interactions between electrons and the crystal lattice.

Recombination:

Before charge carriers are collected, recombination can occur. Such process is detrimental to the solar cell, as it reduces the current available to produce electrical power. Three types of recombination can occur in a classical semiconductor.

Radiative recombination is the symmetrical process to photogeneration: it is the annihilation of an electron with a hole, with the emission of a photon. The number of recombination is directly proportional to the product of electrons and holes, because one particle of each type is necessary. The recombination rate is therefore expressed as:

$$R_{rad} = B \cdot n \cdot p \quad (8)$$

B is the radiative recombination coefficient of the material. Notably, the emission of a semi-conductor material have been expressed by van Roosbroeck and Shockley, according to thermodynamics (here integrated over all solid angles) [3]:

$$R_{rad} = \int \phi_{out}(h\nu)\, dh\nu = \int \alpha(h\nu) \frac{\Omega\ (h\nu)^2}{4\pi^3 \hbar^3 c^2} \frac{1}{exp\left(\frac{h\nu - \Delta E_F}{k_B T}\right) - 1}\, dh\nu \quad (9)$$

When combining with the expression of $n \cdot p$ through the quasi-Fermi levels splitting, this gives:

$$B = \frac{\Omega}{n_i^2 4\pi^3 \hbar^3 c^2} \int \frac{\alpha(h\nu)\,(h\nu)^2}{exp\left(\frac{h\nu}{k_B T}\right) - 1} dh\nu \quad (10)$$

Importantly, the expression of the radiative recombination rate can be employed to relate a ratio of photoluminescence emission ($\frac{\phi_{tot-B}}{\phi_{tot-A}}$) to a variation of quasi-Fermi levels splitting ($\Delta E_{F-B} - \Delta E_{F-A}$). Importantly it is necessary to assume that the optical behavior of the device remains constant, and $h\nu \gg \Delta E_F$ (usually valid for a photon energy range near the bandgap energy). As a result:

$$\frac{\phi_{tot-B}}{\phi_{tot-A}} = \frac{\int \phi_{out-B}(h\nu)\, dh\nu}{\int \phi_{out-A}(h\nu)\, dh\nu} \quad (11)$$

$$= \frac{\int \frac{\alpha(h\nu) h\nu^2}{exp\left(\frac{h\nu - \Delta E_{F-B}}{k_B T}\right) - 1}\, dh\nu}{\int \frac{\alpha(h\nu) h\nu^2}{exp\left(\frac{h\nu - \Delta E_{F-A}}{k_B T}\right) - 1}\, dh\nu} \quad (12)$$

$$\approx \frac{exp\left(\frac{\Delta E_{F-B}}{k_B T}\right)}{exp\left(\frac{\Delta E_{F-A}}{k_B T}\right)} = exp\left(\frac{\Delta E_{F-B} - \Delta E_{F-A}}{k_B T}\right) \quad (13)$$

This result will be particularly useful to analyze coupled measurements of photoluminescence spectra and JV curves, allowing to compare Voc and quasi-Fermi levels splitting variations along degradation.

The second type of recombination is associated to the presence of localized states inside the bandgap, generally due to defects in the crystal. Such state has an occupation probability that depends on the energy distribution (hence the Fermi level). If it is empty at equilibrium, an electron can fall into and recombine with enhanced probability with a hole, inversely if the state is occupied at equilibrium.

This type of recombination is called Shockley-Read-Hall (SRH), according to the researchers who developed the model describing the associated recombination rate [4], [5]. It is obtained by computing the balance of the possible radiative transfers for electrons and holes. It depends on trap energy level (noted E_t), the quasi-Fermi levels and the capture cross section for electrons and holes (σ_n and σ_p, respectively):

$$R_{SRH} = \frac{np - n_i^2}{\tau_{SRH-p}\left(n + n_i e^{\frac{E_t - E_{F-n}}{k_B T}}\right) + \tau_{SRH-n}\left(p + n_i e^{-\frac{E_t - E_{F-p}}{k_B T}}\right)} \quad (14)$$

With $\tau_{\mathrm{SRH}-n} = \frac{1}{N_t \sigma_n v_{th}}$ and $\tau_{\mathrm{SRH}-p} = \frac{1}{N_t \sigma_p v_{th}}$. Notably, these can be the actual SRH-lifetimes for electrons and holes only in the specific cases where all states are occupied by a hole or an electron respectively.

From the above expression, it appears that the recombination rate is maximum when the trap energy level is at the middle of the bandgap. In such case, one can usually consider $\sigma_n = \sigma_p$, therefore $\tau_{SRH-n} = \tau_{SRH-p} = \tau_{SRH}$. Moreover, by assuming $E_t - \mu_n \ll k_B T$ and $E_t - \mu_p \ll k_B T$, the following simplification can be obtained:

$$R_{SRH} = \frac{1}{\tau_{SRH}} \frac{np - n_i^2}{n + n_i e^{\frac{E_t - \mu_n}{k_B T}} + p + n_i e^{-\frac{E_t - \mu_p}{k_B T}}} \quad (15)$$

$$= \frac{1}{\tau_{SRH}} \frac{np - n_i^2}{2n_i + n + p} \quad (16)$$

A third recombination mechanism exists in semi-conductor materials: Auger recombination. It necessitates the simultaneous presence of three carriers and therefore is observed only with very high densities (usually above 10^{18} cm^{-3}). It is most probably not relevant for perovskite materials [6].

Defects are usually in larger concentration at the surface of a material, due to unpaired atoms at the boundary of the crystal or impurities. The physical processes are the same as for SRH recombination, but broader distribution of trap energy levels are usually present. Therefore, surface recombination velocity is employed as a lumped parameter to compute the total recombination rate for electrons and holes, respectively:

$$R_{S-n} = S_n n \quad (17)$$
$$R_{S-p} = S_p p \quad (18)$$

The surface recombination velocity is a function of the surface defect density (N_{t-S}) and the capture cross section (σ_n and σ_p for electrons and holes respectively): $S_n = \sigma_n \cdot N_{t-S}$ and $S_p = \sigma_p \cdot N_{t-S}$.

Finally, A very useful concept to qualify behavior of charge carriers in a semi-conductor material is their lifetime. It is usually defined by considering a spatially homogenous distribution of carriers. The continuity equation is expressed just after switching off any generation process (for electrons here):

$$\frac{\partial n}{\partial t} = -R = -\frac{n}{\tau_n} \quad (19)$$

However, several definitions and expressions arise from the several recombination process and excitation conditions. Moreover, it is necessary to consider an effective lifetime, due to the joint presence of several processes in parallel:

$$\frac{1}{\tau_{eff}} = \sum_i \frac{1}{\tau_i} \quad (20)$$

In Table 1, the lifetimes associated to radiative and SRH recombination are summarized. Several cases have to be considered, being realistic approximations in specific cases and specific parts of a solar cell. Lifetimes associated to surface recombination are more complex to express, due to the influence of bulk properties, such as bulk lifetime and diffusion lengths. Detailed expressions have been reported in literature in order to interpret time resolved measurements [7].

Table 1. *Carrier lifetimes expressed for different recombination processes and usual specific cases. Note that* $n_1 = n_i e^{\frac{E_t - E_{F0}}{k_B T}}$ *and* $p_1 = n_i e^{-\frac{E_t - E_{F0}}{k_B T}}$, N_D *is the donor density and* N_A *the acceptor density.*

Type of recombination	Specific case	Carrier lifetime
Radiative	General case	$\tau_n = \frac{1}{B(n_0 + p_0 + \Delta n)}$ (21)
		$\tau_p = \frac{1}{B(n_0 + p_0 + \Delta p)}$ (22)
	Low injection	$\tau_n = \tau_p = \frac{1}{B(n_0 + p_0)}$ (23)
	Low injection, n doped	$\tau_p = \frac{1}{BN_D}$ (24)
	Low injection, p doped	$\tau_n = \frac{1}{BN_A}$ (25)
SRH	General case	$\tau_n = \tau_{SRH-p}\frac{n_0 + \Delta n + n_1}{n_0 + p_0 + \Delta n} + \tau_{SRH-n}\frac{p_0 + \Delta p + p_1}{n_0 + p_0 + \Delta n}$ (26)
		$\tau_p = \tau_{SRH-p}\frac{n_0 + \Delta n + n_1}{n_0 + p_0 + \Delta n} + \tau_{SRH-n}\frac{p_0 + \Delta p + p_1}{n_0 + p_0 + \Delta n}$ (27)
	Deep defects, low injection	$\tau_n = \tau_p = \tau_{SRH-p}\frac{n_0}{n_0 + p_0} + \tau_{SRH-n}\frac{p_0}{n_0 + p^0}$ (28)
	Deep defects, n doped	$\tau_p = \tau_{SRH-p}$ (29)
	Deep defects, p doped	$\tau_n = \tau_{SRH-n}$ (30)

The processes exposed in this section control the behavior of electrons and holes in a semi-conductor. In a solar cell, generation is maximized in the absorber by employing a material with a high absorption coefficient and by optimizing the optical behavior of the total stack. On the other hand, recombination is minimized by having as low defects as possible, through optimized fabrication processes.

1.1.3 Types of junctions employed to make solar cells

Finally, the concepts exposed in the previous sub-section allow to understand the working principles of pn and pin junctions. They all consist in juxtaposing oppositely doped materials. Notably, perovskite solar cells are fabricated in the form of a pin structure, where the intrinsic absorber is sandwiched between n and p doped layers,

respectively identified as Electron Transporting Layer (ETL) and Hole Extracting Layer (HTL).

When oppositely doped materials are juxtaposed, majority carriers from each side diffuse towards the opposite material and recombine with local opposite majority carriers. Charged region appears (identified as Space Charge Regions, SCR), in equilibrium with a local electrical field. In fact, this electrical field is specifically in charge of separating photo-generated carriers when the solar cell is under illumination. In Figure 1 top, the associated potential drop appears clearly, driving electrons to the right side contact, and holes to the left side contact. In the example of Figure 1, diffusion plays a significant role in the large p doped region. Here no electrical field is present (flat bands) and the local minority carriers (electrons) will have to diffuse towards the junction and its electrical field to be accelerated towards the n region.

On the contrary, an electrical field is present across the whole intrinsic layer in the pin structure (Figure 1, bottom), facilitating charge carrier separation. However, this electrical field depends on the bias applied to the solar cell (see bottom right), contrary to the pn junction case. As a result, charge collection efficiency is not constant and decreases with applied bias.

Finally, Figure 1 displays how the energy bands evolve when a bias is applied. At short circuit, the electrical field is maximal and almost all carriers are immediately extracted: the current produced by the solar cell is maximal (Jsc). When a positive bias is applied, the band bending is reduced, and carriers are less efficiently extracted. As a result they accumulate, quasi-Fermi level splitting increases, and recombination reduce the output current. However, the electrical potential between carriers extracted at electron and hole contacts increases. Finally, open circuit voltage (Voc) is attained when all photogenerated carriers recombine within the solar cell and no current is produced. Notably, lower quality materials with more recombination will find this point at a lower bias, hence having a lower Voc.

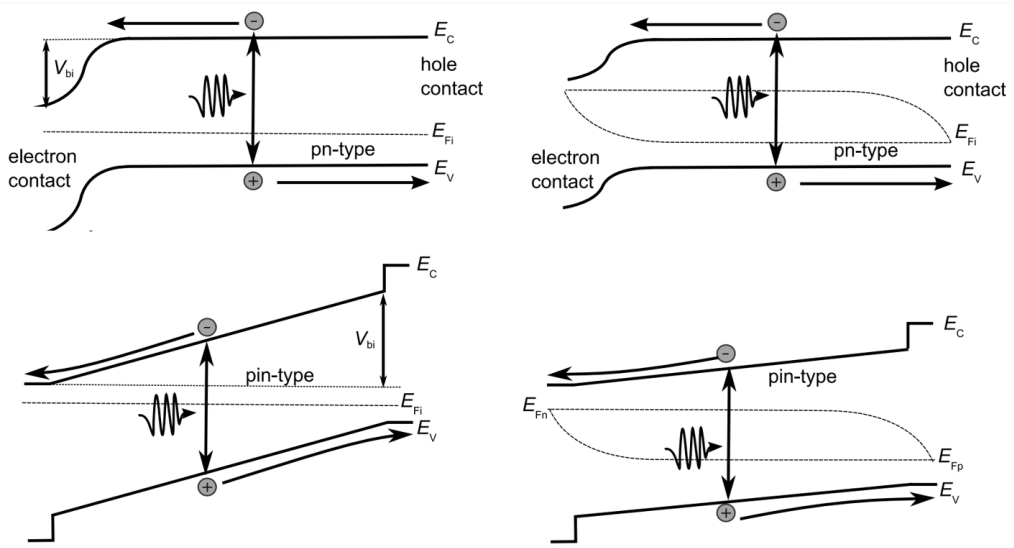

Figure 1. *Band diagram of a pn (top) and pin (bottom) solar cell. Left is at short circuit and right is under a positive bias. Figure is extracted from* [8]

These principles allow to understand the optimization of solar cells. In a pn junction, higher doping allows stronger built-in potential and more efficient charge separation. However, trap energy levels induced by doping impurities enhance SRH recombination and lower carriers' mobility, hindering diffusion through the neutral flat band region.

In the case of perovskite solar cells, high doping of ETL and HTL is used to maximize built in potential. Also, energy levels of the three materials must be carefully adapted to form the right band bending across the perovskite absorber layer.

Finally, high quality materials are always necessary to ensure low defect density, high carrier mobilities, and minimize recombination losses.

1.1.4 Analytical model for a pn homojunction

In order to assess the behavior of a photovoltaic solar cell before performing more complex drift diffusion simulations, the following analytical model has been employed. It is elaborated for a simple pn homojunction displayed in Figure 2: a uniformly n doped layer (length W_{n}, donor density N_D) and a uniformly p doped layer (length W_{p}, acceptor density N_A) are bounded together. They are formed of the same material (absorption coefficient α) and illuminated through the n side with a photon flux ϕ. The model is elaborated by considering that drift currents define the behavior in the doped regions, and SRH recombination are accounted in the space charge region [1], [9].

Notably, it is applied to a different structure from a pin junction perovskite solar cell, without extracting layers and intrinsic absorber. However, it has the advantage to be fully analytical. This will allow to point out the differences and common aspects with a more elaborated numerical model, applied to the more complex perovskite solar cell structure.

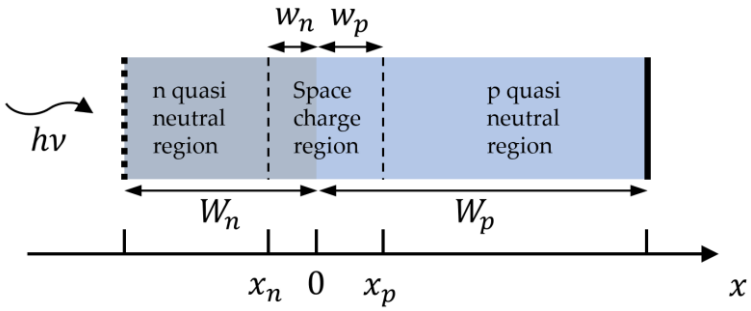

Figure 2. *Considered pn junction and associated x axis. Zero is at the interface and illumination arises upon n doped side.*

First the current extracted from a solar cell, J, is simply expressed from following balance:

$$J = J_G - J_R \quad (31)$$

Where J_G is the photogenerated current and J_R the recombination current. The following section will develop the expressions for both terms.

Size of the space charge region:

As exposed in previous sub-section, a space charge region forms at the interface, due to majority carriers' diffusion. Because of the presence of the electric field, carriers' behavior is different from the rest of the doped regions. This is accounted for in the model, and the size of this space charge region is first computed.

By using the electrical potential continuity, the following expressions are obtained for the space charge regions on n and p doped sides, respectively:

$$w_n = \sqrt{\frac{2\epsilon}{q}\frac{N_A}{N_D}\frac{1}{N_A + N_D}(V_{BI} - V)} \quad (32)$$

$$w_p = \sqrt{\frac{2\epsilon}{q}\frac{N_D}{N_A}\frac{1}{N_A + N_D}(V_{BI} - V)} \quad (33)$$

V_{BI} is the built-in potential, defined as: $V_{BI} = \frac{k_B T}{q} ln\left(\frac{N_D N_A}{n_i^2}\right)$. It is to note that the applied bias is directly playing a role here, by considering negligible electric field in the quasi neutral regions.

Notably, the size of the quasi-neutral regions are expressed as following:

$$W_{nQNR} = W_n - w_n \quad (34)$$
$$W_{pQNR} = W_p - w_p \quad (35)$$

Diffusion lengths:

Furthermore, the minority carrier's diffusion lengths plays a significant role and is expressed from effective carrier lifetime (τ_{eff}) and diffusion coefficient (D):

$$L = \sqrt{D \cdot \tau_{eff}} \quad (36)$$

Importantly carrier lifetime for radiative and SRH recombination has to be considered. For radiative recombination, the low injection hypothesis is employed, for each doped region:

$$\tau_{rad-n} = \frac{1}{BN_A} \quad (37)$$

$$\tau_{rad-p} = \frac{1}{BN_D} \quad (38)$$

Also, deep trap levels are considered, with equal capture cross section and thermal velocity for electrons and holes, the SRH recombination lifetime is therefore equal for both types of carriers:

$$\tau_{SRH} = \tau_{SRH-n} = \tau_{SRH-p} = \frac{1}{N_t \sigma v_{th}} \quad (39)$$

Finally, the effective lifetime is obtained as expressed in previous section. This value will be employed to compute the diffusion lengths employed in the expressions for currents exposed further in this section.

$$\frac{1}{\tau_{eff-n}} = \frac{1}{\tau_{rad-n}} + \frac{1}{\tau_{SRH}} \quad (40)$$

$$\frac{1}{\tau_{eff-p}} = \frac{1}{\tau_{rad-p}} + \frac{1}{\tau_{SRH}} \quad (41)$$

Photocurrent:

In this model, electron-hole pairs are generated along the depth of the solar cell according to the exponential decay of Beer's law. In the quasi neutral regions, diffusion is the limiting factor for minority carriers to reach the electrical field in the space charge region. Moreover, recombination at front and back side are considered, the associated recombination velocity are noted S_{front} and S_{back}, respectively.

At the front n doped side, holes are minority carriers, and the photocurrent is obtained by expressing their diffusion current across a layer of size $W_{\mathrm{n}QNR}$. This current depends on the hole diffusion lengths (noted L_{p}) and diffusion coefficient (noted D_p). Notably the boundary condition at front side is defined by the recombination velocity (noted S_{front}). At the SCR interface it is defined by considering a hole density at zero because they are strongly extracted in the SCR.

$$J_{G-nQNR} = q\phi \frac{\alpha L_p}{\alpha^2 L_p^2 - 1} \left(\frac{\frac{S_{front} L_p}{D_p} + \alpha L_p - \left(\frac{S_{front} L_p}{D_p} cosh\left(\frac{W_{nQNR}}{L_p}\right) + sinh\left(\frac{W_{nQNR}}{L_p}\right) \right) e^{-\alpha W_{nQNR}}}{\frac{S_{front} L_p}{D_p} sinh\left(\frac{W_{nQNR}}{L_p}\right) + cosh\left(\frac{W_{nQNR}}{L_p}\right)} - \alpha L_p e^{-\alpha W_{nQNR}} \right) \quad (42)$$

Similarly, at the back p doped quasi neutral region, electron diffusion current is expressed depending on diffusion length (L_n), diffusion coefficient (D_{n}), and back side recombination velocity (S_{back}).

$$J_{G-pQNR} = q\phi \frac{\alpha L_n}{\alpha^2 L_n^2 - 1} e^{-\alpha(W_n + w_p)} \left(\alpha L_n - \frac{\frac{S_{back} L_n}{D_n} \left(cosh\left(\frac{W_{pQNR}}{L_n}\right) - e^{-\alpha W_{pQNR}} \right) + sinh\left(\frac{W_{pQNR}}{L_n}\right) + \alpha L_n e^{-\alpha W_{pQNR}}}{\frac{S_{back} L_n}{D_n} sinh\left(\frac{W_{pQNR}}{L_n}\right) + cosh\left(\frac{W_{pQNR}}{L_n}\right)} \right) \quad (43)$$

Finally, photocurrent in the space charge region is directly obtained by computing photogeneration, are all carriers are considered to be separated, due to the electrical field:

$$J_{G-SCR} = q\phi e^{-\alpha W_{nQNR}}\left(1 - e^{-\alpha(w_n + w_p)}\right) \quad (44)$$

Importantly, the expressions above are written for a monochromatic illumination, in fact, absorption coefficient (α) and photon flux (ϕ) are wavelength dependent. Therefore, each photocurrent has to be computed for each wavelength, and summed.

Recombination current:

The recombination current is also computed separately in both quasi-neutral regions and in the space charge region. For both quasi neutral regions, it is expressed for the respective minority carrier, from associated diffusion length, diffusion coefficient and surface recombination velocity. For the front n doped quasi neutral region:

$$J_{R-nQNR} = q\frac{D_p n_i^2}{L_p N_D}\frac{\frac{S_{front}L_p}{D_p}cosh\left(\frac{W_{nQNR}}{L_p}\right) + sinh\left(\frac{W_{nQNR}}{L_p}\right)}{\frac{S_{front}L_p}{D_p}sinh\left(\frac{W_{nQNR}}{L_p}\right) + cosh\left(\frac{W_{nQNR}}{L_p}\right)}\left(e^{q\frac{V}{k_B T}} - 1\right) \quad (45)$$

The same expression is employed for the back side p doped region, with the respective parameters for the electron's minority carriers.

Finally, the recombination current in the space charge region is obtained by integrating SRH recombination current over its total width. However, it varies significantly, due to strong variations of carrier densities across its length. Therefore, the integral is approximated by the product of an effective length, w_{eff}, and the maximum value of the recombination rate. It is noted $R_{SRH-max}$, derived from equation (15) where np is expressed from equation (5). Importantly, its maximum is attained when $n + p$ is minimum. Due to the product $n \cdot p$ being constant, it corresponds to $n = p = n_i e^{q\frac{V}{2k_B T}}$, therefore:

$$R_{SRH-max} = \frac{1}{\tau_{SRH}}\frac{n_i^2\left(e^{q\frac{V}{k_B T}} - 1\right)}{2n_i\left(1 + e^{q\frac{V}{2k_B T}}\right)} \approx \frac{1}{\tau_{SRH}}\frac{n_i}{2}e^{q\frac{V}{2k_B T}} \quad (46)$$

Moreover, the effective length is approximated here by considering that this maximum value is constant over a range of variation of the potential of $\frac{k_B T}{q}$. This corresponds to a fraction of the total potential variation across the space charge region

(V_{bi}) of $\frac{k_B T}{q V_{bi}}$. Therefore: $w_{eff} = \frac{(w_p + w_n)}{\frac{q\,V_{bi}}{k_B T}}$. This estimation overestimates SRH recombination, providing an upper limit of its value. As a result:

$$J_{R-SCR} = q \frac{1}{\tau_{SRH}} \frac{n_i}{2} \frac{\left(w_p + w_n\right)}{\frac{q\,V_{bi}}{k_B T}} e^{q\frac{V}{2k_B T}} \quad (47)$$

The output current of the solar cell is finally obtained by adding all the terms expressed above. This model allows to describe the solar cell behavior with fewer parameters than drift diffusion simulation, they are summarized in Table 2. This advantage will be used to compare results derived from both models in parallel, and discuss the advantages and drawbacks associated to more elaborated numerical simulations, applied to a more complex perovskite solar cell structure.

Table 2. *Summary of the 14 input parameters necessary for the analytical model defined in this section.*

Parameter	Description
ϕ	Photon flux entering at the front interface
α	Absorption coefficient
ϵ	Permittivity
W_n, W_p	Size of the n and p doped materials.
n_i^2	Product of intrinsic carrier densities
D_p, D_n	Diffusion coefficients for holes and electrons
B	Radiative recombination coefficient.
N_D, N_A	Donor and acceptor densities in the n and p doped materials.
S_{front}, S_{back}	Front and back side recombination velocity
τ_{SRH}	SRH recombination lifetime

Finally, it is to note that such analytical approach is very useful to relate measured optoelectrical parameters to material characteristic such as recombination regimes. For instance it allows to define general principles governing solar cells performances [10] and decipher some aspects of perovskite reversible degradation processes [11].

1.2 Perovskite solar cells

Perovskite solar cells are a vast family of structures, all having in common an absorbed made of a perovskite material. The absorber is usually not doped, and electron and hole extracting layers (ETL and HTL respectively) are employed to form a pin junction. The role and working principles of such junction have been exposed in the previous section.

Notably, a front transparent electrode is employed, usually a transparent conductive oxide (TCO), and metallic contact at the back.

1.2.1 Perovskite materials

Perovskites are materials having a chemical formula of the type ABX_3 (A is a cation, B a metal and X an anion), the associated cubic crystal is represented Figure 3 (left). In order to fabricate solar cells, lead-halide perovskite materials are widely employed: the B site metal is lead and the X site anion is a halide, such as iodine or bromine. Organic cations such as Methylammonium (MA) or Formamidinium (FA) are frequently employed at A site, but the inorganic cesium cation is also common. Importantly, mixed composition perovskites are also employed, usually by having alternating cations at A site, or X site halide anion [12].

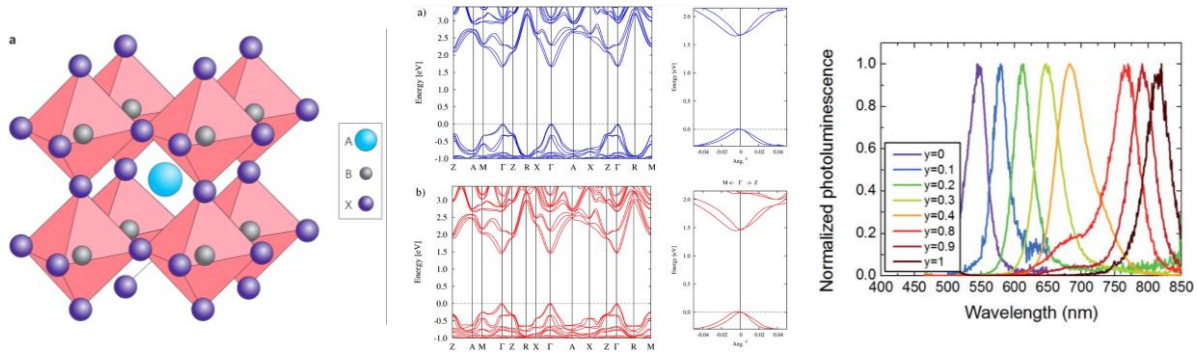

Figure 3. *Left: single crystal of perovskite with cubic structure* [12]. *Middle: band structure of exemplary compositions with two A site cations: $MAPbI_3$ and $FAPbI_3$, top and bottom respectively* [13]. *Right: photoluminescence emission spectra of $FAPbI_yBr_{3-y}$ thin films* [14].

First, modifying the nature or ratios of constituents allows to modify the bandgap from 1.5 to 2.5 eV [15]. In Figure 3 (middle), the changes in band structure are displayed for two compositions, having Methylammonium or Formamidinium as A site organic cations. The similarity of the bands indicates that both materials are very close, with only a shift in bandgap energy [13]. Furthermore, changing the X site halide also modifies the bandgap energy [14], [16], as showed through PL emission spectra having shifted peaks in Figure 3 (right), illustrating the wide achievable range of bandgap energies.

Halide perovskites also have a direct bandgap (see Figure 3, middle). This strongly impacts the mechanism of light absorption in the semi-conductor, making the absorption coefficient in perovskites significantly higher. As a result, only a small

quantity of material is needed to absorb light, and thin layers of several hundreds of nanometers are usually employed.

Not only optical properties of perovskites makes them interesting for solar cells, but they also show good electrical properties for charge carrier transport and extraction. For instance, halide perovskites have a high relative permittivity, making the exciton biding energy relatively low (values reported in literature vary from 2 meV to 80 meV) [6], and therefore easy separation of carriers [17].

Furthermore, this high relative permittivity makes holes and electrons to behave independently, reducing radiative recombination. Moreover, perovskites are not doped, and carrier densities remain low. In such conditions, Auger recombination (needing the meeting of three carriers) is also of low influence [6]. As a result, carrier recombination in perovskites are mainly determined by SRH processes and defect densities in crystals and grain boundaries [18]–[20]. Therefore, carrier lifetime depends greatly on film deposition.

Charge carrier mobilities in perovskites films can also attain relatively high values. For instance ,the sum of both carrier mobilities has been measured to reach approx. 30 $cm^2.V^{-1}.s^{-1}$ [21]. However, a wide range of values are in fact reported in literature, and also low values of 0.1 $cm^2.V^{-1}.s^{-1}$ have been measured [22]. This variability has been associated to "extrinsic" factors that hinder charge transport, such as grain boundaries or impurities. These effects are distinct from the interaction of the charge carrier with the lattice, which is intrinsic to the material [23].

Finally, large values in the range of 100 nm [24] or even more than 1 μm have already been reported in literature [22], greatly sufficient to collect carriers created in a 500 nm thick layer and assuring high collection efficiencies.

These elements show how metal halide perovskite materials attracted interest as good candidates to provide low cost and highly efficient thin film solar cells. Notably it also appears that several of the good properties of the films are greatly dependent on deposition process, grain boundaries and material quality. This is the motivation for the use of the specific simulation procedures employed further in this work.

1.2.2 Electron and hole transporting materials

A first requirement for the transport layers is the energy bands alignment with the perovskite. Holes will face a potential barrier to the extraction if the valence band maximum is lower in the HTL than in the perovskite. Symmetrically, electrons extraction will be hindered if the conduction band is higher in the ETL than the perovskite.

However, it has also been demonstrated that in the presence of interface defects, recombination are enhanced by a large band offset (too high HTL valence band or too low ETL conduction band). Therefore, a theoretical optimum has been determined to be between 0 and 0.2 eV for HTL valence band offset, and between 0 and 0.3 eV for ETL band offset [25] (Spiro-OMeTAD, $MAPbI_{3-x}Cl_x$ and TiO_2 were considered). Moreover, it has even been demonstrated that even a small, inversed band offset could

be beneficial, in the specific case of SnO_2 ETL / $FA_{0.85}MA_{0.15}PbI_3$ perovskite interface [26].

Notably, the extracting layers must also play the role of blocking layers. For instance, the HTL should have low electron affinity, to show a large potential barrier to the electrons in the perovskite. The symmetrical aspect applies for the ETL.

Good carrier transport is also necessary to maximize collection at the electrode. Notably, the materials usually employed have lower mobilities than the perovskite absorber. Therefore, improving the material conductivity through doping can be very helpful. In fact, it also reduces the potential drop across the layer. This, in turn, facilitates carrier flow through the layer, and confines the total voltage drop within the perovskite layer [27]. Notably, these aspects also motivates to employ as thin HTL and ETL layers as possible (usually several tens of nanometers).

In addition to the requirements mentioned here, the front extracting layer needs to have a sufficiently wide bandgap, to transmit most of the light spectrum to the perovskite. Furthermore, it has to be possible to sequentially deposit the films with good morphologies, surface coverage and low interface defects. Therefore, the chemistry between the different materials and deposition temperatures have to be compatible. In fact, significant work has been done to passivate the associated interfaces, by considering various treatments and buffer layers [28], [29].

Materials employed to fabricate hole transporting materials are most frequently organic: for instance spiro-OMeTAD, PEDOT:PSS and PTAA [30]. However, inorganic materials are also investigated, such as NiOx and CuSCN, as they could provide cheaper and more stable alternatives [31], [32].

It is to note that significantly different values have been reported in literature for the hole mobility in these materials. For instance, values down to 10^{-5} $cm^2.V^{-1}.s^{-1}$ have been reported for spiro-OMeTAD thin films [33] and between 10^{-5} [34] and 10^{-2} $cm^2.V^{-1}.s^{-1}$ [35] for PTAA. In fact, this variability has been associated to differences in solvent or material purity, and film deposition techniques [36]. The doping level also plays a significant role here, as hole mobility in NiO_x has been reported to increase from 10^{-3} to 10^{-2} $cm^2.V^{-1}.s^{-1}$ through copper doping [32]. In addition, the extrinsic doping employed can't always be quantified precisely in terms of acceptor density [27].

On the side of electron transporting materials, oxides are frequently employed, such as TiO2, SnO2 or ZnO. For instance, their mobility has been reported to be approx. $1.7x10^{-2}$, $3x10^{-3}$ and $4x10^{-3}$ $cm^2.V^{-1}.s^{-1}$ in thin films [37]. These values attain 1, 250 and 200 $cm^2.V^{-1}.s^{-1}$ respectively in single crystals, according to the same authors. This striking example shows the influence of film morphology, grain boundaries, and therefore deposition technique, in defining the materials properties. Furthermore, several doping elements (for instance Al, Li, Nb or Mg) can be employed, yielding in different doping levels and potentially increasing carrier mobility [38].

As a result, the characteristics of both HTL and ETL can vary significantly from one deposition technique to the other, or one sample to the other. Again, this is a motivation to develop the statistical approach employed in this work to simulate the performances of the solar cells.

1.3 Stability of perovskite solar cells

The characteristics of the materials making perovskite solar cells highly efficient solar cells have been exposed in previous section. However, the long term stability of these device is now a major concern. In this section, the various possible aging mechanisms reported in literature are exposed, and it appears that all materials and interfaces can be the site of degradation. Furthermore, the main techniques employed to assess this stability and investigate degradation causes are exposed.

1.3.1 Reported degradation mechanisms of perovskite solar cells

Numerous studies have reported various degradation mechanisms of perovskite solar cells, potentially enhanced by several environmental stressors: temperature, humidity, light, oxygen and even applied external bias [39]–[43]. The associated mechanisms are exposed in this sub-section.

Temperature:

The main impact of temperature on perovskite material is related to the stability of its crystallinity. In fact, perovskites can usually crystalize into three different phases, depending on temperature. At low temperature, most compositions crystalize into an orthorhombic phase (not photoactive), tetragonal phase (photoactive) at intermediate temperature and cubic phase (photoactive, with best semi-conductor properties) at higher temperatures. The phase transition temperatures depend on the composition and the sizes of the A, B and X constituents [42]. This is a first thermodynamic instability source, when phase transitions occur within usual operation temperature ranges. In some cases the thermodynamically stable phase at ambient temperature is not cubic, and annealing is employed to obtain this phase. This is the case for the classical $MAPbI_3$, for which the transition between tetragonal and cubic phases occurs at 54 °C. Mixed compositions can be employed to avoid such issue. For instance the triple cations composition employed in IPVF, $FA_{0.75}MA_{0.15}Cs_{0.1}Pb(I_{0.83}Br_{0.17})_3$, have the same transition at 25 °C [40].

Beyond the thermodynamics of the crystal, elevated temperature will enhance most of any other degradation mechanism. Importantly, ionic migrations can be favored through expanded or distorted crystal lattice, and more lose bounds [44].

It will be exposed further in this section how halides can migrate across the perovskite layer, upon light exposure or applied bias. In fact, they have already been observed to migrate towards the metallic back contact, simply due to their high reactivity. This causes degradation of the perovskite material, and corrosion of the metallic contact [40]. Here temperature activates the process. Moreover, in n-i-p configurations, iodide can reduce the oxidation level of Spiro-MeOTAD, reducing its conductivity [45]. Notably, the contrary migration has also been reported, with metal diffusion towards the perovskite, inducing defects at its interface [46].

Perovskites are not the only materials having potentially detrimental phase transitions. Organic HTLs have been reported to degrade at high temperatures,

through crystallization or even evaporation [47]. Notably doping additives can enhance this phenomenon, by lowering for instance the crystallization temperature of spiro-MeOTAD from 100 °C to 85 °C [36].

Humidity:

The second major degradation factor for perovskite solar cells is water. It can easily enter the films and crystals and form hydrate phases. Grain boundaries have been reported to be major pathways for water ingress and the starting point of such degradation [48]. In fact the organic cations usually employed, MA and FA are acidic and polar, making them easily interact and even react with water. The formation of monohydrate or dihydrate phases is reversible in theory. However, they have weaker bonds between A site cation and the rest of the crystal, making them prone to various decomposition mechanisms [42]. For instance, the acid-base reaction between water and organic cation can be followed by a transfer of the proton to I^- and finally formations of gaseous CH_3NH_2 and HI. Only the widely reported decomposition product, PbI_2, is left. In fact, FA and Cs are alternative cations to MA that has been employed for their lower acidity and reactivity with water. Alloys of the three cations showed best stability.

Notably, thiocyanate (SCN) has been employed to improve the resistance to water. It replaces I- anions and forms stronger bonds with Pb^{2+}. As a result, the crystal structure is stronger, and formation of hydrate phases is hindered.

Finally, the perovskite layer in not necessarily protected, when included in a solar cell stack. In fact, the usual Li-doped spiro-MeOTAD and PTAA are hygroscopic. They have been demonstrated to attract water into the solar cell and facilitate its penetration through pinholes. As a result, perovskite degradation is enhanced. Even ETL oxides play a role here: SnO_2 has been for instance pointed out for its better resistance to water ingress (lower hygroscopicity) compared to TiO_2. It has already been considered to be a cause of improved device stability [38], [49].

Light:

Some degradation processes have also been reported to be triggered by illumination [50]. For instance, reversible halide segregation have been reported to occur under illumination, with a return to original state when samples are put back in dark [39]. A shifting of PL emission spectrum towards lower energies evidenced the presence of I-rich phases and their smaller bandgap. Notably they would locally enhance radiative recombination and reduce performances. Light is explained to favor this halide segregation by an oxidizing effect of holes on iodide. The smaller size of resulting neutral iodine would facilitate interstitials and form iodide vacancies [51].

Cation migrations could also be triggered by illumination, as reported in FA-MA-Cs triple cations perovskite [40]. Cesium cations have been observed to redistribute across the perovskite towards HTL interface when the solar cell is under illumination. Importantly, changing the TiO_2 ETL to SnO_2 did prevent cation redistributions [28].

Importantly, UV light is a major cause of degradation for ETL such as TiO_2. It causes desorption of oxygen at its surface, that normally passivates oxygen vacancies [40]. As a result, devices rapidly suffer from enhanced interface recombination. Even degradation of perovskite material have been reported [52]. Replacing TiO_2 by SnO_2 is now commonly done to successfully avoid this type of degradation [53].

Oxygen:

The presence of oxygen have also been reported as triggering degradation of the perovskite materials [54]. In the presence of illumination, oxygen coupled with photogenerated electrons could form the superoxide O_2^-, which in turn reacts with acidic cations (MA^+ for instance) and lead. The water formed can even trigger further degradation mechanisms. Notably, oxidized lead in the form of $Pb(OH)_2$ could act as a caping layer, confining degradation at the grain boundaries [51]. However, it is still not clear how protective this layer would be in the presence of other degradation factors . Moreover, larger perovskite grains and passivated defects have been showed to slow this reaction down and for instance, iodide vacancies help the diffusion of oxygen and serve as reaction sites [55].

Applied external bias:

When an external bias is applied to a perovskite solar cell, the change in internal electric field does not only change the charge carrier currents, but it also impact mobile ions. Their nature, mobilities and densities are investigated in numerous studies [56], [57]. It appears now that that A site interstitials cations and X site halide vacancies and interstitials anions could be the most important ones [58].

Importantly, these ions act as dopants, and induce low SRH recombination because of associated shallow trap states [59]. As a result, a first impact is current voltage hysteresis, caused by different ionic redistributions when different biases are applied.

When the applied bias is lower than the solar cell built-in potential, “negative accumulation” occurs: positive ions move towards HTL interface and negative ions towards ETL. Positive ions act as donor dopants and a localized pn junction forms at the HTL interface. The symmetrical phenomenon occurs at the opposite interface. As a result, the built-in electrical field that normally spans across the perovskite layer is screened. Furthermore, interface recombination are enhanced by the larger electron and hole densities near HTL and ETL interfaces respectively, resulting in lower Voc, Jsc and FF [60].

On the contrary, “positive accumulation” occurs when the applied bias is superior to the built in potential. Ions flow in the reverse direction, the internal electric field is enhanced, and the solar cell show improved JV characteristics. However, strong positive accumulation has been showed to reduce Jsc. This has been interpreted as unfavorable band bending when the perovskite becomes too n or p doped near ETL or HTL respectively.

Several factors could enhance migrations, such as humidity and illuminations, that have been associated to phase segregations. For instance, reversible degradation has been observed under dark-light cycles. Strikingly, both opposite cases with recovery or further degradation under dark have been reported. In fact, the bias applied to the solar cells has been explained to cause the different ionic accumulations, inducing the opposite behaviors under dark [61]. Furthermore, film morphology also plays a role, as grain boundaries could be channels for ionic transport. Even if the processes mentioned here are reversible, they could induce long term degradation through formation of deep defects at interfaces or in the bulk [62], [63].

Table 3. *Summary of the degradation mechanisms of perovskite solar cells and their impact on the material parameters (in the context of drift diffusion simulation of the solar cells).*

Degradation mechanism	Environmental factor	Impacted material parameters
Perovskite phase transition.	Temperature	Carrier mobilities and defects density. Eventually change of nature of the material: bandgap and energy bands levels, permittivity.
Reaction between perovskite halide and metallic contact.	Temperature, illumination, applied bias	Defect density in perovskite bulk and interfaces, carrier mobilities.
Reduction of HTL by perovskite halide.	Temperature, illumination, applied bias	Carrier mobilities and doping level in HTL.
Crystallization or evaporation of HTL	Temperature	Carrier mobility and doping level in HTL. Eventually destruction of the material.
Formation of hydrate phases.	Humidity, temperature.	Defect density in perovskite bulk and interfaces, carrier mobilities.
Acid-base reaction of A site cation with water.	Humidity, temperature.	Defect density in perovskite bulk and interfaces, carrier mobilities. Eventually destruction of the material.
Phase segregation.	Illumination, humidity, applied bias, temperature.	Defect density in perovskite bulk and interfaces, carrier mobilities. Bandgap and energy bands levels.
TiO_2 photo-degradation.	Illumination, temperature.	Interface defects, carrier mobility and doping level in ETL.
Photo-oxidation of perovskite.	Illumination, oxygen, temperature.	Defect density in perovskite bulk and interfaces, carrier mobilities. Eventually destruction of the material.
Ionic migrations.	Applied bias, illumination, humidity, temperature.	Carrier mobilities, local doping level and permittivity. Might induce defects in bulk and interfaces on long term.

The various mechanisms reported in this section, and the several triggering factors explain the complexity of investigating the stability of perovskite solar cells. The mechanisms are summarized in Table 3. Notably, it appears that all layers of the solar cell stack and their interfaces can degrade. This situation makes it crucial to distinguish the mechanisms or at least the layer or interface in cause.

Finally, numerous studies focus now on improving device stability through various methods. Composition tuning of the perovskite material can enhance the crystal stability [64], for instance through larger A site cation. The ultimate point achieves 2D perovskite structures, that have better stability than 3D but poorer semi-conductor properties [39]. Combinations of both are therefore employed [65]. The precursors stoichiometry can help to adjust densities of interstitials and vacancies [66]. Finally, additives are also employed to reduce defect densities in grains or at boundaries, improve film morphology and make devices less prone to degradation.

Improving adjacent layers and interfaces is also necessary because they often degrade. New ETL and HTL materials are now selected for their enhanced stability. For instance, tuning the hydrophobicity of the hole transport layer makes the solar cell more resistant to water induced degradation [67]. Combining materials [53] or using inorganic HTL such as NiO_x [31] or replacing TiO_2 with SnO_2 are examples [68].

Furthermore, interface passivation is key not only for performances, but also for stability. It has been exposed that several degradation processes start at the interfaces [63], [69] and for instance, passivation has been showed to reduce ion migrations [51]. Therefore, self-assembling monolayers, and other passivating layers are now intensely studied [29], [70], [71].

Finally, encapsulation enhances stability by preventing reactive species such as water and oxygen to enter the solar cell [41]. Moreover, gaseous decomposition products are also retained at the reaction site, which blocks its advancement [72], [73].

1.3.2 Characterization techniques to study stability and degradation

Perovskite solar cells stability have been investigated through various approaches, all improving the understanding of the various degradation mechanisms exposed in the previous sub section.

The first widely used method is to precisely characterize the materials and interfaces composing the device before and after degradation. As exposed above, the various degradation mechanisms can be specifically triggered by aging conditions. Under operation, perovskite solar cells will face cyclical variations of illumination, temperature and humidity. Importantly, all aspects (even the periodicity and the coupling of factors) play a role in aging mechanisms. Therefore, the best conditions to assess the reliability of perovskite solar cells should be outdoor testing. However, distinguishing the impact of the distinct environmental factors is also useful [74], and it not always possible to place samples under the harsh outdoor conditions. Therefore, procedures inspired from ISOS protocols (already officially defined for other technologies) and adapted for the specific mechanism of perovskite solar cells have

been proposed to the research community [75], they are listed in Figure 4. Notably three levels ranked in harshness and implementation complexity are defined for each category, allowing to progressively couple factors and degrade the solar cells.

Table 1 | Overview of existing ISOS protocols and suggested additional protocols that account for the properties of perovskite materials and devices

Test ID	Light source	Temperature	Rel. humidity	Environment/Set-up	Characterization light source	Load
Dark storage (ISOS-D)						
ISOS-D-1	None	Ambient (23 ± 4 °C)	Ambient	Ambient air	Solar simulator or sunlight	OC
ISOS-D-2	None	65, 85 °C	Ambient	Oven, ambient air	Solar simulator	OC
ISOS-D-3	None	65, 85 °C	85%	Env. chamber	Solar simulator	OC
Bias stability (ISOS-V)						
ISOS-V-1	**None**	**Ambient (23 ± 4 °C)**	**Ambient**	**Ambient air**	**Solar simulator**	**Positive: V_{MPP}; V_{oc}; E_g/q; J_{SC} Negative: $-V_{oc}$, J_{MPP}[a]**
ISOS-V-2	**None**	**65, 85 °C**	**Ambient**	**Oven, ambient air**	**Solar simulator**	
ISOS-V-3	**None**	**65, 85 °C**	**85%**	**Env. chamber**	**Solar simulator**	
Light-soaking (ISOS-L)						
ISOS-L-1	Solar simulator	Ambient (23 ± 4 °C)	Ambient	Light only	Solar simulator	MPP or OC
ISOS-L-2	Solar simulator	65, 85 °C	Ambient	Light & temperature	Solar simulator	MPP or OC
ISOS-L-3	Solar simulator	65, 85 °C	~50%	Light, temperature & RH	Solar simulator	MPP
Outdoor stability (ISOS-O)						
ISOS-O-1	Sunlight	Ambient	Ambient	Outdoor	Solar simulator	MPP or OC
ISOS-O-2	Sunlight	Ambient	Ambient	Outdoor	Sunlight	MPP or OC
ISOS-O-3	Sunlight	Ambient	Ambient	Outdoor	Sunlight and Solar simulator	MPP
Thermal cycling (ISOS-T)						
ISOS-T-1	None	RT to 65, 85 °C	Ambient	Hot plate/ oven	Solar simulator	OC
ISOS-T-2	None	RT to 65, 85 °C	Ambient	Oven/env. chamber	Solar simulator	OC
ISOS-T-3	None	−40 to + 85 °C	**< 55%**[b]	Env. chamber	Solar simulator	OC
Light cycling (ISOS-LC)						
ISOS-LC-1	**Solar simulator/ Dark Cycle period: 2, 8, or 24 h Duty cycle: 1:1 or 1:2**	**Ambient (23 ± 4 °C)**	**Ambient**	**Light only**	**Solar simulator**	**MPP or OC**
ISOS-LC-2		**65, 85 °C**	**Ambient**	**Light & temperature**	**Solar simulator**	**MPP or OC**
ISOS-LC-3		**65, 85 °C**	**< 50%**	**Light, temperature & RH**	**Solar simulator**	**MPP**
Solar-thermal cycling (ISOS-LT)						
ISOS-LT-1	Solar simulator	Linear or step ramping between room temp. and 65 °C	Monitored, uncontrolled	Weathering chamber	Solar simulator	MPP or OC
ISOS-LT-2	Solar simulator	Linear ramping between 5 °C and 65 °C	Monitored, controlled at 50% beyond 40 °C	Env. chamber with sun simulator	Solar simulator	MPP or OC
ISOS-LT-3	Solar simulator	Linear ramping between −25 °C and 65 °C	Monitored, controlled at 50% beyond 40 °C	Env. chamber with sun simulator and freezing	Solar simulator	MPP or OC

Each test group is divided into three levels of sophistication that reflect the complexity of required equipment and the harshness of the applied stress. Reported ISOS protocols are taken from ref. [1]. Proposed additional ISOS protocols are printed in bold. [a]V_{OC}, V_{MPP}, and J_{MPP} are determined from light *J–V* curves measured under standard solar cell testing conditions on a fresh device. E_g and q are the band gap of the active layer and elementary charge, respectively. [b]Relative humidity is controlled at temperatures above 40 °C and is not controlled for the remainder of the cycle. Env., environmental; OC, open-circuit condition; MPP, maximum power point; RT, room temperature; RH, relative humidity.

Figure 4. *List of proposed aging protocols proposed in* [75]*, inspired from existing ISOS standards and adapted to the specific degradation mechanisms of perovskite solar cells.*

In order to investigate the response of perovskite solar cells to these environmental stressors, various characterization techniques are employed [76]. The most frequent ones are summarized in Figure 5, and two categories can be distinguished.

On one side, optoelectrical performances are assessed for instance through JV characteristics measurements, or photo-luminescence spectroscopy. These are indicators of the solar cell photovoltaic behavior and its output power.

On the other side, various techniques are employed to determine characteristics of the materials and interfaces. They can quantify changes in chemistry (or composition) of the materials, morphology of the films and variations in band structure. Some of these techniques are sufficiently spatially resolved to detect uniformities [77], [78], others can probe along depth and therefore also investigate interfaces [79].

As a result, numerous studies combining these characterization techniques could correlate the degradation of solar cells performances to identified material or interfaces changes [80], [81]. It is to note, however, that this approach only demonstrates the coincidence between material changes and photovoltaic performances degradations, not the causality.

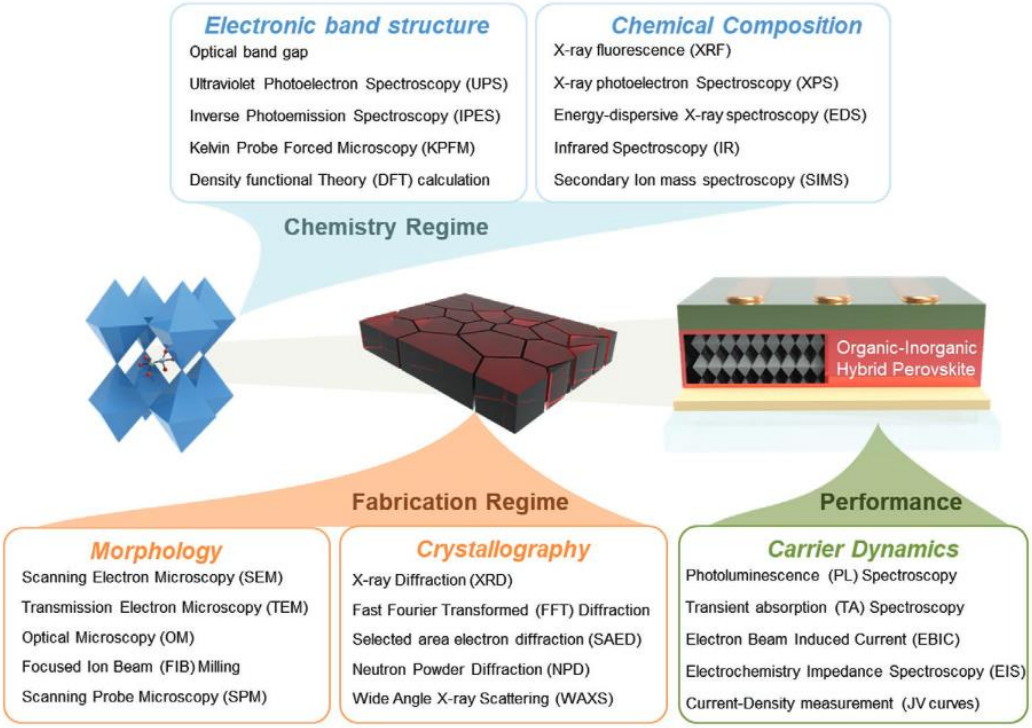

Figure 5. *Summary of main characterization techniques employed to investigate perovskite solar cells stability. Extracted from* [76]

Importantly, the next step in this approach is to characterize the solar cells along aging, not only before and after degradation. This relies on "in-situ" characterization setups that are more and more employed to simultaneously probe structural, compositional, morphological, and optoelectronic changes in real-time. [82].

In fact, periodical records of JV curves along aging are commonly employed to assess the stability of the solar cells. Actually, most advances in perovskite solar cell fabrication are now simultaneously reported in terms of power conversion efficiency, and stability of the JV performances over time [83]–[85]. Such data are, however, often

used only to determine an end-of-life time, or the duration needed to reach a given lower limit, without analyzing dynamics of degradation.

Notably, chemical kinetics approaches have been employed to take more advantage of such measurements. Reaction rates associated to the decays of optoelectrical parameters are determined, and temperature activation (or through other environmental factors) can be assessed [86], [87]. Such approach can employ models to extrapolate from accelerated tests to long term evolution the solar cell performances and even provide predictions of lifetime and produced energy [88]. However, the identification of the underlying degradation mechanism cannot be easily done.

1.4 Models to investigate perovskite solar cells stability

The various degradation mechanisms exposed in the previous section can be triggered by several environmental factors and have dramatic impacts on the solar cell performances. Employing models is therefore useful to better understand the physical and chemical processes at stake.

First, models based on the kinetical aspects of degradation are employed to take advantage of aging measurements. They can allow to determine activation energies, interpret accelerated tests and make predictions on energy production. However, they rely on the assumption that the same mechanism is being observed at the several temperatures. Moreover, this approach can difficultly allow to understand the physical processes and impacts on photovoltaic performances of the degrading solar cells.

Therefore, drift diffusion simulations are usually employed to specifically investigate these impacts on charge carrier generation, transport and recombination. They allow to study the role of each material and interface. However, they can be time consuming and necessitate numerous input parameters.

Finally, more and more approaches employed now are data-oriented, through statistics or machine learning algorithms. An overview of the models and approaches reported in literature is given in this section.

1.4.1 Time dependent models

A first approach employed to investigated degradation is based on temperature activation of most physical processes and associated Arrhenius law. Activation through other conditions, such as illumination has also been considered [89], [90], but less frequently employed to model experimental data. As a result, the reaction rate is usually determined at several temperatures by fitting the temporal evolution of indicators of degradation with kinetics expressions. Notably, a hypothesis on the reaction order is necessary. The degradation indicators are usually JV parameters [86], but others such as XRD peak area [91], [92] can also be employed. When the activation energy is obtained, it provides the acceleration factor to extrapolate the reaction rate at any temperature. As a result, solar cell lifetimes can be assessed [87].

This approach has been interestingly expanded when applied to Voc, Jsc and FF with distinct reaction orders and activation energies. This allows the discussion on potential different processes impacting the optoelectrical parameters. Finally, this model was employed to predict the output power of the perovskite solar cell under several climates, having different temperatures [88].

In fact, prediction of energy production have already been done by employing simple phenomenological degradation rates. With such macroscopic approach, more complex systems such as perovskite – silicon tandems and even economic consideration can be considered [93].

In a more device physics oriented manner, analytical models such as presented in Section 1.1.4 can be combined with time dependent expression of given parameters

(that are assumed to degrade). This approach has been employed to fit the experimental degradation of solar cells JV curves, with time dependent doping levels and space charge region. It provides an interesting reproduction of the observed degradation, but the simplicity of the model (pn junction versus pin experimental structure) makes the interpretation difficultly reliable [94].

1.4.2 Drift diffusion based approaches

In order to investigate deeper the physics of the solar cells, it can be necessary to account for the dynamics of the charge carriers. Drift-diffusion models rely on the local equations governing the behavior of charge carriers: the Poisson equation and the continuity equation. Importantly, the formulation of charge carrier currents in the continuity equation accounts for both drift and diffusion phenomena. Through this approach, the materials characteristics actually defining the performance of the device are considered, and therefore, the causality with degradation mechanisms can be investigated.

Notably, the drift-diffusion expressions are time dependent and can be fully solved to study the dynamics of carriers before reaching steady state. Usually, time resolved characterization techniques are employed in parallel, such as time resolved photo-luminescence [95]. Although such studies can investigate deeply the charge carrier transport and recombination processes, characterizations considered in this work, such as JV curves are in fact recorded under steady state. Therefore, drift diffusion simulations done in this work and most of those reported in this section are under steady state.

In a first step, such simulations are frequently employed to assess the performances of a solar cell with given materials. Studies of the optimization of layer characteristics are numerous and they provide useful insights on the role of drift diffusion input parameters in the case perovskite solar cells [96]–[98]. In fact, the 1D simulation tool employed in this work, SCAPS-1D, has allowed a lot of these studies through its easy and simple use [99].

Importantly, the behavior of the charge carriers is completely resolved, it is therefore possible to reproduce results of various characterization techniques. Not only JV characteristics can be investigated, but also for instance impedance spectroscopy [100], [101], photoluminescence spectroscopy [102] and space charge limited current [103]. Importantly, combining several techniques allows to probe complementary operating regimes of the solar cells, and therefore resolve better the responsible material characteristics.

A first intensely studied aspect is the role of ion migrations on hysteresis of JV characteristics. This necessitates the coupling of ion transport equations and electrons – holes drift diffusion equations [104]–[107]. The associated intensive work as to be acknowledge, because of numerical complexity induced by the large difference between ions and electrons or holes transport timescales. Moreover, a locally finer spatial resolution is necessary to resolve ion accumulation gradients.

For instance, such simulations have been employed to show how ionic accumulation near interface could modify local doping, screen electric field and cause observed JV hysteresis [108], [109]. Notably, the role of extracting layers, through their doping and permittivity, has also been demonstrated [104]. Furthermore, the reversible degradation observed under dark-light cycles with opposite recovery cases under dark or illumination, could be rationalized by simulating the impact of applied bias [61].

In some cases, fabricating more complex structures than the typical solar cell can be useful to probe some properties. For instance with planar structures with both contacts at the back, or lateral junctions. In such case, the usual 1D approximation cannot be done, and drift diffusion simulations provide precious tools to understand better the more complex electric field in such device [102], [110], [111].

Importantly, in the studies reported here, the coupling between ions and electron – holes behavior is done through the Poisson equation the electrical potential. Moreover, constant mobile ion densities are considered. This is crucial to explain JV hysteresis but might not be sufficient to investigate long term degradation. For instance, generation of mobile ions would be consistent with observed behavior under illumination. Interactions between ions and opposite charge carrier, potentially producing a neutral atom or molecule might be to consider as well. Such processes would allow to investigate the long term degradation of perovskite solar cells performances, related to ionic migrations.

Notably, approaches have been reported, by considering oxidation of halides by holes and reduction by electrons. Through first order chemical reactions, the density of interstitial species and associated defect density is related to the operating regime of the solar cells [107], [112], [113]. This paves the way for further investigations of long term impact of ionic migrations.

Large advances in the understanding of the perovskite solar cells hysteresis and reversible processes has been possible through the studies reported here. It is to note, however, that supplementary degrees of freedom arise, such as the densities of mobile species and their diffusion coefficients. Their values are poorly known and can probably vary significantly from sample to sample. Moreover, the precise nature of the reactions responsible for the generation or annihilation of mobile species is still under study, and their reaction rates even less known. Therefore, investigating the long term degradation of the solar cells through these mechanisms is still a hugely interesting open research field. In this work, it has been chosen not to focus on the perovskite layer, but also consider transport layers. No mobile ions were included in the simulations to avoid associated parameters assumptions and cover more broadly the various degradation processes in the solar cells.

1.4.3 Statistical and machine learning approaches

Data oriented approaches are getting a growing interest in photovoltaic research field, thanks to the development of machine learning algorithms and neural networks [114]. The rising data availability is a significant factor, and initiatives have been

proposed to construct global open-access databases with uniformed reporting of various device results of perovskite solar cells [115].

For instance, such large database has been necessary for the training neural networks employed to predict the bandgap of perovskite materials based on their composition [116]. Here the machine learning tools provide powerful elaborated regressions of the data.

At the device scale, a large number of material parameters define the photovoltaic behavior. This precisely constitute a difficulty when employing theoretical oriented approaches such as drift diffusion simulations. Therefore, machine learning algorithms can be employed to find the values of relevant material parameters. For instance, Bayesian parameter estimation is a powerful technique that has been applied to time resolved photoluminescence measurements to determine the underlying carrier mobilities, surface recombination velocities and carrier lifetime [117]. Similarly, tree-based methods (single decision tree and random forest) has allowed to find the major recombination process in perovskite solar cells (radiative, SRH or at interfaces). The algorithms were applied to JV parameters, including diode ideality factor and in some cases, material parameters such as doping levels and carrier mobilities [118]. Importantly, both studies reported here employed drift diffusion simulations to construct their training databases.

The degradation of perovskite solar cells provides interesting tasks for machine learning approaches because of the complexity of the numerous physical and chemical processes at play. As a result, no complete theoretical model can easily be developed and employed, and in some cases machine learning algorithms are more simply and rapidly developed.

For instance, it has been possible to predict the T_{80} (the time elapsed for the solar cell efficiency to drop to 80 % of its initial value) with 40 % accuracy by employing a hybrid machine learning approach. It is to note that the models' inputs were not only device characteristics and ambient conditions parameters. A theoretical model for the water induced decomposition rate of $MAPbI_3$, and its results passed to the machine learning algorithms. This simplification of the problem allows a higher accuracy but restrict the applicability of the model to water induced degradation [119].

Furthermore the ability of neural networks to tackle time series and complex non-linear behavior constitute significant strength. This would justify their use to tackle the reversible degradation behavior of perovskite solar cells and for instance identify cycles of degradation followed by recovery [120]. In another example, neural networks have also been employed to identify and distinguish steps of degradation from transient photocurrent measurements [121].

Interestingly, statistics over sufficiently large datasets can be employed to verify the validity of simplified models. For instance, the validity of a theoretical threshold required for the doping level of the ETL and HTL could be verified by simulating 10 000 cases (again with drift diffusion) and by comparing the FF distributions when the doping threshold is satisfied or not [27].

Notably, machine learning tools have been developed to determine the underlying analytical expression behind experimental data. It has been claimed that the Hamiltonian and Lambertian describing the motion behavior of physical systems had been discovered by analyzing motion-tracking data [122]. One could imagine that such tools could help to find and discuss the doping level threshold investigated in the previous example. Models describing the degradation of the samples could also be proposed.

Principal components analysis is also a powerful tool in the context of highly dimensional problems with numerous parameters. In fact, its main use is to reduce the number of variables in a dataset, by expressing components that are orthogonal to each other [123]. It can be employed as a pre-processing step to reduce the number of inputs passed to a machine learning algorithm [120], [124]. In the field of photovoltaics, principal components analyses have been employed in energy production forecasting. Again, in conjunction with other machine learning algorithms [125].

These examples show how machine learning algorithms attract interest and support the investigation of perovskite solar cells degradation. In some cases, almost no theoretical knowledge on device physics or chemistry seems to be necessary. However, it is to note that the best performing, and most explanatory approaches relied on theoretical models. Moreover, data oriented approaches and statistics can help to evaluate the validity of new models and provide insights on the underlying relations between physical parameters. As a result, the hybrid approaches combining machine learning and theory might have the most added value to construct general knowledge on the physics and chemistry of perovskite solar cells.

Chapter conclusion

Perovskite cells attract a great interest in the photovoltaic research community. Devices attain high power conversion efficiency, and improving their stability is becoming a key aspect in current works. This chapter exposed the elements in cause for these two aspects.

First the necessary concepts of semiconductor and solar cell physics have been exposed in Section 1.1, to be able to explain the good performances of perovskite solar cells. With a direct bandgap and high absorption coefficient, good charge carrier mobilities and long diffusion lengths, perovskites are very promising semiconductor materials for photovoltaic applications. Moreover, the possibility to tune their bandgap through mixed compositions opens optimization possibilities for tandem applications. These aspects are exposed in Section 1.2, together with relevant characteristics of the usual materials employed as transport layers.

However, a significant variability of the material properties is reported in literature. For the perovskite material, thin film quality and morphology depend on deposition process, which impacts relevant semiconductor parameters such as defect densities and carrier mobilities. Moreover, the ETL and HTL materials have also been reported with variable qualities, having different doping levels and carrier mobilities for instance. Importantly, these aspects constitute the motivation to employ the statistical approach exposed in Chapter 3.

Furthermore, numerous chemical and physical processes are responsible for the rapid degradation of optoelectrical performances of the perovskite solar cells, as reported in Section 1.3. First, various triggering environmental factors have been reported: temperature, humidity, light, oxygen and applied bias. The perovskite material itself can for instance react with water, or face phase segregation upon light or applied bias. Moreover, the materials employed to fabricate HTL can also be sensitive to elevated temperature, and ETL materials such as TiO_2 can be photo-oxidized. Even detrimental coupling effects can occur, with for instance migrating halides from the perovskite material that can reduce the HTL material on their way to react with the metallic contact. These examples recall the various sites where degradation can occur: in fact, at every layer and interface. Therefore, the work exposed here in Chapter 4 aims specifically at helping to distinguish degradation mechanisms through their impact on performances.

The existence of various processes with various impacts on optoelectrical performances is at the source of numerous studies in the research community. In Section 1.4, the modeling approaches employed to investigate these issues have been reported. Drift-diffusion simulations have now significantly helped to understand ionic migrations and their impact on the solar cell's performances. However, it is still not clear how coupling ionic and electronic transport will help to investigate long-term degradation. Therefore, the approach employed in this work, exposed in Chapter 2, do not employ such coupling. It focuses therefore on the distinction of degradation mechanisms taking place in the whole solar cell: in any layer or at any interface.

References

[1] Henry Mathieu, *Physique des semiconducteurs et des composants électroniques*, 2nd edition. Masson, 1990.

[2] P. Wurfel and U. Wurfel, *Physics of solar cells: from basic principles to advanced concepts*. 2016.

[3] W. Van Roosbroeck and W. Shockley, "Photon-radiative recombination of electrons and holes in germanium," *Physical Review*, vol. 94, no. 6, pp. 1558–1560, 1954, doi: 10.1103/PhysRev.94.1558.

[4] W. Shockley and W. T. Read, "Statistics of the recombinations of holes and electrons," *Physical Review*, vol. 87, no. 5, pp. 835–842, 1952, doi: 10.1103/PhysRev.87.835.

[5] R. N. Hall, "Electron-hole recombination in germanium," *Physical Review*, vol. 87, no. 2, p. 387, 1952, doi: 10.1103/PhysRev.87.387.

[6] J. Huang, Y. Yuan, Y. Shao, and Y. Yan, "Understanding the physical properties of hybrid perovskites for photovoltaic applications," *Nat Rev Mater*, vol. 2, 2017, doi: 10.1038/natrevmats.2017.42.

[7] T. P. Weiss, B. Bissig, T. Feurer, R. Carron, S. Buecheler, and A. N. Tiwari, "Bulk and surface recombination properties in thin film semiconductors with different surface treatments from time-resolved photoluminescence measurements," *Sci Rep*, vol. 9, no. 1, p. 5385, 2019, doi: 10.1038/s41598-019-41716-x.

[8] T. Kirchartz, *Generalized detailed balance theory of solar cells*, vol. 38. Forschungszentrum Jülich, 2009.

[9] K. L. Chopra and S. R. Das, *Thin Film Solar Cells*, 1st ed. Boston, MA: Springer US, 1983. doi: 10.1007/978-1-4899-0418-8.

[10] T. Kirchartz and U. Rau, "What Makes a Good Solar Cell ?," *Adv Energy Mater*, vol. 8, no. 28, p. 1703385, 2018, doi: 10.1002/aenm.201703385.

[11] W. Tress *et al.*, "Interpretation and evolution of open-circuit voltage, recombination, ideality factor and subgap defect states during reversible light-soaking and irreversible degradation of perovskite solar cells," *Energy Environ Sci*, vol. 11, no. 1, pp. 151–165, 2018, doi: 10.1039/c7ee02415k.

[12] M. A. Green, A. Ho-Baillie, and H. J. Snaith, "The emergence of perovskite solar cells," *Nat Photonics*, vol. 8, no. 7, pp. 506–514, 2014, doi: 10.1038/nphoton.2014.134.

[13] A. Amat *et al.*, "Cation-induced band-gap tuning in organohalide perovskites: Interplay of spin-orbit coupling and octahedra tilting," *Nano Lett*, vol. 14, no. 6, pp. 3608–3616, 2014, doi: 10.1021/nl5012992.

[14] G. E. Eperon, S. D. Stranks, C. Menelaou, M. B. Johnston, L. M. Herz, and H. J. Snaith, "Formamidinium lead trihalide: A broadly tunable perovskite for efficient planar heterojunction solar cells," *Energy Environ Sci*, vol. 7, no. 3, pp. 982–988, 2014, doi: 10.1039/c3ee43822h.

[15] P. Roy, A. Ghosh, F. Barclay, A. Khare, and E. Cuce, "Perovskite Solar Cells: A Review of the Recent Advances," *Coatings*, vol. 12, no. 8, 2022, doi: 10.3390/coatings12081089.

[16] J. Werner *et al.*, "Complex Refractive Indices of Cesium-Formamidinium-Based Mixed-Halide Perovskites with Optical Band Gaps from 1.5 to 1.8 eV," *ACS Energy Lett*, vol. 3, no. 3, pp. 742–747, 2018, doi: 10.1021/acsenergylett.8b00089.

[17] Q. Lin, A. Armin, R. C. R. Nagiri, P. L. Burn, and P. Meredith, "Electro-optics of perovskite solar cells," *Nat Photonics*, vol. 9, no. 2, pp. 106–112, 2015, doi: 10.1038/nphoton.2014.284.

[18] G. J. A. H. Wetzelaer, M. Scheepers, A. M. Sempere, C. Momblona, J. Ávila, and H. J. Bolink, "Trap-Assisted Non-Radiative Recombination in Organic-Inorganic Perovskite Solar Cells," *Advanced Materials*, vol. 27, no. 11, pp. 1837–1841, 2015, doi: 10.1002/adma.201405372.

[19] A. Musiienko *et al.*, "Defects in Hybrid Perovskites: The Secret of Efficient Charge Transport," *Adv Funct Mater*, vol. 31, no. 48, 2021, doi: 10.1002/adfm.202104467.

[20] Y. Yamada, T. Nakamura, M. Endo, A. Wakamiya, and Y. Kanemitsu, "Photocarrier Recombination Dynamics in Perovskite CH3NH3PbI3 for Solar Cell Applications," *J Am Chem Soc*, vol. 136, no. 33, pp. 11610–11613, 2014, doi: 10.1021/ja506624n.

[21] E. M. Hutter, G. E. Eperon, S. D. Stranks, and T. J. Savenije, "Charge Carriers in Planar and Meso-Structured Organic-Inorganic Perovskites: Mobilities, Lifetimes, and Concentrations of Trap States," *Journal of Physical Chemistry Letters*, vol. 6, no. 15, pp. 3082–3090, 2015, doi: 10.1021/acs.jpclett.5b01361.

[22] S. D. Stranks *et al.*, "Electron-Hole Diffusion Lengths Exceeding 1 Micrometer in an Organometal Trihalide Perovskite Absorber," *Science (1979)*, vol. 342, no. 6156, pp. 341–344, 2013, doi: 10.1126/science.1243982.

[23] L. M. Herz, "Charge-Carrier Mobilities in Metal Halide Perovskites: Fundamental Mechanisms and Limits," *ACS Energy Lett*, vol. 2, no. 7, pp. 1539–1548, 2017, doi: 10.1021/acsenergylett.7b00276.

[24] G. Xing *et al.*, "Long-range balanced electron-and hole-transport lengths in organic-inorganic CH3NH3PbI3," *Science (1979)*, vol. 342, no. 6156, pp. 344–347, 2013, doi: 10.1126/science.1243167.

[25] T. Minemoto and M. Murata, "Theoretical analysis on effect of band offsets in perovskite solar cells," *Solar Energy Materials and Solar Cells*, vol. 133, pp. 8–14, 2015, doi: 10.1016/j.solmat.2014.10.036.

[26] Y. Raoui, H. Ez-Zahraouy, S. Kazim, and S. Ahmad, "Energy level engineering of charge selective contact and halide perovskite by modulating band offset: Mechanistic insights," *Journal of Energy Chemistry*, vol. 54, pp. 822–829, 2021, doi: 10.1016/j.jechem.2020.06.030.

[27] V. M. Le Corre *et al.*, "Charge Transport Layers Limiting the Efficiency of Perovskite Solar Cells: How to Optimize Conductivity, Doping, and Thickness,"

ACS Appl Energy Mater, vol. 2, no. 9, pp. 6280–6287, 2019, doi: 10.1021/acsaem.9b00856.

[28] J. A. Christians *et al.*, "Tailored interfaces of unencapsulated perovskite solar cells for >1,000 hour operational stability," *Nat Energy*, vol. 3, no. 1, pp. 68–74, 2018, doi: 10.1038/s41560-017-0067-y.

[29] Z. W. Gao, Y. Wang, and W. C. H. Choy, "Buried Interface Modification in Perovskite Solar Cells: A Materials Perspective," *Adv Energy Mater*, vol. 12, no. 20, p. 2104030, 2022, doi: 10.1002/aenm.202104030.

[30] Z. H. Bakr, Q. Wali, A. Fakharuddin, L. Schmidt-Mende, T. M. Brown, and R. Jose, "Advances in hole transport materials engineering for stable and efficient perovskite solar cells," *Nano Energy*, vol. 34, pp. 271–305, 2017, doi: 10.1016/j.nanoen.2017.02.025.

[31] H. H. Park, "Efficient and stable perovskite solar cells based on inorganic hole transport materials," *Nanomaterials*, vol. 12, no. 1, p. 112, 2022, doi: 10.3390/nano12010112.

[32] D. Huang, H. Xiang, R. Ran, W. Wang, W. Zhou, and Z. Shao, "Recent Advances in Nanostructured Inorganic Hole-Transporting Materials for Perovskite Solar Cells," *Nanomaterials*, vol. 12, no. 15, p. 2592, 2022, doi: 10.3390/nano12152592.

[33] T. Leijtens, I. K. Ding, T. Giovenzana, J. T. Bloking, M. D. McGehee, and A. Sellinger, "Hole transport materials with low glass transition temperatures and high solubility for application in solid-state dye-sensitized solar cells," *ACS Nano*, vol. 6, no. 2, pp. 1455–1462, 2012, doi: 10.1021/nn204296b.

[34] H. D. Pham, T. C. J. Yang, S. M. Jain, G. J. Wilson, and P. Sonar, "Development of Dopant-Free Organic Hole Transporting Materials for Perovskite Solar Cells," *Adv Energy Mater*, vol. 10, no. 13, 2020, doi: 10.1002/aenm.201903326.

[35] J. H. Heo *et al.*, "Efficient inorganic-organic hybrid heterojunction solar cells containing perovskite compound and polymeric hole conductors," *Nat Photonics*, vol. 7, no. 6, pp. 486–491, Jun. 2013, doi: 10.1038/nphoton.2013.80.

[36] F. M. Rombach, S. A. Haque, and T. J. Macdonald, "Lessons learned from spiro-OMeTAD and PTAA in perovskite solar cells," *Energy Environ Sci*, vol. 14, no. 10, pp. 5161–5190, 2021, doi: 10.1039/d1ee02095a.

[37] P. Tiwana, P. Docampo, M. B. Johnston, H. J. Snaith, and L. M. Herz, "Electron mobility and injection dynamics in mesoporous ZnO, SnO 2, and TiO2 films used in dye-sensitized solar cells," *ACS Nano*, vol. 5, no. 6, pp. 5158–5166, Jun. 2011, doi: 10.1021/nn201243y.

[38] L. Xiong *et al.*, "Review on the Application of SnO2 in Perovskite Solar Cells," *Adv Funct Mater*, vol. 28, no. 35, p. 1802757, Aug. 2018, doi: 10.1002/adfm.201802757.

[39] S. P. Dunfield *et al.*, "From Defects to Degradation : A Mechanistic Understanding of Degradation in Perovskite Solar Cell Devices and Modules," *Adv Energy Mater*, vol. 10, no. 26, p. 1904054, 2020, doi: 10.1002/aenm.201904054.

[40] C. C. Boyd, R. Cheacharoen, T. Leijtens, and M. D. McGehee, "Understanding Degradation Mechanisms and Improving Stability of Perovskite Photovoltaics," *Chem Rev*, vol. 119, no. 5, pp. 3418–3451, 2019, doi: 10.1021/acs.chemrev.8b00336.

[41] I. Mesquita, L. Andrade, and A. Mendes, "Perovskite solar cells: Materials, configurations and stability," *Renewable and Sustainable Energy Reviews*, vol. 82, no. July 2017, pp. 2471–2489, 2018, doi: 10.1016/j.rser.2017.09.011.

[42] S. Mazumdar, Y. Zhao, and X. Zhang, "Stability of Perovskite Solar Cells: Degradation Mechanisms and Remedies," *Frontiers in Electronics*, vol. 2, Aug. 2021, doi: 10.3389/felec.2021.712785.

[43] X. Qin, Z. Zhao, Y. Wang, J. Wu, Q. Jiang, and J. You, "Recent progress in stability of perovskite solar cells," *Journal of Semiconductors*, vol. 38, no. 1, p. 011002, Jan. 2017, doi: 10.1088/1674-4926/38/1/011002.

[44] J. W. Lee, S. G. Kim, J. M. Yang, Y. Yang, and N. G. Park, "Verification and mitigation of ion migration in perovskite solar cells," *APL Mater*, vol. 7, no. 4, p. 041111, 2019, doi: 10.1063/1.5085643.

[45] S. Kim *et al.*, "Relationship between ion migration and interfacial degradation of CH3NH3PbI3 perovskite solar cells under thermal conditions," *Sci Rep*, vol. 7, no. 1, p. 1200, 2017, doi: 10.1038/s41598-017-00866-6.

[46] S. Cacovich *et al.*, "Gold and iodine diffusion in large area perovskite solar cells under illumination," *Nanoscale*, vol. 9, no. 14, pp. 4700–4706, 2017, doi: 10.1039/C7NR00784A.

[47] A. D. Sheikh *et al.*, "Effects of High Temperature and Thermal Cycling on the Performance of Perovskite Solar Cells: Acceleration of Charge Recombination and Deterioration of Charge Extraction," *ACS Appl Mater Interfaces*, vol. 9, no. 40, pp. 35018–35029, 2017, doi: 10.1021/acsami.7b11250.

[48] J. Hidalgo *et al.*, "Moisture-Induced Crystallographic Reorientations and Effects on Charge Carrier Extraction in Metal Halide Perovskite Solar Cells," *ACS Energy Lett*, vol. 5, no. 11, pp. 3526–3534, 2020, doi: 10.1021/acsenergylett.0c01964.

[49] Jiaxing Song *et al.*, "Low-temperature SnO2-based electron selective contact for efficient and stable perovskite solar cells," *J Mater Chem A Mater*, vol. 3, no. 20, pp. 10837–10844, 2015, doi: 10.1039/C5TA01207D.

[50] D. R. Ceratti *et al.*, "The pursuit of stability in halide perovskites: The monovalent cation and the key for surface and bulk self-healing," *Mater Horiz*, vol. 8, no. 5, pp. 1570–1586, 2021, doi: 10.1039/D1MH00006C.

[51] J. Wei *et al.*, "Mechanisms and Suppression of Photoinduced Degradation in Perovskite Solar Cells," *Adv Energy Mater*, vol. 11, no. 3, pp. 35–37, 2021, doi: 10.1002/aenm.202002326.

[52] T. Leijtens, G. E. Eperon, S. Pathak, A. Abate, M. M. Lee, and H. J. Snaith, "Overcoming ultraviolet light instability of sensitized TiO2 with meso-superstructured organometal tri-halide perovskite solar cells," *Nat Commun*, vol. 4, Dec. 2013, doi: 10.1038/ncomms3885.

[53] M. Abuhelaiqa, N. Shibayama, X. X. Gao, H. Kanda, and M. K. Nazeeruddin, "SnO2/TiO2 Electron Transporting Bilayers: A Route to Light Stable Perovskite Solar Cells," *ACS Appl Energy Mater*, vol. 4, no. 4, pp. 3424–3430, 2021, doi: 10.1021/acsaem.0c03185.

[54] D. Messou *et al.*, "Stability of triple cation halide perovskites layers: study of the chemical evolution after light soaking thanks to XPS analysis," in *2020 47th IEEE Photovoltaic Specialists Conference (PVSC)*, 2021, pp. 1628–1631. doi: 10.1109/pvsc45281.2020.9300642.

[55] N. Aristidou *et al.*, "Fast oxygen diffusion and iodide defects mediate oxygen-induced degradation of perovskite solar cells," *Nat Commun*, vol. 8, no. 1, p. 15218, 2017, doi: 10.1038/ncomms15218.

[56] P. Lopez-Varo *et al.*, "Device Physics of Hybrid Perovskite Solar cells: Theory and Experiment," *Adv Energy Mater*, vol. 8, no. 14, p. 1702772, May 2018, doi: 10.1002/aenm.201702772.

[57] J. Y. Huang, Y. W. Yang, W. H. Hsu, E. W. Chang, M. H. Chen, and Y. R. Wu, "Influences of dielectric constant and scan rate on hysteresis effect in perovskite solar cell with simulation and experimental analyses," *Sci Rep*, vol. 12, no. 1, p. 7927, Dec. 2022, doi: 10.1038/s41598-022-11899-x.

[58] C. Eames, J. M. Frost, P. R. F. Barnes, B. C. O'Regan, A. Walsh, and M. S. Islam, "Ionic transport in hybrid lead iodide perovskite solar cells," *Nat Commun*, vol. 6, Jun. 2015, doi: 10.1038/ncomms8497.

[59] T. Shi, W. J. Yin, F. Hong, K. Zhu, and Y. Yan, "Unipolar self-doping behavior in perovskite CH3NH3PbBr3," *Appl Phys Lett*, vol. 106, no. 10, Mar. 2015, doi: 10.1063/1.4914544.

[60] D. A. Jacobs *et al.*, "Hysteresis phenomena in perovskite solar cells: The many and varied effects of ionic accumulation," *Physical Chemistry Chemical Physics*, vol. 19, no. 4, pp. 3094–3103, 2017, doi: 10.1039/c6cp06989d.

[61] M. Prete *et al.*, "Bias-dependent dynamics of degradation and recovery in perovskite solar cells," *ACS Appl Energy Mater*, vol. 4, no. 7, pp. 6562–6573, Jul. 2021, doi: 10.1021/acsaem.1c00588.

[62] D. B. Khadka, Y. Shirai, M. Yanagida, and K. Miyano, "Degradation of encapsulated perovskite solar cells driven by deep trap states and interfacial deterioration," *J Mater Chem C Mater*, vol. 6, no. 1, pp. 162–170, 2018, doi: 10.1039/c7tc03733c.

[63] M. Spalla, L. Perrin, E. Planes, M. Matheron, S. Berson, and L. Flandin, "Effect of the Hole Transporting/Active Layer Interface on the Perovskite Solar Cell Stability," *ACS Appl Energy Mater*, vol. 3, no. 4, pp. 3282–3292, Apr. 2020, doi: 10.1021/acsaem.9b02281.

[64] J. Xu *et al.*, "Triple-halide wide-band gap perovskites with suppressed phase segregation for efficient tandems," *Science (1979)*, vol. 367, no. 6482, pp. 1097–1104, 2020.

[65] G. Grancini *et al.*, "One-Year stable perovskite solar cells by 2D/3D interface engineering," *Nat Commun*, vol. 8, p. 15684, 2017, doi: 10.1038/ncomms15684.

[66] M. Al Katrib, E. Planes, and L. Perrin, "Effect of Chlorine Addition on the Performance and Stability of Electrodeposited Mixed Perovskite Solar Cells," *Chemistry of Materials*, vol. 34, no. 5, pp. 2218–2230, 2022, doi: 10.1021/acs.chemmater.1c04021.

[67] C. Xu, Z. Liu, and E. C. Lee, "Stability and efficiency improved perovskite solar cells through tuning the hydrophobicity of the hole transport layer with an organic semiconductor," *J Mater Chem C Mater*, vol. 9, no. 2, pp. 679–686, 2021, doi: 10.1039/D0TC05113F.

[68] M. Spalla, E. Planes, L. Perrin, M. Matheron, S. Berson, and L. Flandin, "Alternative Electron Transport Layer Based on Al-Doped ZnO and SnO2 for Perovskite Solar Cells: Impact on Microstructure and Stability," *ACS Appl Energy Mater*, vol. 2, no. 10, pp. 7183–7195, Oct. 2019, doi: 10.1021/acsaem.9b01160.

[69] W. Nie *et al.*, "Critical Role of Interface and Crystallinity on the Performance and Photostability of Perovskite Solar Cell on Nickel Oxide," *Advanced Materials*, vol. 30, no. 5, p. 1703879, 2018, doi: 10.1002/adma.201703879.

[70] X. Zhao *et al.*, "Accelerated aging of all-inorganic, interface-stabilized perovskite solar cells," *Science (1979)*, vol. 377, no. 6603, pp. 307–310, 2022, doi: 10.1126/science.abn5679.

[71] C. Jiang *et al.*, "Double Layer Composite Electrode Strategy for Efficient Perovskite Solar Cells with Excellent Reverse-Bias Stability," *Nanomicro Lett*, vol. 15, no. 1, p. 12, Dec. 2023, doi: 10.1007/s40820-022-00985-4.

[72] L. Shi *et al.*, "Gas chromatography-mass spectrometry analyses of encapsulated stable perovskite solar cells," *Science (1979)*, vol. 368, no. 6497, pp. 1–14, 2020, doi: 10.1126/science.aba2412.

[73] L. Shi *et al.*, "Accelerated Lifetime Testing of Organic-Inorganic Perovskite Solar Cells Encapsulated by Polyisobutylene," *ACS Appl Mater Interfaces*, vol. 9, no. 30, pp. 25073–25081, 2017, doi: 10.1021/acsami.7b07625.

[74] K. Domanski, E. A. Alharbi, A. Hagfeldt, M. Grätzel, and W. Tress, "Systematic investigation of the impact of operation conditions on the degradation behaviour of perovskite solar cells," *Nat Energy*, vol. 3, no. 1, pp. 61–67, 2018, doi: 10.1038/s41560-017-0060-5.

[75] M. V. Khenkin *et al.*, "Consensus statement for stability assessment and reporting for perovskite photovoltaics based on ISOS procedures," *Nat Energy*, vol. 5, no. 1, pp. 35–49, 2020, doi: 10.1038/s41560-019-0529-5.

[76] M. cheol Kim, S. Y. Ham, D. Cheng, T. A. Wynn, H. S. Jung, and Y. S. Meng, "Advanced Characterization Techniques for Overcoming Challenges of Perovskite Solar Cell Materials," *Adv Energy Mater*, vol. 11, no. 15, p. 2001753, 2021, doi: 10.1002/aenm.202001753.

[77] O. R. Yamilova, "Revealing electrochemical degradation pathways in complex lead halides and design of stable perovskite solar cells," Skolkovo Institute of Science and Technology, Moscow, 2023.

[78] G. Vidon *et al.*, "Mapping transport properties of halide perovskites via short time dynamics scaling laws and sub-nanosecond time resolution imaging," *Phys Rev Appl*, vol. 16, no. 4, p. 44058, 2021, doi: 10.1103/PhysRevApplied.16.044058.

[79] S. Cacovich *et al.*, "In-Depth Chemical and Optoelectronic Analysis of Triple-Cation Perovskite Thin Films by Combining XPS Profiling and PL Imaging," *ACS Appl Mater Interfaces*, vol. 14, no. 30, pp. 34228–34237, 2022, doi: 10.1021/acsami.1c22286.

[80] E. Planes, L. Perrin, M. Matheron, M. Spalla, S. Berson, and L. Flandin, "Degradation Mechanisms in a Mixed Cations and Anions Perovskite Solar Cell: Mitigation Effect of the Gold Electrode," *ACS Appl Energy Mater*, vol. 4, no. 2, pp. 1365–1376, Feb. 2021, doi: 10.1021/acsaem.0c02613.

[81] S. Cacovich *et al.*, "Light-induced passivation in triple cation mixed halide perovskites: Interplay between transport properties and surface chemistry," *ACS Appl Mater Interfaces*, vol. 12, no. 31, pp. 34784–34794, Aug. 2020, doi: 10.1021/acsami.0c06844.

[82] S. Kundu and T. L. Kelly, "In situ studies of the degradation mechanisms of perovskite solar cells," *EcoMat*, vol. 2, no. 2, p. e12025, 2020, doi: 10.1002/eom2.12025.

[83] J. Peng *et al.*, "Nanoscale localized contacts for high fill factors in polymer-passivated perovskite solar cells," *Science (1979)*, vol. 371, no. 6527, pp. 390–395, 2021, doi: 10.1126/science.abb8687.

[84] J. Xu *et al.*, "Triple-halide wide-band gap perovskites with suppressed phase segregation for efficient tandems," *Science (1979)*, vol. 367, no. 6482, pp. 1097–1104, 2020, doi: 10.1126/science.aaz5074.

[85] M. Jeong *et al.*, "Stable perovskite solar cells with efficiency exceeding 24.8% and 0.3-V voltage loss," *Science (1979)*, vol. 369, no. 6511, pp. 1615–1620, 2020, doi: 10.1126/science.abb7167.

[86] J. Lim *et al.*, "Kinetics of light-induced degradation in semi-transparent perovskite solar cells," *Solar Energy Materials and Solar Cells*, vol. 219, p. 110776, 2021, doi: 10.1016/j.solmat.2020.110776.

[87] J. Kim, N. Park, J. S. Yun, S. Huang, M. A. Green, and A. W. Y. Ho-Baillie, "An effective method of predicting perovskite solar cell lifetime–Case study on planar CH3NH3PbI3 and HC(NH2)2PbI3 perovskite solar cells and hole transfer materials of spiro-OMeTAD and PTAA," *Solar Energy Materials and Solar Cells*, vol. 162, pp. 41–46, 2017, doi: 10.1016/j.solmat.2016.12.043.

[88] J. P. Bastos *et al.*, "Model for the Prediction of the Lifetime and Energy Yield of Methyl Ammonium Lead Iodide Perovskite Solar Cells at Elevated Temperatures," *ACS Appl Mater Interfaces*, vol. 11, no. 18, pp. 16517–16526, 2019, doi: 10.1021/acsami.9b00923.

[89] R. De Bettignies, J. Leroy, M. Firon, and C. Sentein, "Accelerated lifetime measurements of P3HT:PCBM solar cells," *Synth Met*, vol. 156, no. 7–8, pp. 510–513, 2006, doi: 10.1016/j.synthmet.2005.06.016.

[90] T. D. Siegler *et al.*, "Water-Accelerated Photooxidation of CH3NH3PbI3 Perovskite," *J Am Chem Soc*, vol. 144, no. 12, pp. 5552–5561, Mar. 2022, doi: 10.1021/jacs.2c00391.

[91] E. Smecca *et al.*, "Stability of solution-processed MAPbI3 and FAPbI3 layers," *Physical Chemistry Chemical Physics*, vol. 18, no. 19, pp. 13413–13422, 2016, doi: 10.1039/c6cp00721j.

[92] W. Tan, A. R. Bowring, A. C. Meng, M. D. McGehee, and P. C. McIntyre, "Thermal Stability of Mixed Cation Metal Halide Perovskites in Air," *ACS Appl Mater Interfaces*, vol. 10, no. 6, pp. 5485–5491, Feb. 2018, doi: 10.1021/acsami.7b15263.

[93] J. Qian, M. Ernst, N. Wu, and A. Blakers, "Impact of perovskite solar cell degradation on the lifetime energy yield and economic viability of perovskite/silicon tandem modules," *Sustain Energy Fuels*, vol. 3, no. 6, pp. 1439–1447, 2019, doi: 10.1039/c9se00143c.

[94] I. Moeini, M. Ahmadpour, A. Mosavi, N. Alharbi, and N. E. Gorji, "Modeling the time-dependent characteristics of perovskite solar cells," *Solar Energy*, vol. 170, no. June, pp. 969–973, 2018, doi: 10.1016/j.solener.2018.05.082.

[95] G. Vidon, "Why do decays decay? Transport and recombination dynamics of solar cells revealed via time resolved photoluminesence imaging : application to hybrid perovskites," Institut Polytechnique de Paris, Palaiseau, 2022.

[96] M. S. Chowdhury *et al.*, "Effect of deep-level defect density of the absorber layer and n/i interface in perovskite solar cells by SCAPS-1D," *Results Phys*, vol. 16, p. 102839, 2020, doi: 10.1016/j.rinp.2019.102839.

[97] K. Bhavsar and P. B. Lapsiwala, "Numerical simulation of perovskite solar cell with different material as electron transport layer using SCAPS-1D software," *Semiconductor Physics, Quantum Electronics and Optoelectronics*, vol. 24, no. 3, pp. 341–347, 2021, doi: 10.15407/spqeo24.03.341.

[98] M. K. Hossain, M. H. K. Rubel, G. F. I. Toki, I. Alam, M. F. Rahman, and H. Bencherif, "Effect of Various Electron and Hole Transport Layers on the Performance of CsPbI3-Based Perovskite Solar Cells: A Numerical Investigation in DFT, SCAPS-1D, and wxAMPS Frameworks," *ACS Omega*, vol. 7, no. 47, pp. 43210–43230, Nov. 2022, doi: 10.1021/acsomega.2c05912.

[99] M. Burgelman, P. Nollet, and S. Degrave, "Modelling polycrystalline semiconductor solar cells," *Thin Solid Films*, vol. 361, pp. 527–532, 2000, doi: 10.1016/S0040-6090(99)00825-1.

[100] A. Riquelme *et al.*, "Identification of recombination losses and charge collection efficiency in a perovskite solar cell by comparing impedance response to a drift-diffusion model," *Nanoscale*, vol. 12, no. 33, pp. 17385–17398, Sep. 2020, doi: 10.1039/d0nr03058a.

[101] Y. Huang *et al.*, "Influence of Schottky contact on the C-V and J-V characteristics of HTM-free perovskite solar cells," *EPJ Photovoltaics*, vol. 8, 2017, doi: 10.1051/epjpv/2017001.

[102] A. Bercegol *et al.*, "Imaging Electron, Hole, and Ion Transport in Halide Perovskite," *Journal of Physical Chemistry C*, vol. 124, no. 22, pp. 11741–11748, 2020, doi: 10.1021/acs.jpcc.9b10876.

[103] V. M. Le Corre *et al.*, "Revealing Charge Carrier Mobility and Defect Densities in Metal Halide Perovskites via Space-Charge-Limited Current Measurements," *ACS Energy Lett*, vol. 6, no. 3, pp. 1087–1094, 2021, doi: 10.1021/acsenergylett.0c02599.

[104] N. E. Courtier, J. M. Cave, J. M. Foster, A. B. Walker, and G. Richardson, "How transport layer properties affect perovskite solar cell performance: insights from a coupled charge transport/ion migration model," *Energy Environ Sci*, vol. 12, no. 1, pp. 396–409, Jan. 2019, doi: 10.1039/c8ee01576g.

[105] M. Koopmans, V. Corre, and L. Koster, "SIMsalabim: An open-source drift-diffusion simulator for semiconductor devices," *J Open Source Softw*, vol. 7, no. 70, p. 3727, Feb. 2022, doi: 10.21105/joss.03727.

[106] M. T. Neukom *et al.*, "Consistent Device Simulation Model Describing Perovskite Solar Cells in Steady-State, Transient, and Frequency Domain," *ACS Appl Mater Interfaces*, vol. 11, no. 26, pp. 23320–23328, Jun. 2019, doi: 10.1021/acsami.9b04991.

[107] Y. Huang, "Drift diffusion modelling of perovskite based solar cells, III-V optoelectronic devices and Kelvin probe force microscopy," Université Bretagne Loire, INSA de Rennes, Rennes, 2018.

[108] A. R. Bowring, L. Bertoluzzi, B. C. O. Regan, and M. D. Mcgehee, "Reverse Bias Behavior of Halide Perovskite Solar Cells," *Adv Energy Mater*, vol. 8, no. 8, p. 1702365, 2017, doi: 10.1002/aenm.201702365.

[109] W. Tress, N. Marinova, T. Moehl, S. M. Zakeeruddin, M. K. Nazeeruddin, and M. Grätzel, "Understanding the rate-dependent J-V hysteresis, slow time component, and aging in CH3NH3PbI3 perovskite solar cells: The role of a compensated electric field," *Energy Environ Sci*, vol. 8, no. 3, pp. 995–1004, Mar. 2015, doi: 10.1039/c4ee03664f.

[110] K. J. Prince *et al.*, "Complementary interface formation toward high-efficiency all-back-contact perovskite solar cells," *Cell Rep Phys Sci*, vol. 2, no. 3, Mar. 2021, doi: 10.1016/j.xcrp.2021.100363.

[111] D. Regaldo *et al.*, "On the equilibrium electrostatic potential and light-induced charge redistribution in halide perovskite structures," *Progress in Photovoltaics: Research and Applications*, vol. 30, no. 8, pp. 994–1002, 2022, doi: 10.1002/pip.3529.

[112] L. Bertoluzzi *et al.*, "Incorporating Electrochemical Halide Oxidation into Drift-Diffusion Models to Explain Performance Losses in Perovskite Solar Cells under Prolonged Reverse Bias," *Adv Energy Mater*, vol. 11, no. 10, Mar. 2021, doi: 10.1002/aenm.202002614.

[113] S. Bitton and N. Tessler, "Perovskite ionics - elucidating degradation mechanisms in perovskite solar cells via device modelling and iodine chemistry," *Energy Environ Sci*, vol. 16, pp. 2621–2628, 2023, doi: 10.1039/d3ee00881a.

[114] A. R. Hering, M. Dubey, and M. S. Leite, "Emerging opportunities for hybrid perovskite solar cells using machine learning," *APL Energy*, vol. 1, no. 2, p. 020901, 2023, doi: 10.1063/5.0146828.

[115] T. J. Jacobsson *et al.*, "An open-access database and analysis tool for perovskite solar cells based on the FAIR data principles," *Nat Energy*, vol. 7, no. 1, pp. 107–115, 2021, doi: 10.1038/s41560-021-00941-3.

[116] Y. Li *et al.*, "Bandgap tuning strategy by cations and halide ions of lead halide perovskites learned from machine learning," *RSC Adv*, vol. 11, no. 26, pp. 15688–15694, Apr. 2021, doi: 10.1039/d1ra03117a.

[117] R. E. Brandt *et al.*, "Rapid Photovoltaic Device Characterization through Bayesian Parameter Estimation," *Joule*, vol. 1, no. 4, pp. 843–856, 2017, doi: 10.1016/j.joule.2017.10.001.

[118] V. M. Le Corre, T. S. Sherkar, M. Koopmans, and L. J. A. Koster, "Identification of the dominant recombination process for perovskite solar cells based on machine learning," *Cell Rep Phys Sci*, vol. 2, no. 2, Feb. 2021, doi: 10.1016/j.xcrp.2021.100346.

[119] W. A. Dunlap-Shohl, Y. Meng, P. P. Sunkari, D. A. C. Beck, M. Meila, and H. W. Hillhouse, "Physiochemical Machine Learning Models Predict Operational Lifetimes of CH3NH3PbI3 Perovskite Solar Cells," 2022. doi: 10.26434/chemrxiv-2022-01p42.

[120] J. M. Howard, E. M. Tennyson, B. R. A. Neves, and M. S. Leite, "Machine Learning for Perovskites' Reap-Rest-Recovery Cycle," *Joule*, vol. 3, no. 2. Cell Press, pp. 325–337, Feb. 20, 2019. doi: 10.1016/j.joule.2018.11.010.

[121] M. Alsari *et al.*, "Degradation Kinetics of Inverted Perovskite Solar Cells," *Sci Rep*, vol. 8, no. 1, pp. 1–6, 2018, doi: 10.1038/s41598-018-24436-6.

[122] M. Schmidt and H. Lipson, "Distilling free-form natural laws from experimental data," *Science (1979)*, vol. 324, no. 5923, pp. 81–85, Apr. 2009, doi: 10.1126/science.1165893.

[123] H. Abdi and L. J. Williams, "Principal Component Analysis," *Wiley Interdiscip Rev Comput Stat*, vol. 2, no. 4, pp. 433–459, 2010, doi: 10.1002/wics.101.

[124] Y. D. Lang, A. Malacina, L. T. Biegler, S. Munteanu, J. I. Madsen, and S. E. Zitney, "Reduced order model based on principal component analysis for process simulation and optimization," *Energy and Fuels*, vol. 23, no. 3, pp. 1695–1706, Mar. 2009, doi: 10.1021/ef800984v.

[125] H. A. Kazem, J. H. Yousif, M. T. Chaichan, A. H. A. Al-Waeli, and K. Sopian, "Long-term power forecasting using FRNN and PCA models for calculating output parameters in solar photovoltaic generation," *Heliyon*, vol. 8, no. 1, p. e08803, Jan. 2022, doi: 10.1016/j.heliyon.2022.e08803.

Chapter 2: Modeling methods and investigated experimental results

Table of contents

Chapter introduction

In this chapter, the methods employed to investigate the degradation of perovskite solar cells are employed.

First, a coupled scheme of optical (based on transfer matrices) and electrical (based on drift diffusion) numerical simulations have been developed and exposed here. The basics of these techniques are recalled in Section 2.1, to clearly expose the input and output parameters of the simulations performed throughout this work.

A crucial output is the simulated current voltage (JV) characteristic of the solar cell. It is exposed in Section 2.2 how this characterization result is reproduced, and how associated parameters are derived.

Photoluminescence (PL) spectroscopy is a second characterization technique that have been considered, and from which the result have been simulated. In Section 2.3, specific models employed to reproduce a PL spectrum are exposed, together with the associated derived parameters.

Moreover, numerous experimental results, obtained by other teams have been analyzed here. They are exposed in Section 2.4, and they all consist in periodic measurements performed over aging studies, of various solar cells under different conditions.

Finally, a specific procedure developed to pre-treat experimental results obtained at IPVF is exposed in Section 2.5. It mainly consists in data cleaning steps and removal of outliers points, in order to extract long term aging trends.

Chapter key points:

- Optical simulations based on transfer matrices are employed to compute absorption in the solar cell and carrier photogeneration rate across depth.
- Electrical simulations through drift diffusion allow to compute charge carrier transport and recombination behavior.
- Combining both steps allow to reproduce current voltage curves and photoluminescence spectra.
- From JV curves, the following parameters are derived: Voc, Jsc, FF, slope at open circuit and slope at short circuit.
- From PL spectra, the following parameters are derived: total emission, photon energy at the maximum of the peak and slope at low energy side.
- Pre-treatment of experimental results is done by removing outliers and applying moving average smoothing, in order to derive long term degradation trends. Forward, reverse and average JV curves are considered and treated.

2.1 Coupled drift diffusion and optical simulations

In order to investigate the degradation of the solar cell performances, a modeling method has been developed. It aims a comparing experimental characterization to simulations in order to associate measured changes of optoelectrical parameters to changes in the materials characteristics. Therefore, it is necessary to accurately simulate the solar cell behavior under the conditions employed to characterize them.

To do so, a coupling scheme of optical and electrical simulations has been developed. First, optical simulations allow to estimate the light behavior in the solar cell, the absorbed fraction, and the associated generation profile of electron-hole pairs. Then, electrical simulations determine the carriers' currents, recombination, and extraction.

For the simulations performed in this work, the perovskite solar cell is considered as a stack of three active layers: hole transporting material, perovskite and electron transporting material. Furthermore, a front stack of glass and transparent conductive electrode, as well as a back metallic contact are considered.

The layers are considered uniform, and all interfaces parallel to each other, the simulations are therefore performed in one dimension.

2.1.1 Optical simulations through transfer matrix method

The optical simulation block employs transfer matrix method to compute the light propagation is the thin-films, and accounts for the transmittance and front side reflection of the glass layer as a filter.

The transfer matrix method is based on Maxwell's equations formalism of electromagnetic waves [1]. Therefore, Fresnel equations describe reflection and transmission of light, through continuity of electric and magnetic fields, at a given interface. When several interfaces are close to each other, a coupling through partial transmissions and reflections occur.

The electric field in the stack is described by two components, propagating in opposite directions (normally to the interfaces): E^+ and E^-. Furthermore, the method takes advantage of the linearity of the propagation equations, as well as the continuity of the tangential component of the electric field at interfaces. As a result, these electrical field components are related to each other through matrix products [2].

First, the interface matrix describes the transmission and reflection of both electrical fields components at a given interface. Between materials j and $j+1$, it relates the electrical fields at both sides of the interface (in $x_{j,j+1-}$ and $x_{j,j+1+}$) by the product:

$$\begin{pmatrix} E^+\left(x = x_{j,j+1-}\right) \\ E^-\left(x = x_{j,j+1-}\right) \end{pmatrix} = \frac{1}{t_{j,k}} \begin{pmatrix} 1 & r_{j,k} \\ r_{j,k} & 1 \end{pmatrix} \cdot \begin{pmatrix} E^+\left(x = x_{j,j+1+}\right) \\ E^-\left(x = x_{j,j+1+}\right) \end{pmatrix} \quad (1)$$

$t_{j,k}$ and $r_{j,k}$ are the Fresnel reflection and transmission coefficients. For instance, they are defined for s-polarized waves as:

$$t_{j,k} = \frac{q_j - q_k}{q_j + q_k} \quad (2)$$

$$r_{j,k} = \frac{2q_j}{q_j + q_k} \quad (3)$$

Here, $q_j = (n_j + i\,k_j)\cos\theta_j$ and θ_j is the angle of refraction angle in the layer j, which can be expressed from Snell-Descartes law.

Furthermore, the layer matrix describes the propagation across a given layer of both components. For the layer j of thickness d_j, it relates the electrical fields at both extremities (in $x_{j,j-1+}$ and $x_{j,j+1-}$) by the product:

$$\begin{pmatrix} E^+(x = x_{j,j-1+}) \\ E^-(x = x_{j,j-1+}) \end{pmatrix} = \begin{pmatrix} exp\left(-i\frac{2\pi}{\lambda}q_j d_j\right) & 0 \\ 0 & exp\left(i\frac{2\pi}{\lambda}q_j d_j\right) \end{pmatrix} \cdot \begin{pmatrix} E^+(x = x_{j,j+1-}) \\ E^-(x = x_{j,j+1-}) \end{pmatrix} \quad (4)$$

Finally, the electrical field is expressed across the whole stack, accounting for all reflections, transmission and propagations is obtained by the product of all associated matrices. The whole problem is reduced to a two-by-two matrix equation. For instance, for three layers, and four interfaces:

$$\begin{pmatrix} E^+(x = 0) \\ E^-(x = 0) \end{pmatrix} = I_{0,1} \cdot L_1 \cdot I_{1,2} \cdot L_2 \cdot I_{2,3} \cdot L_3 \cdot I_{3,4} \cdot \begin{pmatrix} E^+(x = d_{tot}) \\ E^-(x = d_{tot}) \end{pmatrix} \quad (5)$$

$I_{j,k}$ are interface matrices and L_j layer matrices. Importantly, the absorbed power per unit volume (I, in W.m^{-3}) is related to the electric field dissipated power. It is expressed here in material j, for $x \in [x_{j,j-1}, x_{j,j+1}]$:

$$I(x) = \frac{1}{2}c\epsilon_0\alpha_j n_j |E(x)|^2 = \frac{1}{2}c\epsilon_0\alpha_j n_j |E^+(x) + E^-(x)|^2 \quad (6)$$

Here, $\alpha_j = \frac{4\pi}{\lambda}k_j$ is the absorption coefficient, c the speed of light and ϵ_0 the permittivity of vacuum.

Finally, usual quantities such as absorptivity and generation rate are derived from the absorbed power, and accounting for incident light intensity. Importantly, it is not monochromatic, typically the AM1.5g spectrum is considered. In such case, the computations presented above have to be performed for each wavelength.

The absorption rate (at a given depth) is the ratio of absorbed power to incident light intensity (in W.m^{-2}):

$$A_x(x, \lambda) = \frac{I_\lambda(x, \lambda)}{I_{0,\lambda}(\lambda)} \quad (7)$$

It is to note that the absorption rate is in m-1, the absorptivity is then obtained by integrating over the layer thickness:

$$A(\lambda) = \int_0^d A_x(x,\lambda)dx \quad (8)$$

These quantities can be computed for each layer of the solar cell. The example from Figure 1 shows is obtained for a stack composed of: Glass / FTO / TiO_2 / $Cs_{0.05}(MA_{0.17}FA_{0.83})_{0.95}Pb(Br_{0.17}I_{0.83})_3$ / PTAA / Gold. FTO is a transparent conductive oxide (TCO), TiO_2 constitutes the electron transport layer (ETL) and PTAA the hole transporting later (HTL). By adding the absorptivity in each layer (and front reflection) optical behavior of the solar cell is completely resolved.

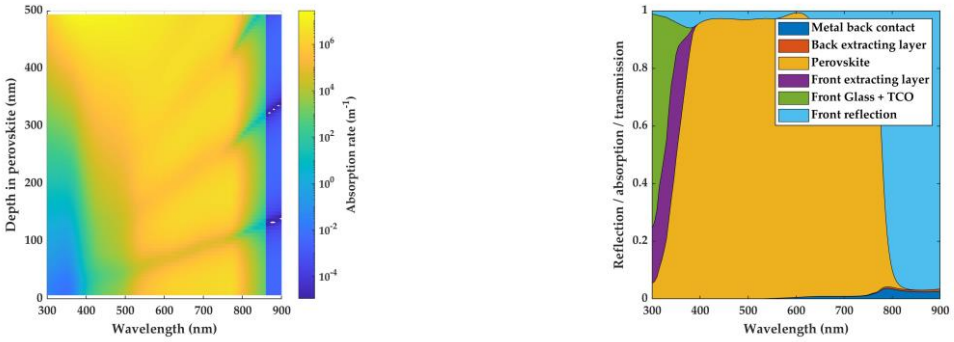

Figure 1. *Left: absorption rate in the perovskite layer of an exemplary solar cell. Note vertical axis starts at the bottom interface and light enters through the side at 500 nm. Right: absorptivity in the perovskite layer as well as all other absorptions and reflections.*

Finally, the locally absorbed power can be expressed as a "photon absorption rate" by dividing by the energy of a photon. This is the electron-hole pair generation rate (in $s^{-1}.m^{-3}$), which is crucial for the electrical simulations.

$$G(x) = \frac{\lambda}{hc} I(x) \quad (9)$$

The generation rate associated to the above example is displayed in Figure 2.

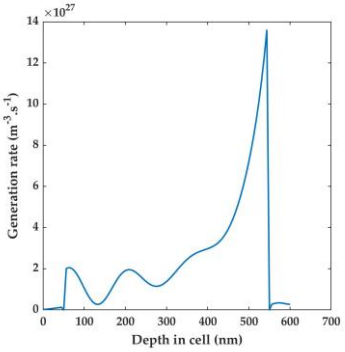

Figure 2. *Generation rate in an exemplary perovskite solar cell. Note x axis starts at the bottom interface and light enters through the side at 500 nm. Only the ETL / perovskite / HTL stack is represented. Both transport layers are 50 nm thick, and the perovskite 500 nm.*

Finally, the optical simulations were performed with an in-house developed tool, OptiPV. Its implementation of the transfer matrix method allows to rapidly obtain the generation rate, for any configuration. The only necessary input parameters are the complex refractive indices of each layer, and their thickness.

2.1.2 Electrical simulations through drift diffusion modeling

The goal of the electrical simulation block is to compute the performances of the solar cell under steady state, given the optical behavior mentioned in the previous section. Densities and currents of charge carriers are computed locally, across the depth of the device, as well as the extracted current at the contacts of the solar cell. These drift diffusion simulations were performed with SCAPS, a 1D-numerical solver developed for thin-films solar cells, freely available [3] and widely used to investigate perovskite solar cells [4]–[8].

The drift diffusion model is based on local equations: the Poisson equation and the continuity equation. Importantly, the formulation of charge carrier currents accounts for both drift and diffusion phenomena. They constitute a system of equations in Φ, n and h, which are respectively the electrical potential, the density of electrons and the density of holes [9].

The Poisson equation relates the electrical potential to the density of charges. In a semi-conductor, not only electrons and holes are present (noted n and p, respectively), but also doping impurities (N_A^- and N_D^+ are the densities of ionized acceptor and donor impurities). Importantly, the positive elementary charge is noted q in this work.

$$\begin{aligned} \nabla \cdot (\epsilon_0 \epsilon_r \nabla \Phi) &= -q\,\sigma \\ &= -q(-n + p - N_A^- + N_D^+) \end{aligned} \quad (10)$$

Here ϕ is the electrical potential, ϵ_0 and ϵ_r are the vacuum and relative permittivity respectively.

Furthermore, the continuity equation is expressed for electrons and holes. It accounts for both generation (noted G) and recombination processes (noted R). Importantly, the currents are expressed as particle flows (in $m^{-2}.s^{-1}$) in this section.

$$\frac{\partial n}{\partial t} = -\nabla \cdot J_n + G - R \quad (11)$$

$$\frac{\partial p}{\partial t} = -\nabla \cdot J_p + G - R \quad (12)$$

Importantly, G is the generation rate, it is exactly the quantity obtained through the optical simulations in the previous section.

The recombination rate is the sum of radiative and non-radiative processes, exposed in Section 1.1. In the perovskite layer, two types of traps were considered: deep traps located at the middle of the bandgap and shallow defects located near the band edges with exponential distributions in energy. All were considered neutral and therefore act as pure recombination centers [10]. The deep traps have a major impact

on recombination, and the shallow traps are mainly used to define sub bandgap absorption, critical for photoluminescence. Furthermore, neutral deep traps were also considered at both perovskite interfaces, with ETL and HTL.

Finally, the charge carrier currents have to be expressed through both drift and diffusion processes:

$$J_n = +n\,\mu_n \nabla\Phi - D_n \nabla n \quad (13)$$
$$J_p = -p\,\mu_p \nabla\Phi - D_p \nabla p \quad (14)$$

These five coupled equations constitute the drift diffusion equations. It is to note that they are nonlinear, due to the expressions of the recombination rate.

The numerical solving procedure, including mesh definition, discretization of the derivative through finite differences is implemented in SCAPS [11]. It consists in a Gummel-Iteration scheme with Newton-Raphson sub-steps, and the equations are expressed in terms of quasi-Fermi level instead of carrier densities [12], [13]. Importantly, only the steady-state working point is calculated.

Finally, the useful outputs for the device analysis, such as external voltage or currents are directly derived from the three unknowns of the system (Φ, n and p) and charge carrier currents. Importantly, the quasi-Fermi levels are obtained across the whole device, as illustrated in Figure 3. Such outputs is crucial to compute the emitted photoluminescence spectrum across depth, as exposed in a further section.

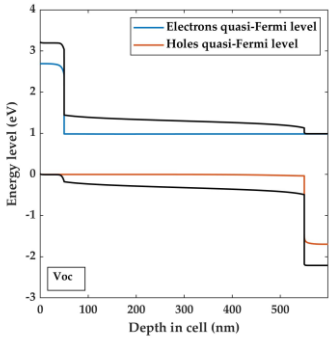

Figure 3. *Example of output of the electrical simulation of a perovskite solar cell. The quasi-Fermi levels are in blue and red lines, conduction and valence bands in black lines. The applied bias here is Voc.*

Importantly, solar cells are simulated here as 1D structures, therefore, lateral average material properties and charge carrier behavior are considered. In fact, spatial non-uniformities at the microscopic level are present in perovskite solar cells. For instance, several layers are multi-crystalline and properties at grain boundaries are different from inside crystals. Moreover, these aspects have been demonstrated crucial in Section 1.3 to understand degradation processes. However, simulating spatially resolved phenomena and their impact on macroscopic current voltage properties would require numerous assumptions. Also, it might not be possible to distinguish these phenomena only by relying on macroscopic measurements such as employed in this work. Therefore, it has been chosen to consider more simple 1D simulation

methods with more reasonable number of parameters and computation time, in order to focus on other aspects.

It has also been exposed in Section 1.3 how ion migrations in perovskite materials can significantly impact the solar cell behavior. In fact, interesting studies coupling these ions and charge carrier dynamics in drift diffusion simulations have been reported in Section 1.4.2. They have notably significantly helped to understand current voltage hysteresis. However, supplementary parameters arise (such as mobile species densities and diffusion coefficients) with poorly known values that can probably vary significantly from sample to sample. Moreover, the precise nature of the reactions responsible for the generation or annihilation of mobile species is still under study, and their reaction rates even less known. As a result simulating the behavior of mobile ions is probably a research field in itself.

Therefore, it has been chosen here not to simulate this coupled behavior to avoid associated parameters assumptions. Therefore, the considered properties of solar cells reflect an "average behavior" between possible ion accumulation regimes, which is believed to still provide valuable insights on perovskite solar cells performances.

Importantly, the simulations done here can capture a "long-term" impact on carrier mobilities or defect densities (or other properties) in the perovskite layer and at its interfaces. The presence of mobile ions is therefore not excluded by the approach employed here, and it can consider the long term impact of migrations on material properties.

This constitutes a tradeoff in terms of number of parameters and assumptions (ion mobilities and JV scan rate for instance) and accuracy at the transient level, allowing to cover more broadly the various degradation processes in the solar cells.

2.2 Current – voltage characterization

The first characterization employed to assess the performances of perovskites solar cells in this work is the current voltage characteristic.

It is obtained experimentally by measuring the cell current at different biases, typically varying between 0 V and its open circuit voltage (Voc). The typical conditions are the normalized Standard Test Conditions (STC): cell temperature at 25 °C, illumination intensity of 1000 $W.m^{-2}$ with AM1.5g spectrum. Therefore, solar cells are placed under a "solar simulator" to ensure the right illumination, and on a "chiller", to ensure the right temperature. Importantly, JV characteristics are also recorded under dark. Both characteristics are complementary and provide insights on different working points of the solar cell.

Some measurements analyzed in this work were done at higher temperature or under a laser illumination, in that case, the simulations parameters have to be set accordingly.

This characterization technique is crucial to assess the performances of a solar cell because it allows to determine its output power under operating conditions. Furthermore, it allows to probe several working points [14], [15], and Figure 4 shows how the proportion of the different recombination channels change across voltage. Recombination at interfaces and contacts only play a role at lower voltages, whereas the SRH recombination account for almost all recombination near Voc. It is to note that radiative recombination do play a minor role, and that controlling defect densities are crucial to improve the perovskite solar cells performances.

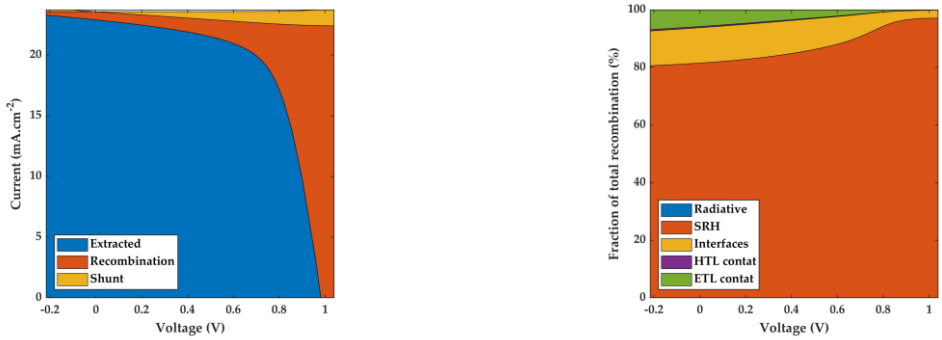

Figure 4. *Simulation of currents balance across a JV characteristic. Left: balance of extracted current (the actually recorded JV characteristic) and losses through recombination or external shunt resistance. Right: composition of recombination losses.*

In order to quantify the performances of a solar cell from its JV characteristic, five parameters are extracted: open circuit voltage (Voc), short circuit current (Jsc), fill factor (FF), the slope at open circuit (OC) and the slope at short circuit (SC). Notably, these parameters have been extracted for simulated or experimental JV characteristics through exactly the same procedure, exposed further.

Importantly, the actual parasitic resistances are not considered in this work. To do so, it would be necessary to fit a model such as a single or double diode model to

the curve. The fitting procedures (usually based on least-squares reductions) of such nonlinear model defined implicitly are however prone to uncertainties or can even be time consuming.

Therefore, it has been chosen in this work to consider the slopes near Jsc and Voc. These quantities are not the usual external resistances but constitutes indicators than can be simply extracted from experimental and simulated JV characteristics. In fact, several thousands of curves had to be treated in this work and performing only simple linear regressions allowed to obtain faster more reliable results.

Figure 5 shows an example of JV characteristics and associated slopes. Importantly the linear fitting ranges are automatically optimized. Multiple ranges are tried, and the fit with the lowest R^2 value is retained. For the slope at SC, regressions were realized between 0 V and 0.4 to 0.9 times Vmpp. For the slope at OC, regressions were done between the lowest current value and 0.2 to 0.9 times Jmpp.

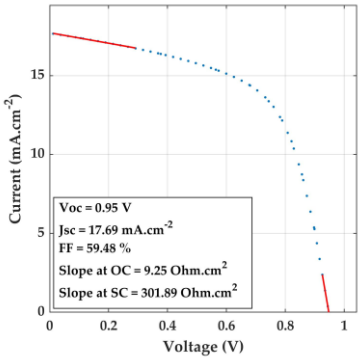

Figure 5. *Example of current voltage and associated optoelectrical parameters. Slopes at OC and SC are represented through red lines.*

As a result, the five extracted optoelectrical parameters provide an interesting overview of the solar cell behavior. The Voc is strongly impacted by the amount of carrier's recombination. For instance, a sample with high defect density will have a lower Voc. The Jsc is in the first order determined by the optical behavior and the number of photo-generated charges. It can also be lowered by poor extraction or low charge carriers mobilities. The FF is modulated by the nature of the recombination and for instance, trap assisted recombination will induce lower FF than radiative recombination. The slope at OC is an indicator of the presence of series resistance in the total electrical circuit. However, it is to keep in mind that it is not the proper series resistance, and it is also dependent on other phenomena such as the nature of the recombination. This is even more significant for the slope at SC, which is not to interpret as a proper shunt resistance. In fact, it very strongly depends on the carrier collection efficiency, and its dependence on bias. This effect is especially more present in pin structures than in pn junctions, as mentioned in Section 1.1.3.

Finally, an important aspect when recording JV characteristics of perovskite solar cells is the voltage scan rate and the scan direction, forward from 0 V to Voc or reverse from Voc to 0 V [16].

In fact, as exposed in Section 1.3.1, mobile ions can migrate when an electric field is present across the perovskite layer [17], [18]. This has been reported to potentially induce local defects and doping effects which could explain the hysteresis frequently obtained between froward and reverse characteristics [19]. These phenomena are still not yet fully understood and several manners to record JV characteristics are reported in literature.

A possibility to reduce the hysteresis is to have a preconditioning step (at 0 V, Vmpp or above Voc) in order to reach a mobile ions equilibrium. Then a fast scan rate ensures that as few migrations as possible occur between forward and reverse scans. However, the state probed by this technique is significantly different from operating conditions, in which the solar cells are tracked at their maximum power point.

The opposite manner, with a low scan rate allowing to reach equilibrium between each point could also be possible. Here, the solar cell would not be in the same state along the JV characteristic, making the results poorly interpretable.

As a result, no perfect solution has been found and measurements performed at IPVF were done with scan rates of approx. 20 $mV.s^{-1}$, in forward and reverse directions. Both characteristics are still not reflecting realistic operating conditions, which probably lies in between with a Vmpp bias. Therefore, the average of both characteristics has been exploited in this work.

2.3 Photoluminescence spectroscopy

Photoluminescence spectroscopy is a useful characterization technique to probe the carrier densities in the perovskite layer. The emission of photons is caused by radiative recombination, which is the reciprocal phenomenon to absorption. Therefore, both electrical and optical characteristics of the solar cell play a role. Contrary to JV characterization, this technique do not need contacts. Therefore, it can be employed on single material layers, or partial solar cell stacks. As a result, it allows to compare optoelectrical characteristics at different steps of the solar cell fabrication process.

The luminescence emission by the sample is experimentally measured by a spectrometer. Importantly, the signal has to be conveyed through lenses and optical fibers. As a result, the exact number of photons emitted by the sample is usually not known absolutely. Resolving this constant is done through "absolute calibration", which is important work by itself. The data analyzed in this work was not obtained through an absolutely calibrated setup. It is not detrimental to the analysis because only relative evolution of the total emission or changes of the spectrum shape was investigated and simulated. In fact, the relative evolution of total emission is precisely the quantity useful to assess the impact of solar cell degradation.

The excitation source in photoluminescence spectroscopy is light, usually done through a laser. For the measurements analyzed in this work, a 660 nm wavelength laser was employed, with variable intensity.

It can be noted that measurements were performed under steady state, with acquisition times in the order of a second.

2.3.1 General case

The luminescence emission from a semi-conductor layer arises from radiative recombination. It is described by the generalized Planck law, derived from black-body radiation theory and Kirchhoff's law of radiation.

The photon flux emitted at the surface of a material, $\phi_{out}(h\nu, \Omega)$, in a solid angle $d\Omega$ with an angle θ, is expressed as (in $m^{-2}.s^{-1}.eV^{-1}$):

$$\phi_{out}(h\nu, \Omega) = A(h\nu, \Omega) \frac{(h\nu)^2}{4\pi^3 \hbar^3 c^2} \frac{1}{exp\left(\frac{h\nu - \Delta E_F}{k_B T}\right) - 1} cos\theta d\Omega \quad (15)$$

$h\nu$ is the photon energy, $\hbar$ the reduced Planck constant and c the speed of light in vacuum. ΔE_F is the difference between electron and hole quasi-Fermi levels: the quasi-Fermi levels splitting. It is the specific quantity that depends on carrier densities.

Importantly $A(h\nu, \Omega)$ is the absorptivity of the material it depends on photon energy and the direction of the incoming or emitted light. In this work, measurements were all performed under normal incidence. Therefore, the angular dependence of the absorptivity is not simulated.

It has been shown in Section 2.1 that both absorptivity and quasi-Fermi levels splitting are calculated across the device depth, from optical and electrical simulations respectively. Therefore, the emitted photon flux across depth can be computed:

$$\phi_{out-x}(h\nu,\Omega,x) = A_x(h\nu,x)\frac{(h\nu)^2}{4\pi^3\hbar^3c^2}\frac{1}{exp\left(\frac{h\nu-\Delta E_F(x)}{k_BT}\right)-1}cos\theta d\Omega \quad (16)$$

The total emitted flux at the surface is then obtained by integrating over the device depth:

$$\phi_{out}(h\nu,\Omega) = \int A_x(h\nu,x)\frac{(h\nu)^2}{4\pi^3\hbar^3c^2}\frac{1}{exp\left(\frac{h\nu-\Delta E_F(x)}{k_BT}\right)-1}cos\theta d\Omega dx \quad (17)$$

The absorption rate has been defined in the previous section as the ratio of the number of absorbed photons at a depth x over the number of incident photons at the surface. In fact, the reciprocity theorem allows to equalize this probability of being absorbed at a depth x with the probability of leaving the material when emitted at this depth x.

The above expression is directly implemented and allows to compute the photoluminescence emission of any perovskite solar cell simulated with the methods from Section 2.1. Interestingly, Figure 6 shows how the shape of the emitted spectrum depends on depth. This reflects the varying absorption depth at different photon energies. It will also allow to reflect the impact of non-uniform quasi-Fermi levels splitting across depth, in the case of localized defect densities for instance.

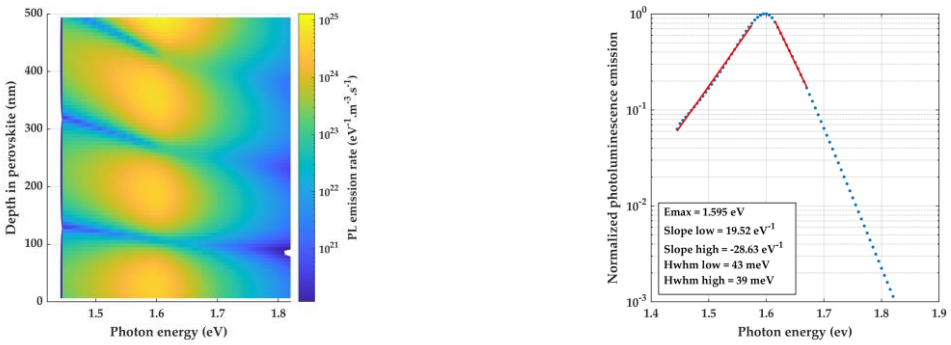

Figure 6. *Left: photoluminescence emission rate simulated across the depth of a perovskite layer within a solar cell. The same structure as employed for the simulations in Figure 1 and Figure 3 is employed. Right: corresponding emitted photoluminescence spectrum at the surface of the device.*

With the same approach as for JV characteristics, optoelectrical parameters are extracted from the simulated and experimental PL spectra. Figure 6, right, shows an example: total emission, position of the maximum of the peak (Emax), slopes on both sides as well as half width at half max are extracted. These parameters will be employed to compare simulated to experimental spectra. Notably, the total emission

can only be used as relative variations because the experimental setup is not absolutely calibrated.

Similarly, to JV characteristics, slopes are extracted to provide practical indicators that can rapidly and easily be extracted for the thousands of simulated PL spectra. The linear regression extent on each side is defined around the inflection point: it range from 0.5 to 1.5 times the PL intensity at this point.

Here again the extracted optoelectrical parameters provide an overview of some characteristics of the perovskite solar cell. The total emission indicates on the number of radiative recombination taking place and the position of the peak is associated the perovskite material bandgap. The slope and width of the spectrum on low energy side are dependent on the optical behavior (the absorptivity). It is for instance an indicator of sub-bandgap absorption behavior, as developed in the next section. Finally, the slope on the high energy side is mainly dependent on temperature.

2.3.2 Sub-bandgap optical behavior in the presence of shallow defects

In the computation of the photoluminescence spectrum presented above, the optical behavior plays a major role through absorptivity. Experimental spectra of perovskite solar cells usually show an important tail on low photon energy side. This means that the material can absorb and emit photons that have a lower energy than the bandgap. Such phenomenon cannot be explained by the classical model in which an electron from the valence band is promoted to a state in the conduction band when a photon is absorbed. It is necessary to account for supplementary states within the bandgap, near the band edges. It is usually referred to as "Urbach tail" and has been already reported for other materials [20].

Multiple causes have been raised in the literature to explain the presence of such tail states in perovskite materials [21]. Structural and dynamical crystal disorder have for instance been considered [22]. Also, optically active shallow trap levels, located near band edges could explain such behavior [23], by providing supplementary states, allowing for lower energy transitions.

In this work, the modeling of sub-bandgap optical behavior has been done considering shallow traps and their optical capture cross section. This quantity defines the probability of a photon to be absorbed and induce an energy transition of an electron. In fact, two processes are possible: the transition of an electron from the valence band to the trap state (this creates a free hole in the valence band), and the transition of an electron from this trap state to the conduction band (this creates a free electron in the conduction band).

Shallow states have been considered in both conduction and valence band tails, and their density is considered following an exponential decay:

$$N_{t-CBT}(E_t) = N_{t0} exp\left(\frac{E_t - E_g}{E_U}\right) \quad (17)$$

$$N_{t-VBT}(E_t) = N_{t0} exp\left(\frac{-E_t}{E_U}\right) \quad (18)$$

E_t is the energy level inside the bandgap, equal to 0 at the valence band edge and positive towards higher energy levels. N_{t0} defines the total density of defects and E_U is the characteristic energy of the exponential distribution of defects.

As a result, the free electron generation in the conduction band (transition of an electron from valence band tail to conduction band), is computed in the form of an absorption coefficient. It is expressed, for a defect level E_t and associated energy transition $E_C - E_t$, as:

$$\alpha_n(h\nu, E_t) = N_{t-VBT}(E_t) f_t(E_t) \sigma(h\nu, E_C - E_t) \quad (19)$$

Here N_{t-VBT} is the density of states in the valence band tail, f_t the occupation probability, and $\sigma(E, E_C - E_t)$ the optical capture cross section for a photon of energy hν.

Symmetrically, the free hole generation in the valence band (transition from valence band to conduction band tail) is expressed as:

$$\alpha_h(h\nu) = N_{t-CBT}(E_t)(1 - f_t(E_t))\sigma(h\nu, E_t - E_V) \quad (20)$$

Here the conduction band tail defect density plays a role, as well as the complementary to the occupation probability.

Notably, the transitions from valence band to valence band tail and from conduction band tail to conduction band are not considered. These transitions follows the same laws and are possible, but are associated to very low photon energies, outside the ranges explored in photoluminescence spectroscopy.

Finally, the total absorption coefficient, accounting for all processes (sub bandgap and band-to-band absorption), is obtained by summing all contributions [24], [25]:

$$\alpha(h\nu) = \alpha_{bb}(h\nu) + \alpha_n(h\nu) + \alpha_h(h\nu) \quad (21)$$

Here $\alpha_{bb}(h\nu)$ is the band-to-band absorption coefficient, it has been taken from ellipsometry measurements in this work.

Two models have been employed to compute the optical capture cross section. First, Lucovsky reported a model based on the expression for the potential responsible for the electrons binding, adjusted from the hydrogen model and considered to be the ion core potential[26]. It is expressed as follows:

$$\sigma(h\nu, E_i) = \frac{1}{n}\left(\frac{E_{eff}}{E_0}\right)^2 \frac{16\pi q^2 \hbar}{3\epsilon_0 c m^*} \frac{E_i^{\frac{1}{2}}(h\nu - E_i)^{\frac{3}{2}}}{(h\nu)^3} \quad (22)$$

$\frac{E_{eff}}{E_0}$ is the effective field ratio. It can be calculated with the Lorentz expression: $\frac{E_{eff}}{E_0} = 1 + \frac{n^2-1}{3}$ [27]. m^* is the effective mass of the electron in the trap state, and n the refractive index. In fact, these parameters are not precisely known for the perovskite materials. The refractive index for energies bellow the bandgap is not accurately obtained from ellipsometry measurements for instance.

Therefore, a simpler approach has also been employed, considering an absorption threshold, with a constant value for photon energies above the transition value, or zero.

$$\sigma(h\nu, E_i) = \begin{cases} \sigma_C \; if \; h\nu \geq E_i \\ 0 \; if \; h\nu < E_i \end{cases} \quad (23)$$

Both models have been implemented and compared. An example case is displayed in Figure 7, left and middle, for three exemplary defect energy levels (not exponential distributions) located near the conduction band edge. In this example, σ_C was set to 10^{-17} cm2, a realistic value also chosen to be consistent with Lucovsky model result. The optical capture cross section associated to the most significant process is displayed: the generation of a hole in the valence band.

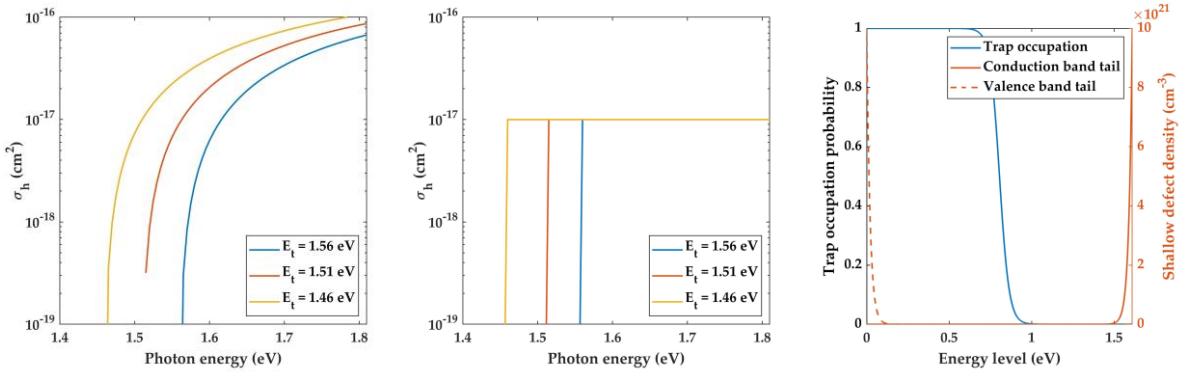

Figure 7. *Optical capture cross section for three defect state energy levels. Left: Lucovsky model, the effective mass was set to its value in the valence band and the refractive index to its average value in the known range. Middle: constant model,* $\boldsymbol{\sigma_C}$ *was set to* 10^{-17} *cm². Right: trap occupation probability across the perovskite bandgap material, assuming it is intrinsic and at equilibrium. The shallow defects from both band tails are also superposed.*

Both models appear to show different absorption edges in Figure 7, left and middle, being much less sharper according to Lucovsky model. However, the final impact on absorption coefficient and photoluminescence spectrum will have to be assessed, to compare the models on usual physical quantities.

On Figure 7, right, the trap occupation probability used in this work is displayed. It is computed by making strong assumptions: the material is intrinsic and at equilibrium. The difference with using the actual carrier concentrations has been quantified in terms of absorption coefficient and it is negligible. Furthermore, the necessary coupling of optical and electrical simulations would be very time consuming.

Finally, the band tails represented in Figure 7, are employed to compute the corresponding absorption coefficient, displayed in Figure 8, top. Moreover, associated optical and electrical calculations are performed and provide the corresponding photo-luminescence spectra.

In fact, a third model has been employed to generate absorption coefficient and PL spectrum: the widely used model proposed by Katahara and Hillhouse [28]. It

directly expresses the total absorption coefficient through a convolution product of a term accounting for band-to-band and a term for sub-bandgap absorption.

The first term follows the square dependence on energy of the band's density of states. The second term has the form of an exponential decay (with a possible exponent, θ). It is actually consistent with the exponential form of the band tails considered in this work. Finally, a multiplicative constant, α_0, scales the absorption intensity. As a result, this model is not related to any defect density, but proposes a purely phenomenological expression:

$$\alpha(h\nu) = \frac{\alpha_0}{2\,E_U\,\Gamma(1+1/\theta)} \int_{-\infty}^{\infty} exp\left(-\left|\frac{u}{E_U}\right|^{\theta}\right)\sqrt{h\nu - E_g - u}\,du \quad (24)$$

The absorption coefficient and PL spectrum obtained through this model have been compared to those obtained through the previously described models, and the same exponential decay characteristic energy (E_U) has been considered.

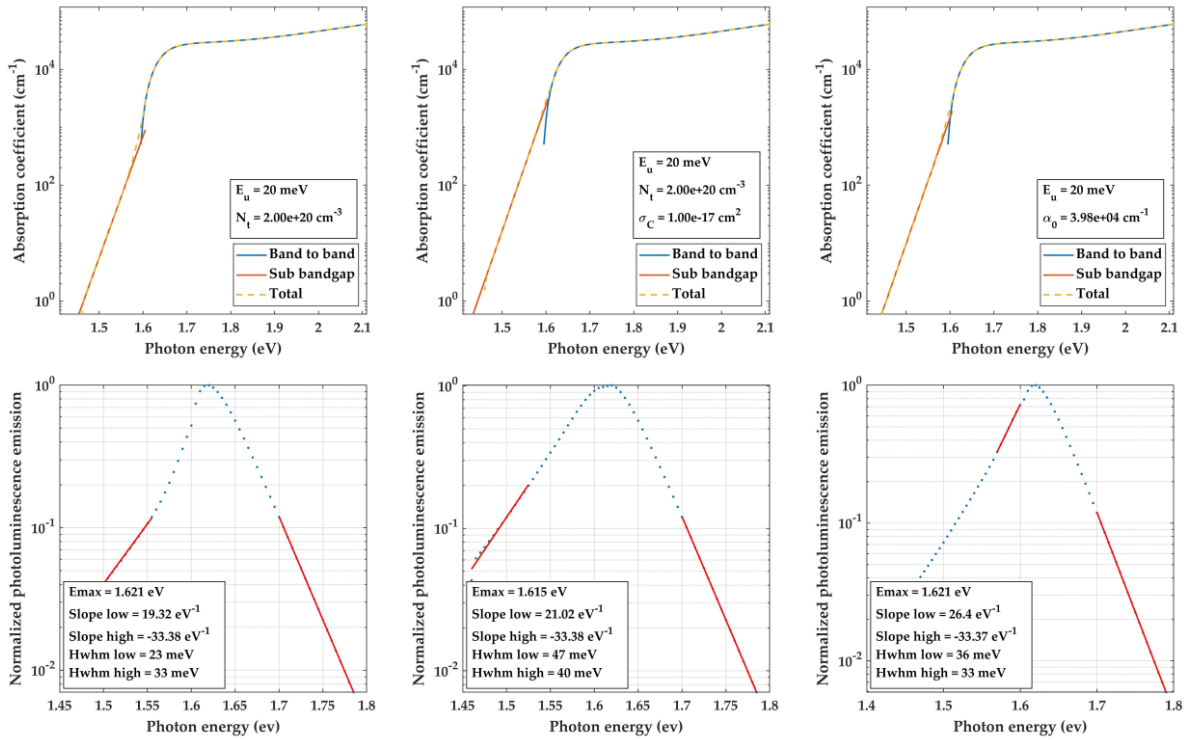

Figure 8. *Top: absorption coefficient computed from three models for sub-bandgap absorption, and from experimental ellipsometry measurements for band-to-band. The sum of hole and electron generation contributions is directly displayed. Bottom: associated photoluminescence spectrum obtained by performing optical and electrical simulations with the above absorption coefficient. Left: Lucovsky model. Middle: constant model. Right: Katahara-Hillhouse model.*

Finally, Figure 8 shows that all three models provide very similar absorption coefficients, and as a result, comparable photoluminescence spectra. It is to note, however, that the total density of shallow defects considered in this example is significantly high: 10^{20} cm^{-3}. It has been adjusted to provide a realistic PL spectrum

with Lucovsky model. However, its validity in the present case can be questioned, and it might underestimate the actual optical capture cross section.

As a result, it has been chosen to use the constant value further in this work: it provide a realistic photon energy dependence of the absorption coefficient and combines advantages of both other models. It allows for free adjustment through the constant σ_C, similarly to α_0 in Katahara Hillhouse model. Moreover, it accounts for a realistic shallow defect distribution of the band tails, like with Lucovsky model.

2.4 Studied devices and experimental results

The modelling methods exposed in previous section have been developed to be able to analyze experimental measurements of degrading perovskite solar cells performances.

Various characterization techniques can be employed to understand better degradation mechanisms, as exposed in Section 1.3.2. Notably, recording the evolution of the solar cells performances along aging allow to track the dynamics of degradation and provide supplementary information than having only two measurements points, before and after degradation. Here such results, recorded along aging under constant conditions, are investigated. Samples and the employed aging conditions are exposed in this section.

First, experimental results of aging studies published in literature were analyzed. This allowed to start investigating concrete examples without yet having results from IPVF. Furthermore, this allowed to demonstrate the capabilities of the methods developed, in a constrained context, without having full access to all material properties or aging characteristics, as it is for studies performed at IPVF.

In a second step, results obtained in-house were analyzed. It has been the opportunity to enhance the methods by considering more comprehensively the results (full JV characteristics) and supplementary characterization techniques (PL spectroscopy).

2.4.1 Experimental results extracted from literature

Evolution of optoelectrical performances along degradation are more and more reported in literature, as stability becomes a main concern of the perovskite research community. However, the vast majority reports only evolutions normalized to the initial performances and mostly only efficiency. The papers used in this section were selected because they are among the few report the evolution of Voc, Jsc and FF over time, as well as enough characteristics of the devices: the materials employed and the solar cell structure with its performances before degradation.

The first experimental results extracted from literature were record devices: by the time of publication, Peng *et al*. reported the highest efficiency for perovskite solar cells [29]. They studied $Cs_{0.05}FA_{0.88}MA_{0.07}PbI_{2.56}Br_{0.44}$ based perovskite solar cells (see details in Table 1) and focused on both ETL and HTL to optimize performance and stability. Results extracted for this work are displayed in Figure 9: they were recorded under STC on encapsulated solar cells having a Spiro-OMeTAD or P3HT:CuPc HTL layer. Importantly, aging (in between measurements points) was done under damp-heat: 85 °C, 85 % relative humidity under dark.

Interestingly, authors found the devices with P3HT:CuPc HTL significantly more stable. Degradation of doped Spiro-OMeTAD has been widely reported (see Section 1.3.1), it is therefore consistent to correlate it with the degradation observed here. Accordingly, authors attributed the degradation of electrical performances to a

deterioration of the HTL/perovskite interface, caused by lithium-ion diffusion (Spiro-OMeTAD dopant).

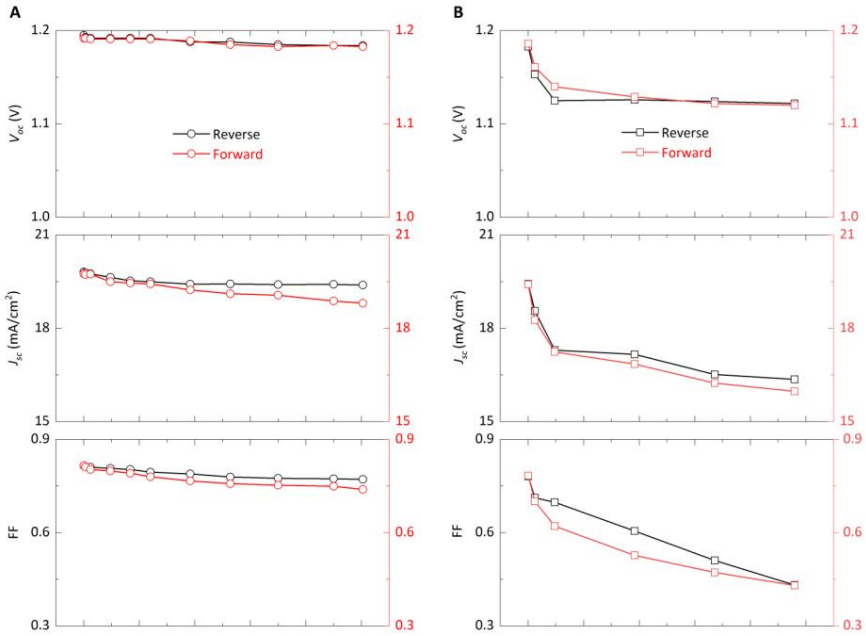

Figure 9. *Evolution of JV parameters reported by Peng* et al*, for devices fabricated with P3HT:CuPc (left) and Spiro-OMeTAD (right) HTL. Aging conditions were 85 °C, 85 % relative humidity and dark.*

The next results published in literature analyzed in this work have been reported by Li *et al*. [30]. They studied the degradation of unencapsulated, $FA_{0.9}Cs_{0.1}PbI_3$ based devices (see details in Table 1) under N2 atmosphere during 600h. Among other degradation conditions, cells were kept under one sun illumination, at 35 °C, and were tracked at maximum power point (MPP) or kept at open circuit (Voc). For each aging conditions, eight devices were used, and their JV characteristics recorded periodically. Finally, authors reported their average result.

Furthermore, they employed before and after degradation several microscopy characterization techniques with nanoscale spatial resolution, to evidence phase segregation of the perovskite material (distinct Cs-rich and FA-rich areas). Furthermore, the detrimental impact of Cs-rich areas was demonstrated through X-ray beam induced current measurements. In addition, authors also focused on HTL and gold back contact, by re-coating aged samples with fresh HTL and gold or even aging half stacks without HTL and gold from the beginning. As a results, Li *et al*. conclude that the main source of electrical performance degradation is the phase segregation of the perovskite itself, not being specifically triggered by HTL or gold.

Chen *et al*. optimized the composition of $Cs_{1-x}FA_xPbI_2Br$ perovskites and studied the stability of associated devices [31]. Results analyzed here were obtained with x = 0.3 (see details in Table 1) and devices were kept unencapsulated under ambient atmosphere. As a result, other compositions were proved to be all less stable and more prone to phase change.

Authors measured photoluminescence spectra and decays on fresh and aged cells, as well as XRD spectra on fresh and aged perovskite films. They conclude that

the studied compositions suffered from phase instability, and the composition with x = 0.3 delayed the most the phase change. Notably, a light soaking step associated with improved efficiency at the beginning of the aging study was attributed to better charge collection, coming from better interfaces and stress relaxation (supported by higher photoluminescence intensity and longer carrier lifetime).

In order to understand mechanisms occurring during degradation, Lim *et al*. focused on the kinetics of the degrading electrical parameters [32]. In this fourth experimental study analyzed here; devices are semi-transparent encapsulated cells with $FA_{0.95}MA_{0.05}PbI_{2.85}Br_{0.15}$ layer (see details in Table 1). They are exposed to air under one sun at constant temperature, ranging from 25 to 70 °C and results are reported in Figure 10. Importantly, all JV characteristics measurements were performed at 25 °C, even if devices were aged at higher temperature. Therefore, all associated simulations were also done at 25 °C.

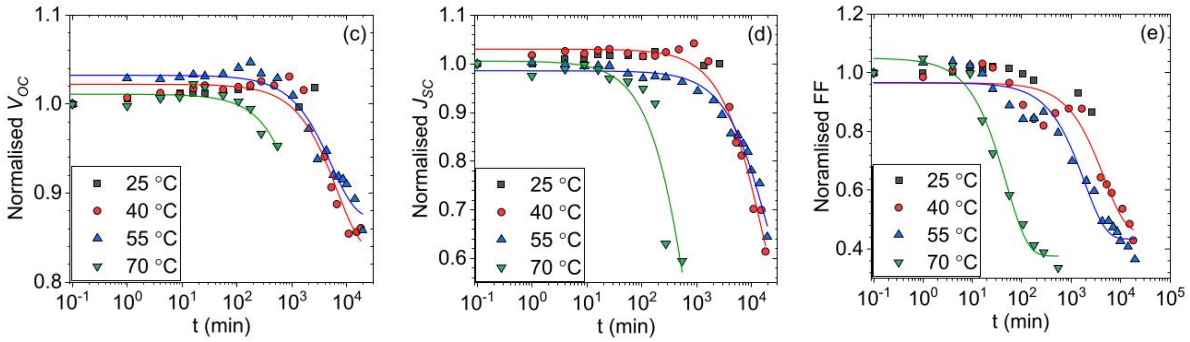

Figure 10. *Evolution of JV parameters reported by Lim* et al.*, recorded at 25, 40, 55 and 70 °C. Extracted from* [32]

Interestingly, authors determined reaction rates at each temperature and deduced activation energies with an Arrhenius law. Furthermore, they combined XRD and cross-sectional scanning electron microscopy to compare the perovskite material properties before and after degradation. They noted the absence of formation of PbI2, as a sign for stability. Similarly, UV-visible spectroscopy measurements done before and after aging are analyzed. Authors attributed the main cause of performance losses to an oxidation of the Spiro-OMeTAD HTL and iodide ions diffusion from the perovskite towards the HTL.

Finally, the results obtained from all these published studies will be investigated in Section 4.4.

Table 1. *Characteristics of the devices and aging studies reported in literature and investigated in this work. They were all aged under constant conditions periodically characterized through JV measurements.*

Source	Structure	Initial performances (STC)	Aging conditions	Measurement conditions
Peng *et al*.	Spiro-OMeTAD / $Cs_{0.05}FA_{0.88}MA_{0.07}PbI_{2.56}Br_{0.44}$ / TiO_2 (nip) P3HT:CuPc / $Cs_{0.05}FA_{0.88}MA_{0.07}PbI_{2.56}Br_{0.44}$ / TiO_2 (nip)	Voc = 1.18 V Jsc = 19.41 mA.cm^{-2} FF = 78.0 % Voc = 1.19 V Jsc = 19.80 mA.cm^{-2} FF = 81.0 %	85 % RH, 65 °C, dark.	AM1.5g, 1000 W.m^{-2}, 25 °C. Scan rate 20 mV.s^{-1}.
Li *et al*.	Spiro-OMeTAD + PTAA / $FA_{0.9}Cs_{0.1}PbI_3$ / SnO_2 (nip)	MPP tracked: Voc = 1.079 V Jsc = 22.77 mA.cm^{-2} FF = 76.3 % Voc tracked: Voc = 1.092 V Jsc = 22.89 mA.cm^{-2} FF = 77.1 %	N2 atmosphere, 35 °C. AM1.5g, 1000 W.m^{-2} MPP or Voc tracking.	Measurement after 0, 192, 408, and 600 h. AM1.5g, 1000 W.m^{-2}, 25 °C.
Chen *et al*.	NiO_x / $Cs_{0.7}FA_{0.3}PbI_2Br$ / C60 (pin)	Voc = 1.09 V Jsc = 15.65 mA.cm^{-2} FF = 72.0 %	Ambient atmosphere.	AM1.5g, 1000 W.m^{-2}, 25 °C.
Lim *et al*.	Spiro-OMeTAD / $FA_{0.95}MA_{0.05}PbI_{2.85}Br_{0.15}$ / SnO_2 (nip)	Aged at 40 °C: Voc = 1.027 V Jsc = 22.29 mA.cm^{-2} FF = 59.8 % Aged at 55 °C: Voc = 1.012 V Jsc = 23.34 mA.cm^{-2} FF = 62.4 % Aged at 70 °C: Voc = 1.042 V Jsc = 23.16 mA.cm^{-2} FF = 57.4 %	Ambient atmosphere. 1000 W.m^{-2}. 25, 40, 55 or 70 °C.	AM1.5g, 1000 W.m^{-2}, 25 °C. Scan rate 100 mV.s^{-1}.

2.4.2 Experimental results obtained at IPVF

Aging experiments are also performed at IPVF by a dedicated team. Such studies are critical to assess the long term stability of perovskite solar cells. They provide insights to the fabrication teams on the aspects that needs to be further developed to improve the solar cells stability. Two sets of results obtained by the stability team have been gathered and investigated in this work.

First, aging measurements under constant illumination with periodic measurements of JV characteristics were gathered for eight samples.

These devices were all fabricated with the same materials, but the perovskite layer was deposited with four different variations. In fact, this layer is deposited by spin-coating of a precursor solution and annealed for crystallization. The precursor

solution was prepared following two timelines: either the day before spin-coating, or the same day. Moreover, the solution was pre-heated at 70 °C for one hour before deposition or kept at room temperature.

For each method, two samples have been fabricated, they are listed in Table 2, and their JV characteristics before degradation reported in Appendix B, Figure B1. Finally, the stability of these devices have been recorded under N_2 atmosphere, ambient temperature and constant illumination for more than 1000 h, with JV measurements every 15 minutes. The associated results will be investigated in Section 4.5.1.

Table 2. *Characteristics of the devices prepared with four different methods. They were aged under constant conditions and periodically characterized through JV measurements.*

Description	Structure	Name	Name in manuscript	Aging conditions	Measurement conditions
Prepared on deposition day. Room temperature.	Glass / FTO / TiO_2 / $Cs_{0.05}(MA_{0.17}FA_{0.83})_{0.95}Pb(Br_{0.17}I_{0.83})_3$ / PTAA / Gold	JC17-03 JC17-04	JV-1.1 JV-1.2	N2 atmosphere. Ambient temperature. Constant illumination, AM1.5g, 1000 $W.m^{-2}$.	Measurements every 15 min. Scan rate 20 $mV.s^{-1}$.
Prepared on deposition day. Pre-heated @ 70 °C.		JC17-07 JC17-08	JV-2.1 JV-2.2		
Prepared one day before deposition. Room temperature.		JC17-09 JC17-10	JV-3.1 JV-3.2		
Prepared one day before deposition. Pre-heated @ 70 °C.		JC17-15 JC17-16	JV-4.1 JV-4.2		

Furthermore, an in-situ characterization setup has been developed in a climatic chamber. It allows to measure periodically current-voltage characteristics and photoluminescence spectra, under various environmental conditions. The degradation of five samples is investigated in this work, they were all subjected to a damp heat test: 85 % relative humidity, 65 °C and dark. These conditions correspond to one of the standards proposed to the perovskite research community [33], mentioned in Section 1.3.2.

The solar cells were fabricated with slightly different HTLs and ETLs, as reported in Table 3. Notably TiO_2 and SnO_2 ETLs have been considered, and PTAA and Spiro-MeOTAD HTLs. Only three of the four possible configurations were available, but these results can provide insights on the stability of potential substitutes to TiO_2 and Spiro-MeOTAD, as their poor stability has been mentioned in Section 1.3.1. The JV characteristics before degradation of these devices is reported in Appendix B, Figure B2.

Importantly, the illumination source employed for the PL and light-JV measurements is the same, a laser with a 660 nm wavelength. This allowed to minimize the time necessary for the measurements, by avoiding waiting for the stabilization of

a AM1.5g illumination source. As a result, the device remained as much as possible under the dark aging conditions. This atypical illumination source for JV measurements is the reason for very high Jsc in three cases. Importantly, it has been taken into account when performing simulations, as mentioned in Section 2.1. Finally, the associated results will be investigated in Section 4.5.2.

Table 3. *Characteristics of the devices aged under constant conditions in a climatic chamber and periodically characterized through JV and PL measurements.*

Description	Structure	Name	Name in manuscript	Aging conditions	Measurement conditions
IPVF baseline with PTAA HTL.	Glass / FTO / TiO_2 / $Cs_{0.05}(MA_{0.17}FA_{0.83})_{0.95}Pb(Br_{0.17}I_{0.83})_3$ / PTAA / Gold	JC18-02 JC18-13 1 JC18-13 2	JV-PL-1 JV-PL-2 JV-PL-3	85 % R.H. 65 °C. Dark.	Measurements every 20 min. Illumination through 200 mW laser @ 660 nm. Scan up to Voc.
IPVF baseline with SnO_2 ETL and PTAA HTL.	Glass / FTO / SnO_2 / $Cs_{0.05}(MA_{0.17}FA_{0.83})_{0.95}Pb(Br_{0.17}I_{0.83})_3$ / PTAA / Gold	MP118-2	JV-PL-4		Measurements every 20 min. Illumination through 50 mW laser @ 660 nm. Scan up to 1.2 V.
IPVF baseline with Spiro-MeOTAD HTL.	Glass / FTO / TiO_2 / $Cs_{0.05}(MA_{0.17}FA_{0.83})_{0.95}Pb(Br_{0.17}I_{0.83})_3$ / Spiro-MeOTAD / Gold	SG-11	JV-PL-5		Measurements every 20 min. Illumination through 50 mW laser @ 660 nm. Scan up to 1.2 V.

These two sets of aging studies performed at IPVF are accompanied with a comprehensive knowledge on the device characteristics, for instance on the layer thicknesses. Moreover, the full JV characteristics (under AM1.5g or laser illumination) and PL spectra are available, making possible to extract all optoelectrical parameters mentioned in Sections 2.2 and 2.3. This provides a more favorable context compared to using experimental data extracted from literature and allows to perform more confidently and precisely the analyses reported in this work. In fact, the interactions with the fabrication and characterization teams were crucial to properly perform these analyses.

2.5 Pre-treatment of experimental results

Experimental data recorded at IPVF were obtained in the form of JV characteristics and PL spectra, and optoelectrical parameters were extracted as explained in Sections 2.3 and 2.4.

In facts, thousands of points are available because measurements were performed every 15 to 20 minutes during several hundreds of hours. When plotting their evolution along time, it appears that measurement noise is present, and some points are clear outliers. A pre-treatment procedure have therefore been developed and is summarized in Table 4 for JV parameters.

The first step has to be very carefully tuned, because it directly modifies the JV characteristics. It is crucial not to modify them, as it would "flattens" them and modify the slopes at SC and OC. The associated voltage window is therefore kept very low. Unfortunately, it has been necessary to introduce this step to overcome some obvious noise occurred during the measurement of given JV characteristics.

The second step aims at removing full JV characteristics from the dataset and avoid their perturbation of the smoothing step afterwards. It simply works by defining thresholds for quantities that are extracted at each JV characteristics. For instance, the too low FF or ratio of slopes at SC and OC allow to remove curves that appear shunted. Importantly, the time derivative is computed for each optoelectrical parameter and compared to its respective median value over the full aging experiment. Too strong variations are identified when the value is too far from the median by a certain number of times the standard deviation.

Lastly, a moving median filtering is applied along time at each voltage. Here the median has the advantage to be less impacted by outliers than the mean value. This finally allows to keep working with a set of full JV characteristics, not only the extracted optoelectrical parameters.

Table 4. *Summary of the steps employed to remove noise and outliers from JV parameters along time. Values of the associated parameters and thresholds are slightly adjusted for each device, an example is exposed in Table 5.*

Task	Comments
Smooth JV characteristics along voltage	Savitzky-Golay filter: a quadratic polynomial is fitted over each voltage window.
Remove outliers	Identifiers: Too low Voc or FF value. Too low slope at SC / slope at OC ratio. Too high time derivative.
Smooth JV characteristics along time	Moving median filter: the median is retained over each time window.

When performing such pre-processing, it is absolutely crucial to remain true to the original data and avoid creating fake trends for instance. Therefore, the optoelectrical parameters are extracted from the JV characteristics after each step and

plotted together over time. This allows to ensure the validity of the finally obtained smoothed data.

The conformity of the processed data for device JV-1.1 is illustrated in Figure 11, where the purple points ("Smoothed along time") remain close to the "Raw" data. The parameter values for the pre-processing steps employed in this example are summarized in Table 5.

Table 5. *Pre-processing parameters employed for JV measurements of device JV-1.1.*

Parameter	Value
Voltage smoothing window (V)	0.3
Voc min (V)	0.2
FF min (%)	30
Rsh/Rs min ratio	5
JV time derivative relative max	3
JV time smoothing window (h)	30

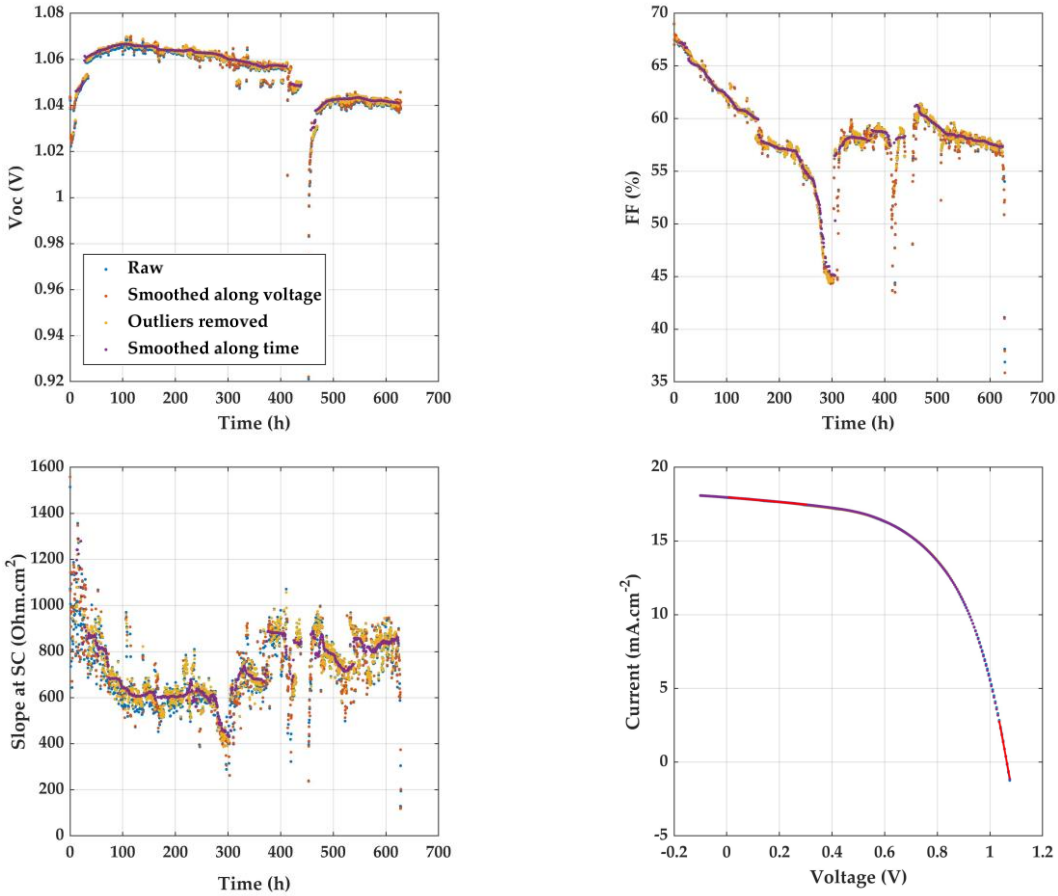

Figure 11. *Degradation over time of device JV-1.1 for reverse measurements. The parameters are extracted from the JV characteristics at each step of the pre-treatment. Bottom right show an example of JV characteristic, at 190 h of aging. Other optoelectrical parameters are displayed in Appendix B, Figure B3.*

It is to note that the Voc and FF thresholds were not employed here, and most of the outliers were identified through the time derivative, as a result 743 out of 1958 recorded JV characteristics were discarded.

Furthermore, the slope at SC shows a very significant noise but even Voc, Jsc and FF have noise that needs to be filtered out. This example illustrates how the procedure allows to extract a true trend. Here the JV characteristic recorded after 190 h of aging also illustrates the conformity of the treated data to the original measurement.

Results for device JV-3.1 in Figure 12 show similar features, however, the slope at OC is here noisier. One could also argue that the values after the voltage smoothing step are slightly higher than the raw data and could attribute this to too strong smoothing. However, the associated example of JV characteristic shows that it remained very close. This points out a strength of this procedure, as it makes the extraction of the slopes more reliable.

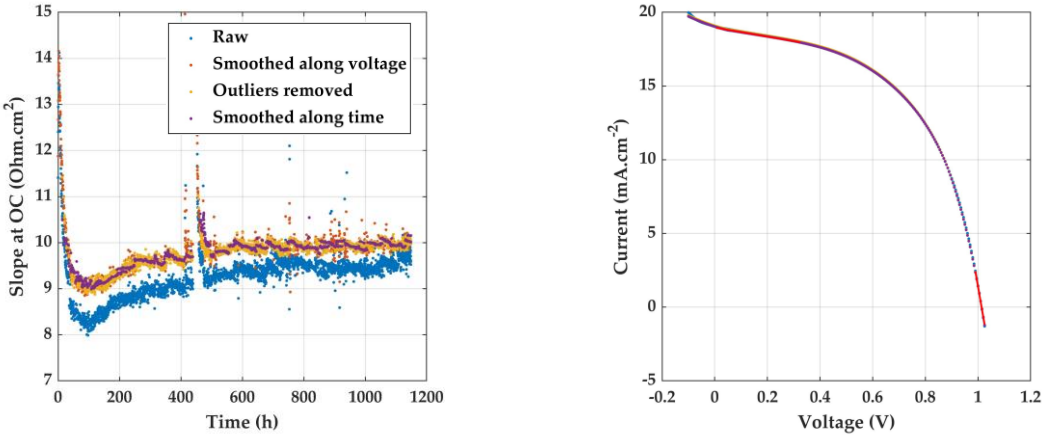

Figure 12. *Degradation over time of device JV-3.1 for forward measurements. Slope at OC is extracted from the JV characteristics at each step of the pre-treatment. Right show an example of JV characteristic, at 850 h of aging. . Other optoelectrical parameters are displayed in Appendix B, Figure B4.*

When photoluminescence spectra were simultaneously recorded with JV characteristics, a similar procedure was employed, with a first smoothing step along photon energy. The device JV-PL-1 is illustrated as an example, with associated parameters in Table 6 Only a prior step, to remove the setup dark signal, and account for its bandwidth was necessary. In fact, not all photon energies are received with the same efficiency (because of the spectrometer and the optics) and calibration of data is necessary.

Results for device JV-PL-1 are exposed in Figure 13. In this example, 213 JV characteristics and 50 PL spectra were identified as outliers, out of 768 measurements. In fact, the solar cell might have stopped functioning at approx. 275 h: Voc and FF instantaneously drop to 0.2 V and less than 25 % respectively. The following points are discarded. This could be associated to the solar cell to become shunted. Notably, such almost instantaneous variation cannot be easily analyzed through the methods developed here because it is not sufficiently resolved in time. However, the previous

long term decrease Voc and FF decrease is a good example of degradation trend that will be investigated further.

Table 6. *Pre-processing parameters employed for JV and PL measurements of device JV-PL-1.*

Parameter	Value
Voltage smoothing window (V)	0.3
Voc min (V)	0.2
FF min (%)	30
Rsh/Rs min ratio	5
JV time derivative relative max	3.5
JV time smoothing window (h)	20
Photon energy smoothing window (eV)	0.05
PL time derivative relative max	3
PL time smoothing window (h)	20

It is to note that the value of the slope on low energy side appears strongly shifted by the procedure on Figure 13. However, the PL spectrum recorded after 62 h of aging shows that the slope extraction on the raw spectrum is strongly inaccurate.

Importantly, the improved reliability after smoothing is also illustrated on the JV characteristic. Here, obvious un-physical variations of current occur between 0.2 and 0.4 V. Here, the smoothing along voltage removed part of the noise, and the smoothing along time allowed to obtain the realistic slope. In fact, such artefact do not remain the same on consecutive measurements, making the time smoothing at each voltage appropriate.

The examples reported in this section illustrate that a pre-processing step is necessary, not only to facilitate the interpretation, but also to improve the reliability of the extracted optoelectrical parameters. Furthermore, the procedure is not applied to the parameters, but to full JV characteristics and PL spectra. Therefore, the curves associated to the smoothed parameters are still available, allowing to keep taking advantage of the full measurements in the following analysis steps.

Importantly, various physical processes can perturb the results over such long lasting aging studies. Experimental setups are natural sources of noise and errors can occur when acquiring JV characteristics or PL spectra, but also the environment, controlled or not can be perturbed. Therefore, it has been necessary to develop this pre-processing strategy in order to facilitate interpretation when comparing to simulation results. Results obtained aim at accounting for these effects and removing them. In fact, such procedures could be useful outside degradation studies, by identifying acquisition errors in a broader context. However, it has to be kept in mind that a common pitfall at such step is to create arbitrary trends, losing the physical meaning of the measurements.

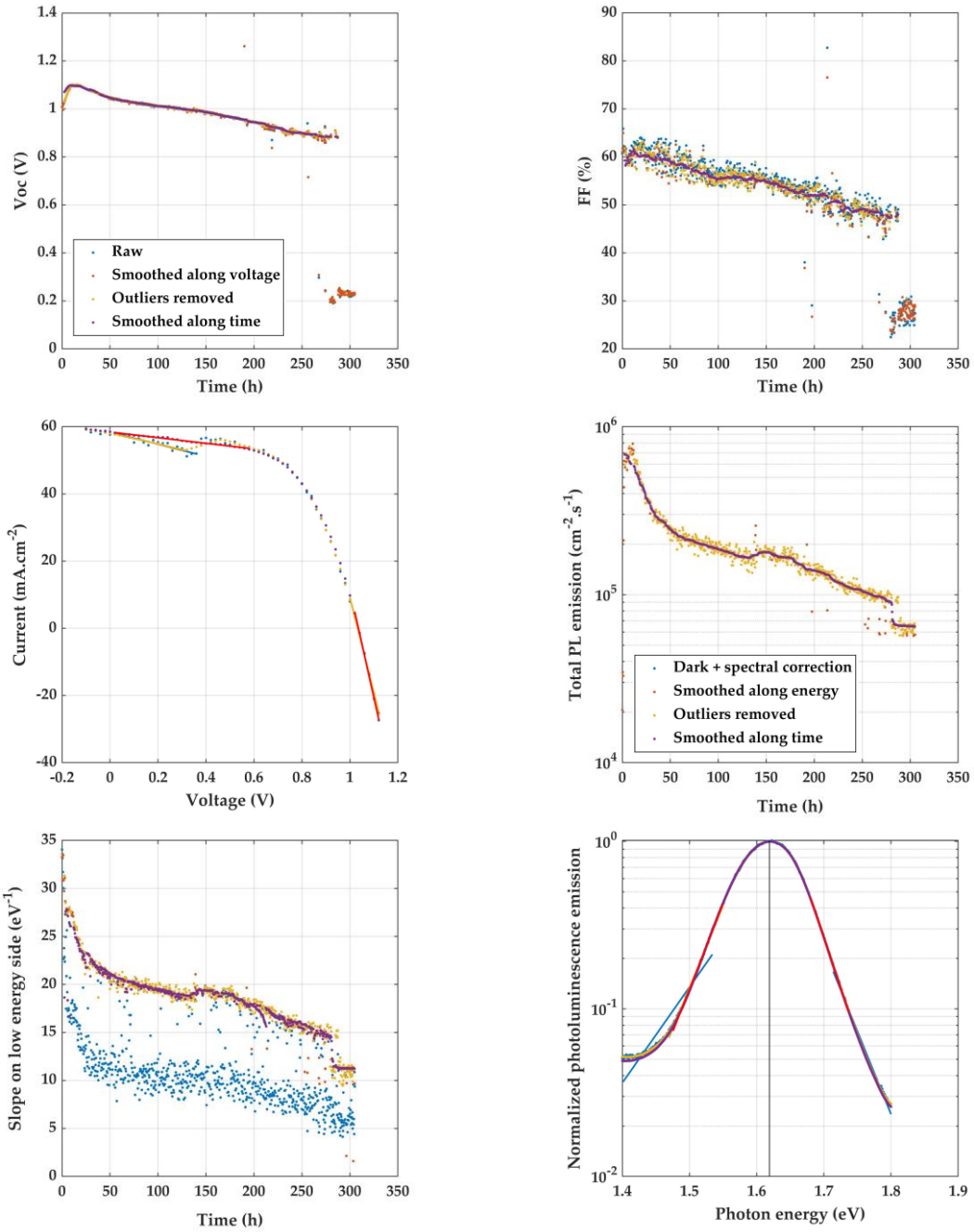

Figure 13. *Degradation over time of device JV-PL-1 (reverse JV measurements). The parameters are extracted from the JV characteristics and PL spectra at each step of the pre-treatment. Example of JV characteristic and PL spectrum were measured at 62 h of aging. Other optoelectrical parameters are displayed in Appendix B, Figure B5.*

Chapter conclusion

This works aims at providing insights on experimental degradation measurements of perovskite solar cells, through modeling. In this section, both simulation (models and numerical solvers) and experimental (measurements of degradation) tools have been exposed.

First, a coupling scheme of optical and electrical simulations has been employed to reproduce experimental optoelectrical performances of perovskite solar cells.

Importantly, the transfer matrix method is used to fully describe the optical behavior of the solar cell. It provides the spectral absorption rate along depth, total absorptivity and charge carriers generation rate. The latter is then used by the drift diffusion block, to obtain a full description of the charge carrier densities, recombination and currents.

As a result, current voltage characteristics and photoluminescence spectra are simulated. Both provide complementary insights on the optoelectrical performances of a solar cell, by probing different regimes. The current voltage characteristic is directly related to the maximum power point and output power when the photoluminescence spectrum provides insights on the material quality through carrier densities and associated radiative recombination. It has been also shown how the sub-bandgap optical behavior is considered in this work.

Moreover, these modeling tools have been used to analyze various experimental measurements. Aging studies with periodical measurements of JV characteristics and PL spectra have been investigated, through the evolution of associated optoelectrical parameters over time and along degradation. Notably, these experimental results are widely reported, although often to merely demonstrate the stability of a given sample (at least for JV characteristics).

First, periodical measurements published in literature have been investigated. It demonstrated the capabilities of the methods developed in this work. This also supports the idea that sharing data between research groups can allow to take more advantage of given experimental results. Initiatives have been proposed to construct global open-access databases with uniformed reporting of various device results [34]. Furthermore, experiments performed at IPVF, were also employed. In this case, very useful complementary information on the nature of the perovskite samples and aging conditions was available. Therefore, aging experiments employing only JV or coupled JV and PL tracking were analyzed.

Importantly, a pre-processing procedure has been developed remove noise and outliers from experimental measurements. It has been finely tuned to retain the physical meaning of the data, without creating arbitrary trends.

Finally, these coupled modeling and experimental approaches will permit comparisons between each other because both can subject the solar cells to the same conditions and characterize the same working points. These comparisons will be the core of the work presented further, associated to selections of simulation inputs in Chapter 3, or distinctions of degradation mechanisms in Chapter 4.

References

[1] C. C. Katsidis and D. I. Siapkas, "General transfer-matrix method for optical multilayer systems with coherent, partially coherent, and incoherent interference," *Appl Opt*, vol. 41, no. 19, p. 3978, 2002, doi: 10.1364/ao.41.003978.

[2] L. A. A. Pettersson, L. S. Roman, and O. Inganäs, "Modeling photocurrent action spectra of photovoltaic devices based on organic thin films," *J Appl Phys*, vol. 86, no. 1, pp. 487–496, 1999, doi: 10.1063/1.370757.

[3] M. Burgelman, P. Nollet, and S. Degrave, "Modelling polycrystalline semiconductor solar cells," *Thin Solid Films*, vol. 361, pp. 527–532, 2000, doi: 10.1016/S0040-6090(99)00825-1.

[4] A. Slami, M. Bouchaour, and L. Merad, "Numerical Study of Based Perovskite Solar Cells by SCAPS-1D," *International Journal of Energy and Environment*, vol. 13, pp. 17–21, 2019.

[5] K. Bhavsar and P. B. Lapsiwala, "Numerical simulation of perovskite solar cell with different material as electron transport layer using SCAPS-1D software," *Semiconductor Physics, Quantum Electronics and Optoelectronics*, vol. 24, no. 3, pp. 341–347, 2021, doi: 10.15407/spqeo24.03.341.

[6] M. S. Chowdhury *et al.*, "Effect of deep-level defect density of the absorber layer and n/i interface in perovskite solar cells by SCAPS-1D," *Results Phys*, vol. 16, p. 102839, 2020, doi: 10.1016/j.rinp.2019.102839.

[7] F. Jannat, S. Ahmed, and M. A. Alim, "Performance analysis of cesium formamidinium lead mixed halide based perovskite solar cell with MoOx as hole transport material via SCAPS-1D," *Optik (Stuttg)*, vol. 228, p. 166202, 2021, doi: 10.1016/j.ijleo.2020.166202.

[8] M. K. Hossain, M. H. K. Rubel, G. F. I. Toki, I. Alam, M. F. Rahman, and H. Bencherif, "Effect of Various Electron and Hole Transport Layers on the Performance of CsPbI3-Based Perovskite Solar Cells: A Numerical Investigation in DFT, SCAPS-1D, and wxAMPS Frameworks," *ACS Omega*, vol. 7, no. 47, pp. 43210–43230, Nov. 2022, doi: 10.1021/acsomega.2c05912.

[9] P. Wurfel and U. Wurfel, *Physics of solar cells: from basic principles to advanced concepts*. 2016.

[10] E. Raza *et al.*, "Numerical simulation analysis towards the effect of charge transport layers electrical properties on cesium based ternary cation perovskite solar cells performance," *Solar Energy*, vol. 225, pp. 842–850, 2021, doi: 10.1016/j.solener.2021.08.008.

[11] M. Burgelman, K. Decock, A. Niemegeers, J. Verschraegen, and S. Degrave, "SCAPS manual." 2021.

[12] D. Vasileska, "Drift-Diffusion Model: Solution Details." Accessed: May 15, 2023. [Online]. Available: https://nanohub.org/resources/1565/download/ddmodel_solution_details_word.pdf

[13] D. Vasileska, D. Mamaluy, H. R. Khan, K. Raleva, and S. M. Goodnick, "Semiconductor device modeling," *J Comput Theor Nanosci*, vol. 5, no. 6, pp. 999–1030, 2008, doi: 10.1166/jctn.2008.2538.

[14] N. E. Courtier, "Interpreting ideality factors for planar perovskite solar cells: Ectypal diode theory for steady-state operation," *Phys Rev Appl*, vol. 14, no. 2, p. 024031, 2020, doi: 10.1103/PhysRevApplied.14.024031.

[15] W. Tress *et al.*, "Interpretation and evolution of open-circuit voltage, recombination, ideality factor and subgap defect states during reversible light-soaking and irreversible degradation of perovskite solar cells," *Energy Environ Sci*, vol. 11, no. 1, pp. 151–165, 2018, doi: 10.1039/c7ee02415k.

[16] J. Y. Huang, Y. W. Yang, W. H. Hsu, E. W. Chang, M. H. Chen, and Y. R. Wu, "Influences of dielectric constant and scan rate on hysteresis effect in perovskite solar cell with simulation and experimental analyses," *Sci Rep*, vol. 12, no. 1, p. 7927, Dec. 2022, doi: 10.1038/s41598-022-11899-x.

[17] Y. Zhao, W. Zhou, Z. Han, D. Yu, and Q. Zhao, "Effects of ion migration and improvement strategies for the operational stability of perovskite solar cells," *Physical Chemistry Chemical Physics*, vol. 23, no. 1, pp. 94–106, 2021, doi: 10.1039/d0cp04418k.

[18] Y. Yuan and J. Huang, "Ion Migration in Organometal Trihalide Perovskite and Its Impact on Photovoltaic Efficiency and Stability," *Acc Chem Res*, vol. 49, no. 2, pp. 286–293, 2016.

[19] D. A. Jacobs *et al.*, "Hysteresis phenomena in perovskite solar cells: The many and varied effects of ionic accumulation," *Physical Chemistry Chemical Physics*, vol. 19, no. 4, pp. 3094–3103, 2017, doi: 10.1039/c6cp06989d.

[20] F. Urbach, "The long-wavelength edge of photographic sensitivity and of the electronic Absorption of Solids," *Physical Review*, vol. 92, no. 5, p. 1324, 1953, doi: 10.1103/PhysRev.92.1324.

[21] N. Droseros, D. Tsokkou, and N. Banerji, "Photophysics of MethylammoniumLead Tribromide Perovskite: Free Carriers, Excitons and Sub-Bandgap States," *Adv Energy Mater*, vol. 10, no. 13, p. 1903258, 2020, doi: https://doi.org/10.1002/aenm.201903258.

[22] N. Falsini, G. Roini, A. Ristori, N. Calisi, F. Biccari, and A. Vinattieri, "Analysis of the Urbach tail in cesium lead halide perovskites," *J Appl Phys*, vol. 131, no. 1, p. 010902, 2022, doi: 10.1063/5.0076712.

[23] A. D. Wright, R. L. Milot, G. E. Eperon, H. J. Snaith, M. B. Johnston, and L. M. Herz, "Band-Tail Recombination in Hybrid Lead Iodide Perovskite," *Adv Funct Mater*, vol. 27, no. 29, p. 1700860, Aug. 2017, doi: 10.1002/adfm.201700860.

[24] S. Khelifi, M. Burgelman, J. Verschraegen, and A. Belghachi, "Impurity photovoltaic effect in GaAs solar cell with two deep impurity levels," *Solar Energy Materials and Solar Cells*, vol. 92, no. 12, pp. 1559–1565, 2008, doi: 10.1016/j.solmat.2008.07.003.

[25] M. J. Keevers and M. A. Green, "Efficiency improvements of silicon solar cells by the impurity photovoltaic effect," *J Appl Phys*, vol. 75, no. 8, pp. 4022–4031, 1994, doi: 10.1063/1.356025.

[26] G. Lucovsky, "On the photoionization of deep impurity centers in semiconductors," *Solid State Commun*, vol. 3, no. 9, pp. 299–302, 1965, doi: 10.1103/PhysRevB.41.5131.

[27] J. W. McPherson, "Lorentz factor determination for local electric fields in semiconductor devices utilizing hyper-thin dielectrics," *J Appl Phys*, vol. 118, no. 20, p. 204106, 2015, doi: 10.1063/1.4936271.

[28] J. K. Katahara and H. W. Hillhouse, "Quasi-fermi level splitting and sub-bandgap absorptivity from semiconductor photoluminescence," *J Appl Phys*, vol. 116, no. 17, p. 173504, 2014, doi: 10.1063/1.4898346.

[29] J. Peng *et al.*, "Nanoscale localized contacts for high fill factors in polymer-passivated perovskite solar cells," *Science (1979)*, vol. 371, no. 6527, pp. 390–395, 2021, doi: 10.1126/science.abb8687.

[30] N. Li *et al.*, "Microscopic Degradation in Formamidinium- Cesium Lead Iodide Perovskite Solar Cells under Operational Stressors," *Joule*, vol. 4, no. 8, pp. 1743–1758, 2020, doi: 10.1016/j.joule.2020.06.005.

[31] M. Chen *et al.*, "Inverted CsPbI2Br perovskite solar cells with enhanced efficiency and stability in ambient atmosphere via formamidinium incorporation," *Solar Energy Materials and Solar Cells*, vol. 218, p. 110741, 2020, doi: 10.1016/j.solmat.2020.110741.

[32] J. Lim *et al.*, "Kinetics of light-induced degradation in semi-transparent perovskite solar cells," *Solar Energy Materials and Solar Cells*, vol. 219, p. 110776, 2021, doi: 10.1016/j.solmat.2020.110776.

[33] M. V. Khenkin *et al.*, "Consensus statement for stability assessment and reporting for perovskite photovoltaics based on ISOS procedures," *Nat Energy*, vol. 5, no. 1, pp. 35–49, 2020, doi: 10.1038/s41560-019-0529-5.

[34] T. J. Jacobsson *et al.*, "An open-access database and analysis tool for perovskite solar cells based on the FAIR data principles," *Nat Energy*, vol. 7, no. 1, pp. 107–115, 2021, doi: 10.1038/s41560-021-00941-3.

Chapter 3: Exploration of parameter space

Table of contents

Chapter introduction

It has been exposed in the previous chapters how drift diffusion simulations are employed here, and how they can help to investigate degradation mechanisms of perovskite solar cells. A crucial aspect is the significant number of necessary input parameters, along with the uncertainty around the value of some of them.

Therefore, the nature of the inputs needing to be statistically considered because of their importance and their variability are exposed in Section 3.1.

The method employed to explore the associated highly dimensional space is defined in Section 3.2.

Next, in Section 3.3, distributions of inputs parameters obtained with this genetic algorithm for exemplary samples are reported, already allowing to discuss the characteristics of these solar cells.

Finally, the results of the genetic algorithms are employed as a basis to simulate the impact of given degradation mechanisms. The statistics of the responses are discussed in Section 3.4.

Chapter key points:

- Drift diffusion simulations require numerous input parameters. Some values are not confidently known for a given sample.
- An input parameters space of dimension 13 has been defined, with up to 4e15 potential configurations to explore.
- A genetic algorithm (based on randomized generation, mutation and selection of simulation inputs) has been developed to reproduce closely the optoelectrical performances of a given solar cells with approx. 100 inputs configurations.
- Three configurations have been employed to select the proper inputs: only Voc, Jsc and FF were available from literature data, slopes at SC and OC were added for IPVF devices, and peak position and slope on low energy side when PL spectra were recorded.
- Unitary degradation mechanisms are considered by simulating the response to a variation of a given material parameters.
- Statistics of the responses among all sets reproducing a given sample performances are determined for further use in the next chapter.

3.1 A highly multidimensional space to explore

In this work, optoelectrical performances of perovskite solar cells are simulated by drift-diffusion, coupled with transfer matrix optical simulations. Details of the modeling methods are available in Section 2.1.

The solar cells are simulated as a stack of hole transport layer (HTL) / perovskite / electron transport layer (ETL) and for each layer, numerous parameters are necessary, listed in Table 1. Importantly, they are divided into several categories, depending on their importance and the reliability of available values.

First, some parameters are directly determined by the experimental conditions, or the device fabrication: for instance illumination intensity, or layer thickness. They are "fixed for each experiment" in Table 1.

Other parameters are considered to be reliably available in literature or through measurements. They do not vary significantly between fabrication techniques or from one sample to the other. For instance, bandgap, electron affinity and density of states are core characteristics of a material, and are assumed not to change, unless the nature of the material is strictly different. They are "fixed for each material" in Table 1.

In some cases their role is sufficiently minor that fixed values from literature can be employed without impacting too significantly the output. For instance, minority carrier mobilities in transport layers or carriers capture cross sections at defects (under steady state only the product with defect density will impact recombination). Deep defects are considered to be located at mid perovskite bandgap, where their role as SRH recombination centers is the strongest. They are fixed to given values in Table 1.

Importantly several parameters are assumed to be variable from one sample to the other. For instance, carrier mobilities and defect densities can vary significantly even within a single fabrication batch. This is a main cause for the variability of the optoelectrical performances of perovskite solar cells (even with same fabrication scheme), as mentioned in Section 1.2. Finally, parameters such as doping level of extracting layers also vary between experiments because extrinsic doping can be tuned on purpose for optimization. However, the actual value of acceptor or donor densities are not always available or known.

Table 1. *List of all 50 simulation parameters necessary to perform a drift-diffusion - transfer matrix simulation of a perovskite solar cell. Parameters are divided into several categories, depending on their importance and the reliability of available values.*

Simulation parameter		**Fixed / Variable**
Illumination intensity		Fixed for each experiment
Temperature		Fixed for each experiment
External Rs		Variable
External Rsh		Variable
Optical filter average transmission		Fixed for each device
Hole transporting material	Thickness	Fixed for each device
	Refractive indices	Fixed for each material
	Bandgap	Fixed for each material
	Electron affinity	Fixed for each material
	Relative permittivity	Fixed for each material
	Conduction band effective density of states	Fixed for each material
	Valence band effective density of states	Fixed for each material
	Electron mobility	Fixed for each material
	Hole mobility	Variable
	Donor density	Fixed to 0 cm^{-3}
	Acceptor density	Variable
HTL / pvk interface	Defect density	Variable
	Electron and holes capture cross section	Fixed to 10^{-15} cm^2
	Defects energy distribution	Fixed to mid pvk gap
Perovskite	Thickness	Fixed for each device
	Refractive indices	Fixed for each material
	Bandgap	Fixed for each material
	Electron affinity	Fixed for each material
	Relative permittivity	Fixed for each material
	Conduction band effective density of states	Fixed for each material
	Valence band effective density of states	Fixed for each material
	Electron mobility	Variable
	Hole mobility	Variable
	Donor density	Fixed to 0 cm^{-3}
	Acceptor density	Fixed to 0 cm^{-3}
	Deep defects density	Variable

	Shallow defects density	Variable
	Electron and holes capture cross section	Fixed to 10^{-15} cm^2
	Deep defects energy distribution	Fixed to mid gap
	Shallow defects energy distribution	Variable
	Optical capture cross section	Fixed to 10^{-15} cm^2
ETL / pvk interface	Defect density	Variable
	Electron and holes capture cross section	Fixed to 10^{-15} cm^2
	Defects energy distribution	Fixed to mid pvk gap
Electron transporting material	Thickness	Fixed for each device
	Refractive indices	Fixed for each material
	Bandgap	Fixed for each material
	Electron affinity	Fixed for each material
	Relative permittivity	Fixed for each material
	Conduction band effective density of states	Fixed for each material
	Valence band effective density of states	Fixed for each material
	Electron mobility	Variable
	Hole mobility	Fixed for each material
	Donor density	Variable
	Acceptor density	Fixed to 0 cm^{-3}

It is crucial to be able to account for these variabilities when modelling the performances of perovskite solar cells. Therefore, ranges of possible values are defined and explored, they are summarized in Table 2 for an exemplary device. These ranges are discretized to avoid considering too close values and to be able to store simulation results in a database. The discretization is done in logarithmic scale, as the parameters can vary over several orders of magnitude, and they often play a role on outputs in logarithmic scale. This also justifies considering logarithmic scales in statistical analyses in Chapter 5. Note that shallow defects energy distribution is defined in linear scale because of smaller range of variation and its almost direct impact on the PL emission spectrum slope at low energy side. In fact, both parameters related to shallow defects are very finely discretized, because they alone define the shape of emitted spectrum.

Table 2. *Example of discretization of the possible values for the parameters considered to be variable between experiments. The total number of configurations adds up to 4e15. JV-PL-1 device is considered, constituted of PTAA / $Cs_{0.05}(MA_{0.17}FA_{0.83})_{0.95}Pb(Br_{0.17}I_{0.83})_3$ / TiO_2.*

Simulation parameter		**Minimum value**	**Maximum value**	**Number of possible values**
External Rs		0.5 Ohm.cm²	15 Ohm.cm²	29
External Rsh		100 Ohm.cm²	5000 Ohm.cm²	34
Hole transporting material	Hole mobility	0.001 $cm^2.V^{-1}.s^{-1}$	0.5 $cm^2.V^{-1}.s^{-1}$	14
	Acceptor density	2e16 cm^{-3}	2e18 cm^{-3}	10
HTL / pvk interface	Defect density	1e13 cm^{-2}	1e20 cm^{-2}	36
Perovskite	Electron mobility	0.05 $cm^2.V^{-1}.s^{-1}$	50 $cm^2.V^{-1}.s^{-1}$	30
	Hole mobility	0.05 $cm^2.V^{-1}.s^{-1}$	50 $cm^2.V^{-1}.s^{-1}$	30
	Deep defects density	1e13 cm^{-3}	1e17 cm^{-3}	41
	Shallow defects density	1e18 cm^{-3}	8e18 cm^{-3}	10
	Shallow defects energy distribution	20 meV	28 meV	17
ETL / pvk interface	Defect density	1e13 cm^{-2}	1e20 cm^{-2}	36
Electron transporting material	Electron mobility	0.5 $cm^2.V^{-1}.s^{-1}$	50 $cm^2.V^{-1}.s^{-1}$	10
	Donor density	1e17 cm^{-3}	1e19 cm^{-3}	11

This discretization also allows to quantify the size of the space to explore by computing all possible parameters combinations. As a result, the total number of potential configurations to simulate adds up to approx. 10^{15}, in a space of dimension 13. Considering all of them would not be possible, it is therefore crucial to develop a procedure to find the suitable parameters combinations necessary to analyze the degradation of a given solar cell.

3.2 Exploration of the space with a genetic algorithm

In order to analyze the degradation of a given perovskite solar cell, it is necessary to adjust the simulation parameters as close as possible to their actual value. The characterizations of the solar cell performances, current voltage (JV) characteristics and photoluminescence (PL) spectra, are therefore used as indicators of the validity of a set of simulation parameters. In fact, the more characterization techniques are employed the more constrained is the exploration of the simulation space.

In the work presented here, three case were employed. First, experimental results extracted from literature (details in Section 2.4.1) were analyzed, in this case, only three JV parameters (under illumination) were available: Voc, Jsc and FF. That means that the validity of the simulations performed was evaluated on the values of these three parameters only. Second, ageing experiments performed at IPVF through periodical JV measurements under illumination were obtained. Here the full JV characteristics were available, the exploration could be more constrained by adding the slopes at open circuit (OC) and short circuit (SC) to the constraints of the problem. Finally, aging experiments with periodical measurements of JV curves under (laser) illumination and PL spectra were also performed at IPVF. Details on experimental measurements are available in Section 2.4.2. This supplementary data allowed to constraint further the input parameters by also considering the position of the peak, its slopes and the half width at half maximum.

Although up to height optoelectrical parameters were available to evaluate the validity of simulations, the number of parameters sets to explore adds up to 4e15. It has been therefore necessary to develop an automated procedure to find suitable sets, in the form of a genetic algorithm.

First, a randomized generation step creates input sets with a log-uniform distribution in the ranges defined in Table 2. At this step, typically 2000 sets are generated.

Second, a selection step based on the available optoelectrical parameters is employed. It is simply defined by relative error thresholds to the experimental value, for each output. Inputs sets that correspond to results within boundaries for all optoelectrical parameters are selected.

The selected sets are then mutated: the parameters are multiplied by coefficient, randomly picked within given boundaries. Here again, a log-uniform distribution is used.

In total, three series of selection and mutation steps are employed one after the other, plus a final selection step. This allows to finally obtain, several tens of input sets, all reproducing the experimental optoelectrical parameters with typically less than 2 % relative error. Importantly, thresholds for the maximum authorized relative error (at selection steps) have to be adjusted for each experimental device. If too few sets are selected at a given step, the mutated sets at the next step might be too close from each other, as they would all stem from too few “parents”. On the contrary, if the selection thresholds are too broad, convergence towards the experimental value is too low. In

fact, the maximum mutation ratio can also be tuned to counterbalance these effects: when few sets are selected, wider mutation are authorized, and inversely.

The values of the parameters associated to the genetic algorithm (size of the generated sets, selection thresholds, mutation bounds) are presented in Table 3, for two examples. Due to PL parameters, the second example has more constraints, it has therefore been necessary to start from a bigger generated set at the first step, and the selection steps are slightly broader.

Table 3. *Parameters for the genetic algorithm and example of values for the analysis of two devices.*

Step	Genetic algorithm parameter	Device JV1.1	Device JV-PL-5
Generation	Number of sets	2000	4000
Selection 1	Voc / Jsc / FF maximum relative error (%)	10	10
	Slope at OC / SC maximum relative error (%)	15	40
	Emax maximum relative error (%)		7.5
	Low side slope / half width at half max maximum relative error (%)		30
Mutation 1	Number of sets	1000	2000
	Maximum mutation ratio	2	2
Selection 2	Voc / Jsc / FF maximum relative error (%)	5	5
	Slope at OC / SC maximum relative error (%)	10	20
	Emax maximum relative error (%)		5
	Low side slope / half width at half max maximum relative error (%)		20
Mutation 2	Number of sets	1000	1000
	Maximum mutation ratio	1.5	1.5
Selection 3	Voc / Jsc / FF maximum relative error (%)	2.5	2.5
	Slope at OC / SC maximum relative error (%)	6	20
	Emax maximum relative error (%)		2.5
	Low side slope / half width at half max maximum relative error (%)		17.5
Mutation 3	Number of sets	750	1000
	Maximum mutation ratio	1.25	1.25
Selection 4	Voc / Jsc / FF maximum relative error (%)	2	2
	Slope at OC / SC maximum relative error (%)	5 / 7.5	20
	Emax maximum relative error (%)		2
	Low side slope / half width at half max maximum relative error (%)		20

3.3 Reproduction of a solar cell performances through simulations

The genetic algorithm exposed in previous section is applied here. Results obtained with experimental measurements performed at IPVF, either only through JV characterization or both JV and PL are reported in this section.

Notably, experimental characterization of the fresh solar cells is considered. In fact, the genetic algorithm is employed to reproduce the starting point of degradation, and the results of the last selection step will be used in a further process to simulate degradation mechanisms.

3.3.1 Distributions of optoelectrical parameters and experimental values

Results at each step of the genetic algorithm are presented in Figure 1 for the initial characterization of the sample JV-1.1. Noticeably, the initial generation step shows a very broad range of shapes for the JV characteristics. This is expected, because the log-uniform distribution employed to generate the inputs aims at exploring uniformly the whole parameters space. In a sense, these characteristics represent the range experimental devices that can be analyzed with this method (for a specific set of fixed parameters).

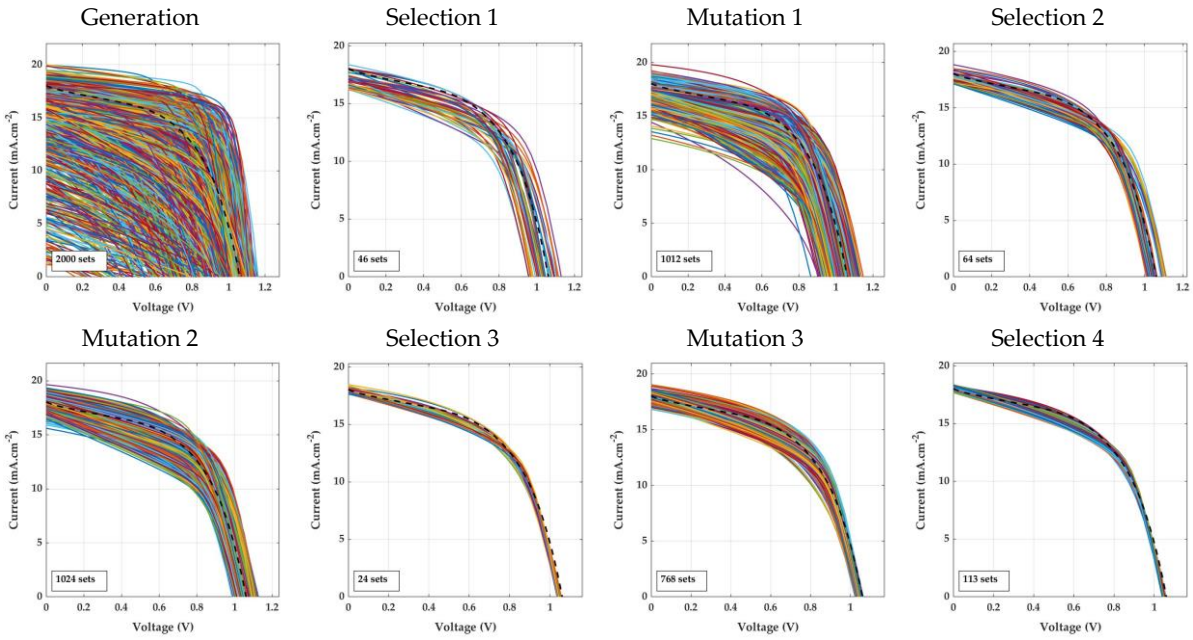

Figure 1. *JV characteristics generated and selected at each step of the genetic algorithm for the device JV-1.1. Dotted line shows the experimental JV characteristic.*

Furthermore, the need of multiple mutation and selection steps is illustrated by the low number of sets obtained at the first selection steps: only 46, within a wide range of 10 % error around the experimental value. However, step after step the selection thresholds narrow down and the size of the selected population rises. This is also visible in Figure 2, where generated and mutated populations show closer distributions to the experimental results along execution of the algorithm.

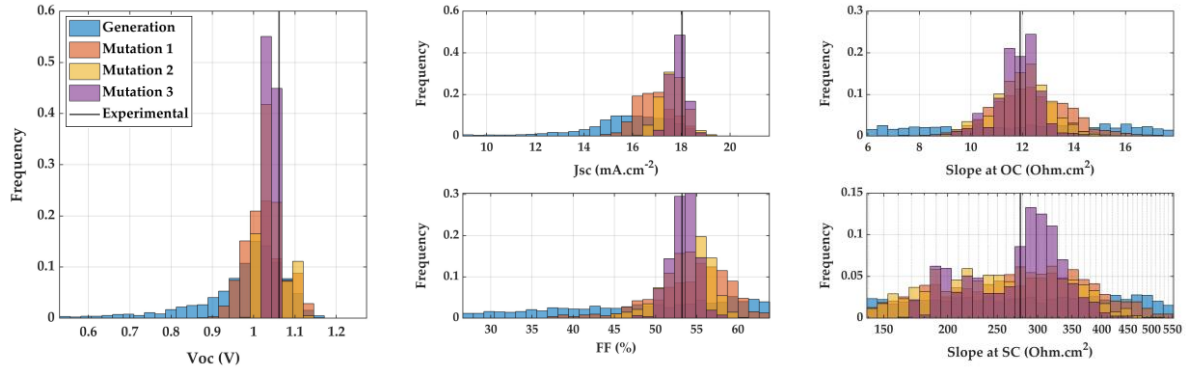

Figure 2. *Distribution of optoelectrical parameters at each generation and mutation step of the genetic algorithm for the device JV-1.1.*

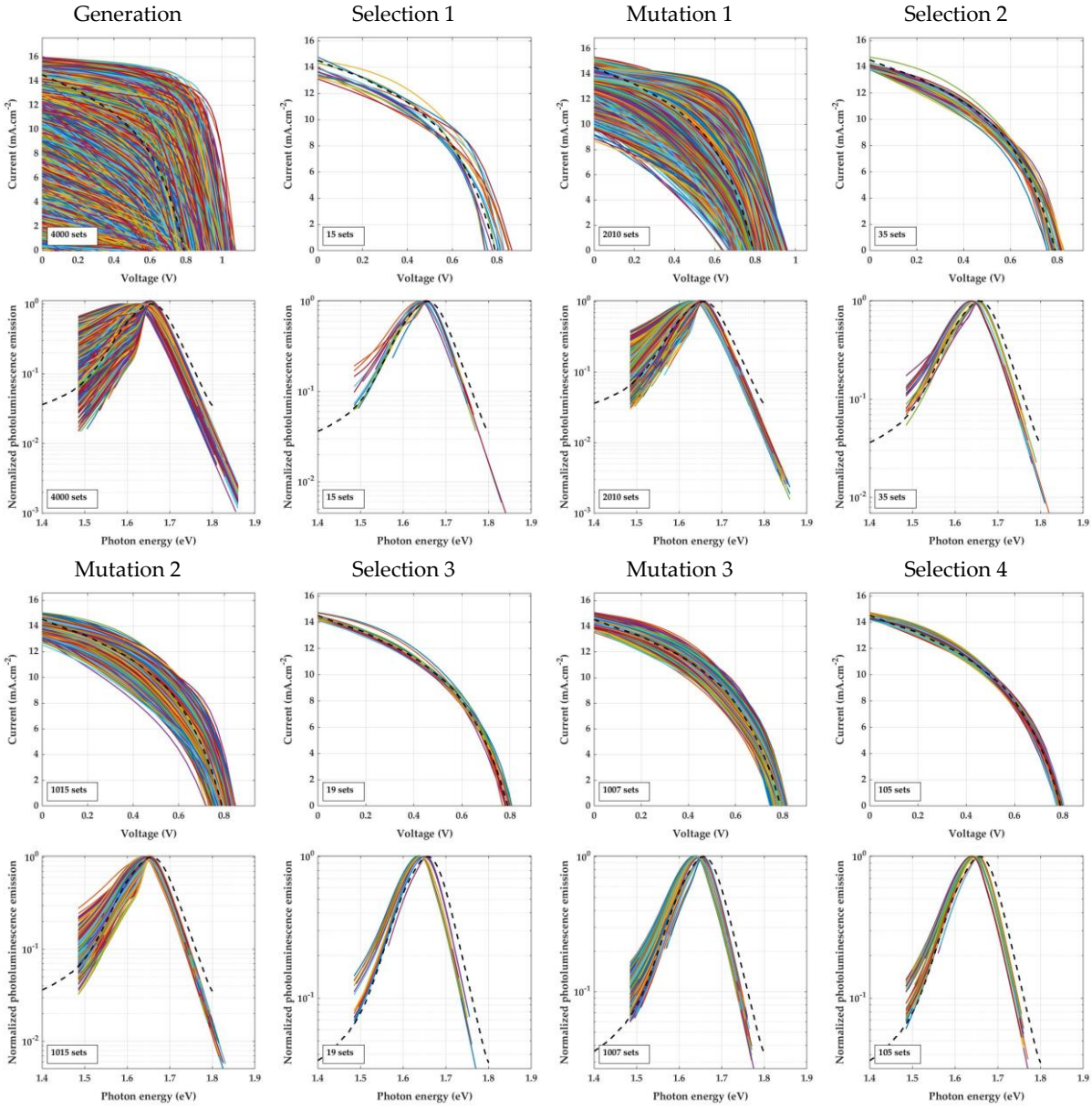

Figure 3. *JV characteristics and PL spectra generated and selected at each step of the genetic algorithm for the device JV-PL-5. Dotted lines show the experimental JV characteristic and PL spectrum.*

When photoluminescence spectra are available, the procedure remains similar, and Figure 3 shows the results at each step of the genetic algorithm for device JV-PL-5. Here again, the initial generation step provides widely spread results. In terms of PL spectra, it is to note that only the low side of the spectrum significantly varies. The shallow defect density and their energetic distribution across the bandgap are the two parameters that strongly impact the spectrum.

In fact, the total emission also varies importantly, depending for instance on recombination regimes and defect densities. However, it is not considered here (PL spectra are normalized to their maximum) because no experimental value can be compared, as the experimental setup was not absolutely calibrated. Therefore, only relative evolutions will be considered for the total photoluminescence emissions.

The distributions of optoelectrical parameters extracted from the JV characteristics and PL spectra of Figure 3 are displayed in Figure 4. Although the distributions narrow down around the experimental values, they remain wider than in the previous case, with only experimental JV parameters. This is because the supplementary constraints from PL parameters complicate the exploration of the parameters space. However, 105 sets are still finally selected with the acceptable threshold of 2 % error for the Voc, Jsc, FF and Emax and 20 % for the JV and PL slopes.

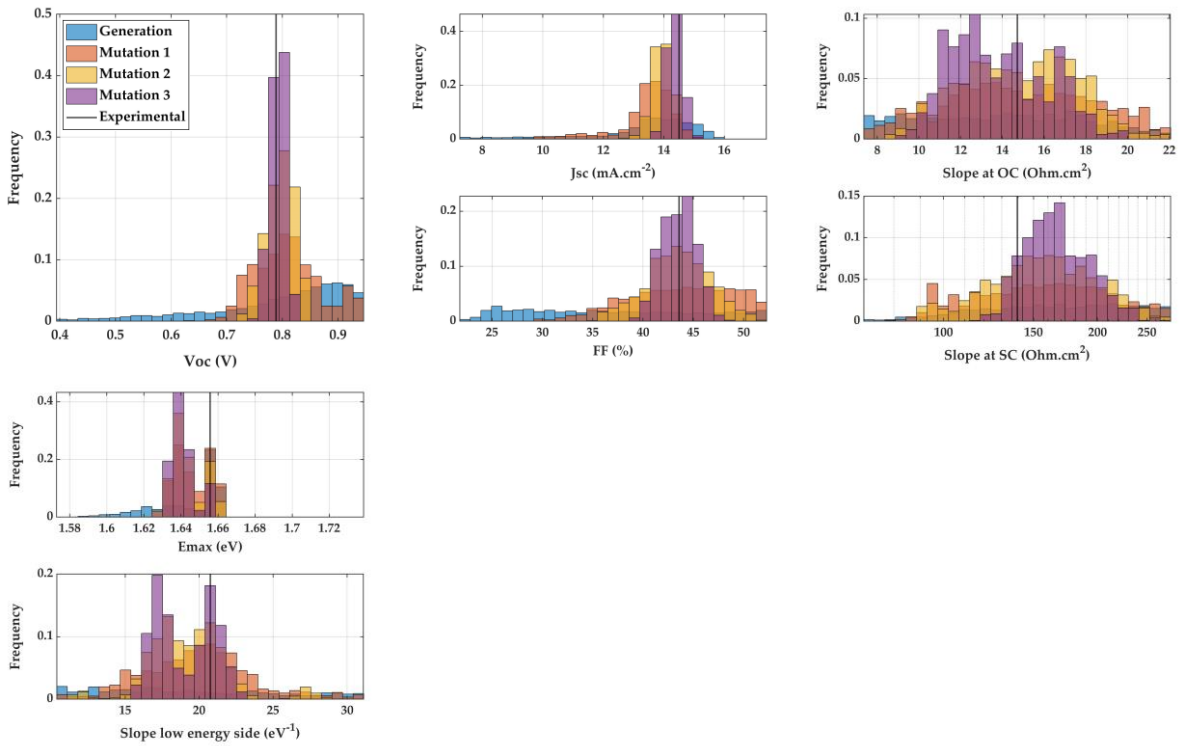

Figure 4. *Distribution of optoelectrical parameters at each generation and mutation step of the genetic algorithm for the device JV-PL-5.*

Importantly, the genetic algorithm developed here has been applied to the initial performances of all various devices considered in this work, because the selected input parameters provide the basis for the simulation of degradation exposed further.

In the case, of experimental measurements reported in literature, only three optoelectrical parameters were available, and employed to select the appropriate simulation parameters. Associated results at the last selection step are displayed in Appendix C, Figure C1. Moreover, results for each device characterized at IPVF through JV measurements are also exposed in Appendix C, Figure C2, and Figure C3 – C4 for coupled JV and PL measurements.

Finally, it is demonstrated that approx. 100 sets could be obtained at the last selection step for each device. Moreover, all the associated input sets reproduce closely the experimental performances of the solar cells.

This number of values for the material parameters constitutes a strength of the probabilistic approach employed here. Even if numerous material characteristics are not known for a given perovskite solar cell, it is possible to simulate its performances. More importantly, it provides distributions of probable values for these material parameters.

3.3.2 Distributions of material parameters

The distributions of material parameters obtained at the final selection step do not only constitute the basis for further simulations of degradation mechanisms, but they also provide interesting insights on the device and material characteristics.

For instance, they are reported for device JV-1.1 in Figure 5. This device, like others characterized only with JV measurements, was fabricated in a nip structure, with TiO_2 ETL, $Cs_{0.05}(MA_{0.17}FA_{0.83})_{0.95}Pb(Br_{0.17}I_{0.83})_3$ perovskite and PTAA HTL.

The difference between the primarily log-uniform distribution at the generation step and the final selection inform on the importance of the material parameters to define the optoelectrical outputs. For instance, the carrier mobilities in the transport layers for device JV-1.1 are still widespread, indicating that they do not play a significant role (or at least are not limiting factors for the performances) in this case. Notably, it is not the case for all devices, for instance more specific values were obtained for device JV-4.2 in Appendix C, Figure C5.

On the contrary, the defect densities are for instance thinner. Here high defect densities in the perovskite layer (approx. 10^{16} cm^{-3}) and rather high carrier mobilities (between 1 and 10 $cm^2.V^{-1}.s^{-1}$) were obtained, indicating that the experimental JV characteristic could be explained by a perovskite material having a high defect density counterbalanced by high carrier mobilities.

It is to note that some distributions show two distinctive peaks, such as the defect density at ETL – perovskite interface and the ETL donor density. This probably indicates that the electron extraction is either limited at the interface or in the ETL, and the experimental data available here cannot help to discriminate.

Notably, selected distribution of interface defect densities of device JV-4.2 (Appendix C, Figure C5) are centered around lower values (approx. 10^{16} cm^{-2}) than device JV-1.1, but carrier mobilities in the perovskite layer could also be lower (down to approx. 10^{-1} $cm^2.V^{-1}.s^{-1}$ for electron mobility). These differences are crucial aspect that will define the responses to degradation mechanisms. One can expect the

performances of these devices to evolve differently to the same mechanism, emphasizing the need to accurately investigate the initial characteristics of each solar cell.

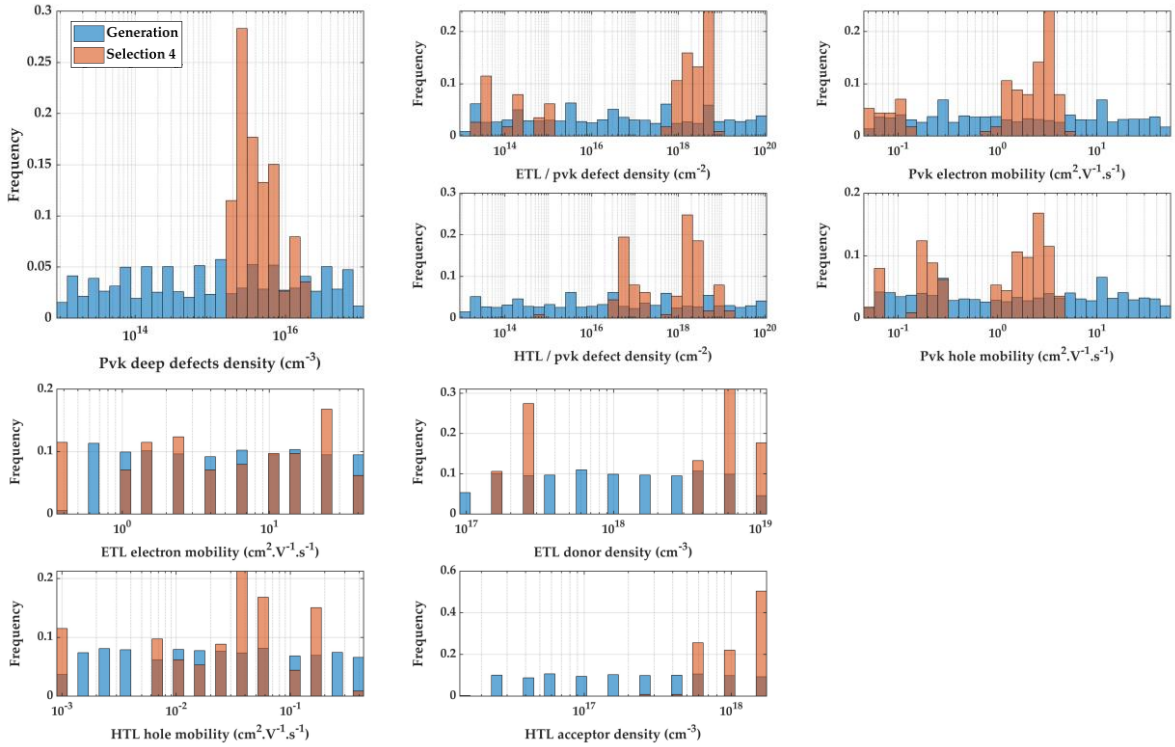

Figure 5. *Frequency distribution of material parameters in the initial generation and after the final selection step of the genetic algorithm for the device JV-1.1. The number of counts per bin in the histogram is normalized by the total number of sets.*

For device JV-PL-5, supplementary experimental optoelectrical parameters were available to obtain the distributions in Figure 6: its photoluminescence spectrum. As a result, the constraints to select appropriate input parameters are more strict, and less flat distributions were obtained at the final selection step (see also distributions for device JV-PL-3 in Appendix C, Figure C6).

Notably, shallow defect densities and distribution are the main parameters responsible for the shape of the PL spectrum on the low energy side. Their distributions are therefore finely defined.

Here, hole mobility in the perovskite layer and HTL as well as defects at the HTL-perovskite interface are strikingly all of bad quality. In fact this is consistent with the device JV characteristic in Figure 3, which shows very low Voc and FF. This shows that the method exposed here can already provide insights for the development of perovskite solar cells, helping to discriminate the aspects that need to be further optimized.

Both JV-PL-5 and JV-PL-3 were fabricated with TiO_2 ETL, however, the HTL materials employed were respectively Spiro-MeOTAD and PTAA. Notably, parameters distributions obtained for JV-PL-3 indicate lower doping level, but higher hole mobility in the HTL. Only two examples do not provide sufficient statistics to

properly compare these materials in general. However, these results show again that the method developed here could support perovskite solar cells development, by allowing to compare material properties usually difficult to access.

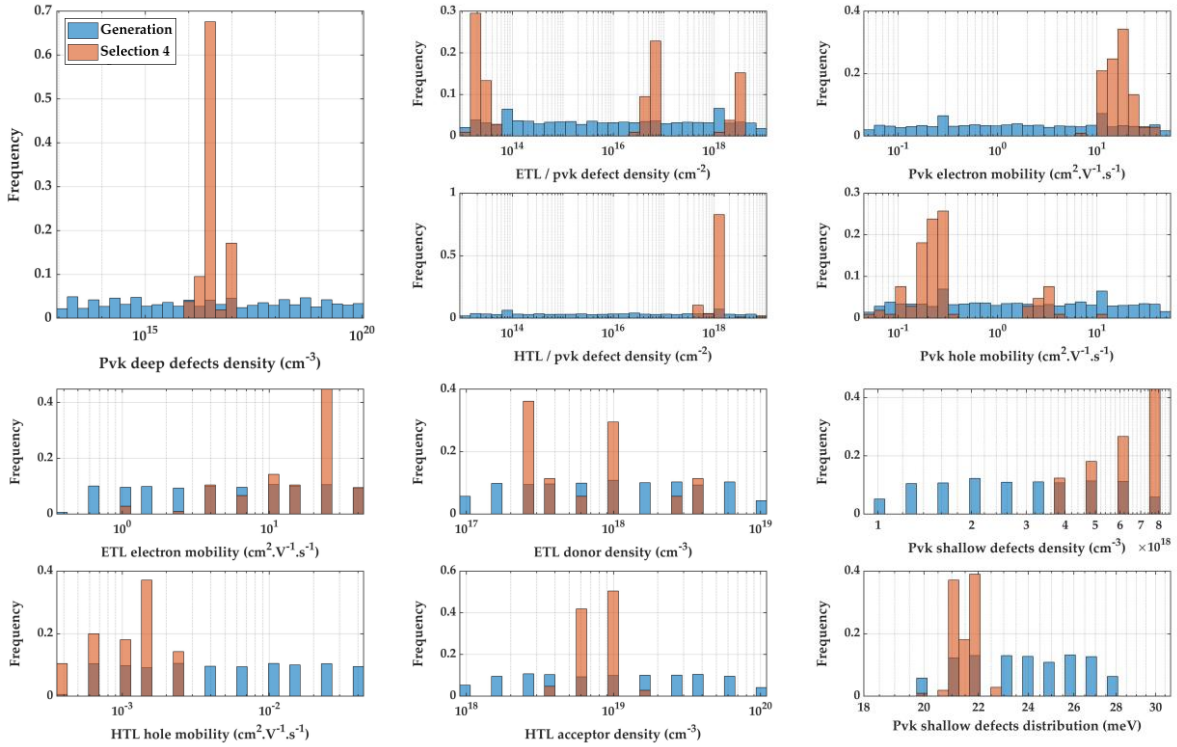

Figure 6. *Frequency distribution of material parameters in the initial generation and after the final selection step of the genetic algorithm for the device JV-PL-5. The number of counts per bin in the histogram is normalized by the total number of sets.*

Finally the results obtained here can serve a double purpose. First this demonstrates that statistics based approaches can help to estimate material properties within the solar cell stack. When applied to more exhaustive studies with larger sample statistics, distributions of material parameters such as defect densities could allow to more precisely discriminate materials and fabrication techniques that need to be further developed on, or that are responsible for better solar cell performances.

Combining several characterization techniques (here JV and PL) has been showed to improve the reliability of the results by adding more constraints on the input parameters space exploration. Moreover, other techniques easily reproduced by drift diffusion simulation could also be added. For instance capacitance spectroscopy would be expected to provide more reliable results on interface behavior.

Finally, the results of the genetic algorithms will be employed in this work as basis for the simulation of the subsequent performance degradation. Notably, the unwell determined distributions of parameters (flat or with several peaks) are part of the robustness of the method. In fact, all these undiscriminated possibilities will be accounted for when computing responses to degradation mechanisms, without needing to do assumptions on given values, that would not be possible to verify.

3.4 Simulated degradation of selected sets

It has been exposed in Section 2.4 that the experimental data investigated in this work are constituted of periodic characterization of the solar cell along aging time. They allow to consider the temporal evolution of parameters such as Voc or total PL emission.

In order to investigate these measurements, several mechanisms are considered and their impact on optoelectrical performances simulated. Similarly to the experiment, multiple simulations are performed along the progress of the mechanisms. This also allows to track the evolution of the same optoelectrical parameters.

Importantly, the precise nature of the mechanisms and the methods to investigate the experimental results through these simulations will be exposed in a next chapter. Here, only the statistical aspects of the simulation results are treated.

In order to simulate through drift diffusion the response of a given solar cell to a degradation mechanism, the inputs sets selected by the genetic algorithm are employed. An example is displayed in Figure 7 for device JV-PL-5: the formation of defects in the perovskite layer is considered, and the response of the 105 selected sets is simulated.

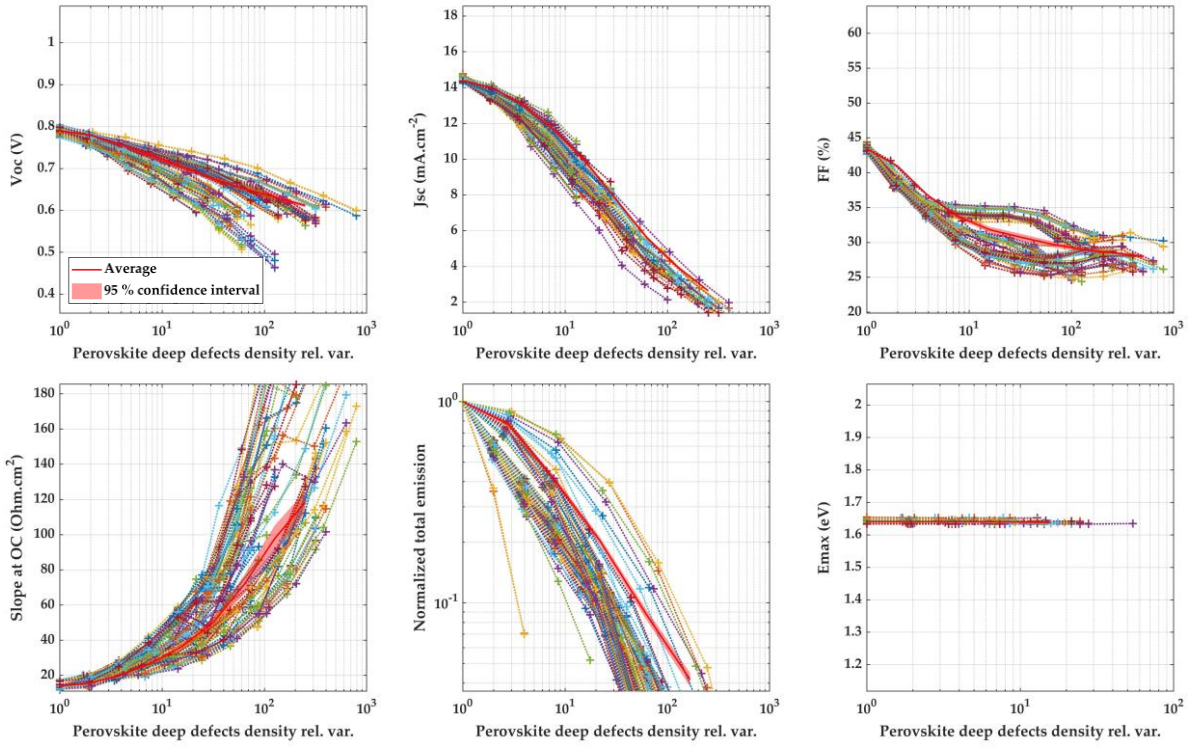

Figure 7. *Simulated response to an increase of defect density in the perovskite layer. The 105 inputs sets reproducing the initial performances of JV-PL-5 are subjected to the same mechanism and represented with dotted lines and crosses. Average and 95 % confidence intervals are calculated at each degradation step.*

Importantly, each of the input set has a different initial defect density, due to the statistical approach employed here. These different initial values represent however

the same state for the solar cell. Therefore, the relative variation of defect density to the starting point is considered for each selected set.

As a result, it is possible to compute the average response along the relative increase of defect density, among the 105 simulated responses. It is displayed as the plain red line in Figure 7. Moreover, the standard deviation is employed to compute the 95 % confidence interval. Importantly, it appears that all responses follow the same trend along the increase of defect density, justifying calculating the average response.

Another example of degradation mechanism is considered in Figure 8: a decrease of electron mobility in the perovskite layer. Again, most of the responses follow the same trend, which is well reproduced by the average response. This illustrate the importance of having a sufficiently large number of sets selected through the genetic algorithm. Some selected sets can respond with distinct trends and here they can be considered as outliers because a vast majority of selected sets respond similarly.

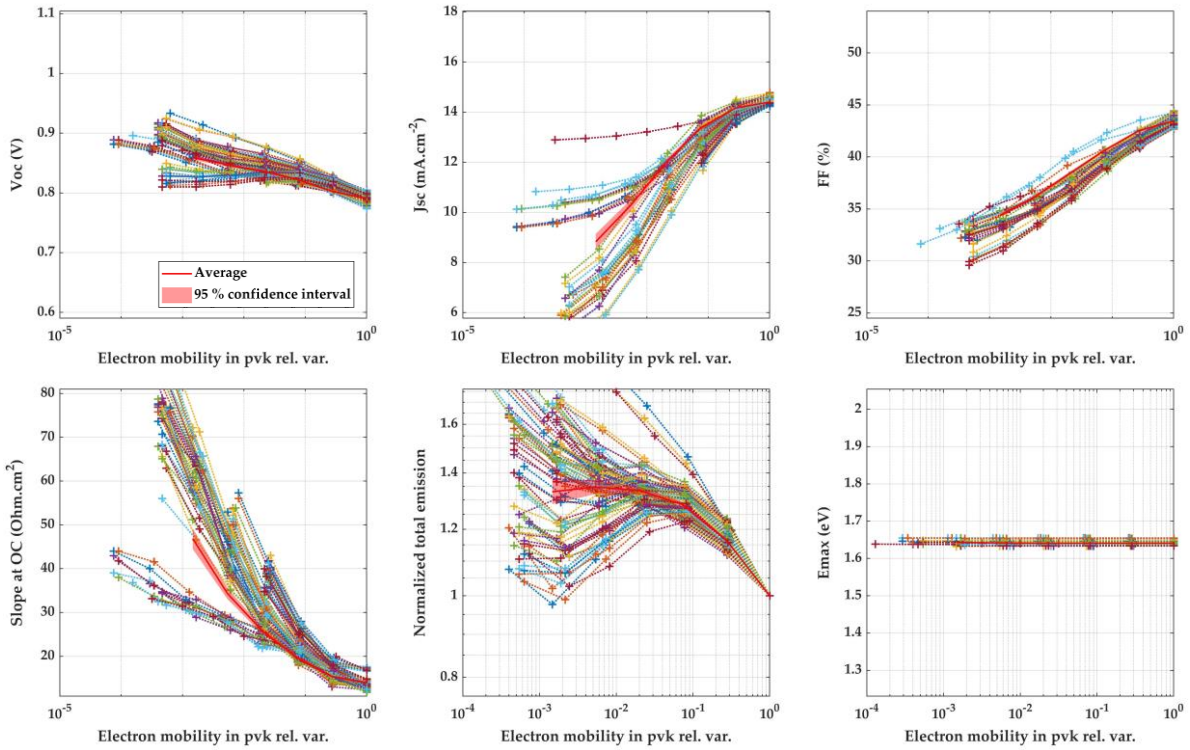

Figure 8. *Simulated response to a decrease of the electron mobility in the perovskite. The 105 inputs sets reproducing the initial performances of JV-PL-5 are subjected to the same mechanism and represented with dotted lines and crosses. Average and 95 % confidence intervals are calculated at each degradation step.*

These examples show how input parameters sets selected through the genetic algorithm can be employed to investigate degradation of perovskite solar cells. Importantly, their similar responses to degradation mechanisms is consistent with the hypothesis that they all reproduce the optoelectrical performances of a given perovskite solar cell.

Finally, the average response and associated confidence interval will be the simulation outputs employed to analyze the experimentally recorded degradation. The associated method will be exposed in Chapter 4.

Chapter conclusion

From the elements exposed in Chapters 1 and 2, it appears that the simulation methods employed here (drift diffusion and transfer matrices) implies the need to define numerous material parameters. Moreover, it is possible to reliably assess the value of some of them, such as the materials bandgap and electron affinity or the thickness of the layers. However, some are not easily measured, or can vary a lot from sample to sample within the same fabrication batch.

It is therefore necessary to define possible ranges for the value of these parameters. This defines a high dimensional space, and it has been quantified and discretized here to have a dimension of 13 and contain approx. 10^{15} elements.

Therefore, a genetic algorithm has been designed and employed to explore this space with a randomized approach. By combining several generation, selection and mutation steps, numerous sets of inputs parameters that reproduce the experimental performances can be obtained. They define distributions of simulated optoelectrical parameters that finally approach the experimental value with less than 2 % relative error.

This has been illustrated here with several examples, comprising either only experimental JV characterization, or combined JV characteristic and PL spectrum. As a result, it demonstrated that combining several characterization methods constrains more the selection of valid input parameters, finally providing more reliable distributions. Importantly, further characterization techniques could be added, for instance capacitance spectroscopy, as drift diffusion simulations allow to compute the behavior of solar cells under various conditions.

At this step, it is moreover already possible to discuss the performances of the solar cells through the associated distributions of material parameters. It has been showed how interpretation and understanding of the performances of a given solar cell can be enhanced. This could provide a useful tool to support perovskite solar cells optimizations.

Moreover, the selected input parameters sets constitute the basis on which simulations of the degradation mechanisms are performed. Exemplary processes have been simulated, and the evolution of optoelectrical performances tracked over their course. Importantly, average responses among the selected sets for a given sample can be computed.

As a result, this procedure aims at providing simulated responses to degradation mechanisms that are in coherence with the actual experimental performances of each considered sample.

Finally, these results also show that a probabilistic approach can allow to go beyond the difficulty of finding the actual values of input parameters. First, it provides a sense of the importance of the parameters in defining the outputs by associating broader or thinner distributions. Also, distributions not only provide insights on the parameter's values, but also on the confidence on these values through their spread.

Chapter 4: Modeling degradation mechanisms

Table of contents

Chapter introduction

In this work, degradation of perovskite solar cells has been investigated through periodical measurements of optoelectrical performances over aging time.

The temporal evolution of these parameters is considered in Section 4.1. Time sequences of interest are extracted to facilitate interpretations. Also, chemical kinetics models have been considered to determine and interpret the thermal activation of degradation processes.

Importantly, degradation pathways, consisting in the evolution of the correlation of optoelectrical parameters over aging are a major tool employed in this work. In Section 4.2., they allow to compare the experimental behavior of the various perovskite solar cells investigated in this chapter.

Moreover, exemplary degradation pathways are simulated in Section 4.3 by using an analytical model and drift diffusion numerical simulations.

This approach is applied first to aging measurements reported in literature in Section 4.4, demonstrating the capabilities of the approach developed here.

It is then employed to investigate two sets of solar cells fabricated and aged at IPVF in Section 4.5. A first batch of samples having the same structure but fabricated through varying deposition method is analyzed through periodically measured current voltage (JV) characteristics. A second set of solar cells having different electron transport layer (ETL) and hole transport layer (HTL) materials is investigated through this time coupled JV and photoluminescence (PL) measurements.

The results exposed in this chapter allow to evaluate the capacities of the method developed here. These examples show how this modeling based approach can support the development of stable perovskite solar cells by distinguishing the processes causing the degradation optoelectrical performances.

Chapter key points:

- Degradation pathways are obtained by considering the evolution of the correlation of solar cells optoelectrical parameters.
- The position of these pathways is independent from time and therefore any speed of reaction: it constitutes a characteristic footprint of the underlying process.
- Unitary degradation mechanisms are simulated by considering the variation of a single material parameter. They are distinguishable from each other through their distinct pathways.
- Combining characterization techniques (here JV and PL) allow further distinction of degradation pathways.
- Experimental measurements reported in literature have been investigated in Section 4.4 to provide a proof of concept of the methodology exposed here.
- Several degradation sequences over time can be analyzed to consider multiple successive degradation mechanisms.
- The approach employed here directly tackles the cause of optoelectrical performance losses. Conducting complementary characterization demonstrates concomitance with material evolutions.
- For most samples investigated in Section 4.5.1 (except from one deposition technique), the perovskite layer might have remained stable, and the transport layers caused the performance losses. This constitute guidelines for further improvements of stability.
- A protective effect of the HTL by SnO_2 could be envisaged for samples investigated in Section 4.5.2. It has been reported in literature to be less hygroscopic and more stable than TiO_2.
- Complementary analyzes are necessary to demonstrate this hypothesis and the method exposed here could support a more exhaustive study.

4.1 Degradation through temporal evolutions

The first approach to consider degradation and available experimental results is to investigate the evolution of optoelectrical parameters over time. Therefore, this section will explain first how useful time sequences are identified and extracted from data obtained at IPVF by pointing out artefacts of measurements that must be removed from the analysis. In a next step, kinetics of degradation are investigated by associating degradation of performances to chemical reaction. Results recorded at different temperatures and published in literature are employed here.

4.1.1 Interpretable time sequences from experimental measurements

In this section, degradation measurements are considered through their time dependence in order to extract meaningful and interpretable sequences. Experimental results obtained at IPVF over two types of aging studies are investigated. Details on the solar cells characteristics, aging conditions, and characterization techniques are exposed in Section 2.4.2.

First, a set of experiments was performed through periodic measurements of JV characteristics and eight devices were investigated. They were all of the same nip structure: TiO_2 / $Cs_{0.05}(MA_{0.17}FA_{0.83})_{0.95}Pb(Br_{0.17}I_{0.83})_3$ / PTAA, and aged under the same conditions: ambient temperature, N2 atmosphere and constant one sun illumination during 1000 h. Associated devices are labelled JV-1.1 to JV-4.2.

Also, coupled measurements of JV curves and PL spectra along degradation were performed on five solar cells. They were all fabricated with the same $Cs_{0.05}(MA_{0.17}FA_{0.83})_{0.95}Pb(Br_{0.17}I_{0.83})_3$ perovskite material, but with different HTL and ETL materials: PTAA for JV-PL-1 to 4 and Spiro-MeOTAD for JV-PL-5, and TiO_2 for JV-PL-1, 2, 3, 5 and SnO_2 for JV-PL-4. The aging of these samples was recorded in a climatic chamber under damp heat: 85 % R.H, 65 °C and dark.

Evolution of the JV parameters over time for the device JV-1.1 is displayed in Figure 1 and in Appendix D, Figure D1. It appears clearly that the behavior is not monotonous, and several sequences can be identified. A large increase of Voc and Jsc occurs in the first 100 h, strongly different from the slower decrease that follows. This clearly indicates that a distinct process occurs from the rest of the aging experiment. Importantly, the measurements (and the solar cell illumination) has been stopped between 440 and 450h of aging: the same large increase of Voc and Jsc is triggered after 450h. These sequences are not analyzed in this study, but it is to note that the methods developed here could help understanding this form of light soaking effect.

In order to focus on a sequence with stable environmental conditions, only the degradation between 170 and 290 h in the aging experiment from Figure 1 is extracted. It is to note that a Jsc shift at 160 h is visible for all devices recorded through periodical measurement (see JV-3.2 in Appendix D, Figure D2), this could indicate a variation of the illumination intensity, rather than a process related to the solar cells. Therefore, the extracted sequences for all these devices start after this point.

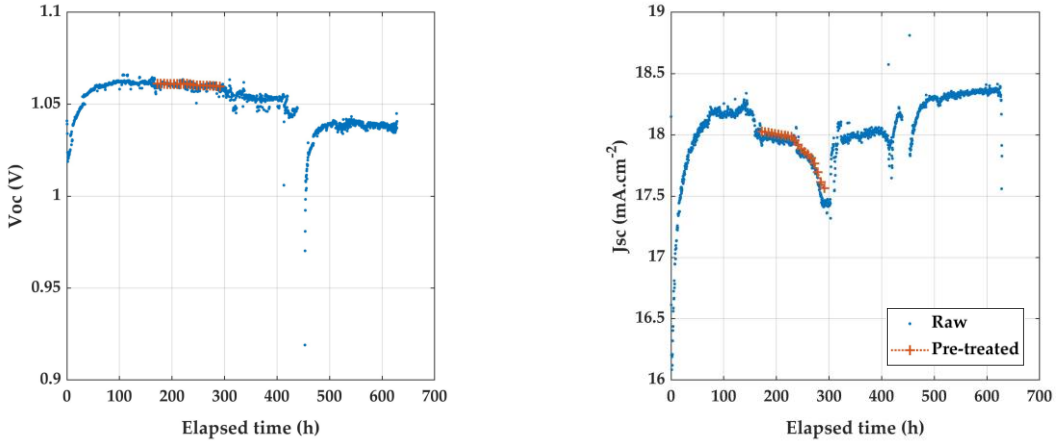

Figure 1. *Degradation over time of the device JV-1.1. Only part of the recorded degradation is extracted to be investigated, from 170 to 290 h of aging. All optoelectrical parameters are displayed in Appendix D, Figure D1.*

Unstable conditions are not the only cause of extracting only short term sequences. For instance, JV-2.2 (Appendix D, Figure D3) shows very rapidly an erratic behavior which cannot easily be interpreted. This can be caused by faulty contact at the electrode. Therefore, only the first (short) monotonous degradation trend is extracted.

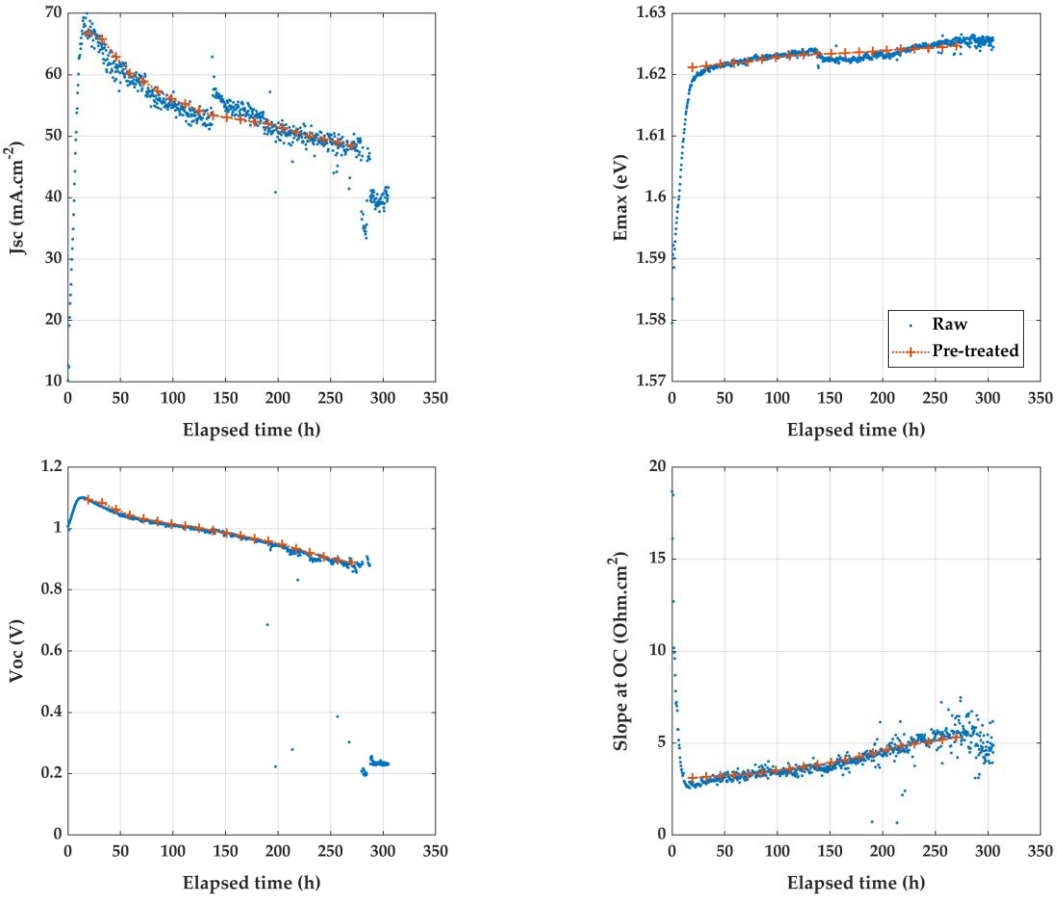

Figure 2. *Degradation over time of the device JV-PL-1. Only part of the recorded degradation is extracted to be investigated, from 20 to 272 h of aging. All optoelectrical parameters are available in Appendix D, Figure D4.*

For other samples, it has been possible to extract more long-term degradation trends, for instance for device JV-PL-1, in Figure 2 and in Appendix D, Figure D4. Here, a shift in Jsc and Emax is noticeable at 135 h. This can probably be associated to an external factor, or at least to a process different from the long-term degradation. However, the evolution trends remain significantly the same after the event. Therefore, it has been possible to extract the global degradation, characterized by slow and steady Voc and Jsc loss, accompanied by a rising slope at short circuit (SC). This constitute the long term degradation trend that can perfectly be compared to simulated mechanisms.

On this second example the light soaking step is characterized in by a rise of Voc and Jsc until 20 h. Importantly, it is also clearly distinguishable in terms of total photoluminescence emission and energy of the peak maximum (Emax). Another example is displayed in Appendix D, Figure D5, for device JV-PL-3.

On Figure 3, the advantage of considering both JV and PL characterization techniques is also demonstrated to help distinguish degradation sequences. The PL parameters seem to follow a unique degradation trend after 25 h: a steady decrease of PL emission and rather stable Emax (in Appendix D, Figure D6).

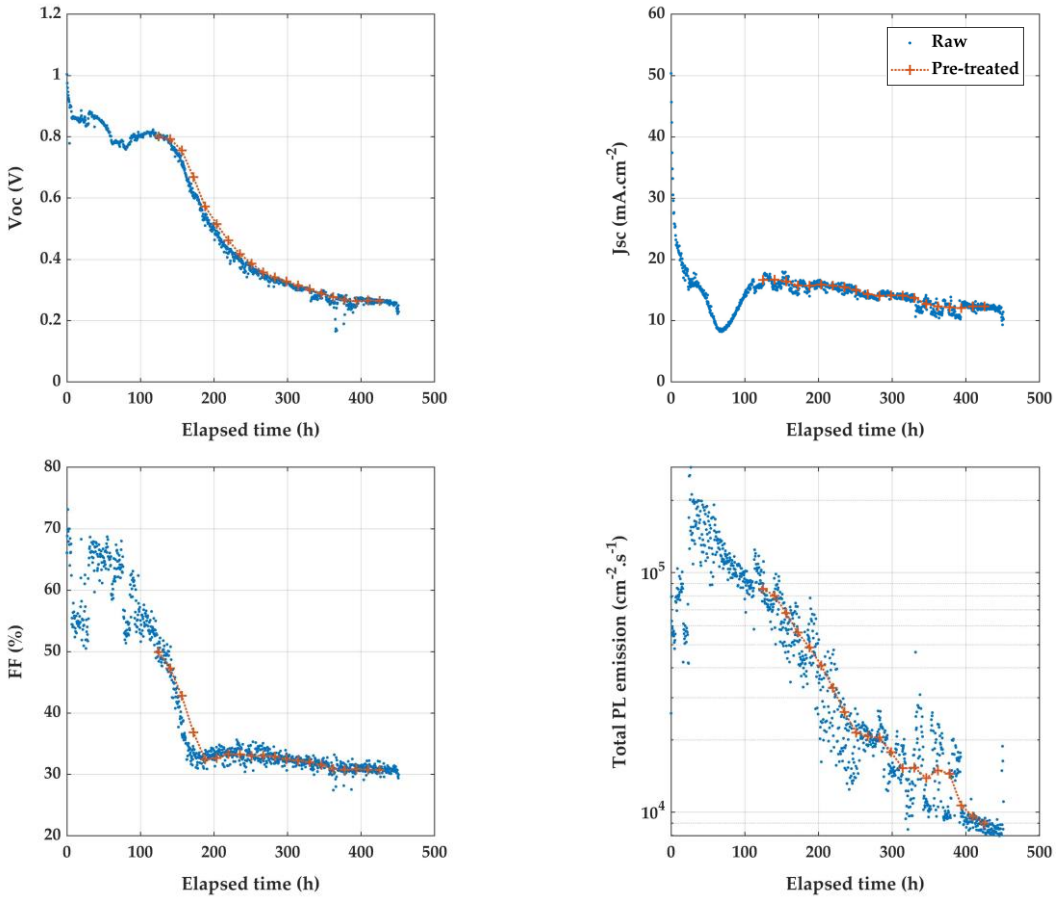

Figure 3. *Degradation over time of the device JV-PL-4. Only part of the recorded degradation is extracted to be investigated, from 125 to 425 h of aging. All optoelectrical parameters are available in Appendix D, Figure D6.*

However, JV parameters show a break at 125 h: the Voc decreases abruptly after being relatively stable and inversely, FF becomes stables after having significantly

decreased between 25 and 125 h. This can be associated to a hypothesis of distinct degradation mechanisms, having different impacts on the solar cell performances.

The approach employed in this work allows to tackle this aspect, by successively considering different time sequences of the aging experiment. Therefore, two cases will be investigated further in this chapter: either considering the degradation starting at 25 h (covering both trends), and only after 125 h (focusing on the second trend).

The same questions arise for device JV-PL-5, where non monotonous Jsc behavior might be difficult to interpret (see Appendix D, Figure D7). A first sequence starting at 20 h to grasp the full extent of the degradation, and a second sequence after 85 h, avoiding non-uniformities.

The examples illustrated in this section show that displaying the optoelectrical parameters against time is crucial to point out artefacts of measurements that must be removed from the analysis.

Notably, the approach developed here is robust towards interruptions, non-monotonous trends and possible multiple behaviors, by distinguishing sequences of degradation. In fact, it can be applied to any aging sequence and the genetic algorithm exposed in Section 3.2 will allow to investigate the associated starting point. As a result, most aging experiments available for this work have been investigated, even when the degradation behavior appear unclear at first glance.

4.1.2 Chemical kinetic models applied to perovskite solar cells

A first approach used to model the degradation of perovskite solar cells associates degradation of the performances with chemical reactions. It has been applied to measurements reported in literature [1] and performed at several temperatures.

Kinetics of chemical reactions are employed by determining reaction rates and associated activation energies [1], [2]. In literature, it has been used to derive acceleration factors and even potential realistic-conditions lifetimes [3].

Progress of the reaction over time has to be measured under several conditions. For instance, thermal activation is commonly studied by measuring the reaction rate at various temperatures and fitting its temperature dependence to an Arrhenius law [4]: $k(T) = A \cdot \exp\left(-\frac{E_A}{k_B T}\right)$, where k is the reaction rate, E_A the activation energy, and A a constant. Other models have been developed, to account for activation through light for instance [4]: $k(T, I) = A_I \cdot I \cdot \exp\left(-\frac{E_A}{k_B T}\right)$, where I is the perceived irradiance.

A key aspect of this approach is to determine the reaction rate, k, as its definition depends on the reaction order. For a chemical reaction $A \xrightarrow{k} B$, the three first orders have been considered in this work as follow:

- Zero order: $\frac{d[A]}{dt} = -k$ so: $[A](t) = [A]_0 - kt$ (1)
- First order: $\frac{d[A]}{dt} = -k[A]$ so: $[A](t) = [A]_0 \exp(-kt)$ (2)
- Second order: $\frac{d[A]}{dt} = -k[A]^2$ so: $[A](t) = \frac{[A]_0}{1+kt[A]_0}$ (3)

$[A]$ is the concentration of specie A and $[A]_0$ its initial value. In the context of photovoltaic solar cells, optoelectrical parameters such as Voc, Jsc and FF are measured and their evolution over time can be studied. As a result, it is possible to assume that the evolution of these parameters is proportional to the progress of a chemical reaction (not necessarily known). For instance, for Jsc:

$$\widetilde{J_{sc}(t)} = \frac{J_{sc}(t)}{J_{sc0}} = \frac{[A](t)}{[A]_0} \quad (4)$$

As a result, the expressions of the three orders can be fitted to the experimental measurements, as displayed in Figure 4. In fact, experimental measurements on semi-transparent encapsulated cells with $FA_{0.95}MA_{0.05}PbI_{2.85}Br_{0.15}$ layer, reported by Lim *et al*. [1] are employed here (see Section 2.4 for details). Authors periodically measured current-voltage curves of devices that were kept under air and 1-sun illumination at 25, 40, 55 or 70°C.

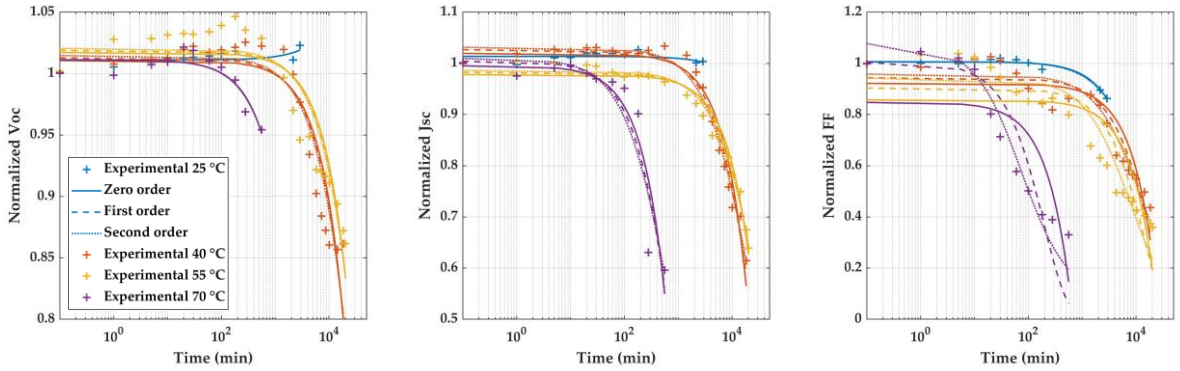

Figure 4. *Evolution of normalized optoelectrical parameters reported by Lim* et al *(crosses). Perovskite devices were aged under one sun, air and at 25, 40, 55 or 70 °C. Fittings of the three investigated reaction orders are in lines.*

Although all three orders can reproduce the experimental data, it appears clearly that is not possible to distinguish between them and the fit quality remains comparable. However, an acceptable fit is still obtained in most cases, as the major dynamic of the decay is well reproduced. It allows to draw the temperature dependence of the reaction rates in an Arrhenius plot, in Figure 5. A linear regression of the Arrhenius law is done, and for each optoelectrical parameter, close activation are obtained for all orders.

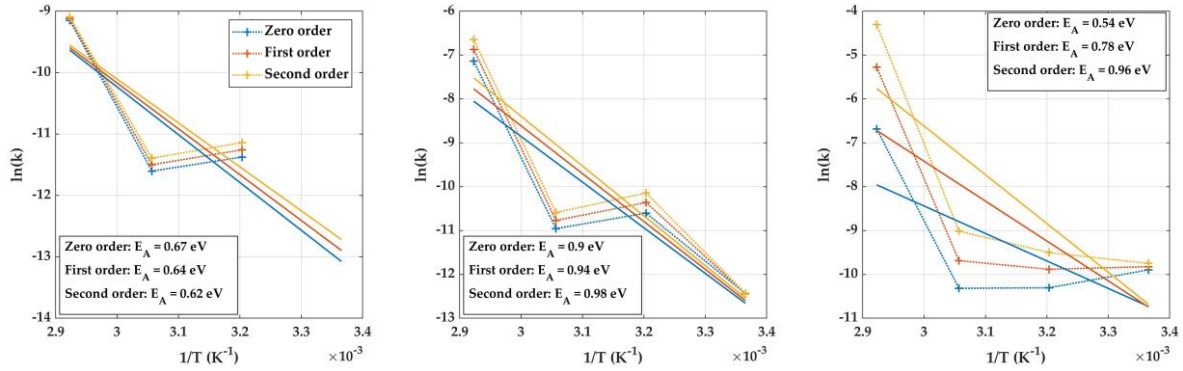

Figure 5. *Arrhenius plot of the temperature dependence of reaction rates for Voc, Jsc and FF (left middle and right, respectively) are displayed with crosses and dotted lines. Associated linear regressions (plain lines) provide activation energy through the slope. The negative reaction rate obtained for Voc at 25 °C with all orders is responsible for the blank in left graph.*

Noticeably, the quality of the linear regression is poor, especially for the FF, where the extracted activation energy should not be trusted. In fact, not only the reaction orders are poorly distinguishable, but the reliability of the derived activation energies is questionable.

Therefore, another method to determine the order of the reaction has been employed. It consists in plotting, for instance for Jsc, $\log\left(\frac{dJsc}{dt}\right)$ versus $\log(Jsc)$. If the reaction follow a given order, points should be aligned, and the slope should provide the reaction order. Figure 6 shows that the points are not always well aligned, and some linear regressions are not realistic.

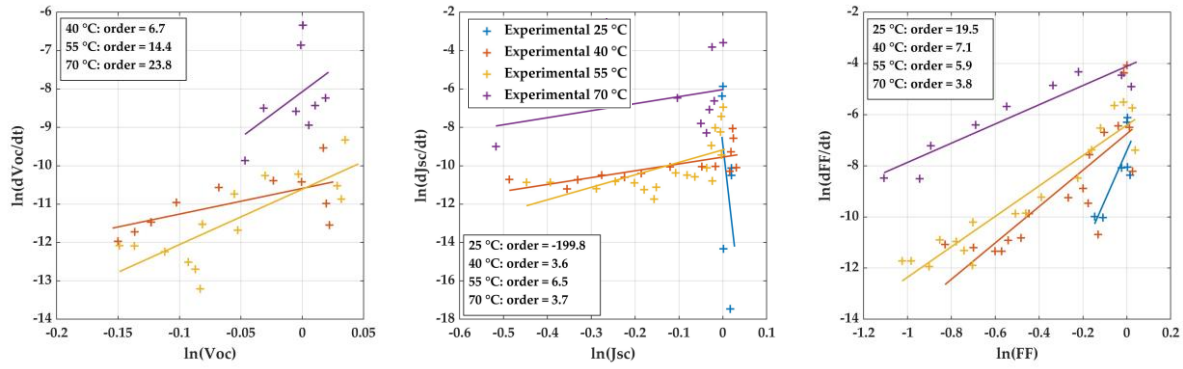

Figure 6. *Normalized Voc, Jsc and FF reported by Lim et al., plotted as* $\boldsymbol{\log\left(\frac{dX}{dt}\right)}$ *versus* $\boldsymbol{\log(X)}$ *(crosses). Linear regressions are displayed in plain lines and give estimations of reaction orders.*

Furthermore, different reaction orders are obtained for distinct temperatures (the values obtained being valid or not). This raises a significant issue for the kinetics approach. It is necessary to have the same reaction occurring at all investigated temperatures in order to study the thermal activation of this reaction (or any activation process). However, numerous distinct degradation processes have been reported for perovskite solar cells. Therefore, it appears inappropriate to analyze the behavior of complex optoelectrical parameters with this approach. Studying the degradation of

perovskites solar cells needs an approach less dependent on multiple experimental conditions, and more compatible with multiple processes.

In fact, the methods exposed further in this work, allowing to identify compatible mechanism could support such kinetics approach, by being applied to each temperature degradation. It could indicate if results obtained at different temperatures are actually compatible with the same mechanism and help to justify the investigation of its thermal activation.

4.2 Degradation through pathways

Instead of focusing on the evolution of the solar cell optoelectrical parameters over time, it is useful to consider their correlations. The evolution of such correlations describes the several states by which the device passes through, without considering the speed with which it passes from one state to another. In other words, the evolution of the correlation of the optoelectrical parameters describes pathways that are independent from time and any speed of reaction.

In fact, this allows to avoid considering any activation process through environmental conditions such as temperature or irradiance for instance. The series of states described by the degradation pathways are finally characteristics footprints of the processes responsible for the observed degradation. As a result, it makes possible to simulate the degradation of perovskite solar cells without implementing time dependent (potential activated by environmental conditions) kinetical models.

First, the experiments performed through periodic measurements of JV characteristics are investigated. As explained in Section 2.4, eight solar cells were prepared with four different techniques for depositing the perovskite layer. They were all aged under the same conditions. The recorded JV parameters were first analyzed through their evolution over time, and sequences of interest extracted as explained in Section 4.1.

Results in Figure 7 show results for all eight devices. It appears clearly that devices JV-2.1 and JV-2.2 follow a distinct degradation trend from all other samples. Notably they were both fabricated preparing the perovskite solution the same day of deposition, with a pre-heating step. These devices show an increase of Voc, and device JV-2.1 exhibits even a significant increase of Jsc and a decrease of slope at open circuit (OC). This strongly indicates that a distinct mechanism was at play for these two devices. It is to note that only short time sequences could be extracted for these devices (for 10 to 100 h and 50 to 160 h respectively), because they very rapidly had erratic behaviors or stopped functioning, see Appendix D, Figure D3 for JV-2.2. In fact, device JV-2.1 is probably still in the light soaking phase, also observed for other devices.

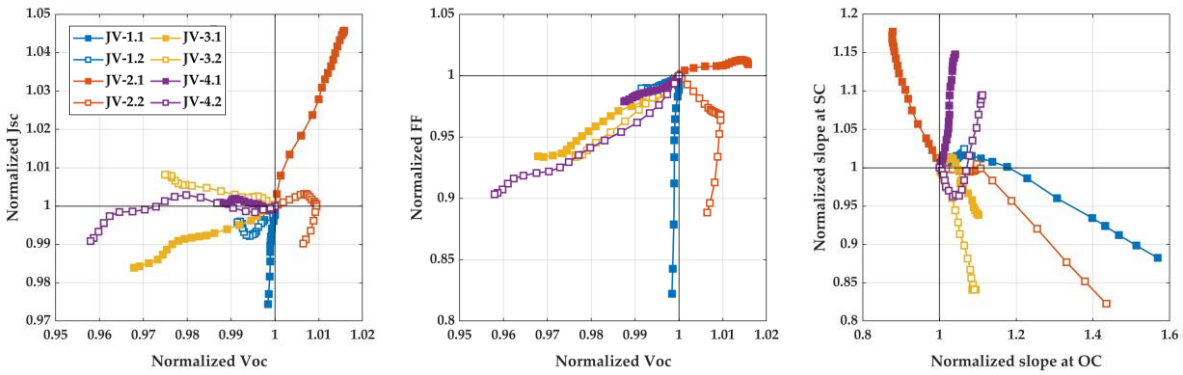

Figure 7. *Experimental degradation pathways of eight devices characterized through periodic JV measurements. Four techniques were employed to prepare the perovskite solution: the day of deposition or one day before, and with a pre-heating step of the solution or not. The optoelectrical parameters are normalized to the initial value before degradation.*

The other devices show degradation pathways that resemble more closely to each other, with a rather stable Jsc and more significant drop of Voc and FF.

One exception stands out: device JV-1.1 follow almost orthogonal pathways with no Voc loss, only Jsc variation and very strong loss of FF. In fact the strong increase of slope at OC can be related to this FF reduction. Notably, a short time sequence was also extracted for this device, with very distinct trends from the rest of the (too noisy and slightly erratic) degradation.

Also, devices JV-4.1 and JV- 4.2 show a notable increase of slope at SC (only after a first decrease for JV-4.2), potentially indicating a specific mechanism inducing this improvement.

Finally, the pathways divide the results into three groups, summarized in Table 1. Notably, the first group contains devices fabricated with three techniques, but the present results indicate that the same mechanism can have degraded the sample performances. Importantly, this hypothesis will be discussed when comparing simulated degradation pathways.

Table 1. *Groups of aging behaviors derived from degradation pathways of the eight devices characterized through periodic JV measurements.*

Devices	Features of degradation pathways
JV-1.2, JV-3.1, JV-3.2, JV-4.1, JV-4.2	Stable Jsc, joint FF and Voc decrease.
JV-1.1	Significant Jsc and FF loss. Important increase of slope at OC.
JV-2.1, JV-2.2	Increase of Voc. Strong increase of Jsc for JV-2.1.

As explained in detail in Section 2.4, coupled JV and PL measurements were also performed on five samples, and their evolution over time is discussed in Section 4.1. All solar cells were aged in a climatic chamber, at 65 °C under 85 % relative humidity atmosphere and dark. Notably the same perovskite material was employed for all samples, but combinations of two ETL and HTL materials were employed: TiO_2 / PTAA for JV-PL-1, 2 and 3, SnO_2 / PTAA for JV-PL-4, and TiO_2 / Spiro-MeOTAD for JV-PL-5.

Coupling these characterizations delivers complementary insights to the degradation process as illustrated in Figure 8. For instance, JV-PL-2, JV-PL-3 and JV-PL-5 show similar pathways according to JV parameters, characterized by similar losses of Voc, Jsc and FF. However, the device JV-PL-5 seem to have a smaller reduction of PL emission. Importantly, it is displayed here in terms of variation of quasi-Fermi level splitting through the following expression (obtained in Section 1.1.2 by considering constant optical behavior):

$$\Delta E_{F-B} - \Delta E_{F-A} = k_B T \, ln\left(\frac{\phi_{tot-B}}{\phi_{tot-A}}\right) \quad (5)$$

Noticeably, device JV-PL-4 follows distinct pathways from JV-PL-1, as it shows a much more pronounced loss of Voc and a slower decrease of quasi-Fermi level

splitting. This aspect is interesting because it shows that both quantities do not always follow the same trend. Photoluminescence intensity and associated quasi-Fermi level splitting are often compared to a "maximum achievable Voc". Analyzing these examples through simulations in the next steps will allow to discuss cases where this maximum is attained to different extents.

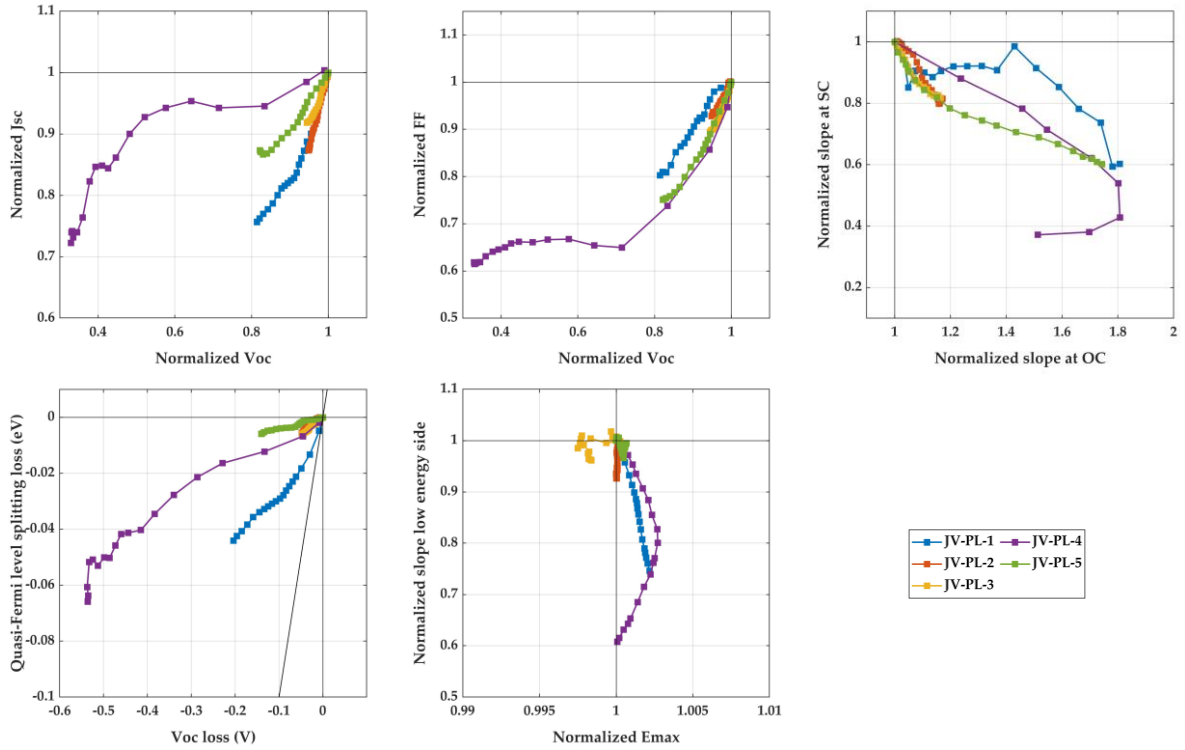

Figure 8. *Experimental degradation pathways of five devices characterized through periodic JV and PL measurements. Aging sequence of JV-PL-4 and JV-PL-5 starts at 125 and 85 h respectively. The optoelectrical parameters are normalized to their initial value before degradation.*

The selection of the analyzed degradation sequence has been discussed in Section 4.1. The cases of devices JV-PL-4 and JV-PL-5 are significative, as their parameters follow non-monotonous behaviors. In Figure 8 the extracted sequences were restricted to the last decrease of Jsc. This choice is questioned through the pathways of Figure 9: here the extracted sequence includes the non-monotonous variations of Jsc and FF for both devices. Degradation pathways of other devices remain the same as in Figure 8.

For both JV-PL-4 and JV-PL-5, considering a degradation sequence starting earlier is associated with an apparently more stable Jsc, resulting in more distinct pathways from the other samples. On the contrary, the quasi-Fermi levels splitting versus Voc pathways of all five samples are now more close to each other. As a result, the distinction of the degradation of these five samples cannot be clearly done yet.

Notably, the very fast decrease and subsequent increase of Jsc for JV-PL-4 (and associated inverse trend of FF) is not interpretable, but can maybe be ignored, as the device comes back to a similar state.

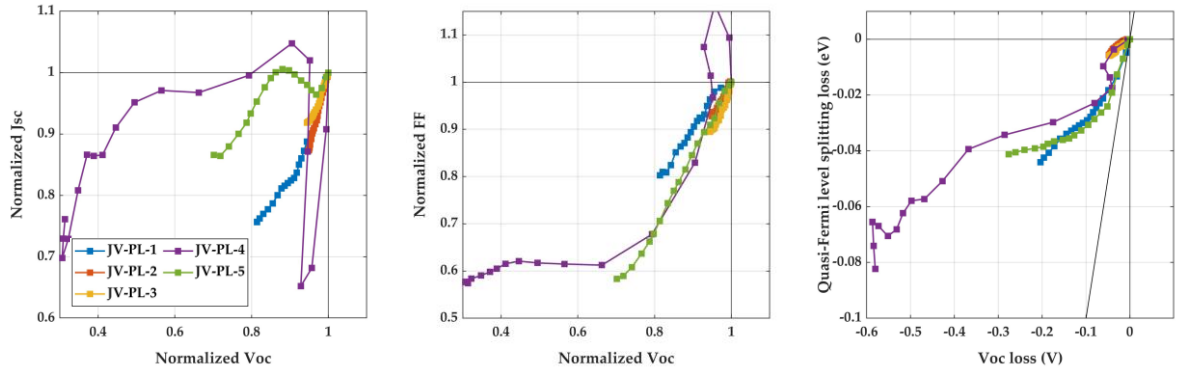

Figure 9. *Experimental degradation pathways of five devices characterized through periodic JV and PL measurements. Aging sequence of JV-PL-4 and JV-PL-5 starts at 25 and 20 h respectively. The optoelectrical parameters are normalized to their initial value before degradation.*

The examples of this section illustrate the possibilities offered by comparing experimental degradation pathways, as well as the limitations. First, it can allow to categorize degradation in some cases. For instance, distinguishing increases from decreases of parameters remains mostly valid and provide insights on the possible distinct nature of the underlying degradation mechanism. This has allowed to distinguish the degradation of devices JV-2.1 and JV-2.2, from the other devices of the same batch.

However, the variability of the degradation pathways to the starting point can be a source of uncertainty for the analysis. It is important to note that relative variations to the starting point have been compared here. In fact, the same degradation mechanism can have different impacts on the pathways (with different slopes for instance), depending on the initial characteristics of the device (the starting point).

As a result, comparing pathways that come from distinct starting point remains to be validated with further analyses. This aspect will be specifically addressed in the next sections, by considering simulated degradation pathways.

Section key points:

- Degradation pathways are obtained by considering the evolution of the correlation of solar cells optoelectrical parameters.
- The position of these pathways is independent from time and therefore any speed of reaction: they constitute characteristics footprints of the underlying processes.
- Plotting together experimental degradation pathways of several samples provides insights on potential distinction of the underlying mechanism.
- Comparison of degradation pathways in terms of normalized optoelectrical parameters must be considered with caution: apparent distinction of behavior must be validated with complementary simulations.

4.3 Simulated degradation pathways

In order to investigate further degradation pathways presented in previous section, models are employed. First, the analytical model for a pn junction reported in Section 1.4 is employed to estimate the impact of degrading input parameters. This constitute several hypothetical degradation mechanisms that are represented together in the form of pathways.

Similarly, the coupled optical and electrical simulation tools exposed in Section 2.1 are employed to investigate the degradation of a perovskite solar cell. Again, several mechanisms, related to the materials and interfaces of the perovskite solar cell, are considered and pathways can be compared.

Simulation results are displayed in the form of degradation pathways: for each considered scenario, the correlated evolution of optoelectrical parameters are plotted together, defining a degradation pathway.

Importantly, the degradation mechanisms simulated in this work are all unitary processes: only a single material parameter is considered to degrade monotonously (for instance defect density in the perovskite layer, or hole mobility in HTL). No combinations are simulated because these would induce supplementary degrees of freedom through parameters mutual relative speeds of variation. In such case, assumptions on these speeds would multiply greatly the number of simulated cases, and counterproductively re-introduce a time dependence in the study.

It is possible that in reality, degradation processes impact several material parameters. As a result, the objective of the study is to determine if a main one had a major impact on solar cell performances.

4.3.1 Degradation using analytical model

The analytical model reported in Section 1.4, applied to a pn junction, considers carriers' diffusion through quasi-neutral regions and radiative recombination to compute photocurrent. Furthermore, radiative, SRH as well as surface recombination are considered.

In this section, a hypothetical pn junction composed of two layers of doped perovskite material is considered, see Figure 10. Illumination is done through the 50 nm thick, n-doped side. The p-doped side at the back is 450 nm thick. This is comparable to the 500 nm thick absorber in the solar cells investigated in this work.

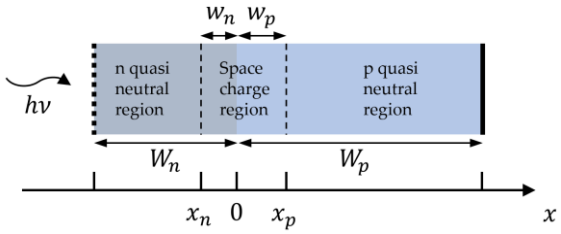

Figure 10. *Considered pn junction for analytical model. Illumination arises upon n doped side.*

Three exemplary devices are considered, having variations of a rather good, representative perovskite material, with for instance 1.62 eV bandgap, 10 $cm^2.V^{-1}.s^{-1}$

carrier mobilities, 10^{14} cm^{-3} defect densities. Parameters are summarized in Appendix D, Table D1.

Pathways associated to the nine considered degradation mechanisms are represented in Figure 11 for the three examples of initial devices. One parameter is modified in each case: on left column the defect density is raised to 10^{17} cm^{-3}, and on respectively middle and right columns, the hole and electron mobilities are lowered to 0.1 $cm^2.V^{-1}.s^{-1}$.

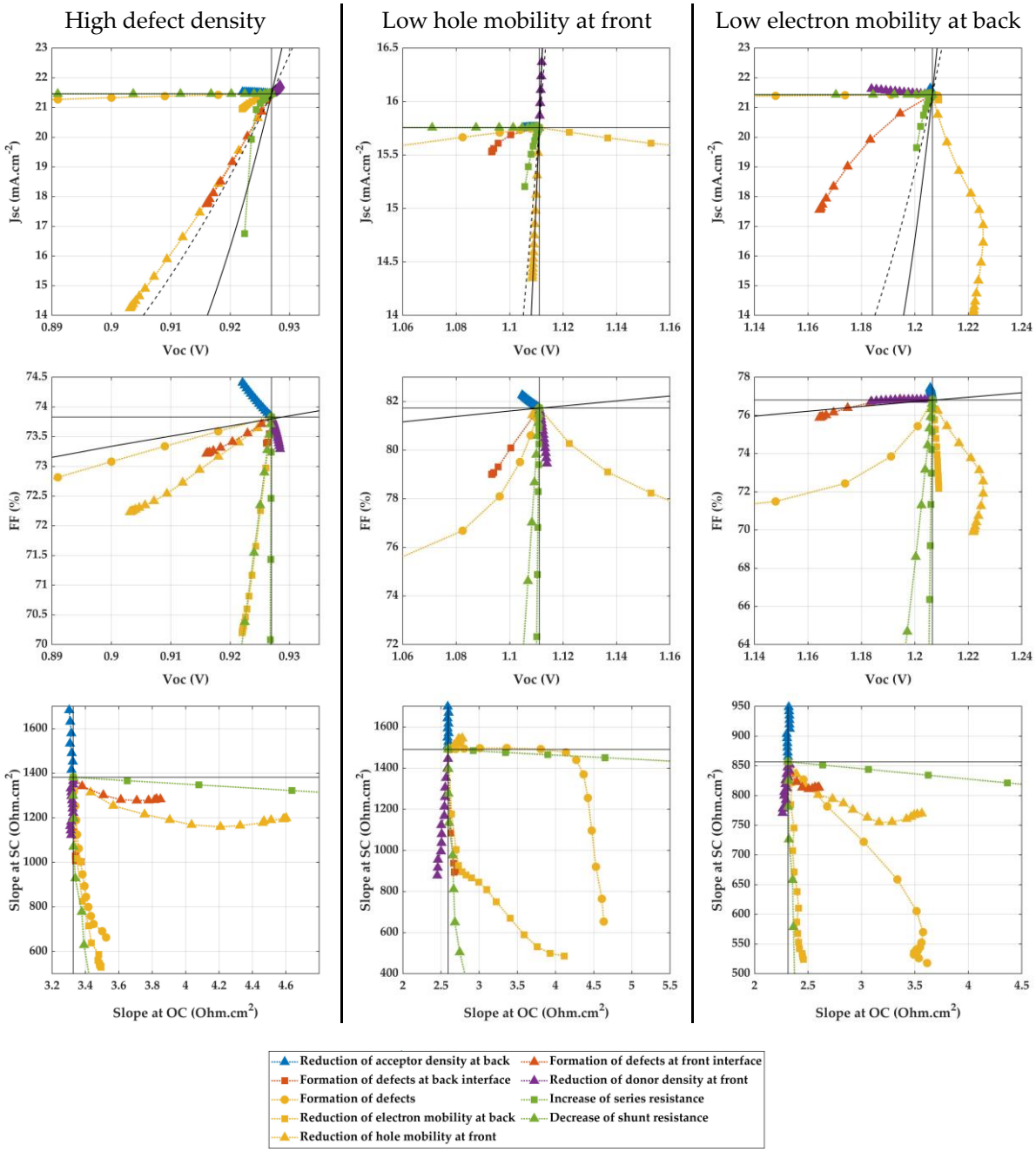

Figure 11. *Simulated degradation pathways obtained through analytical model of a pn junction. Left column: high defect density (10^{17} cm^{-3}). Middle column: low hole mobility in n doped front layer (0.1 $cm^2.V^{-1}.s^{-1}$). Right column: low electron mobility in p doped back layer (0.1 $cm^2.V^{-1}.s^{-1}$). All input parameters are in Appendix D, Table D1. On Jsc-Voc graphs, plain and dashed black lines show the Jsc-Voc relation according to the single diode model, with ideality factor equal to 1 and 2, respectively.*

The mechanisms can be distinguished through their different pathways. For instance, the formation of defects in the space charge region (yellow circles) induces a strong loss of Voc and stable Jsc, contrarily to other defects or decreasing mobilities.

The black lines on Jsc – Voc graphs are obtained with the single diode model (ideality factor, n, equal to 1 and 2 for plain and dotted lines respectively):

$$Voc = n\, k_B T ln\left(\frac{Jsc}{J_0} + 1\right) \quad (6)$$

These lines show the expected variation of Voc if Jsc decreases with the same recombination regime (same dark saturation current, J_0). As expected, the increase of defect density induces a strongly different behavior, as it would be associated to an increase of J_0.

It is interesting to note that formation of interface defects follow the dotted line ($n = 2$) in the high defect density case (left), similarly to the reduction of hole mobility. However, they induce a relatively stronger Voc loss in both other cases, contrary to reduced mobility. This is a sign that the impact of interface recombination is not the same in both cases on charge carrier, between inducing more recombination, and hindering transport through modified carrier distributions along depth.

On FF – Voc graphs, the black plain line is obtained from the following expressions for the relationship Voc and FF [5]:

$$FF_0 = \frac{v_{OC} - ln(v_{OC} + 0.72)}{v_{OC} + 1} \quad (7)$$

$$FF_1 = FF_0(1 - 1.1\, r_S) + \frac{r_s^2}{5.4} \quad (8)$$

$$FF = FF_1\left(1 - \frac{(v_{OC} + 0.7)}{v_{OC}}\frac{FF_1}{r_{Sh}}\right) \quad (9)$$

Here, $v_{OC} = \frac{Voc}{nk_BT/q}$, $r_S = \frac{R_s}{Voc/Jsc}$, $r_{Sh} = \frac{R_{Sh}}{Voc/Jsc}$ and n has been adjusted to reproduce initial fresh FF value. Similarly to diode model, it estimates the expected FF loss when Voc decreases, in the frame of classically functioning solar cell. It appears here that all mechanisms induce a stronger reduction of FF than expected by the model. This demonstrates stronger modifications of the solar cell behavior.

Notably, the impact of mobilities is more distinguishable when an asymmetry is present. In the middle and right column of Figure 11, the hole mobility in the front n-doped layer, or the electron mobility in the back p-doped layer have respectively low values. The reduction of electron mobility in the back layer is even associated to an increase of Voc. This trend could be counter-intuitive, but it is in fact associated to a decrease of recombination current in the back quasi neutral region. This is probably caused by electrons diffusing less towards the back of the device, and remaining closer to the space charge region, where they were mostly generated and where they must be accelerated towards front interface.

Finally, doping levels define the size of the space charge region, which influences greatly the extraction. In fact an optimum can be found, explaining the rise of Jsc with decreasing doping levels. They are associated to wider space charge regions, better accordance to the photogeneration profile and therefore better extraction of photogenerated carriers.

It is to note that the doping levels in this model are kept sufficiently high to ensure thinner space charge region than the total material length. Therefore, no significant decrease could be considered, only down to 3.10^{17} cm^{-3} and 8.10^{15} cm^{-3} for the donor and acceptor density respectively. Furthermore, the impact of these parameters is expected to be significantly different than ETL and HTL doping levels in perovskite solar cells. In nip or pin structure, there is no optimum position of a space charge region in regard to photogeneration profile.

4.3.2 Degradation using drift diffusion simulations

Employing an analytical model allowed to derive degradation pathways for a simplified pn structure. However, the carrier's behavior is slightly different in a nip perovskite solar cell, as discussed in Section 1.1.3. Notably, extraction relies on diffusion in the quasi-neutral regions of the pn junction, where an electrical field normally spans the entire absorber depth in the pin structure. Therefore, the modeling procedure exposed in Section 2.1, has been applied to exemplary solar cells, with the same approach has in the previous section.

Importantly, degradation scenarios defined here are more consistent with realistic processes that could occur in a perovskite solar cell. For the HTL and ETL, they consist in losses of carrier mobility (holes or electrons respectively) and decrease of doping. Concerning the perovskite layer, increase of defect density as well as decrease of carrier mobility are considered. Furthermore, increase of interface defect density at its interfaces and respectively increase or decrease of external series and shunt resistances are also implemented.

Similarly to previous section, examples here are based on a hypothetical realistically good device. Perovskite material has for instance 1.62 eV bandgap, 10 $cm^2.V^{-1}.s^{-1}$ carrier mobilities, 10^{14} cm^{-3} defect densities. Transport layers are also highly doped (up to the corresponding density of states) and have high carrier mobilities of 0.5 $cm^2.V^{-1}.s^{-1}$. Details on the material characteristics are in Appendix D, Table D2.

Degradation pathways of this good device are displayed in Figure 12. Again, the distinction of the mechanism through different pathways is a very useful feature for the next step of this work.

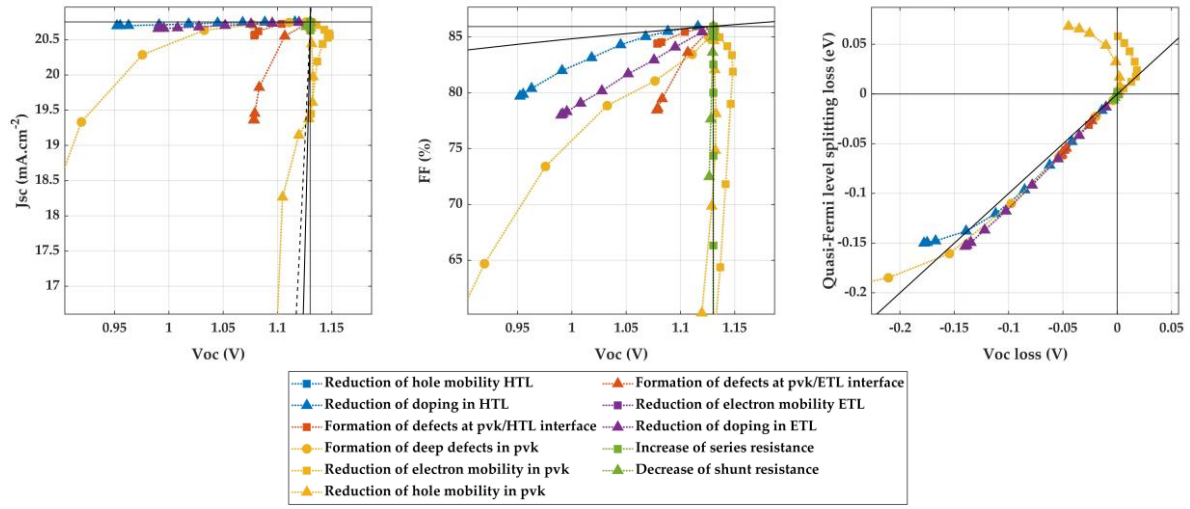

Figure 12. *Simulated degradation pathways obtained through drift diffusion simulations of a perovskite solar cell. Exemplary hypothetical device with good material qualities (details are in Appendix D, Table D2).*

Here, JV and PL related optoelectrical parameters are used to define the pathways. Interestingly, the relation between quasi-Fermi level splitting and Voc follows perfectly a 1 to 1 slope for all mechanisms. It can be therefore considered here that photoluminescence is very good indicator of the Voc.

However, it is to note that this specific example is a very good performing hypothetical device. Therefore, three variations of this examples are considered, with one parameter changed at a time: the defect density in the perovskite layer is raised to 10^{17} cm^{-3}, or the hole or electron mobilities are lowered to 0.1 $cm^2.V^{-1}.s^{-1}$. Interestingly, the relation between Voc and quasi-Fermi level splitting changes in these cases, as it appears in Figure 13. This is most probably related to changes in carriers' distributions across the depth of the perovskite layer, and the different impacts it can have on the recombination regimes.

In the previous section, a rise of Voc was observed when the mobility of the minority carriers at the back side (electrons) decreases. Here, a comparable trend occurs for the good performing device of Figure 12 and devices with high defect density (left column) and low hole mobility (right column) in Figure 13. Again, the carriers might remain closer to the interface where they have to be extracted (through the ETL).

Furthermore, the device with low electron mobility shows a reversed behavior: in this case, the reduction of hole mobility induces the increase of Voc (reversely for the device with low hole mobility). Here, hole extraction is not a limiting factor for the carrier extraction. This is supported by the fact that reduction of HTL doping is not significant anymore. Therefore, reducing their mobility might not limit extraction, but only avoid recombination by limiting their diffusion.

Notably, with asymmetrical carrier mobilities, the impact of doping levels of both extracting layers is significantly distinguishable, in terms of Voc, FF and quasi-Fermi levels splitting.

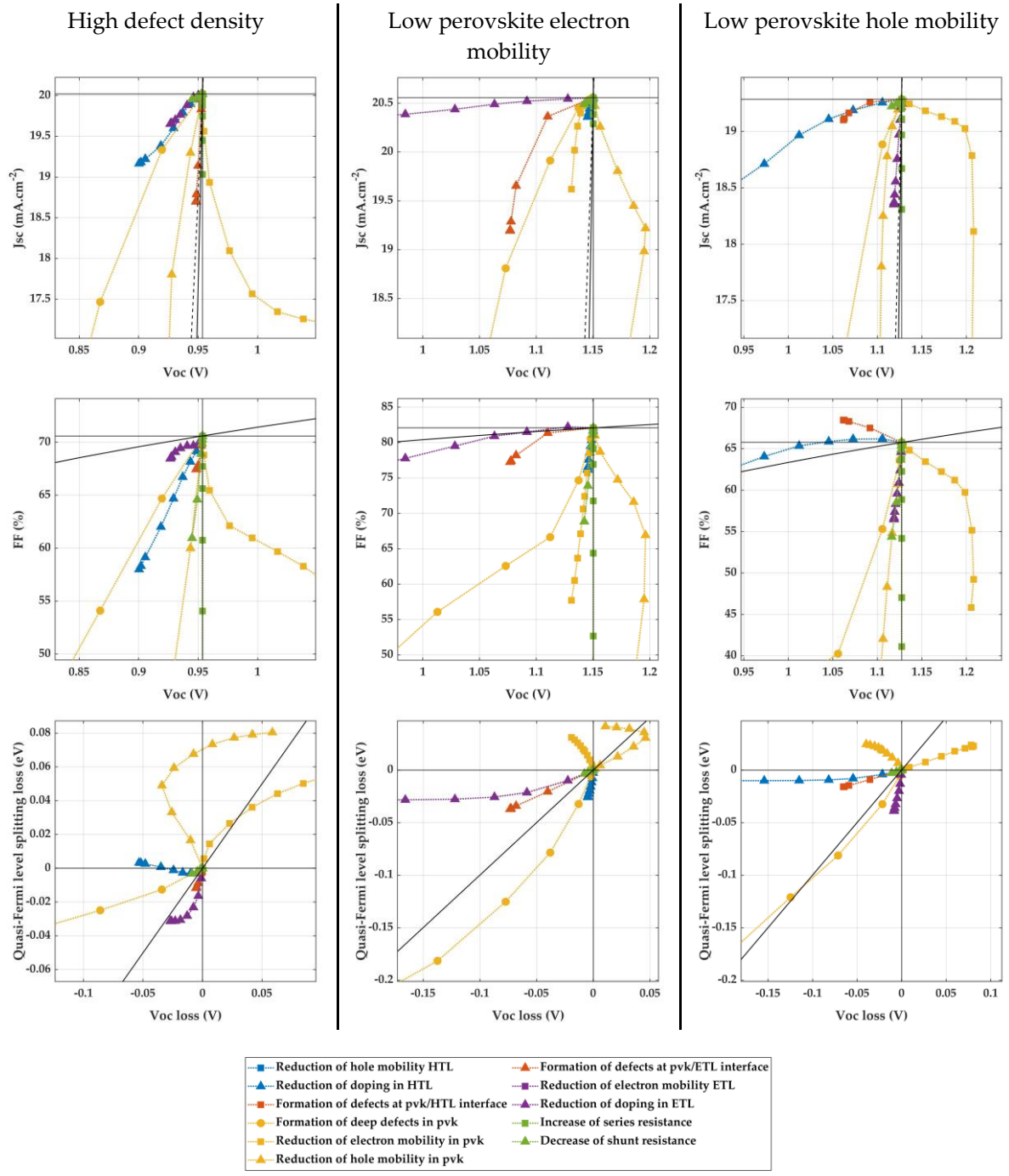

Figure 13. *Simulated degradation pathways obtained through drift diffusion simulations of a perovskite solar cell. Left: high defect density (10^{17} cm^{-3}). Middle: low perovskite electron mobility (0.01 $cm^2.V^{-1}.s^{-1}$). Right: low perovskite hole mobility (0.01 $cm^2.V^{-1}.s^{-1}$). All material parameters are in Appendix D, Table D2.*

Similarly to previous sub-section, the diode model and the phenomenological relations are employed to obtain the black lines on Jsc – Voc and FF – Voc graphs respectively. Notably, no mechanism induces any close behavior to diode model prediction with Jsc loss (black plain and dotted lines), all inducing significantly more Voc variations. This might be related to the nip structure being less dependent on transport processes: when any degradation occur, it mainly impacts the solar cell through enhanced carrier recombination and stronger Voc reduction. Also, similarly

to results obtained for the pn junction, the phenomenological relation of FF and Voc strongly underestimates the FF loss for all mechanisms.

Finally, the examples exposed here show that simulated degradation mechanisms induce distinguishable pathways. The extend of the optoelectrical performance losses depends on the initial characteristics of the device and the factor limiting carriers' behavior. However, it is to note that the position of the pathways remains similar from one device to the other. In fact, the statistical approach employed in this work can allow to estimate the sensitivity of the degradation pathways to the initial point.

As a result, this constitutes a valuable tool to assess the compatibility of the considered mechanisms with the experimental results. Moreover the specific procedure presented in Section 3.2 considers the starting point of experimental degradation sequences and have been demonstrated to statistically reproduce its performances (see Section 3.3). As a result, consistent degradation pathways are generated and compared to the experimental ones in the next sections.

Section key points:

- Unitary degradation mechanisms are simulated by considering the variation of a single material parameter. They are distinguishable from each other through their distinct pathways.
- The position of a given degradation pathway depend on the characteristics of the device before degradation.
- Combining characterization techniques (here JV and PL) allow further distinction of degradation pathways.
- Two models have been employed: an analytical model for a pn homojunction, and a drift diffusion model for a pin structure.
- Several mechanisms show common trends with both models (minority carriers at one side of the pn junction must be compared to the carriers extracted at the same side in the pin structure).

4.4 Analysis of experimental results from literature

In this section, experimental measurements reported in literature are investigated by coupling the approaches employed in both previous sections (4.2 and 4.3). Results are represented in terms of degradation pathways, and experimental and simulated mechanisms are superimposed.

For almost all published results investigated here, Voc, Jsc and FF were the only available optoelectrical parameters from which evolution over time was reported by authors (details are in Section 2.4.1). Therefore, reproduction of the degradation starting point was assessed on these parameters only, as exposed in Section 3.3.

As a result the following degradation mechanisms were simulated: losses of majority carrier mobility and decrease of doping in HTL and ETL and increase of defect density and decrease of carrier mobility in the perovskite layer. Finally, increase of interface defect density at the perovskite/HTL or perovskite/ETL interfaces are also considered.

Importantly, it has been exposed in Section 2.1 that solar cells are simulated here as 1D structures. Therefore, lateral average material properties, and carrier behavior are considered. In reality degradation phenomena do first have an impact at the microscopic level. However, simulating these phenomena and their impact on macroscopic current voltage properties would require numerous assumptions. Also, it might not be possible to distinguish these phenomena only by relying on macroscopic measurements such as current voltage characteristics. For these reasons, mechanisms related to lateral heterogeneity, such as phase segregations are not directly implemented. They can only be expected to resemble to an average degradation of carrier mobility or defect densities.

Moreover, ion migrations are also not simulated, and the transient effects that cause hysteresis, such as electric field screening, variations of defect densities at interfaces or local doping are not considered. Therefore, even if considering mobile ions would more exactly reproduce the behavior of the devices, the simulations done here capture a "long-term" impact on carrier mobilities or defect densities in the perovskite layer and its interfaces. This constitutes a tradeoff in terms of number of parameters and assumptions (ion mobilities and JV scan rate for instance) and accuracy.

Finally, mechanisms implemented here do remain in the frame of working solar cells, where the models used are applicable. Therefore, phenomena associated to a strong destruction of a material and potentially to the failure of the solar cell are not considered.

Degradation results published by Peng *et al.*:

Peng *et al.* studied $Cs_{0.05}FA_{0.88}MA_{0.07}PbI_{2.56}Br_{0.44}$ based devices with Spiro-OMeTAD and P3HT:CuPc HTL [6], details on the devices structures and aging conditions are presented in Section 2.4.1. Authors found the devices with P3HT:CuPc HTL significantly more stable and degradation of doped Spiro-OMeTAD has been

widely reported, it is therefore consistent to correlate it with the degradation observed here. Accordingly, authors attributed the degradation of electrical performances to a deterioration of the HTL/perovskite interface, caused by lithium-ion diffusion (Spiro-OMeTAD dopant).

Initial performances of the devices with Spiro-OMeTAD HTL were reproduced with 98 different material parameters sets (details are in Section 3.3). On

left, experimental Jsc/Voc pathway resembles to a loss of hole mobility in perovskite layer (brown). This mechanism is also a consistent explanation on FF/Voc plane: although the FF drop is less pronounced at first, the final stage of degradation meets the simulated pathway. Another interpretation of these results arise by looking at only the three first points: they describe a significantly distinguishable trend (which is already observable when the results are displayed against time by the authors). This first part of degradation is close to the simulated pathway for a formation of defects at ETL/perovskite interface (pink), on all three planes.

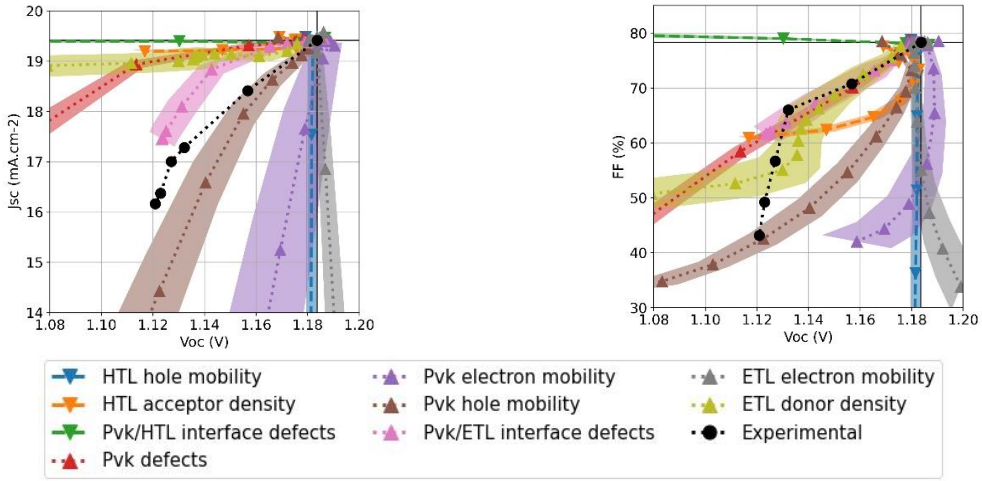

Figure 14. *Experimental degradation pathways from results published by Peng* et al.*: perovskite devices were aged under dark, at 85 °C and 85 % relative humidity. Associated simulated pathways (average over 98 material parameters sets used to reproduce initial performances) are superposed (down triangles and dashed lines for causes identified by authors, up triangles and dotted lines for others). A formation of defects at ETL/perovskite interface (pink) or a decrease of hole mobility in perovskite layer (brown) are the two closest mechanisms explaining experimental degradation.*

Devices with P3HT:CuPc HTL have also been investigated, details are in Section 2.4.1. Reproduction of initial performance are reported in Section 3.3 and superposition of experimental and simulated pathways in Appendix D, Figure D8. Interestingly, experimental pathway is close to a loss of hole mobility in the perovskite layer (brown), similarly to devices with Spiro-OMeTAD HTL. This would be consistent with the fact that both structures rely on the same perovskite material, potentially being the "limiting factor" for stability of electrical performances.

As a result, the analysis done here questions the causality of HTL degradation on electrical performance losses. Reduction of HTL hole mobility or doping (blue or orange) and perovskite/HTL interface deterioration (green) are very distinct from experiments. The loss of mobility does not induce Voc variation, and the loss of doping

and interface deterioration does not induce Jsc losses. Therefore, these three mechanisms could difficultly explain the performance losses reported here. This interpretation doesn't oppose a concomitant degradation of HTL: it can still have occurred without being the main cause of performance degradation.

Degradation results published by Li *et al.*:

Li *et al.*[7] reported the degradation of unencapsulated $FA_{0.9}Cs_{0.1}PbI_3$ based devices kept at MPP or Voc (average behavior over eight samples were reported) and details are available in section 2.4.1. Furthermore, they performed before and after degradation X-ray diffraction (XRD) measurements and PL- and synchrotron-based X-ray fluorescence microscopy with nanoscale spatial resolution, to evidence phase segregation of the perovskite material (distinct Cs-rich and FA-rich areas). Furthermore, the combination with X-ray beam induced current measurements showed that Cs-rich areas are photo-inactive and current blocking. In addition, authors also focused on HTL and gold back contact. They re-coated aged samples with fresh HTL and gold and measured PCE. For some samples, they degraded the full cell and removed aged HTL and gold. For other samples, they aged half stacks without HTL and gold from the beginning. As a results, Li *et al.* conclude that the main source of electrical performance degradation is the phase segregation of the perovskite itself, not being specifically triggered by HTL or gold.

In the present study, initial reported performances were reproduced with 104 and 125 different material parameters sets for the cells aged at MPP and Voc respectively. First, degradation pathways have been derived for both cases separately. It appears that pathways are similar for both groups of devices, which is consistent with the fact that they were fabricated in the same batch, with similar performances. Therefore, average responses over all simulations for both groups are computed, and associated pathways are used to analyze together both experimental results. Experimental pathways are superposed on Figure 15 and the similarity of both experimental results indicates that similar dominant degradation mechanisms occurred.

Furthermore, On Jsc/Voc plane (left), the closest mechanisms to experimental points are defects formation in the perovskite layer (red), or loss of doping in ETL (yellow) the extent of the Voc loss being more consistent with the first one. This is confirmed by the FF/Voc graph, showing a better agreement of experimental behavior with defect formation in perovskite layer (red). On FF/Voc graph, the loss of doping in ETL (yellow) is significantly different because it starts with a sharp decrease of FF without Voc loss.

The formation of defects in perovskite layer is consistent with the phase segregation identified by Li *et al.* In fact, such spatially resolved phenomenon cannot be simulated with 1D drift diffusion simulations. However, the results obtained here show that even if all possible mechanisms cannot be simulated, the analysis presented here can help to identify the faulty layer or interface.

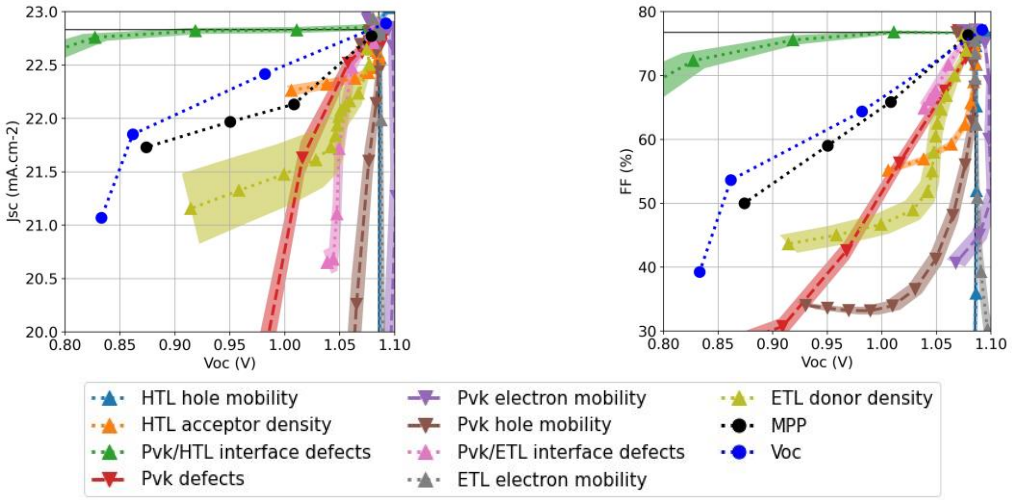

Figure 15. *Experimental degradation pathways from results published by Li* et al.*: devices were aged under one sun, N2 atmosphere, at 35 °C and tracked at maximum power point or kept at open circuit voltage. Associated simulated pathways are superposed (down triangles and dashed lines for causes identified by authors, up triangles and dotted lines for others). A formation of defects in the perovskite layer (red) is the closest mechanism explaining experimental degradation.*

Degradation results published by Chen *et al.*:

Chen *et al.*[8] optimized the composition of Cs1−xFAxPbI2Br perovskites and studied the stability of associated devices (results analyzed here were obtained with x = 0.3), see Section 2.4.1. Authors measured photoluminescence spectra and decays on fresh and aged cells, as well as XRD spectra on fresh and aged perovskite films. They conclude that the composition with x = 0.3 delayed the most the phase change. Initial performances of these most stable devices were reproduced with 87 different material parameters sets, see Section 3.3. Simulated degradation pathways and measured degradation pathways are superposed in Figure 16. Although noisy experimental pathway, the closest simulated mechanism is the reduction of electron mobility in the perovskite layer (purple). On the other hand, authors explained the improvement of efficiency during the experiment by better charge collection, coming from better interfaces and stress relaxation (supported by higher photoluminescence intensity and longer carrier lifetime). This, however, would not explain the degradation observed during the whole experiment. Supplementary "degradation" mechanisms have been simulated for this example, considering respectively reductions of defect densities at perovskite/HTL and perovskite/ETL interface. It appears in Figure 16 that a rise of FF is associated with the healing of the perovskite/HTL interface, contrary to the lowering tendency in experimental results. Furthermore, the perovskite/ETL interface healing does not induce the rise of Voc observed experimentally.

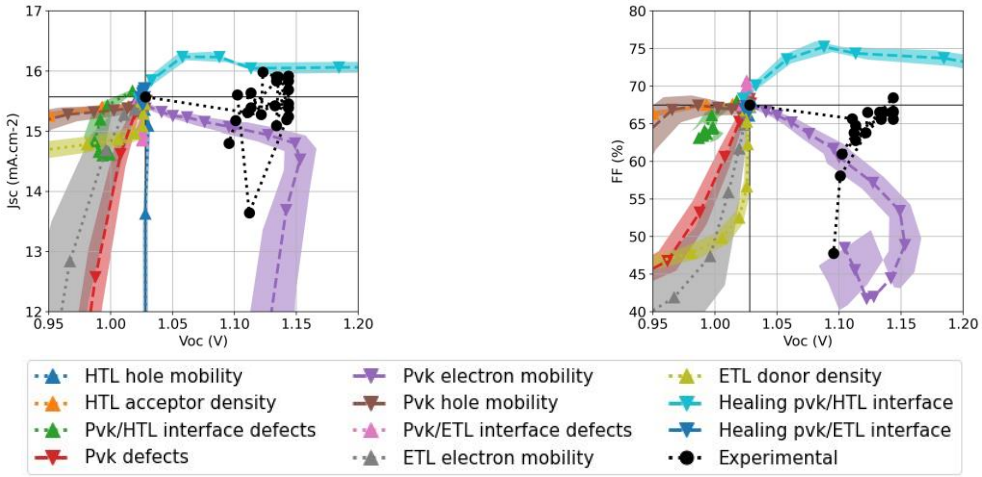

Figure 16. *Experimental degradation pathways from results published by Chen* et al.*: perovskite devices were unencapsulated and aged under ambient conditions. Associated simulated pathways are superposed (down triangles and dashed lines for causes identified by authors, up triangles and dotted lines for others). A decrease of electron mobility in perovskite layer (purple) is the closest mechanism explaining experimental degradation.*

Therefore, the analysis here directly suggest the cause of the reduction of power conversion efficiency: even with the best composition the perovskite layer itself is in cause. This pave the way for further work on devices stability by showing that focusing on perovskite is still necessary, after the first optimization step reported by Chen *et al*.

Degradation results published by Lim *et al.*:

The objective of the study published by Lim *et al*.[1] was to study the thermal activation of the perovskite degradation, details on the $FA_{0.95}MA_{0.05}PbI_{2.85}Br_{0.15}$ based devices are reported in Section 2.4.1. Authors determined reaction rates at each temperature and deduced activation energies with an Arrhenius law. Importantly, it is necessary to presuppose that the same mechanism is occurring and being activated at all measurements temperatures. This will be discussed, as the method employed here allows to distinguish mechanisms at each temperature. Furthermore, authors combined X-ray diffraction and cross-sectional scanning electron microscopy to compare the perovskite material properties before and after degradation. They noted the absence of formation of PbI_2, as a sign for stability. Similarly, UV-visible spectroscopy measurements done before and after aging are analyzed. They support an oxidation of the Spiro-OMeTAD HTL, together with iodide ions diffusion from the perovskite towards the HTL. As a result, authors attributed the main cause of performance losses to a degradation of HTL.

Initial performances of the devices aged at 40, 55 and 70 °C were reproduced with respectively 101, 109 and 49 different material parameters sets. In Figure 17, experimental data recorded at 40 and 55 °C follow a behavior close to a loss of hole mobility (brown) or a formation of defects (red) in the perovskite layer. Noticeably, behavior tends to be different at 70 °C, having a lower variation of Voc and more distinct fall of both other parameters. As a result, a loss of hole mobility in HTL (blue) appears to be a closer mechanism.

The fact that distinct degradation mechanisms occurred at different temperatures questions the kinetics approach used by the authors, which aims at studying the thermal activation of a given process. However, the higher temperature record has a significantly different pathway. If only a thermal activation of the same mechanism had been involved, the same pathway would have simply been followed at a different speed.

Moreover, experimental data shows a two-steps trend: first a clear increase of open circuit voltage associated with low or positive variations of Jsc and FF, followed by a decrease of all parameters. This feature motivates to study these results in two steps, extracting first the time period with Voc increase, and then considering the second part as being a distinct device, starting from another point. This would correspond to a plausible situation in which a first mechanism has the main impact on electrical performances during the first part of the experiment, and a second one drives the evolution during the second step.

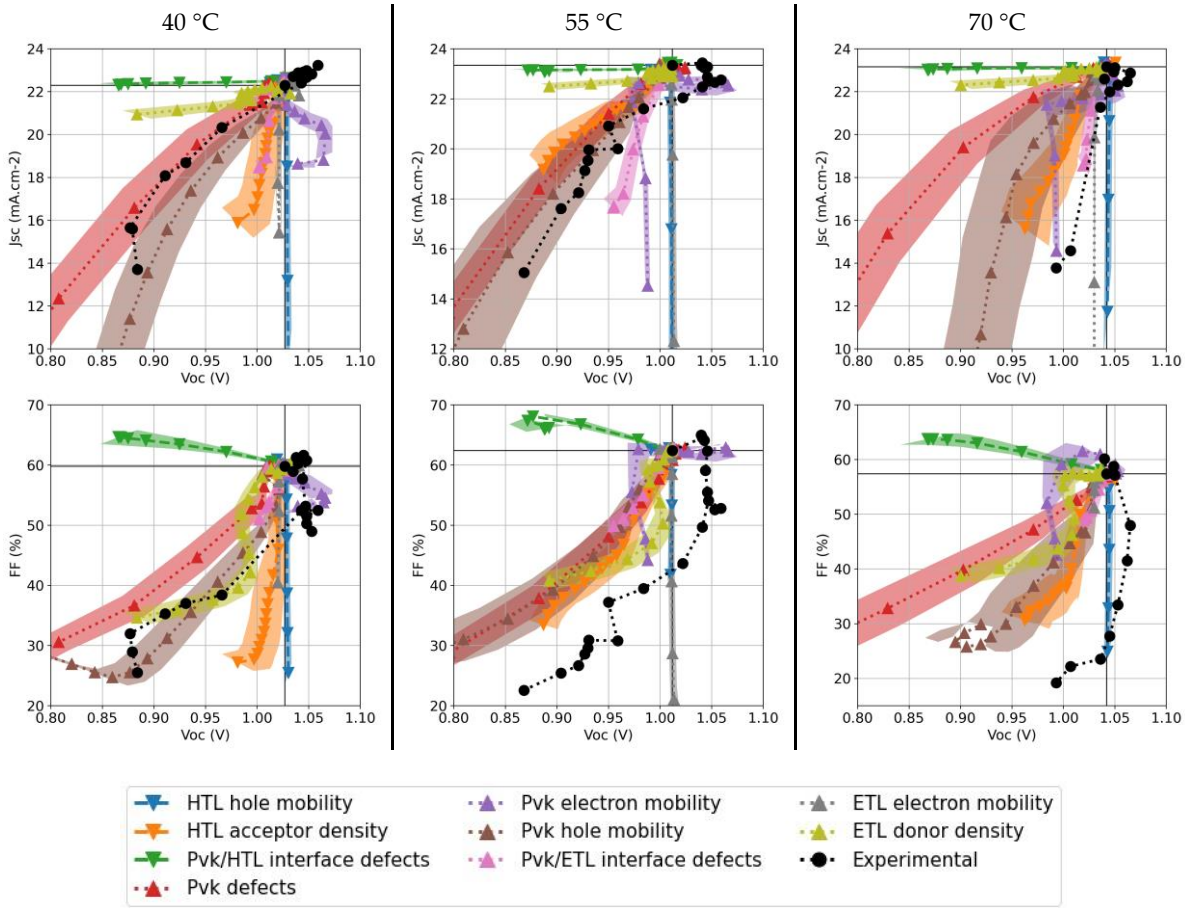

Figure 17. *Experimental degradation pathways from results published by Lim* et al.*: perovskite devices were aged under one sun, air and at 40, 55 or 70 °C (left, middle, and right respectively). Associated simulated pathways are superposed (down triangles and dashed lines for causes identified by authors, up triangles and dotted lines for others). At 40 and 55 °C, the closest mechanism are a loss of hole mobility (brown) or a formation of defects (red) in the perovskite layer. At 70 °C, a reduction of hole mobility in HTL (blue) is closer to experimental results.*

The first part of degradation is simply analyzed by considering the first experimental points (from 0 to 475, 175 and 10 minutes for measurements done at 40,

55 and 70 °C, respectively) with the same simulated behaviors, as showed in Appendix D, Figure D9. A loss of perovskite electron mobility (purple) can explain the behavior: increase of Voc and decrease of FF. It is to note that at this step, degradations at all temperatures induce comparable paths, advocating for a same mechanism, and being compatible with kinetics approach.

In order to simulate degradation pathways for the second step, the procedure has been applied to the partially degraded devices, as if they were new fresh devices with lower performances. This time, performances of devices aged at 40, 55 and 70 °C were reproduced with respectively 72, 74 and 87 material parameters sets. Contrary to the first part of degradation, Figure 18 shows two distinct trends at distinct temperature levels. At 40 and 55 °C, the increase of defect density (red) is confirmed by a very good agreement of the experimental and simulated pathways on all three planes. However, at 70 °C, a reduction of acceptor density in the HTL (orange) would be a closer mechanism. In fact, two other mechanisms related to extracting layers are close to experimental results, as they all induce almost no Voc loss: reduction of mobility in HTL (blue) and in ETL (grey). Interestingly, this analysis is consistent with authors' findings.

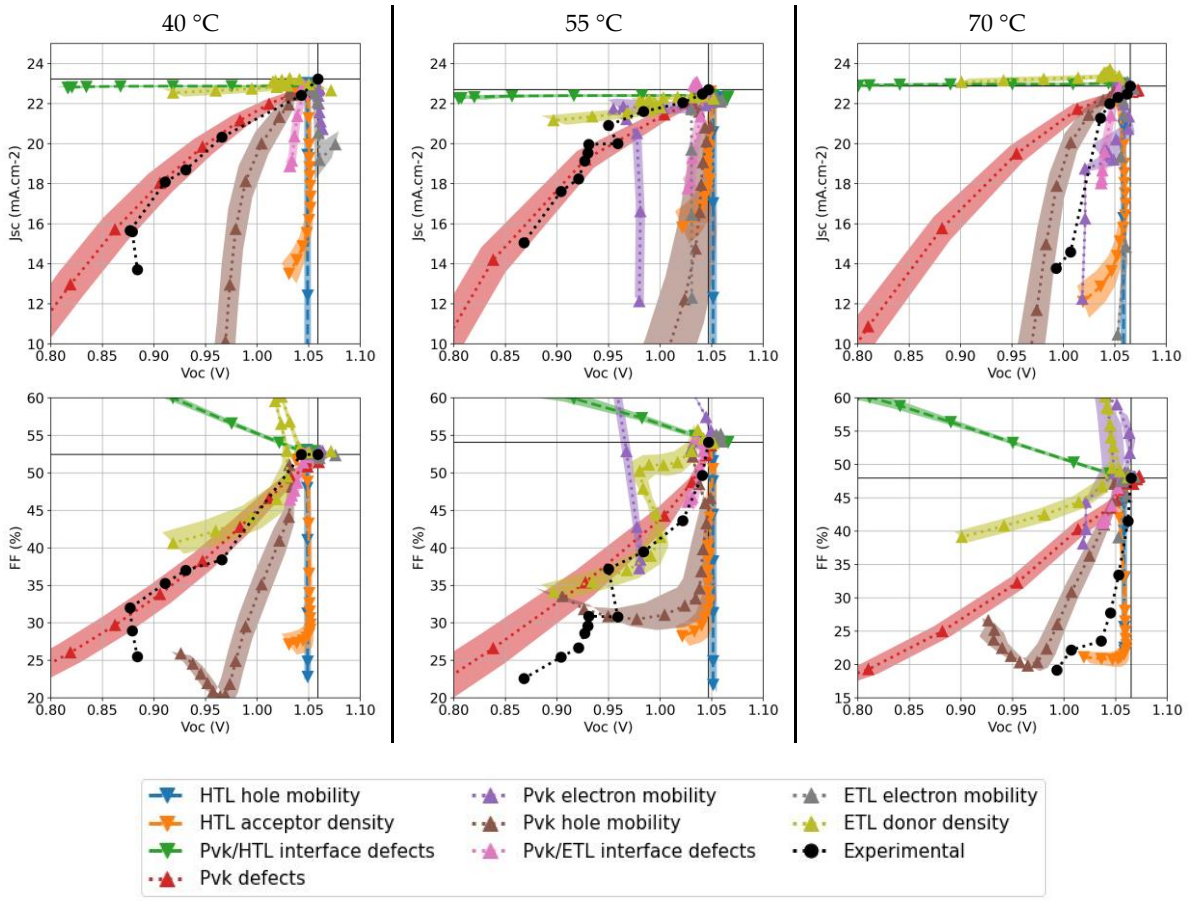

Figure 18. *Experimental degradation pathways from results published by Lim* et al.*, measured at 40, 55 and 70 °C (left, middle and right respectively). Associated simulated pathways are superposed. Second degradation step is analyzed. Only the second part of the experimental degradation is extracted from respectively 475, 175 and 10 minutes. A formation of defects in the perovskite layer (red) is the closest mechanism at lower temperatures and experimental pathway at 70 °C is close to a reduction of acceptor density in the HTL (orange).*

This second step impacts device performances much more than the first one: approximatively 40 and 60 % of Jsc and of FF losses respectively, versus almost no Jsc variation and a 20 % loss of FF during the first step. This explains why the interpretation with a single mechanism leads to comparable conclusions.

Finally, the analysis done here with results published by Lim *et al*. shows well the strength of the proposed method. It is not necessary to use heavy characterization techniques to question the kinetics approach of the authors. Furthermore, the two steps analysis shows that it is possible to consider several degradation mechanisms, impacting performance sequentially. The degradation mechanism proposed by the Lim *et al*., involving the degradation of the HTL could be responsible for the performance losses, but only in combination with another mechanism, and only at higher temperatures. This shows that directly studying the causality of degradation mechanisms instead of concomitance with material evolutions strengthens the analysis.

Section key points:

- Experimental measurements reported in literature have been investigated to provide a proof of concept of the methodology exposed here.
- Pathways of the data reported by Peng *et al*. attribute performances losses to degradation of the perovskite layer. This can be concomitant with the apparent degradation of the HTL layer reported by the authors.
- Consistent results with the interpretation of authors are obtained with degradation data published by Li *et al*.: the perovskite layer is in cause.
- Even with the optimized composition reported by Chen *et al*, the perovskite layer is still in cause for performance losses of these devices.
- Kinetics approach employed by Kim *et al*. is discussed: distinct mechanisms might have caused the degradation measured at several temperatures.
- Several degradation sequences over time can be analyzed to consider multiple successive degradation mechanisms.
- The approach employed here directly tackles the cause of optoelectrical performance losses. Conducting complementary characterization can only demonstrate concomitance with material evolutions.

4.5 Analysis of experimental results from IPVF

Here, aging experiments performed at IPVF are investigated with the same approach as in the previous section.

First, the study of a set of perovskite solar cells made of the same materials, degraded under constant illumination and ambient conditions is investigated. Then, results obtained in a climatic chamber for solar cells aged under dark are also analyzed, this time through coupled JV and steady state PL measurements. Details on the samples are reported in Section 2.4.2.

Here, the full JV curves (measured under illumination) were available, contrary to results extracted from literature. Therefore, slopes at SC and OC could be extracted and employed to define more precisely the initial performances (details are in Section 3.3), and degradation pathways in terms of these quantities have been investigated. Therefore, two supplementary mechanisms have been simulated, associated to the increase of both external resistances.

Furthermore, the availability of the PL spectrum allowed to constraint even more the reproduction of the starting point of degradation. Moreover, a widening of the shallow defect distribution could be considered.

4.5.1 JV characteristics recorded along degradation

Devices JV-1.1 to JV-4.2 were all fabricated with the same structure (TiO2 ETL, triple cations perovskite and PTAA HTL) and four variations were employed to prepare the perovskite solution, with a preparation on the day of deposition or one day before and preheated or not. Furthermore, these devices were aged under constant illumination in ambient air during 1200 h. Their performances were tracked through periodic JV measurements. Details on samples and aging conditions are reported in Section 2.4.2.

Devices JV-1.1 and JV-1.2:

First, devices for which the perovskite solution was prepared on the day of deposition, without pre-heating are investigated. Only a short time sequence was extracted for device JV1.1 (from 170 to 290 h), because of unstable measurements conditions and noisy experimental results. Notably, the sample continued to operate after 290 h, but the causes of the distinct further behavior are not investigated here.

The associated degradation pathway is displayed in Figure 19, along with associated simulated pathways. The initial experimental JV characteristic was reproduced with 113 sets (see Section 3.3), and all were subjected to the 12 mechanisms considered in this section. It appears that the increase of external resistance follows a very close behavior to the experiment on all graphs, characterized by a sharp decrease of Jsc and FF, with no Voc loss. It is in fact the only compatible mechanism, without Voc variation.

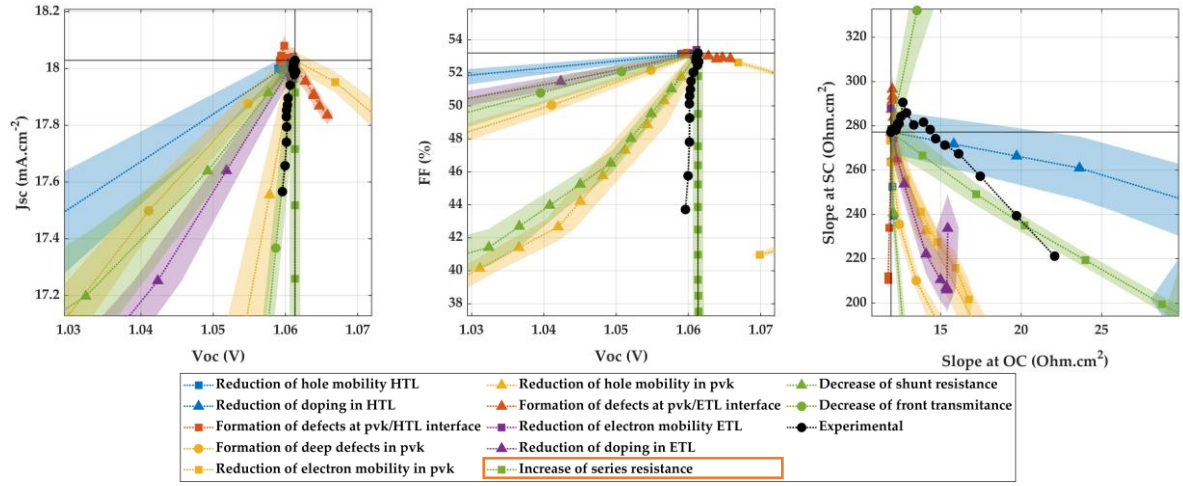

Figure 19. *Experimental degradation pathway of device JV-1.1 and associated simulated mechanisms. The increase of external series resistance (green squares) is very close to experiment.*

The next device was fabricated in the same conditions, it is JV-1.2 and experimental measurements for this device could be extracted from 170 to 320 h. Here the initial point was reproduced with 107 sets.

Results are displayed in Appendix D, Figure D10. Here, the reduction of HTL doping (blue triangles) is the most compatible with the joint reduction of Voc and Jsc and small FF variation. However, a reduction of electron mobility in the ETL (purple triangles) cannot be excluded neither. It would induce variations similar to the experiment, with only a slightly higher decrease of FF and slope at SC.

Devices JV-2.1 and JV-2.2:

The degradation of both devices for which the perovskite layer was deposited from a preheated solution prepared the on the day of deposition occurred quickly. Both rapidly stopped operating or showed an erratic behavior. Furthermore, only device JV2.2 is considered because device JV-2.1 showed a significant increase of Jsc and Voc, probably associated to light soaking and not investigated here.

The initial JV characteristic of JV-2.2 was reproduced with 114 sets, and experimental behavior was extracted from 50 to 160 h, covering most of the recorded performances. Results are displayed in Figure 20, and an increase of Voc clearly visible. The only compatible mechanism is an increase of hole mobility in the perovskite layer. It also explains the FF and Jsc losses, as well as the slopes behavior.

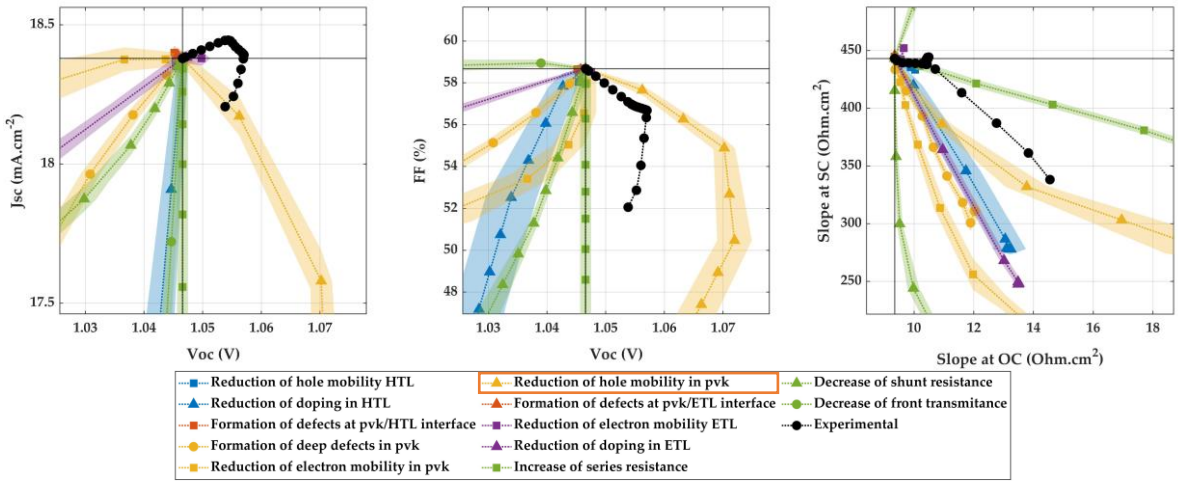

Figure 20. *Experimental degradation pathway of device JV-2.2 and associated simulated mechanisms. The reduction of hole mobility in perovskite (yellow triangles) is compatible, other mechanisms do not induce an increase of Voc.*

Devices JV-3.1 and JV-3.2:

The perovskite solution for both next devices was prepared the day before deposition, without pre-heating. First, aging of device JV-3.1 was extracted from 530 to 1150 h, covering the long term degradation trend. Its initial point was reproduced with 110 sets.

As a result, degradation pathways in Figure 21 point out two compatible mechanisms: reduction of ETL doping (purple triangles) and formation of perovskite deep defects (yellow circles). Both can't be excluded because they induce degradations of Voc, FF and slopes of the same order of magnitude as the experiment.

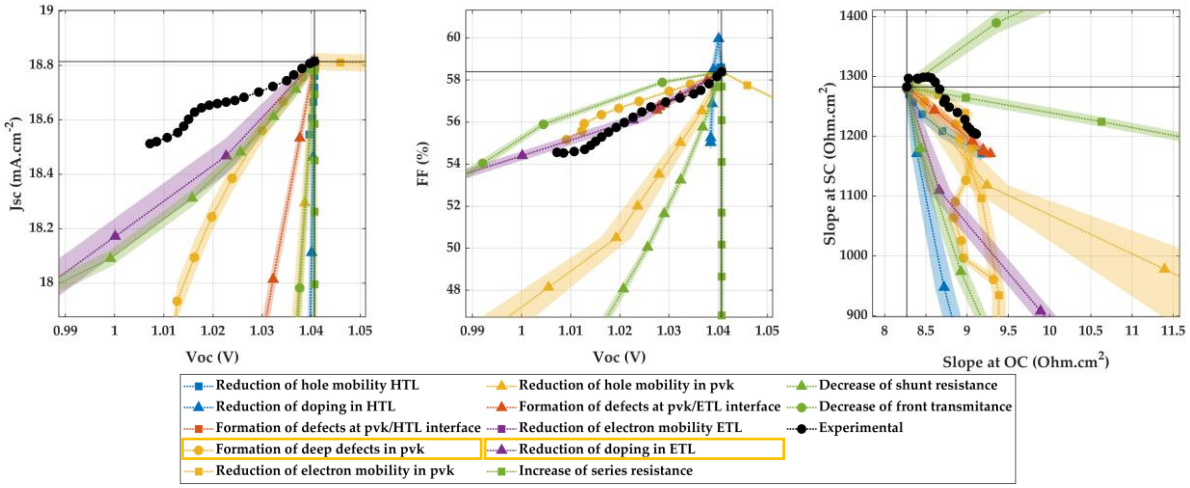

Figure 21. *Experimental degradation pathway of device JV-3.1 and associated simulated mechanisms. Reduction of ETL doping (purple triangles) and formation of perovskite deep defects (yellow circles) are compatible. Other mechanisms mostly induce too strong Jsc or FF losses.*

Degradation of device JV-3.2, prepared in the same conditions, was only extracted between 175 and 410 h. Its initial JV characteristic was reproduced with 111 sets and results are displayed in Appendix D, Figure D11.

Importantly, all simulated mechanisms could be excluded at first, because none can explain the stable, even increasing Jsc. The closest mechanisms on this aspect are a reduction of electron mobility in ETL (purple squares) or formation of defects at pvk – HTL interface (red squares). The first one underestimates slightly the reduction of FF and slope at SC but might remain compatible. However, the second would not induce any slope variation. Furthermore, the loss of ETL doping (purple triangles) and defect formation in perovskite (yellow circles) could explain well all experimental pathways, excepted the Jsc behavior.

Devices JV-4.1 and JV-4.2:

The last deposition method included preparation of the perovskite solution one day before deposition, and a pre-heating step. Degradation of JV-4.1 was extracted between 580 and 1160 h (most of the aging experiment) and initial point reproduced with 110 sets.

In Appendix D, Figure D12, no simulated mechanism is compatible with such stable Jsc and increase of slope at SC. None of the close mechanisms on FF-Voc plane, such as reduction of HTL or ETL doping, or formation of perovskite defects, could be associated to increase of slope at SC. Furthermore, the decrease of front transmittance induces a purely orthogonal behavior in terms of Jsc-Voc.

Degradation of the last device investigated in this section, JV-4.2, could also be extracted for most of the aging study, from 170 to 1150 h. Its initial point was reproduced with 114 sets.

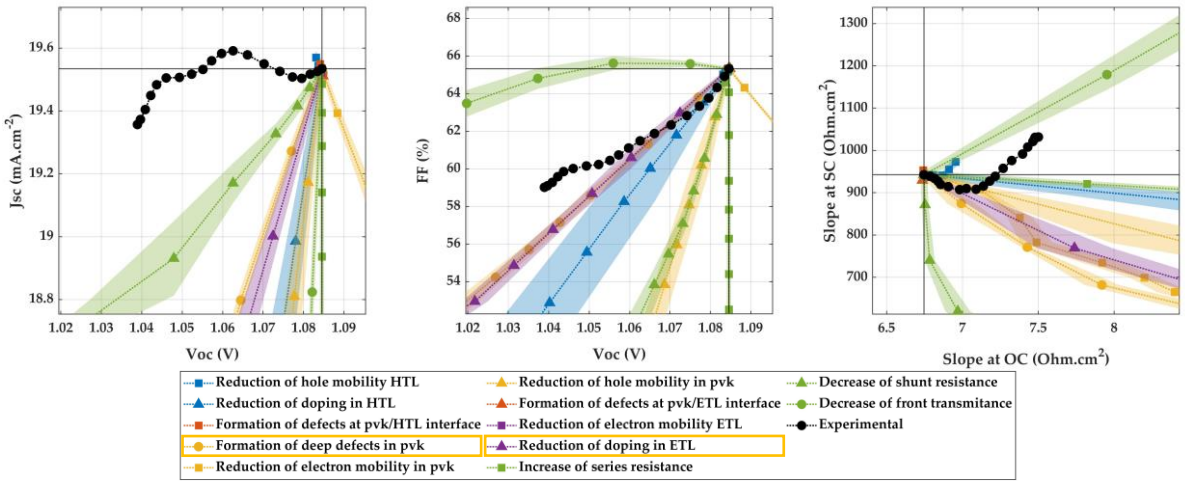

Figure 22. *Experimental degradation pathway of device JV-4.2 and associated simulated mechanisms. No simulated mechanism explains such a stable Jsc. However, a loss of ETL doping (purple triangles) and formation of defects in perovskite layer (yellow circles) can't be totally excluded.*

Again, JV-4.2 also shows stable Jsc and increasing slope at SC, that is not explained by any simulation. A loss of ETL doping (purple triangles) and formation of defects in perovskite layer (yellow circles) are still compatible with Voc and FF behavior, and the first degradation points of JV slopes. However, the discrepancies in terms of Jsc evolution make this interpretation lowly probable.

Intermediate conclusions:

It has to be kept in mind that the studies done here are not exhaustive in terms of considered mechanisms. In fact, when a simulated pathway superposes with the experiment, it is only the proof that the mechanism is compatible and a possible explanation. It is not the proof that no other mechanisms (potentially not considered here, or a combination) can also reproduce the experimental behavior.

Also, the simulated pathways for these samples were all different to a certain extend. This emphasizes the need to accurately reproduce the initial performances before degradation to be able to associate the right simulated pathways to the right device.

As a result, Table 2 summarizes the lists of compatibles mechanisms found in this study. Importantly, the two cases where a single mechanism was found compatible with good fitting correspond to short degradation sequences: the increase of series resistances of device JV-1.1 and reduction of hole mobility in the perovskite layer of device JV-2.2. In fact, when analyzing short time sequences, a concomitant major impact of several mechanisms might be less probable than over a longer period of time. This facilitates the comparison with the unitary degradation mechanisms simulated here.

Table 2. *Mechanisms associated to the devices investigated in this sub-section. Red: closest mechanism: experimental and simulated pathways superpose significantly. Yellow: compatible mechanism: experimental and simulated pathways follow mostly similar trends. Green: excluded mechanism: experimental and simulated pathways are significantly different.*

Device	JV-1.2	JV-3.1	JV-3.2	JV-4.1	JV-4.2	JV-1.1	JV-2.1	JV-2.2
Features of degradation pathways	Stable Jsc, joint FF and Voc decrease					Jsc and FF loss	Increase of Voc, increase of Jsc (JV-2.1)	
HTL hole mobility							Not simulated	
HTL doping								
Pvk-HTL interface								
Pvk defects								
Pvk electron mobility								
Pvk hole mobility								
Pvk-ETL interface								
ETL electron mobility								
ETL doping								
External shunt resistance								
External series resistance								
Front transmittance								

The five devices with stable Jsc and joint FF and Voc decrease, which apparently followed the similar degradation pathways in Figure 7, might not have been subjected to the same mechanisms. However, degradation of the perovskite layer can be excluded for all of them.

Notably, JV-1.2, JV-3.1 and JV-3.2 are mostly compatible with ETL related mechanisms (decrease of doping level or mobility). Furthermore, both devices JV-4.1 and JV-4.2 have most probably been subjected to distinct mechanisms from the twelve considered here, that notably allow a stable Jsc. This means that degradation of the perovskite layer can be excluded here also. In fact, only JV-3.1 has been found compatible with perovskite layer degradation, but also with a loss of ETL doping.

The goal of the study done by the IPVF fabrication team was to investigate the deposition method of the perovskite layer and try to define an optimum. The results obtained here show that none of the four methods stands out and performs better. On the contrary, the preparation on the day of deposition with pre-heating (JV-2.1 and JV-2.2) under-perform significantly, and the results obtained here indicate that the perovskite layer might be in cause.

Devices prepared with other techniques do not necessarily follow the same mechanisms. However, results show that their perovskite layer might have remained stable, or at least is not in cause for the recorded degradation of performances.

Also, both devices with solution prepared the day before deposition and pre-heated (JV-4.1 and JV-4.2) showed an experimental degradation that was not compatible with any simulated mechanism in this work, because of the rise of JV slope at SC and stable Jsc. It seems possible that both were subjected to the same mechanism, but complementary analyses are necessary to provide more reliable indications on this aspect.

Importantly, these results illustrate a powerful aspect of the methodology employed here: specific degradation mechanisms can be excluded when pathways are incompatible. Here it allows to provide guidelines to improve the stability of the perovskite solar cells studied here: it is necessary to focus on the transport layers and interfaces. As long as the solution is not prepared and pre-heated on the day of deposition, the perovskite layer should be stable.

Section key points:

- Pathways that appeared similar when compared in terms of normalized parameters are not necessarily attributed to the same mechanism.
- The two samples with the most clear interpretation and attribution of a single mechanism were investigated over short time periods.
- Among the four deposition techniques employed for the perovskite layer, one stand out: preparation on the day of deposition with pre-heating under-perform significantly and results obtained here attribute the degradation to the perovskite layer.
- For most other samples, the perovskite layer might have remained stable, and the transport layers caused the performance losses. This constitute guidelines for further improvements of stability.

4.5.2 JV characteristics and PL spectra recorded along degradation

In this section, solar cells periodically characterized during aging through current voltage characteristic and photoluminescence spectrum are investigated. Device characteristics (materials and structure) and aging conditions are reported in detail in Section 2.4.2. Notably the same perovskite material was employed for all samples, but combinations of two ETL and HTL materials were employed: TiO_2 / PTAA for JV-PL-1, 2 and 3, SnO_2 / PTAA for JV-PL-4, and TiO_2 / Spiro-MeOTAD for JV-PL-5.

As done in previous sub-sections, the variations of photoluminescence intensity are represented here in terms of quasi-Fermi levels splitting (expression derived in Section 1.1.2).

Device JV-PL-1:

The first characterized through coupled JV and PL measurements is JV-PL-1. It was fabricated with TiO_2 ETL, PTAA HTL and its initial performances were reproduced with 116 sets.

According to JV parameters in Figure 23, four simulated degradation mechanisms are compatible with the experiment: reduction of electron mobility (yellow squares) or formation of defects (yellow circles) in the perovskite layer, or reduction of doping in HTL (blue triangles) or ETL (purple triangles).

However, a reduction of perovskite hole mobility would induce an increase of quasi-Fermi levels splitting, and the opposite is observed experimentally. Moreover, a reduction of doping in ETL seem to induce a slight increase of slope on low energy side of PL spectrum, and slight shifting of the peak maximum towards lower photon energies. Again, these are inverse trends to experimental results. It is to note however, that low confidence is to attribute to these last pathways: the ranges of observed variations are extremely low. As a result, only the quadrant in which degradation occur might be to interpret.

Finally, formation of defects in the perovskite layer (yellow circles) and reduction of doping in the HTL (blue triangles) are the two mechanisms that can't be excluded.

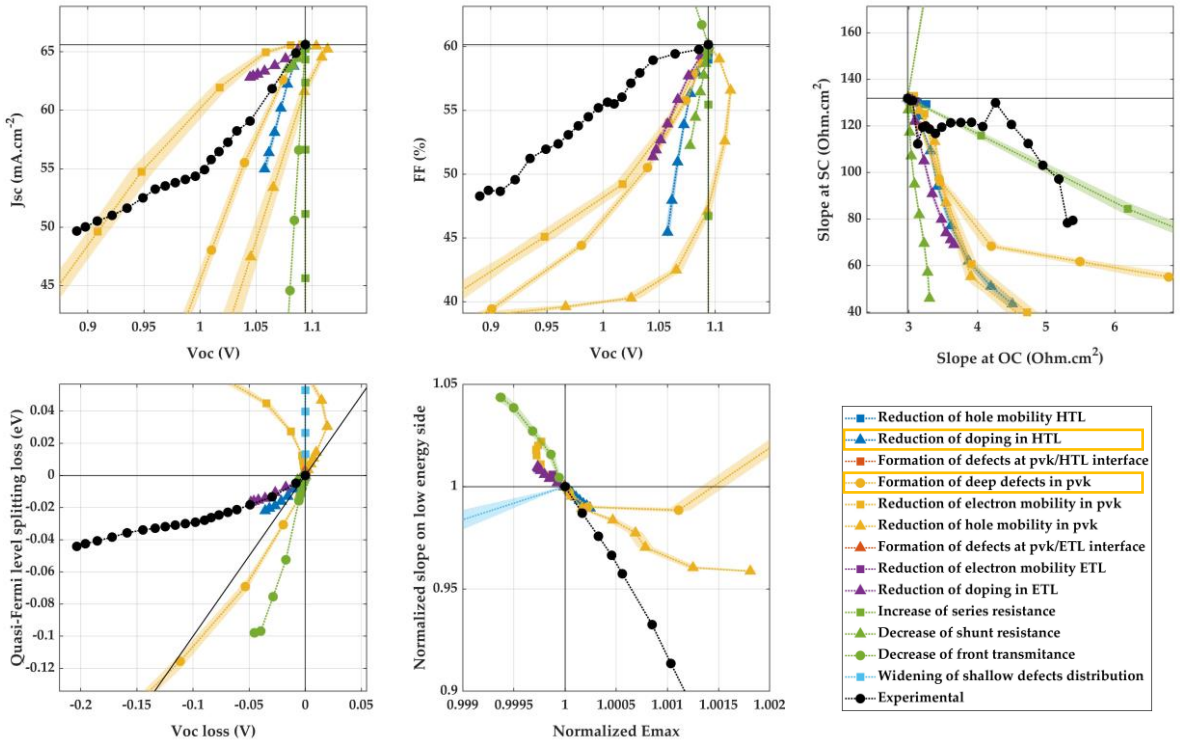

Figure 23. *Experimental degradation pathway of device JV-PL-1 and associated simulated mechanisms. Two mechanisms are compatible on all planes: formation of defects in the perovskite layer (yellow circles) and reduction of HTL doping (blue triangles).*

Device JV-PL-2:

JV-PL-2 has the same structure as previous device, with TiO_2 ETL and PTAA HTL. In in order to simulate degradation pathways, initial performances were reproduced with 114 sets.

Here again, combining JV and PL parameters in Figure 24 allows to point more confidently incompatible mechanisms. For instance, reduction of hole mobility in the perovskite layer (yellow triangles) is compatible with the experiment according to all JV parameters. However, it would induce a rise of both quasi-Fermi levels splitting and low energy side slope, which is opposite to experimental behavior.

As a result, reduction of HTL doping (blue triangles) is the most compatible mechanism. Notably, two further mechanisms can't be excluded with strong confidence. The reduction of hole mobility in HTL (blue squares) is also compatible on most planes, but with lower decrease of Voc. The reduction of ETL doping (purple triangles) is also mostly consistent, with only low increase of JV slope at OC and stronger decrease of quasi-Fermi levels splitting.

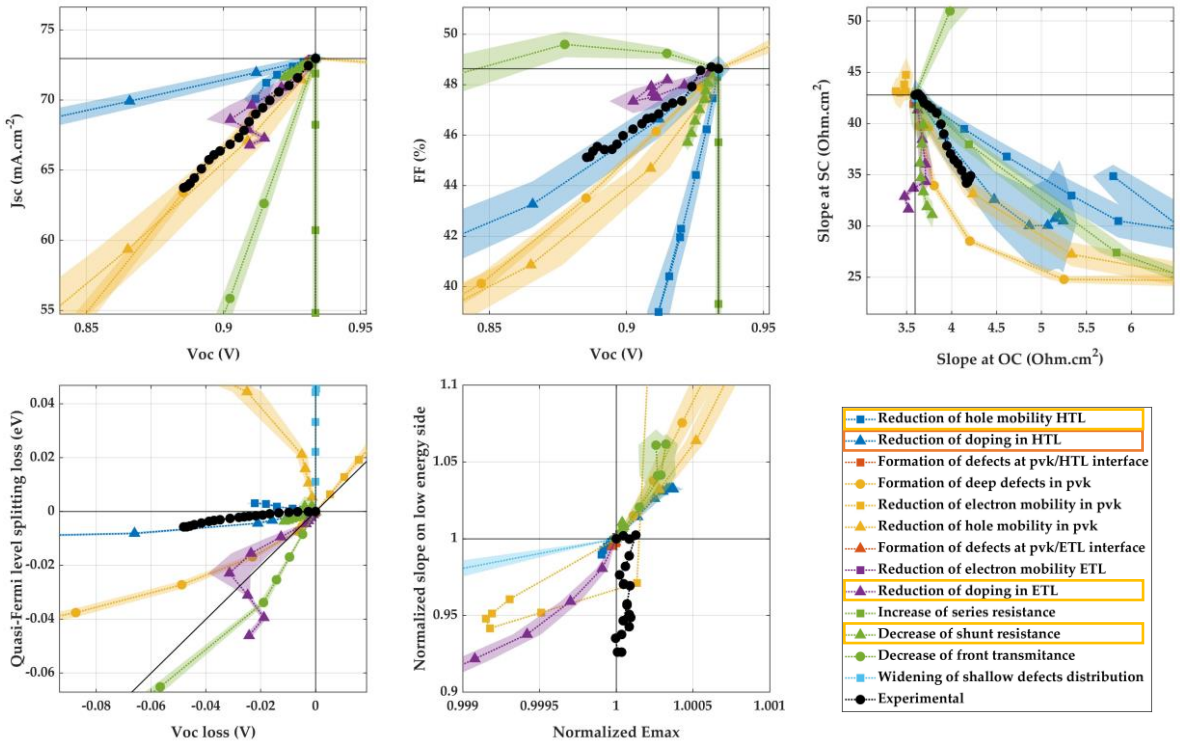

Figure 24. *Experimental degradation pathway of device JV-PL-2 and associated simulated mechanisms. Reduction of HTL doping (blue triangles) is the most compatible, but reduction of hole mobility in HTL (blue squares), reduction of ETL doping (purple triangles), or reduction of shunt resistance (green triangles) can't be totally excluded.*

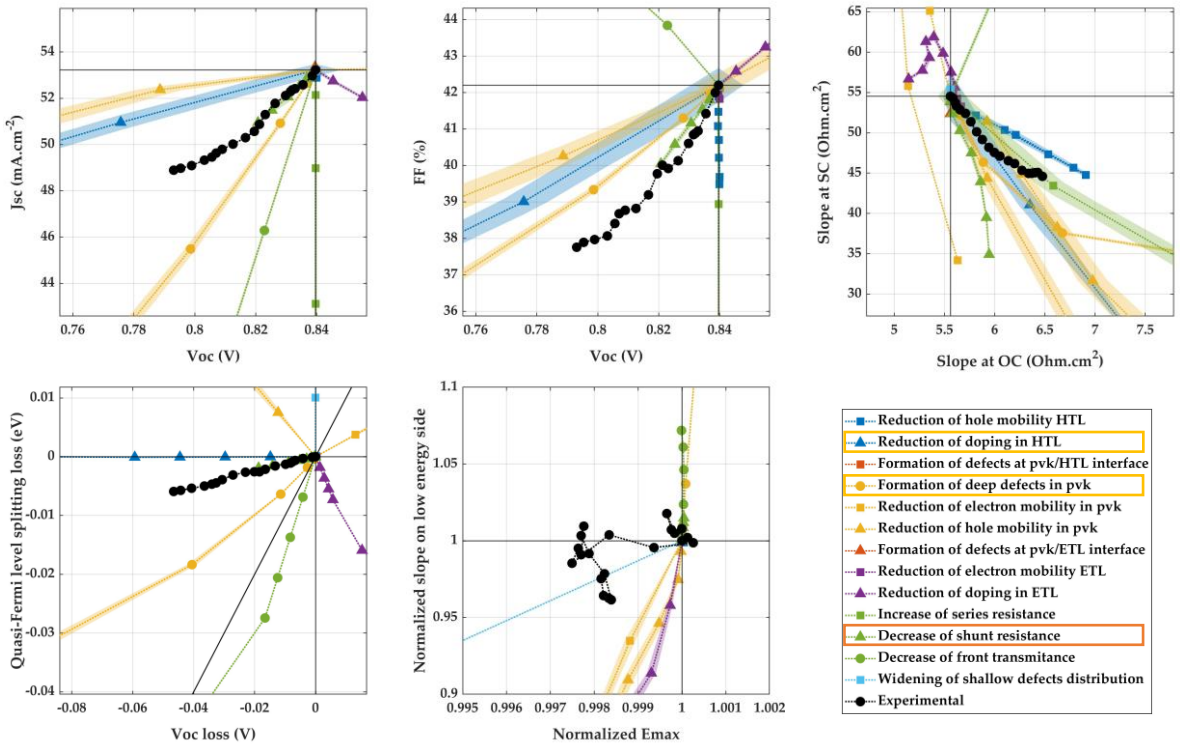

Figure 25. *Experimental degradation pathway of device JV-PL-3 and associated simulated mechanisms. Reduction of shunt resistance (green triangles) is the closest mechanism. Formation of defects in the perovskite layer (yellow circles) and reduction of HTL doping (blue triangles) are also compatible with experiment.*

Device JV-PL-3:

Initial performances of JV-PL-3, the last device with the same structure (TiO_2 ETL and PTAA HTL), were reproduced with 108 sets.

In Figure 25, the closest mechanisms is the reduction of shunt resistance (green triangles), however other mechanisms could also explain the experimental behavior: formation of perovskite defects (yellow circles) and reduction of HTL doping (blue triangles). Regarding the pathways in terms of PL spectrum slope versus position of the maximum, it is to note that in this example, even the range of variation of the slope is very low.

Device JV-PL-4:

The performances of device JV-PL-4 at 25 h were reproduced with 107 sets. Contrary to previous devices, JV-PL-4 was fabricated with SnO_2 ETL.

In Appendix D, Figure D13, reduction of electron mobility in perovskite (yellow squares) is compatible in terms of JV parameters but has to be excluded according to quasi-Fermi levels splitting evolution. In fact, reduction of ETL doping (purple triangles) or shunt (green triangles) could be compatible with the beginning of degradation, but simulations did not induce such a large drop of Voc.

It is to note that here interpretation is not easy: the non-monotonous drop of Jsc, associated to a rise of FF is not compatible with any simulated mechanism. Furthermore, the interpretation of the rest of the experimental degradation cannot confidently by analyzed with the initial point chosen here, before the Jsc drop.

Because previous results in Appendix D, Figure D13 were difficult to interpret, the same experimental degradation experiment was considered only starting at 125 h to avoid the initial non monotonous behavior. The same simulation procedure has therefore been applied again and initial performances at 125 h were reproduced with 114 sets.

In Figure 26, however, no simulated mechanism explains the large experimental drop in Voc. Again, although slightly compatible in terms of JV performances, reduction of perovskite electron mobility (yellow squares) has to be excluded because of quasi-Fermi levels splitting behavior. As a result, only a decrease of shunt resistance (green triangles) might not be to exclude, although this mechanism does not explain well the Voc behavior.

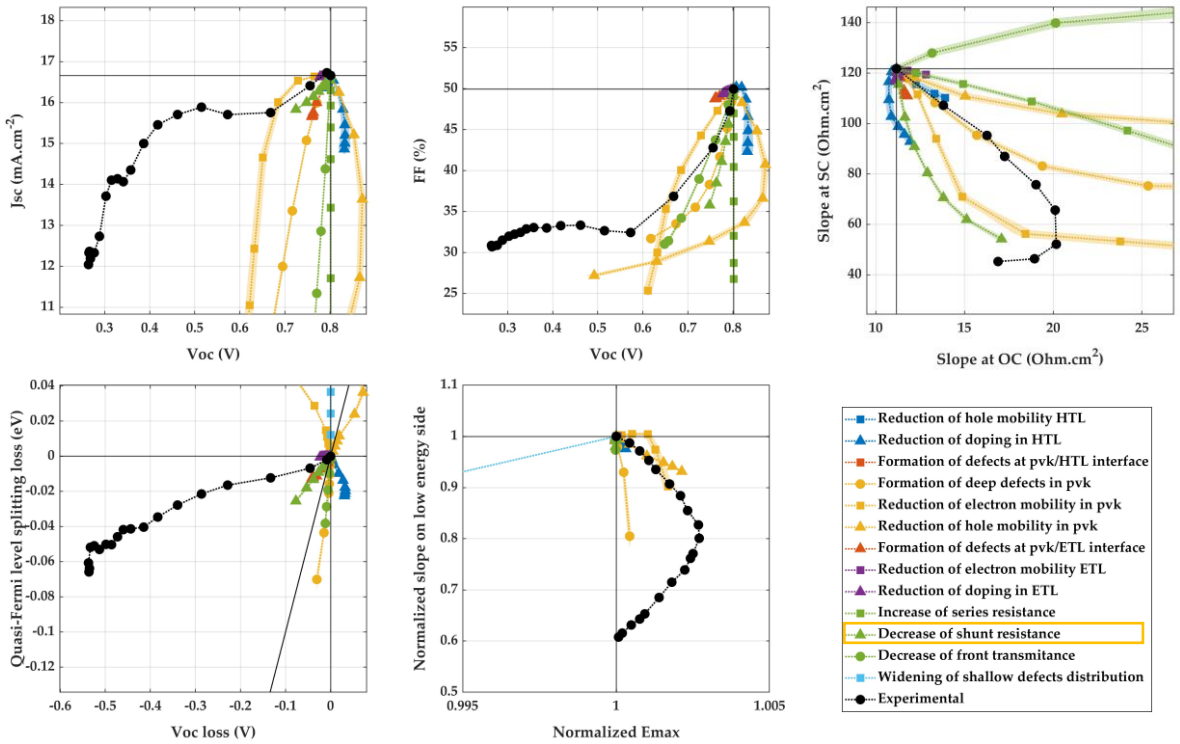

Figure 26. *Experimental degradation pathway of device JV-PL-4 (starting at 125 h) and associated simulated mechanisms. No mechanism reproduces the large Voc drop accompanied with stable Jsc. Decrease of shunt resistance (green triangles) might not be excluded.*

Device JV-PL-5:

The last device investigated in this sub-section, JV-PL-5, was fabricated with TiO_2 ETL and Spiro-MeOTAD HTL. Its initial performances at 20 h were reproduced with 131 sets.

In Appendix D, Figure D14, the non-monotonous behavior of the Jsc makes it difficult to point out compatible mechanisms. In fact, no mechanism induces such stable Jsc for the same Voc loss. The reduction of HTL doping (blue triangles), which could be slightly compatible in this plane clearly induces no reduction of PL intensity, contrary to the experiment.

Only the very first experimental points of could be associated to compatible simulated mechanisms. The formation of defects in the perovskite layer (yellow circles) and the reduction of doping in ETL (purple triangles) actually reproduce the experimental behavior in term of FF and JV slopes. Even the initial decrease of quasi-Fermi levels splitting is compatible.

However, the variations of PL peak slope and position might contradict this analysis. The formation of defect would induce an increase of the slope, and the reduction of ETL doping a peak shift towards lower energies, both trends are opposite to the experiment. As mentioned previously, the ranges of variations for both quantities are significantly small (especially Emax), making their interpretation less reliable. Therefore, both mechanisms are not totally excluded.

The non-monotonous Jsc behavior of device JV-PL-5 cannot easily be attributed to any simple mechanism and could even be related to external factors such as

variations of illumination intensity. Therefore, the experimental behavior recorder after 85 h is also studied. Likewise for device JV-PL-4, the whole procedure has been applied a second time, and 105 sets reproduce the initial performances.

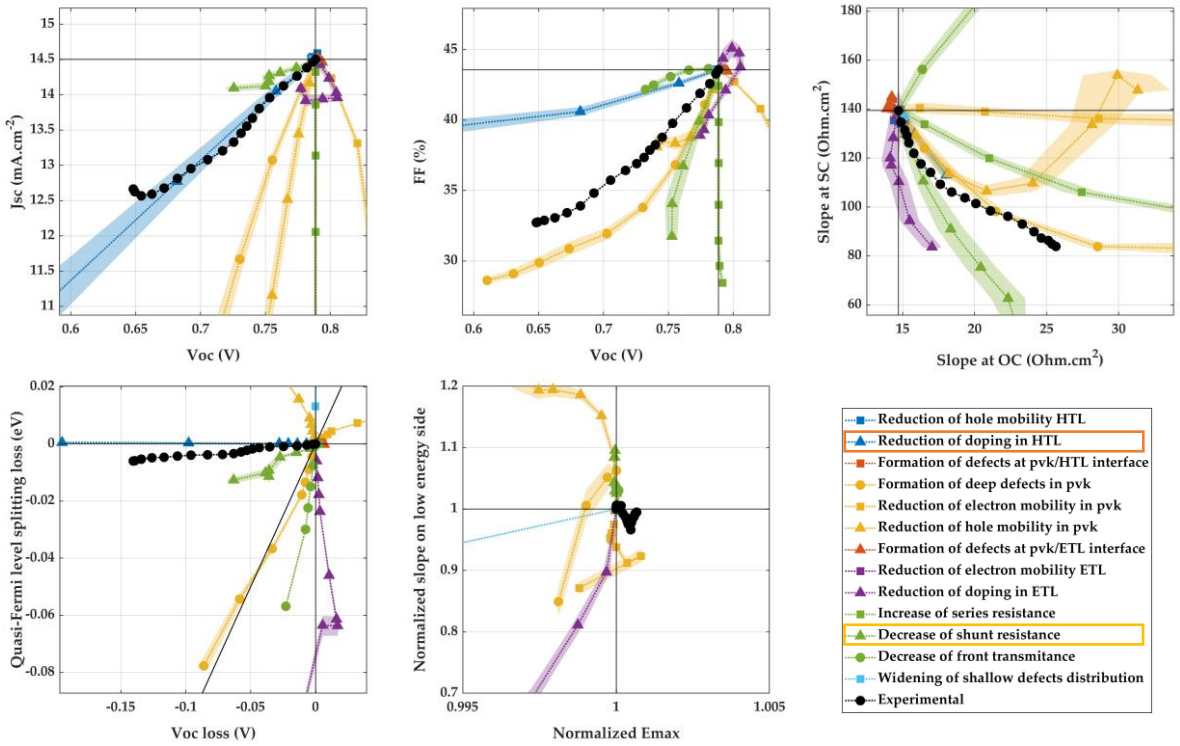

Figure 27. *Experimental degradation pathway of device JV-PL-5 (starting at 85h) and associated simulated mechanisms. Reduction of doping in HTL (blue triangles) is close to the experiment but decrease of shunt resistance (green triangles) is also compatible.*

This time, the experimental pathway in Figure 27 can be more confidently associated to simulated mechanisms. First, the reduction of doping in HTL (blue triangles) is compatible on all planes, also explaining the stable quasi-Fermi levels splitting with strong Voc loss. However, it is to note that the reduction of shunt resistance (green triangles) is also compatible and should not be excluded.

Intermediate conclusions:

First, the analyses of both last devices showed that interpretation of experimental degradation in Figure 26 and Figure 27 is clearer, respectively for devices JV-PL-4 and JV-PL-5. This illustrates again that shorter and monotonous degradation sequences are more easily compared to the simulated unitary degradation mechanisms, as mentioned in previous sub-section.

Also, the different variations of quasi-fermi level splitting (reduction of mobilities or increase of defect density in perovskite layer for instance) did allow to confidently exclude some mechanisms. Moreover, even if the slope on the low energy side of the spectrum and the position of the peak maximum do not vary significantly in most experimental and simulated cases, they could provide insights according to their

direction of variation. The five examples of devices investigated here demonstrate well the interest of coupling characterization techniques.

It is to note that the simulation results provide greater insights on the distinction of mechanisms than by only comparing experimental degradation pathways. For instance, the distinct behavior of JV-PL-1 from JV-PL2 and JV-PL-3 in Figure 8 has been envisaged in Section 4.2 to be linked to a distinct cause. However, simulated pathways show here that the same mechanism, the reduction of HTL doping, could induce a pronounced loss of PL intensity versus Voc (for device JV-PL-1) as well as an almost stable emission (devices JV-Pl2 and JV-PL-3). This demonstrates that degradation pathways depend on the initial performances of the solar cell, and how reproducing this initial point is crucial for the present work.

The identified compatible mechanisms for the samples investigated in this sub-section are summarized in Table 3, along with characteristics of the devices and their characterization conditions. As a reminder, they were all aged under the same conditions: dark, 85 % R.H. and 65 °C (see Section 2.4.2 for all details).

Table 3. *Mechanisms associated to the devices investigated in this sub-section. Red: closest mechanism: experimental and simulated pathways superpose significantly. Yellow: compatible mechanism: experimental and simulated pathways follow mostly similar trends. Green: excluded mechanism: experimental and simulated pathways are significantly different.*

Device	**JV-PL-1**	**JV-PL-2**	**JV-PL-3**	**JV-PL-4**	**JV-PL-5**
ETL / HTL	TiO2 / PTAA	TiO2 / PTAA	TiO2 / PTAA	SnO2 / PTAA	TiO2 / Spiro
HTL hole mobility					
HTL doping					
Pvk-HTL interface					
Pvk defects					
Pvk electron mobility					
Pvk hole mobility					
Pvk-ETL interface					
ETL electron mobility					
ETL doping					
External shunt resistance					
External series resistance					
Front transmittance					

Interestingly, it appears that a loss of HTL doping is compatible for all four samples with TiO_2 ETL (JV-PL1 to JV-PL-3 and JV-PL-5). Of course, other mechanisms are compatible, such as the formation of defects in the perovskite for devices JV-PL-1 and JV-PL-3, or a reduction of shunt resistance.

These devices were fabricated with two HTL materials, PTAA for devices JV-PL1 to JV-PL-3 or Spiro-MeOTAD for JV-PL-5. However, the low stability of both organic HTL materials has already been reported, and their sensitivity to heat and moisture demonstrated [9].

In fact, the only sample fabricated with a different ETL (SnO_2) is JV-PL-4. It is also the only sample from which the degradation is not compatible with HTL related mechanisms. Therefore, a protective effect of SnO_2, retarding HTL degradation, could be envisaged. For instance, its better resistance to water ingress (lower hygroscopicity) compared to TiO_2 has already been considered to be a cause of improved device stability [10], [11].

Finally, this second study of samples fabricated at IPVF stresses again the importance of the transporting layers for the stability of perovskite solar cells. Importantly, exhaustive exploration of materials combinations and higher batch statistics are necessary to demonstrate the higher stability of SnO2 based samples. Applying the method exposed here would then provide stronger conclusions on the processes degrading the solar cells performances and significantly help to point the most stable structure.

Section key points:

- Non-monotonous degradation sequences can't be clearly interpreted, mostly because simulated processes are monotonous.
- Combining JV and PL allow to distinguish mechanisms that have similar pathways in terms of only JV parameters.
- Simulation results are necessary to achieve the distinction between experimental pathways of distinct devices: because of different starting points, the same process can induce different pathways.
- Degradation of device having a TiO2 ETL might have been caused by the HTL layer, regardless of its nature (PTAA or Spiro).
- The sample fabricated with a SnO2 ETL is the only one not being compatible with HTL degradation.
- A protective effect of the HTL by SnO2 could be envisaged. It has been reported in literature to be less hygroscopic and more stable than TiO2.
- Complementary analyzes are necessary to demonstrate this hypothesis and the method exposed here could support a more exhaustive study.

Chapter conclusion

In this chapter, degradation mechanisms of perovskite solar cells have been investigated by analyzing the available experimental results summarized in section 2.4. They all consist in records of the evolution of optoelectrical parameters (derived from JV curves or PL spectra) over time, under constant conditions. Two approaches were employed to model and analyze degradation

First, kinetics of the optoelectrical parameters over time at several temperatures are investigated. Simple models for the speed of chemical reactions, with several reaction orders, were considered. Results showed that all orders could be fitted with similar quality, and no clear linear dependence was found on the Arrhenius plots.

In fact, perovskite solar cells are complex systems, and the degradation reactions might have complex impacts on recorded optoelectrical parameters. Furthermore, thermal activation studies assume that the same reaction is being observed at different temperatures. This cannot be assured with perovskite solar cells, where potential mechanisms are numerous. Finally, finding the activation energy of a given degradation process might be difficult to interpret, and would not allow to determine its nature, for instance.

Therefore, another approach has been employed for most of the work presented here. It is based on considering degradation through the evolution of the mutual correlation of recorded optoelectrical parameters. This produces degradation pathways that are independent from time, and therefore independent from any activation process (through temperature, illumination, humidity, etc.). In fact, these pathways are intrinsic characteristics of the mechanisms (for a given device) and can be used to distinguished them.

Experimental results can be represented in the form of pathways and comparing them provides insights on the potential common or distinct nature of underlying mechanisms. However, the degradation pathways depend on the initial properties of the device. In fact, it has been showed that the same mechanism could induce distinct pathways. Experimental results that seemed following distinct pathways has been finally showed to be compatible with the same mechanism.

Therefore, it is highly important to compare experimental results to simulated pathways that have been specifically tailored for the considered sample. This is why part of this work has been done on reproducing accurately the initial performances of the considered devices.

Importantly, this approach has been applied in a first step to experimental measurements reported in literature. This allowed to compare results and demonstrate the validity of the novel approach employed here. Interestingly, the method employed here directly address the cause of the performance losses. It can therefore provide complementary insights to analyses based on materials characterizations before and after degradation. Such results only point out the material properties that concomitantly changed along performances degradation.

Finally, aging experiments performed at IPVF were investigated. More exhaustive data on the perovskite solar cells materials and fabrication techniques were available. Importantly, the full current-voltage curves were available, allowing to consider slopes at OC and SC, and photoluminescence emission spectra were simultaneously recorded in some cases.

Results on the first set of samples, prepared with four variations in the deposition method of the perovskite layer, showed that no technique significantly improved the solar cells stability. On the contrary one variant (perovskite solution prepared on the day of deposition, with pre-heating) did degrade significantly faster than the others. Results obtained here indicate that the perovskite layer might be in cause.

Devices prepared with other techniques do not necessarily follow the same mechanisms. However, results show that their perovskite layer might have remained stable, or at least is not in cause for the recorded degradation of performances.

Finally, both devices with solution prepared the day before and pre-heated showed an experimental degradation that was not compatible with any simulated mechanism in this work.

The second set of samples contained devices with various structure (different HTL and ETL materials). Notably, they were fabricated with two HTL materials, PTAA or Spiro-MeOTAD and the sensitivity of both organic materials to heat and moisture has already been reported in literature. These samples were investigated under the same conditions, through coupled JV and PL measurements in a climatic chamber (65 °C and 85 % R.H.).

Interestingly, it appears that among compatible mechanism found here, a loss of HTL doping is common to all four samples with TiO_2 ETL. In fact, the only sample fabricated with a different ETL (SnO_2) is also the only sample from which the degradation is not compatible with HTL related mechanisms. Therefore, a protective effect of SnO_2 (through lower hygroscopicity than TiO_2), retarding HTL degradation, could be envisaged. Here, the complementarity with other characterization techniques could be particularly useful to investigate deeper this interpretation.

The work presented in this chapter show how modeling can be employed to take the full advantage periodic measurements. JV characteristics were investigated, coupled with PL or not, and further techniques could be envisaged, such as capacitance spectroscopy, UV-visible spectroscopy or EQE measurements. It has been showed here how coupling techniques can help to distinguish pathways through new planes. Furthermore, this would constraint more the reproduction of the degradation starting point, by considering more comprehensively the associated performances. As a result, the confidence in the applicability of the simulated pathways to the specific considered sample would be improved.

Finally, degradation pathways defined here, as being independent from time, easily provide intrinsic characteristics of the degradation mechanisms. They provide a powerful tool to compare simulated and experimental results, and to distinguish chemical-physical processes.

References

[1] J. Lim *et al.*, "Kinetics of light-induced degradation in semi-transparent perovskite solar cells," *Solar Energy Materials and Solar Cells*, vol. 219, p. 110776, 2021, doi: 10.1016/j.solmat.2020.110776.

[2] J. Kim, N. Park, J. S. Yun, S. Huang, M. A. Green, and A. W. Y. Ho-Baillie, "An effective method of predicting perovskite solar cell lifetime–Case study on planar CH3NH3PbI3 and HC(NH2)2PbI3 perovskite solar cells and hole transfer materials of spiro-OMeTAD and PTAA," *Solar Energy Materials and Solar Cells*, vol. 162, pp. 41–46, 2017, doi: 10.1016/j.solmat.2016.12.043.

[3] J. P. Bastos *et al.*, "Model for the Prediction of the Lifetime and Energy Yield of Methyl Ammonium Lead Iodide Perovskite Solar Cells at Elevated Temperatures," *ACS Appl Mater Interfaces*, vol. 11, no. 18, pp. 16517–16526, 2019, doi: 10.1021/acsami.9b00923.

[4] O. Haillant, D. Dumbleton, and A. Zielnik, "An Arrhenius approach to estimating organic photovoltaic module weathering acceleration factors," *Solar Energy Materials and Solar Cells*, vol. 95, no. 7, pp. 1889–1895, 2011, doi: 10.1016/j.solmat.2011.02.013.

[5] M. A. Green, "Accuracy of analytical expressions for solar cell fill factors," *Solar Cells*, vol. 7, no. 3, pp. 337–340, 1982, doi: 10.1016/0379-6787(82)90057-6.

[6] J. Peng *et al.*, "Nanoscale localized contacts for high fill factors in polymer-passivated perovskite solar cells," *Science (1979)*, vol. 371, no. 6527, pp. 390–395, 2021, doi: 10.1126/science.abb8687.

[7] N. Li *et al.*, "Microscopic Degradation in Formamidinium- Cesium Lead Iodide Perovskite Solar Cells under Operational Stressors," *Joule*, vol. 4, no. 8, pp. 1743–1758, 2020, doi: 10.1016/j.joule.2020.06.005.

[8] M. Chen *et al.*, "Inverted CsPbI2Br perovskite solar cells with enhanced efficiency and stability in ambient atmosphere via formamidinium incorporation," *Solar Energy Materials and Solar Cells*, vol. 218, p. 110741, 2020, doi: 10.1016/j.solmat.2020.110741.

[9] F. M. Rombach, S. A. Haque, and T. J. Macdonald, "Lessons learned from spiro-OMeTAD and PTAA in perovskite solar cells," *Energy Environ Sci*, vol. 14, no. 10, pp. 5161–5190, 2021, doi: 10.1039/d1ee02095a.

[10] Jiaxing Song *et al.*, "Low-temperature SnO2-based electron selective contact for efficient and stable perovskite solar cells," *J Mater Chem A Mater*, vol. 3, no. 20, pp. 10837–10844, 2015, doi: 10.1039/C5TA01207D.

[11] L. Xiong *et al.*, "Review on the Application of SnO2 in Perovskite Solar Cells," *Adv Funct Mater*, vol. 28, no. 35, p. 1802757, Aug. 2018, doi: 10.1002/adfm.201802757.

Chapter 5: Principal component analysis

Table of contents

Chapter introduction

The objective in this chapter is to help designing further simulation studies by two ways: first, reducing the number of necessary input parameters and second, identifying the most important ones.

First, meta-parameters, defined as combinations of material parameters that actually define the solar cell behavior are considered. In Section 5.1, an analytical model is employed to propose candidates meta-parameters.

Important, results exposed in the previous chapter were all based on a statistical approach, and a large number of simulations was performed. For each simulation, inputs and outputs were stored together in the database described in Section 5.2.

In order to assess the validity of candidate meta-parameters to define the solar cell performance, their correlation to the output optoelectrical parameters is investigated in Section 5.3.

Furthermore, Principal Component Analyses (PCA) are employed in this work to investigate the statistics of the available database. The mathematical framework to determine components is exposed in Section 5.4.

Finally this method is applied in Section 5.5 to subsets of the database, extracted by selecting entries having given output values. Two orthogonal configurations are employed by allowing all except one, or one variable output parameter. The first approach allows to point out the important input parameters, and the second to propose simple phenomenological models.

Chapter key points:

- Statistical approaches can be applied to databases of simulated configurations to help simplifying further studies.
- Meta-parameters are combinations of input parameters (dimensionless or not) that actually define the solar cell behavior.
- Analytical models can provide insights on the role of material parameters even in more complex numerical simulations.
- Principal components analyses provide components in the form of combinations of original variables. They are independent from each other and ranked in terms of importance.
- The statistics of the underlying input parameters, all allowing a fixed output value can be investigated through PCA. This allows to point out the important input parameters to focus on when designing simulations, or when developing solar cells.
- When performing PCA on entries having all output parameters fixed except one, the correlation of the first component with the variable output allows to propose simple phenomenological models.

5.1 What is a meta-parameter ?

It has been showed in the previous chapters that numerical simulations of perovskite solar cells provide insights on the degradation of their performances. However, a very large number simulations was necessary, because numerous input parameter combinations needed to be explored. In this chapter, methods to reduce the number of necessary parameters are explored.

Such simplification can be done by using meta-parameters. These are combinations of input parameters (dimensionless or not) that actually define the solar cell behavior. If such parameter exist, it is not necessary to explore combinations of the constitutive parameters, only the values of the meta-parameter.

An example is the diffusion length of carriers in a semi-conductor. It is based on the product of the diffusion coefficient and lifetime and defines the behaviors of the carriers. If this is a meta-parameter for the perovskite solar cells considered in this work, only one of the two material parameters need to be explored.

5.1.1 Meta-parameters derived from analytical solar cell model

The first approach to define meta-parameters is based on the model proposed in Section 1.1.4. Although it is established for a pn junction, without transport layers, it accounts for most physical phenomenon present in a perovskite solar cell. Moreover, its analytical nature directly provides combinations of material parameters that could be meta-parameters.

It expresses the output current produced by the solar cell through a sum of three terms, respectively accounting for photogeneration, recombination in the quasi neutral regions, and recombination in the space charge region [1], [2].

The photocurrent from the front n doped region is expressed as follows:

$$J_{G-nQNR} = q\phi \frac{\alpha L_p}{\alpha^2 L_p^2 - 1}\left(\frac{\frac{S_{front}L_p}{D_p} + \alpha L_p - \left(\frac{S_{front}L_p}{D_p} cosh\left(\frac{W_{nQNR}}{L_p}\right) + sinh\left(\frac{W_{nQNR}}{L_p}\right)\right) e^{-\alpha W_{nQNR}}}{\frac{S_{front}L_p}{D_p} sinh\left(\frac{W_{nQNR}}{L_p}\right) + cosh\left(\frac{W_{nQNR}}{L_p}\right)} - \alpha L_p e^{-\alpha W_{nQNR}}\right) \quad (1)$$

From this expression, already two meta-parameters can be identified: L_p and $\frac{S_{front}}{D_p}$, out of three material parameters. Also, the expression for the back p doped regions is almost symmetrical with respect to hole and electron parameters, see Section 1.1.4. Moreover, the photocurrent from the space charge region:

$$J_{G-SCR} = q\phi e^{-\alpha W_{nQNR}}\left(1 - e^{-\alpha(w_n + w_p)}\right) \quad (2)$$

Importantly, the expressions above are written for a monochromatic illumination, in fact, absorption coefficient (α) and photon flux (ϕ) are wavelength dependent. Therefore, each photocurrent has to be computed for each wavelength, and summed.

Moreover, the recombination current is also distinguished between quasi neutral regions and space charge region. For the first one, expressions are symmetrical with respect to hole and electron parameters, it is reported here for the front n doped region:

$$J_{R-nQNR} = q\frac{D_p n_i^2}{L_p N_D}\frac{\frac{S_{front}L_p}{D_p}cosh\left(\frac{W_{nQNR}}{L_p}\right)+sinh\left(\frac{W_{nQNR}}{L_p}\right)}{\frac{S_{front}L_p}{D_p}sinh\left(\frac{W_{nQNR}}{L_p}\right)+cosh\left(\frac{W_{nQNR}}{L_p}\right)}\left(e^{q\frac{V}{k_BT}}-1\right) \quad (3)$$

Finally, the expression of the recombination current in the space charge region is approximated by the product of an effective length, $\frac{(w_p+w_n)}{\frac{q\,V_{bi}}{k_BT}}$, and the maximum value of the recombination rate. This estimation overestimates SRH recombination, providing an upper limit of its value:

$$J_{R-SCR} = q\frac{1}{\tau_{SRH}}\frac{n_i}{2}\frac{(w_p+w_n)}{\frac{q\,V_{bi}}{k_BT}}e^{q\frac{V}{2k_BT}} \quad (4)$$

Importantly, the following quantities play a significant role in the above expressions. First, the size of the space charge region at n doped side (symmetrical expression for p doped side):

$$w_n = \sqrt{\frac{2\epsilon k_B T}{q}\frac{N_A}{N_D}\frac{1}{N_A+N_D}\,V_{bi}-V} \quad (5)$$

Moreover, the effective lifetime (τ_{eff}) accounts for both radiative and recombination processes, and is employed to compute the diffusion length (L):

$$\frac{1}{\tau_{eff}} = \frac{1}{\tau_{rad}}+\frac{1}{\tau_{SRH}} \quad (6)$$

$$L = \sqrt{D\cdot\tau_{eff}} \quad (7)$$

Expressions related to the front n doped side and holes minority carriers can mostly be symmetrically translated for the back p doped side and electron minority carriers. Similarly, the following discussion focuses on holes related quantities, but can be symmetrically transposed for electrons minority carriers.

From above photogeneration term, two dimensionless quantities appear: αL_p and $\alpha(\mathrm{w_n}+\mathrm{w_p})$. The first one arise from minority carriers' diffusion through the n quasi neutral region, and the second from absorption in the space charge region.

Furthermore, for the recombination and diffusion through the space charge regions, the ratio $\frac{W_{nQNR}}{L_p}$ appears. It relate the respective region size and minority carriers' diffusion length. Together with the quantity $\frac{D_p}{L_p N_D} = \frac{1}{N_D}\sqrt{\frac{D_p}{\tau_p}}$, they could be related to propagation of minority carriers in a doped semi-conductor.

Finally, the last meta-parameter is maybe the most obvious: the diffusion length $L_p = \sqrt{D_p \tau_p}$ which describes the transport of carriers.

These six examples of quantities are meta-parameters for a pn homojunction but could provide candidates for perovskite solar cells. In fact all translated meta-parameters candidates are listed in Table 1 and will be investigated in the following sections.

However, limiting transport processes differ in nip structures and pn junctions because there are no minority carriers in the intrinsic perovskite material. Therefore, hole diffusions lengths and coefficients are translated into electron ones but still associated to ETL doping level. Even if electrons are collected at front side, electron transport is limiting in the first case and hole transport in the second.

Importantly, the meta-parameter related to surface / interface defects is split into two versions for both carriers, because both densities play a role for recombination.

Table 1. *Meta-parameters established for a pn junction from an analytical model and translated candidates for perovskite solar cells.*

pn homojunction		**Perovskite solar cell**	
τ_{rad-p}	$L_{p-rad} = \sqrt{D_p \tau_{rad-p}}$	τ_{rad}	$L_{n-rad} = \sqrt{D_n \tau_{rad}}$
τ_{SRH}	$L_{p-SRH} = \sqrt{D_p \tau_{SRH}}$	τ_{SRH}	$L_{n-SRH} = \sqrt{D_n \tau_{SRH}}$
τ_{eff-p}	$L_p = \sqrt{D_p \tau_{eff-p}}$	τ_{eff}	$L_n = \sqrt{D_n \tau_{eff}}$
	αL_p		$\alpha_{pvk} L_n$
	$\frac{\alpha L_p}{\alpha^2 L_p^2 - 1}$		$\frac{\alpha_{pvk} L_n}{\alpha_{pvk}^2 L_n^2 - 1}$
	αw_{SCR}		$\alpha_{pvk} W_{pvk}$
	$\frac{S_{front} L_p}{D_p} \propto N_{t-front}\sqrt{\frac{\tau_{eff-p}}{D_p}}$		$N_{t-ETL/pvk}\sqrt{\frac{\tau_{eff}}{D_n}}$
			$N_{t-ETL/pvk}\sqrt{\frac{\tau_{eff}}{D_p}}$
	$\frac{W_{nQNR}}{L_p}$		$\frac{W_{pvk}}{L_n}$
	$\frac{D_p}{N_D L_p} = \frac{1}{N_D}\sqrt{\frac{D_p}{\tau_{eff-p}}}$		$\frac{1}{N_{D-ETL}}\sqrt{\frac{D_n}{\tau_{eff}}}$
	$\frac{N_A}{N_D}$		$\frac{N_{A-HTL}}{N_{D-ETL}}$
	$N_A + N_D$		$N_{A-HTL} + N_{D-ETL}$

5.2 Available dataset of simulations

In the previous sections numerous simulations have been executed to investigate the degradation of given solar cells. Reproducing their initial performances before degradation required to explore the input parameters space (see Section 3.2), and supplementary simulations have been made to consider several degradation mechanisms (see Section 3.4).

Several devices investigated in this work (JV-1.1 to 4.2) share the same architecture (TiO2 / triple cation perovskite / PTAA) and were simulated under the same conditions. As a result, all associated simulations share the same fixed parameters (bandgap energies, electronic affinities, etc.), see Table 2.

Table 2. *Fixed material parameters defining the solar cell structure and common to all simulation entries in the investigated dataset.*

Simulation parameter		**Value**
Illumination intensity		AM1.5g / 1000 $W.m^{-2}$
Temperature		20 °C
HTL (PTAA)	Thickness	100 nm
	Bandgap	3.2 eV
	Electron affinity	2.22 eV
	Relative permittivity	3.5
	CB / VB effective density of states	$2x10^{18}$ cm^{-3}
	Electron mobility	$1x10^{-2}$ $cm^2.V^{-1}.s^{-1}$
Perovskite	Thickness	500 nm
	Bandgap	1.62 eV
	Electron affinity	2.22 eV
	Relative permittivity	64
	CB / VB effective density of states	$2x10^{18}$ cm^{-3}
	Donor / acceptor density	0 cm^{-3}
Electron transporting material	Thickness	100 nm
	Bandgap	3.2 eV
	Electron affinity	2.22 eV
	Relative permittivity	3.5
	CB / VB effective density of states	$2x10^{18}$ cm^{-3}
	Hole mobility	$1x10^{-2}$ $cm^2.V^{-1}.s^{-1}$

As a result, statistical analyses will be performed over the associated dataset. In total, 51 053 entries are available, with different values for the varying parameters

(defect densities, carriers mobilities, etc.). Finally, parameters investigated here (inputs and outputs) are listed in Table 3, they will constitute the original variables of the principal component analyses.

Table 3. *Variables (simulation inputs and outputs) considered for the principal component analysis.*

Parameters		
Inputs	HTL	Hole mobility
		Acceptor density
	HTL / pvk interface	Defect density
	Perovskite	Electron mobility
		Hole mobility
		Deep defects density
	ETL / pvk interface	Defect density
	ETL	Electron mobility
		Donor density
Outputs		Voc
		Jsc
		FF

Importantly, this dataset was generated through the genetic algorithm developed to reproduce given experimental performances, and by gathering simulations of degradation mechanisms. As a result, the input parameters are not distributed uniformly, and this could impact the parameters correlations and principal components. Therefore, a subset is extracted by randomly picking entries at equal distance, in order to obtain a uniformly distributed dataset.

In the example of the full 51 053 entries dataset, 27 472 are uniformly extracted, distributions before and after extraction are reported in Appendix E, Figure E1. The variables are then normalized and considered in logarithmic scale, as explained in the previous section.

The advantage of extracting a uniformly distributed subset is already visible when computing the covariance matrix. When computed before extraction, as displayed in Appendix E, Figure E2, pollutions through correlations of materials parameters make the interpretation less reliable.

However, the covariance matrix in Figure 1, on the uniformly distributed subset, provides insights on the importance of material parameters to define the solar cell performances. For instance, the defect density in the perovskite layer is strongly anti-correlated with Voc. This is due to the fact that non radiative recombination impact the Voc strongly. Interestingly, it appears that the perovskite hole mobility is much more correlated to outputs than electron mobility. Moreover, HTL related parameters play a more significant role than ETL properties. This is most probably related to fact that devices are illuminated through their ETL side. Carriers are photo-generated near

this interface and as result, transport properties of holes, which has to cross the whole perovskite layer, are more impacting performances.

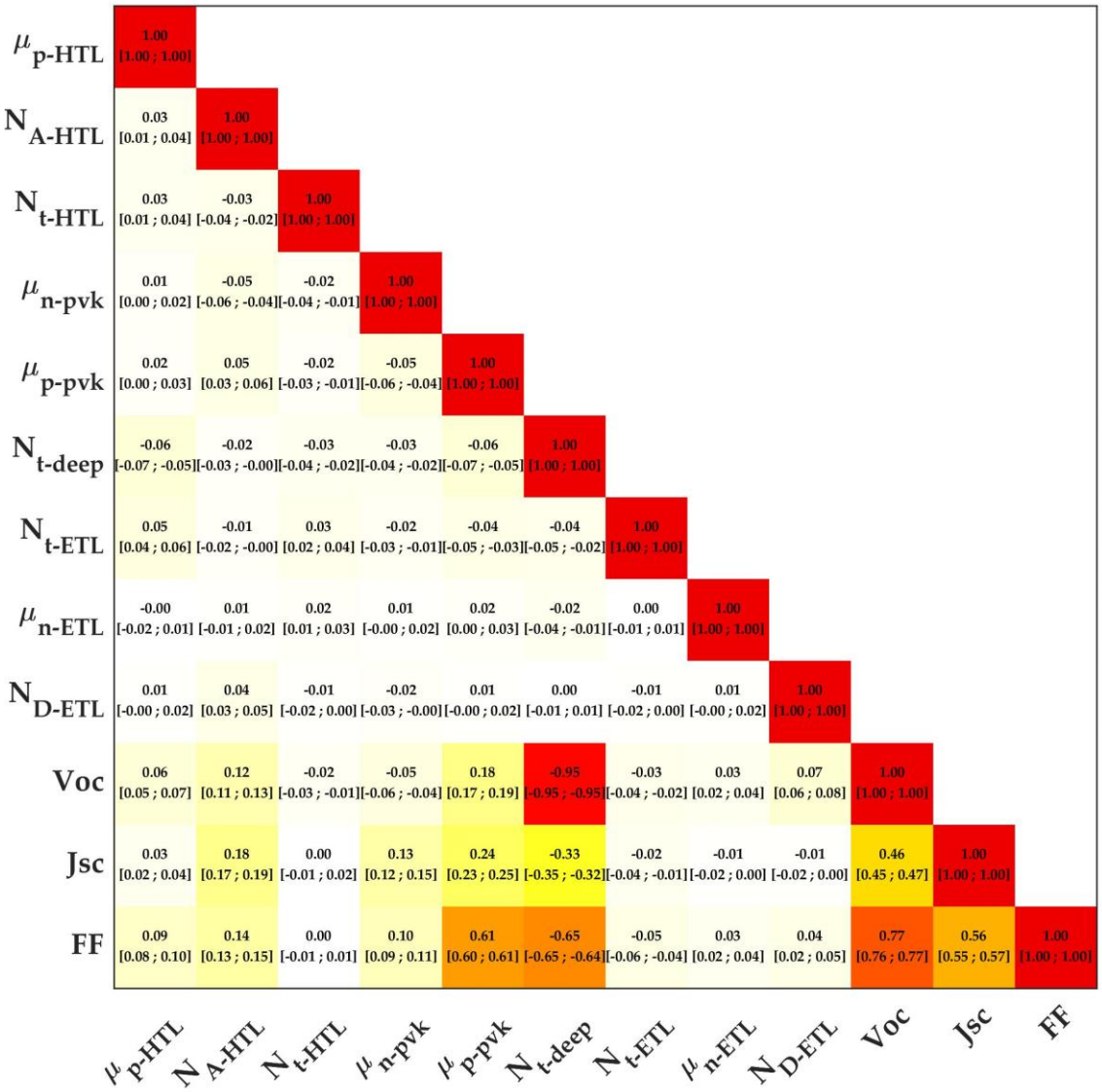

Figure 1. *Covariance matrix of the uniformly distributed subset (27 472 entries) for all variables. Associated 95 % confidence interval is in brackets.*

5.3 Assessment of meta-parameters candidates

The meta-parameters candidates established in Section 5.1 are investigated here by considering their correlations with the output optoelectrical parameters: Voc, Jsc and FF. This provides a quantification of their relation to the performances of the solar cell. Therefore, for each entry of the uniformly distributed subset described in Section 5.2, the associated values of meta-parameters candidates is computed. The covariance matrix is then computed, and relevant elements are reported in Figure 2. Importantly, the logarithmic value of the meta-parameters has been considered.

SRH diffusion lengths are always significantly more correlated to the outputs than their radiative recombination counterparts. This is consistent with a behavior of the simulated solar cells being more dependent on trap assisted than radiative recombination.

Furthermore, consistency with previous covariance matrix is also illustrated by the larger correlation of holes transport related meta-parameters, than electron related ones. The SRH lifetime and associated diffusion lengths are clear examples.

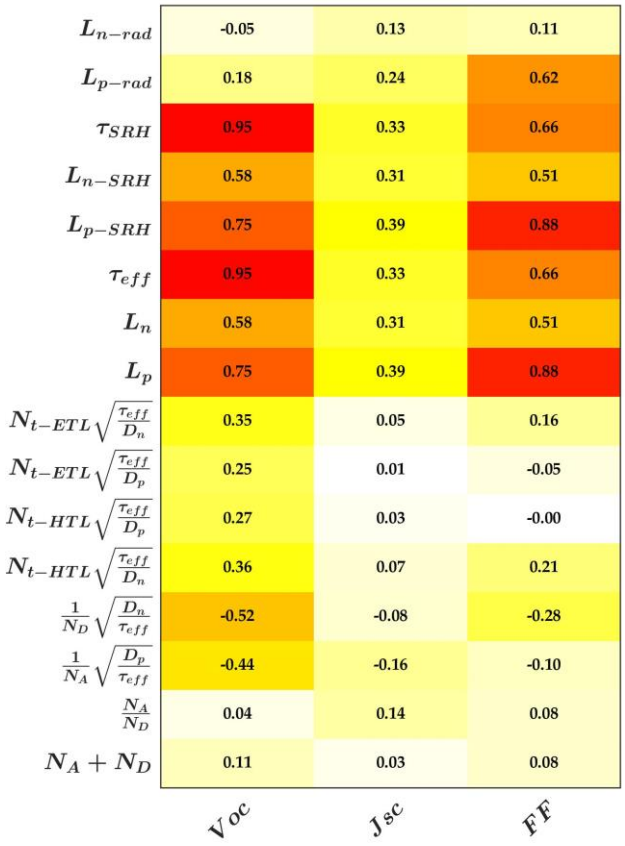

Figure 2. *Correlation coefficients of meta-parameters candidates with output optoelectrical parameters.* N_{t-ETL} *and* N_{t-HTL} *are the defect densities at the ETL-pvk and HTL-pvk interfaces respectively, and* N_D *and* N_A *the doping levels in ETL and HTL, respectively.*

It is to note that in the available database, no variation of absorption coefficient has been explored, therefore, associated meta-parameters can't be properly assessed.

Finally, the characteristics of HTL and ETL are only grasped by the meta-parameters considered here through their doping levels. Their ratio appear not to be correlated with outputs in Figure 2, and other meta-parameters including these quantities might not be more instructive on the role of the ETL and HTL.

This section shows how an analytical model can help to obtain useful meta-parameters. For instance, the diffusion length in the perovskite layer (associated to SRH lifetime) seem to be a very good indicator. However, because assumptions are necessary to derive analytical expressions, the model employed here is applied to a pn homojunction. As a result, specific aspects of the perovskite solar cell, such as the nature of the ETL and HTL are not properly grasped here. Therefore, principal component analyses will be performed in the next section to investigate meta-parameters in a more statistical oriented approach.

5.4 Mathematical formalism of principal component analysis

The principal component analysis is a common technique employed to reduce the number of variables in multidimensional datasets[3]–[7]. The principle is to do a linear transformation of the dataset variables towards new coordinates[8]. These new variables are as much decorrelated as possible, and they are called the principal components. Importantly, they are also ranked in terms of explained fraction of dataset variance. Therefore, they will be employed to determine the most significantly varying quantities in various subsets in the following sections.

5.4.1 General case

The problem can be expressed in terms of vector spaces, and the new components constitute an orthonormal basis of the dataset space. Finding this family is therefore done by performing the singular-value decomposition of the $m \times n$ rectangle matrix, associated to the m realizations of n variables of the dataset.

This matrix is noted X, and the singular value decompositions gives [8]:

$$X = P\Delta Q^T \quad (8)$$

P and Q are respectively $m \times m$ and $n \times n$ square matrices of singular vectors. Both constitute orthonormal bases of their respective spaces.

Importantly, Q defines the composition of the new components in terms of original variables: it is the projection matrix. The values of the realizations in terms of the new components (called factor scores) is expressed by the $m \times n$ matrix F:

$$F = P\Delta = XQ \quad (9)$$

Not all components have the same importance, and this is quantified through the fraction of variance they contain from the whole dataset. By using the orthonormal property of P, the covariance of F is expressed as [8]:

$$Cov(F) = F^T F = \Delta^T P^T P \Delta = \Delta^2 \quad (10)$$

The variance of the component i is the square of the associated singular value:

$$Var(F_i) = d_i^2 \quad (11)$$

Finally, the fraction of total variance explained by the component:

$$\frac{Var(F_i)}{\sum_{i=1}^{n} Var(F_i)} = \frac{d_i^2}{\sum_{i=1}^{n} d_i^2} \quad (12)$$

This demonstrates how the diagonal matrix Δ is employed to rank the components. The "principal" components are the ones having the largest d_i^2 value and containing the largest fraction of total variance.

Instead of performing the singular decomposition of X, the components can also be obtained by diagonalizing its covariance matrix. In fact, this square matrix can be expressed as:

$$Cov(X) = X^T X \quad (13)$$
$$= Q\Delta^T P^T P \Delta Q^T \quad (14)$$
$$= Q\Delta^2 Q^T \quad (15)$$

Therefore, the eigen values of $Cov(X)$ are the squared singular values of X, and the eigenvectors are the singular vectors in Q, defining the composition of the principal components.

5.4.2 Vector spaces associated to perovskite solar cells simulations

In this work, the dataset is composed of simulation input and output parameters (for instance defect density and Voc). In total, n different parameters are considered and are available for m realizations (from m simulations).

Furthermore, the data is centered and reduced in order to use dimensionless quantities and avoid being impacted by numerical un-balance between variables. Very importantly, the variables are considered through their log value, being the quantity actually centered and reduced. This will allow to express the components, that are linear combinations, in terms of products of physical quantities. Without this step, sums of defect densities with carrier mobilities could not be physically interpretable for instance. Moreover, material parameters values explored in the database cover several orders of magnitude, which have already been discretized in logarithmic scale as exposed in Section 3.1.

Therefore, with $\overline{\ln X_\iota}$ and σ_{lnX_i} being respectively the mean value and standard deviation of $\ln X_i$, the following expression of $\widetilde{X_\iota}$ is employed:

$$\widetilde{X_\iota} = \frac{ln\, X_i - \overline{ln\, X_\iota}}{\sigma_{lnX_i}} \quad (16)$$

As a result, the values of the components, obtained by analyzing the variables $\widetilde{X_\iota}$ are expressed as:

$$F_k = \sum_{i=1}^{n} \widetilde{X_\iota} \cdot q_{i,k} \quad (17)$$
$$= \sum_{i=1}^{n} \frac{ln\, X_i - \overline{ln\, X_\iota}}{\sigma_{lnX_i}} q_{i,k} \quad (18)$$
$$= ln\left(\prod_{i=1}^{n} X_i^{\frac{q_{i,k}}{\sigma_{lnX_i}}}\right) - \sum_{i=1}^{n} \frac{\overline{ln\, X_\iota}}{\sigma_{lnX_i}} q_{i,k} \quad (19)$$

Finally, this shows the framework of the analyses done further in this chapter. The importance of the components will be assessed through their associated singular value and explained fraction of total variance and composition of the first component will be used to point out the nature of the important variables when simulating the behavior of perovskite solar cells. Furthermore, the associated products of physical quantities will potentially provide meta-parameters that could be employed to elaborate simpler models to describe the solar cells performances.

5.5 Principal components extracted from sub-datasets

In this section, subsets of the main simulation dataset exposed above are considered. Here, output variables are not included in the analysis in order to focus on the correlation of the material parameters. Two complementary approaches are considered to select useful subsets, based on outputs.

First, a fixed value of one optoelectrical parameter, for instance Voc, is considered. The subset is therefore constituted of all available input configurations compatible with the considered Voc value. The statistics of these input parameters are investigated through principal component analyses.

In a second step, the orthogonal subset is defined by fixing all output variables, except one. Here, all entries of subsets have for instance the same Jsc and FF, but any Voc value. Again, principal components are employed to investigate the relevant input parameters.

5.5.1 Fixed value for one optoelectrical parameter

In this section, specific subsets of the global database are defined by gathering all entries having the same value for a given output parameters. For instance, all simulations for which output Voc is 1.05 V. The objective is then to investigate the distributions of input parameters allowing this Voc value. Studying their correlations is expected to point out the most relevant input parameters under the Voc value constraint.

The approach is first illustrated in a simple and favorable case. This allows to analytically express the expected relationship between the composition of the first component, and the input parameters. Details are exposed in Appendix E, together with examples.

The following expression is considered, where Y is the single output, and A, B and C the inputs:

$$Y = ln\left(A^{\alpha} \cdot B^{\beta} \cdot C^{\delta}\right) \quad (20)$$

α, β and γ are fixed parameters, and their relation to the PCA results is investigated.

The simple model can be thought as a very simple expression describing a relationship similar to the dependence of Voc to dark saturation current and Jsc in a single diode model. For instance, if SRH recombination is predominant:

$$Voc = nk_BT\ ln\left(\frac{J_G}{J_0}\right) \approx 2\ k_BT\ ln\left(\frac{J_G}{q\frac{1}{\tau_{SRH}}\frac{n_i}{2}\frac{k_BTw_{SCR}}{q\ V_{bi}}}\right) \quad (21)$$

The principal component analysis is then performed over a database of (A, B, C) triplets, all associated to the same Y value. Importantly, the principal component analysis is performed over normalized values, as exposed in Section 5.4.2: for instance

$\tilde{A} = \frac{ln\,A - \overline{ln\,A}}{\sigma_{ln\,A}}$. In the associated space, the first component is associated to the direction containing in which data varies the most, described by the vector: $\begin{pmatrix} q_{A,1} \\ q_{B,1} \\ q_{C,1} \end{pmatrix}$. Moreover, the reduced database investigated here has been precisely defined through a fixed value of the output, the orthogonal directions to the first component should therefore provide insights on the relationship with the output.

In fact, the ensemble of orthogonal directions to a vector define a hyperplane, expressed as follow in an affine space:

$$\tilde{A}q_{A,1} + \tilde{B}q_{B,1} + \tilde{C}q_{C,1} = ln\left(A^{\frac{v_{A,j}}{\sigma_{ln\,A}}} \cdot B^{\frac{v_{B,j}}{\sigma_{ln\,B}}} \cdot C^{\frac{v_{C,j}}{\sigma_{ln\,C}}}\right) + C_2 = C_1 = f(Y) \quad (22)$$

C_1 is a constant defined by the fixed output value, and C_2 contains the term $\sum_i q_{i,j} \frac{\overline{ln\,X_i}}{\sigma_{ln\,X_i}}$. Importantly, f is the unknown function relating C_1 to the fixed output value.

By differentiating both sides of this expression with respect to A, B or C, the following relations can be obtained (details of the derivation are reported in Appendix E):

$$\frac{\frac{v_{A,j}}{\sigma_{ln\,A}}}{\alpha} = \frac{\frac{v_{B,j}}{\sigma_{ln\,B}}}{\beta} = \frac{\frac{v_{C,j}}{\sigma_{ln\,C}}}{\gamma} \quad (23)$$

Notably, it is also necessary to consider that the $q_{i,j}$ elements are defined up to a multiplicative constant. This demonstrates that the exponents in the first component expression are indicators of the weight of the inputs to define the output. Also, even if the considered database subset is associated to a fixed output value, the higher the exponent for a given parameter, the higher its weight.

Importantly, the expressions derived here are based on the simple model in equation (20). It is not a proof that for other models, the same ratios hold. However, Voc depends on a logarithmic scale on dark saturation current, and associated material parameters. Therefore, the simple model might not be too far from the actual relations. As a result, the approach exposed here will not be used to quantitatively determine α, β and γ, but rather qualitatively compare the weight of the different input parameters.

Finally, the calculations exposed here justify employing the same approach on the dataset exposed in Section 5.2, in which drift diffusion simulations inputs and outputs have been gathered for the structure TiO2 / triple cation perovskite / PTAA. Voc, Jsc and FF will be alternatively considered as outputs, in place of Y in above computation, and investigated inputs are the nine parameters listed in Table 3.

Moreover, the whole range of available optoelectrical output values is probed: the study is performed multiple times by alternatively fixing the output to different values. In the following figures, the component's exponents are displayed across the

probed output range. Notably, exponents are all normalized so that one remains fixed to +1. This is possible because they are all defined to a multiplicative constant and facilitate readability.

It is to keep in mind that results are impacted by the ranges of explored values for each input parameter. In the simplified examples displayed in Appendix E, it appears that the exponents can diverge from expected ratios when available data points are less uniformly distributed. This is especially clear at the boundaries of the explored input space. This aspect can be tracked by the standard deviation of each input within the subsets, as illustrated in Appendix E.

Subsets having fixed Voc value

Figure 3 shows results for Voc, and the exponent associated to the defect density in the perovskite layer has been fixed to +1. The standard deviations of each parameter, displayed in Appendix E, Figure E8 remain stable between 1.05 and 1.1 V, indicating that PCA results in this range might be reliable. This also indicates that the peaks for low and high Voc values in Figure 3 are not necessarily meaningful. However, the size of the selected sub-set also varies along Voc range due to the nature of the gathered database. Therefore, the interpretation of varying standard deviation might not be as direct as in the simplified case.

It appears first that all other parameters from defect density might be of smaller importance because their exponents remain significantly lower than 1. This confirms that Voc is primarily controlled by defect density. Moreover, the electron mobility remains near zero: this could be correlated to the fact that devices considered here were all in nip configurations, where electron transport is less crucial than hole transport.

Finally, the doping level of each transport layer are associated to slightly higher exponents that respective carrier mobility. This might be caused by the fact no current flows at Voc, making carrier transport less impacting than band alignment through doping. However, a slight rise of importance of perovskite/ETL interface defects from 1.05 V to 1.15 V could be associated to a higher contribution of this recombination term for better performing devices.

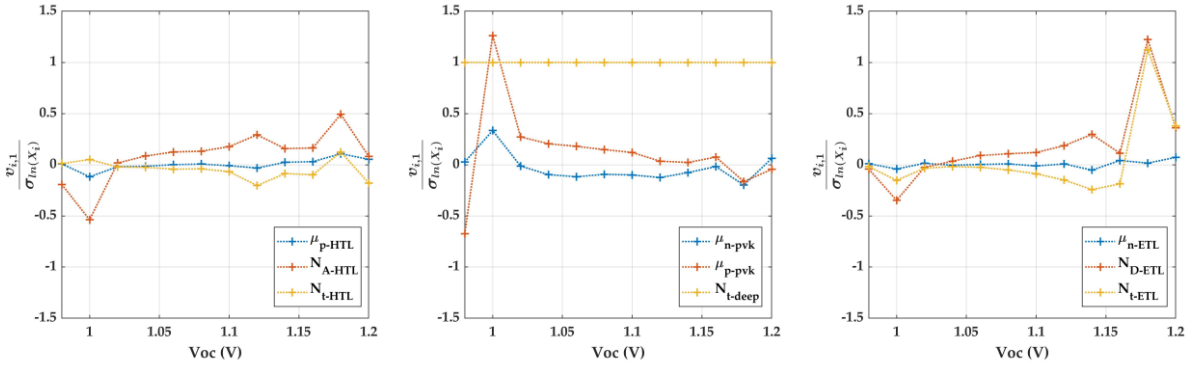

Figure 3. *Exponents of the first component for fixed values of Voc. For each point, entries within 25 mV are aggregated. Associated standard deviations are stable in the range 1.05 – 1.1 V, see Appendix E, Figure E8.*

Subsets having fixed Jsc value

Results across the Jsc values in Figure 4 vary more and no clear trend seem to be distinguishable. This can be interpreted as an indication that always combinations of factors drive the Jsc value. Furthermore, optical parameters such as the transmittance of the front layers are not included here, which would be of very significant importance. Also, the standard deviations in Appendix E, Figure E9 are stable above 16 mA.cm^{-2} and cannot explain the noisy results. Moreover, Jsc does not depend on logarithmic laws on input parameters as clearly as Voc. This can make the conclusions on exponents ratios to be less valid for this more distinct case.

The common importance of perovskite hole mobility and defect density exponents is notable, especially below 18 mA.cm^{-2}. However, this might not be compatible with hole diffusion length $L_{p-SRH} \propto \sqrt{\frac{\mu_p}{N_{t-deep}}}$, the most correlated meta-parameter candidate in Figure 2, because expected opposite signs. It could be possible that this ratio is approached between 18 and 20 mA.cm^{-2}, however with a very large uncertainty due to noisy result. Also, the electron mobility and defect density could be compatible with electron diffusion lengths, but the first exponent is only at approx. -0.5, and -1 would be expected.

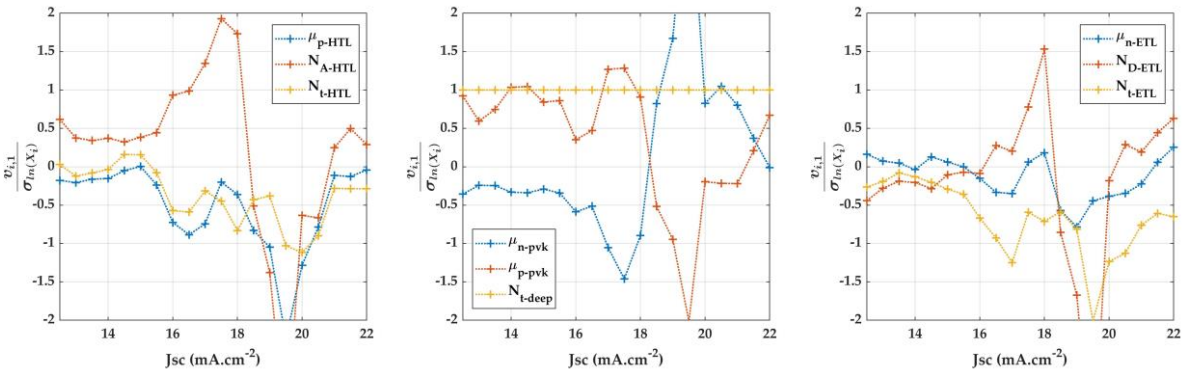

Figure 4. *Exponents of the first component for fixed values of Jsc. For each point, entries within 1 mA.cm^{-2} are aggregated. Associated standard deviations are stable above 16 mA.cm^{-2}, see Appendix E, Figure E9.*

Subsets having fixed FF value

Finally, the procedure has been employed across FF values, in Figure 5. Unfortunately, standard deviations in Appendix E, Figure E10 do not allow to easily point out a zone where it remains stable, only between 65 and 70 % could be suitable. Here, components exponents indicate that the perovskite defect density and hole mobility are the major parameters. The first one translates the expected correlation of FF with Voc. For the second, this is different from Voc analysis, where hole mobility was almost at zero, but consistent with the fact that good carrier transport is important for a good FF.

Moreover, holes generally have to travel more to reach the HTL at back side, than electrons to reach ETL at front side, due to front side illumination and mostly exponentially decreasing photogeneration rate.

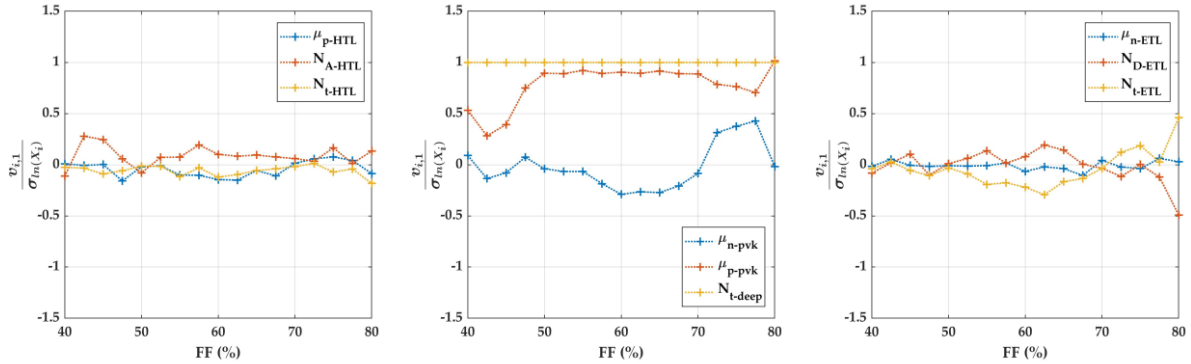

Figure 5. *Exponents of the first component for fixed values of FF. For each point, entries within 5 % are aggregated. Associated standard deviations are stable in the range 65 – 70 %, see Appendix E, Figure E10.*

Importantly, the simple model employed to illustrate the interpretation of such PCA results do not constitute a demonstration in the general case. Also, dataset boundaries and parameters distributions impact the results to an extend that remains not fully understood. Therefore, the interpretation of results exposed here might have to remain qualitative.

However, they still provide insights on the important parameters to focus on. This could help to design simulations, but also to develop solar cells and to guide on the aspects to be more carefully considered.

5.5.2 Fixed value for all optoelectrical parameters except one

The second approach to define sub-sets and perform principal components analysis gives an orthogonal perspective to the parameters space. Here, two parameters, for instance Jsc and FF, are fixed. All associated entries in the total database are gathered, with any possible Voc value.

In this example, all variability of the sub-dataset could be related to the Voc. This is evaluated through the first principal component, which contains the most variance of the dataset, and its correlation to the Voc.

Again, only input material parameters are considered as variables for the determination of components, to specifically investigate the relation between input parameters and output.

This approach has been employed for several exemplary subset selection and expressions of the first principal component are summarized in Table 4. Importantly, for the same reasons exponents are defined to a multiplicative constant, the first component is defined in absolute value. Therefore, signs in Table 4 are adjusted for consistency among reported case.

Interestingly, the product of perovskite hole mobility with defect density is present in five out of six expressions. This confirms that the product of both quantities generally defines the quality of holes extraction. However the ratio of their exponents vary significantly from one case to another, potentially related to boundaries effects that could hinder the interpretation.

Furthermore, it is envisaged that most variability of the sub-dataset is correlated to the specific output parameter that was not fixed. Therefore, the correlation between

the principal component and this variable is investigated. The linear regressions are displayed in Figure 6 for three examples presented above. Notably, the correlation is not convincing for Jsc, and the graph rather demonstrates an absence of correlation. This questions the physical meaning of the associated components presented in Table 4.

Table 4. *Examples of sub-sets selected with a single parameter left variable. Associated expression of first component and explained fraction of variance. Precision for fixed outputs is ± 0.01 V, ± 0.5 mA.cm^{-2} and ± 2 % for Voc, Jsc and FF respectively.*

Variable param.	Fixed other parameters	Subset size	Variance fraction	First component expression
Voc	Jsc = 19.5 mA.cm^{-2} FF = 72 %	1268	17.7 %	$F_1 = \ln\left(\mu_{p-pvk}^{0.5} \cdot N_{t-deep}^{0.6}\right) + C_2$
Voc	Jsc = 18.0 mA.cm^{-2} FF = 70 %	1113	19.2 %	$F_1 = \ln\left(\mu_{p-pvk}^{0.5} \cdot N_{t-deep}^{0.6}\right) + C_2$
Jsc	Voc = 1.02 V FF = 50 %	438	27.1 %	$F_1 = \ln\left(\frac{\mu_{p-pvk}^{1.1} \cdot N_{t-deep}^{2.2}}{N_{A-HTL}^{0.2} \cdot \mu_{n-pvk}^{0.3}}\right) + C_2$
Jsc	Voc = 0.98 V FF = 40 %	159	18.5 %	$F_1 = \ln\left(\frac{\mu_{n-pvk}^{0.3} \cdot N_{t-deep}^{5.7}}{N_{A-HTL}^{0.5} \cdot N_{t-HTL}^{0.3} \cdot \mu_{p-pvk}^{1.0} \cdot N_{t-ETL}^{0.2} \cdot \mu_{n-ETL}^{0.3} \cdot N_{D-ETL}^{0.4}}\right) + C_2$
FF	Voc = 1.02 V Jsc = 19.0 mA.cm^{-2}	278	20.5 %	$F_1 = \ln\left(\frac{\mu_{p-pvk}^{0.7} \cdot N_{t-deep}^{2.4}}{N_{A-HTL}^{0.5}}\right) + C_2$
FF	Voc = 1.02 V Jsc = 18.5 mA.cm^{-2}	369	19.0 %	$F_1 = \ln\left(\mu_{p-pvk}^{0.7} \cdot N_{t-deep}^{3.5}\right) + C_2$

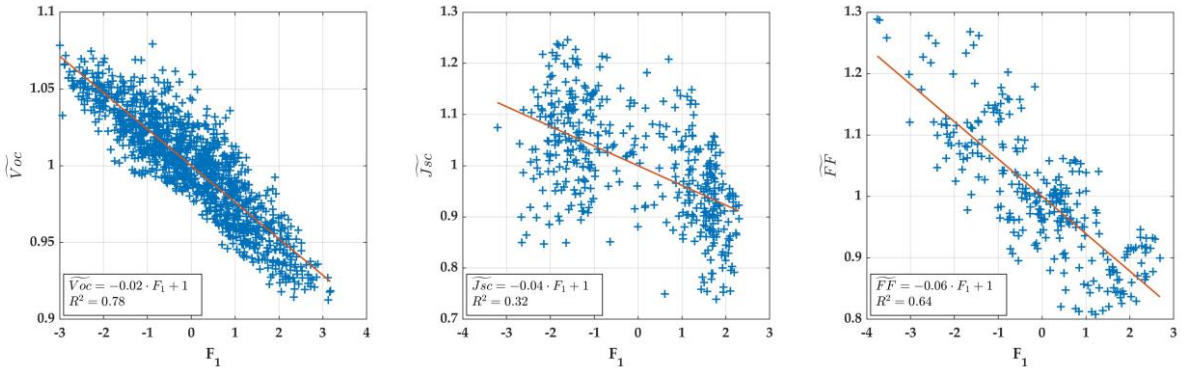

Figure 6. *Correlation plot of first component with variable output parameter, in the examples of Table 4. The linear regression quantifies the correlation strength.*

In fact, not only these examples of fixed parameters combinations have been considered, but all possibles in the available dataset. In Appendix E, Figures E11-E13 display R^2 values of the associated linear regressions, and correlation plots of the three best regressions. It shows that it is of low quality for most cases, especially when Jsc and FF are left variable.

However, the correlation of Voc with its associated principal component is still significant in several cases, with R^2 values approaching 0.8. This could validate the hypothesis that the variability of the sub-dataset is correlated to the output parameter.

The linear regression from Figure 6 is expressed as (note that normalized Voc is considered to use dimensionless quantities):

$$\widetilde{V_{OC}} = \alpha \cdot F_1 + \beta \quad (24)$$

When combined with the formulation of the component, this has the advantage of providing an analytical expression of the optoelectrical parameter, based on material parameters:

$$\widetilde{Voc} = \alpha\, ln\left(\prod_{i=1}^{n} X_i^{\frac{q_{i,k}}{\sigma_{lnX_i}}}\right) - \alpha \sum_{i=1}^{n} \frac{\overline{ln\, X_i}}{\sigma_{lnX_i}} q_{i,k} + \beta \quad (25)$$

Results for both cases with variable Voc from Table 4 are expressed in Table 5. This provides new analytical models for Voc, that could be employed to help simulating the behavior of perovskite solar cells. However, when looking at the role of the different material parameters, questions arise. For instance, Voc decreases with perovskite hole mobility.

Notably, the product carrier mobility – defect density does not correspond to the SRH diffusion length, which was the meta-parameter candidate the most correlated to Voc in Figure 2. However, some other meta-parameters extracted from the expressions of recombination current did include the ratio $\frac{D_{p-pvk}}{L_p} \propto \sqrt{\frac{D_{p-pvk}}{\tau_{eff}}} \propto \sqrt{\mu_{p-pvk} N_{t-deep}}$, especially because the effective lifetime is almost equal to the SRH lifetime in the cases present in the database. This quantity is proportional to the recombination current, which explains its inverse proportionality to Voc in Figure 6.

Table 5. *Expressions for Voc derived from first component and its linear regression with Voc. Precision for fixed outputs is ± 0.01 V, ± 0.5 mA.cm^{-2} and ± 2 % for Voc, Jsc and FF respectively.*

Variable param.	Fixed other parameters	R^2	First component expression
Voc	Jsc = 19.5 mA.cm^{-2} FF = 72 %	0.78	$\widetilde{Voc} = 0.02 \ln\left(\frac{1}{\mu_{p-pvk}^{0.5} \cdot N_{t-deep}^{0.6}}\right) + 1.1$
Voc	Jsc = 18.0 mA.cm^{-2} FF = 70 %	0.77	$\widetilde{Voc} = 0.02 \ln\left(\frac{1}{\mu_{p-pvk}^{0.5} \cdot N_{t-deep}^{0.6}}\right) + 1.0$

Finally, the domain of validity of these expressions have to be kept in mind. All solar cells considered in this chapter have the same structure (details are in Table 2), and the subsets considered to obtain these expressions focuses on specific values for Jsc and FF. The particularity of the subset could allow to envisage very local validity of these results, but also question their use.

Chapter conclusion

Meta-parameters have been defined as combinations of material parameters (dimensionless or not) that actually define the solar cell behavior. An example is the diffusion length of carriers in a semi-conductor. It is based on the product of the diffusion coefficient and lifetime and defines the transport behavior of carriers.

For modeling studies with statistical approaches, such as presented in Chapters 3 and 4, meta-parameters could allow to reduce the dimensionality of the input space to explore. In fact, the work presented in these chapters demanded numerous simulations, and a large dataset constituted of inputs and outputs could be gathered. This allowed to perform the several statistical analyses in this chapter.

Two methods have been employed to investigate the role of input parameters. First, an analytical model for a pn homojunction has been derived, and important quantities extracted from its expressions. They have been translated and assessed for a perovskite solar cell structure through their correlation with the optoelectrical outputs in the available dataset. Some could be validated, such as diffusions lengths. However, because of the simplified nature of the structure considered for the analytical model, not all characteristics of perovskite solar cells are investigated.

Therefore, a second method have been considered to investigate deeper the role of inputs in the available dataset, through principal components analysis. Computing components and ranking them by fraction of explained variance is a common technique to extract the most fraction of variability in a database. Furthermore, log value of the material parameters were considered, converting the linear combinations of the components' expressions into products that can be related to meta-parameters.

In a simplified case, it has been showed that extracting the principal component of inputs subsets selected according to output values reflects the role of the inputs. For instance, the crucial role of defect density to define Voc and FF is illustrated, as expected. The role of hole mobility for FF and not Voc is also an interesting result.

Finally, orthogonal selection of subsets was performed to obtain components correlated to the optoelectrical outputs. This even allowed to express their value as functions of material parameters and finally provide new simple phenomenological models.

However, it is to be kept in mind that the results obtained in this chapter are specific to the perovskite solar cell structure simulated here. Their validity outside this configuration is not straightforward and should be assessed. Finally, having a better (more uniformly) distributed databased, with specifically chosen varied inputs, would probably allow to obtain clearer and more general results. The work presented here gives in fact insights on how statistical approaches could support the solar cell modeling research field.

References

[1] Henry Mathieu, *Physique des semiconducteurs et des composants électroniques*, 2nd edition. Masson, 1990.

[2] K. L. Chopra and S. R. Das, *Thin Film Solar Cells*, 1st ed. Boston, MA: Springer US, 1983. doi: 10.1007/978-1-4899-0418-8.

[3] A. A. M. H. Al Asbahi, F. Z. Gang, W. Iqbal, Q. Abass, M. Mohsin, and R. Iram, "Novel approach of Principal Component Analysis method to assess the national energy performance via Energy Trilemma Index," *Energy Reports*, vol. 5, pp. 704–713, Nov. 2019, doi: 10.1016/j.egyr.2019.06.009.

[4] Y. D. Lang, A. Malacina, L. T. Biegler, S. Munteanu, J. I. Madsen, and S. E. Zitney, "Reduced order model based on principal component analysis for process simulation and optimization," *Energy and Fuels*, vol. 23, no. 3, pp. 1695–1706, Mar. 2009, doi: 10.1021/ef800984v.

[5] M. Hasanzadeh Azar *et al.*, "SCAPS Empowered Machine Learning Modelling of Perovskite Solar Cells: Predictive Design of Active Layer and Hole Transport Materials," *Photonics*, vol. 10, no. 3, p. 271, Mar. 2023, doi: 10.3390/photonics10030271.

[6] H. A. Kazem, J. H. Yousif, M. T. Chaichan, A. H. A. Al-Waeli, and K. Sopian, "Long-term power forecasting using FRNN and PCA models for calculating output parameters in solar photovoltaic generation," *Heliyon*, vol. 8, no. 1, p. e08803, Jan. 2022, doi: 10.1016/j.heliyon.2022.e08803.

[7] R. K. S. S. Vuppala and K. Kara, "A non-intrusive reduced order model using deep learning for realistic wind data generation for small unmanned aerial systems in urban spaces," *AIP Adv*, vol. 12, no. 8, p. 085020, Aug. 2022, doi: 10.1063/5.0098835.

[8] H. Abdi and L. J. Williams, "Principal Component Analysis," *Wiley Interdiscip Rev Comput Stat*, vol. 2, no. 4, pp. 433–459, 2010, doi: 10.1002/wics.101.

Conclusion

Table of contents

The work presented here is summarized in the first section. It relied on new modeling techniques that have been specifically designed to investigate the degradation of perovskite solar cells. Results have been obtained on several examples of aging studies, demonstrating the capabilities and limits of the proposed method. The statistical approach, at the core of this work at each step, even allowed to look back towards the underlying physics of solar cells.

Furthermore, this paves the way for further developments in several directions. First to overcome some present limitations, listed in the second section, but also to broaden the scope of the studies reported here. Examples are exposed in the third section.

Summary of the work

In this work, common characterizations performed periodically over the course of aging experiments have been investigated. The associated evolutions of optoelectrical parameters over time were at the core of the approach developed here.

In order to reproduce the photovoltaic behavior of perovskite solar cells, coupled optical (transfer matrices) and electrical (drift diffusion) modeling have been employed. Furthermore, a statistical approach has been developed, because of some unwell known input parameters. A genetic algorithm has been designed, providing numerous sets of inputs that reproduce the initial experimental performances of any given sample. These sets were the basis to simulate the impact of various hypothetical unitary degradation mechanisms.

Importantly, degradation pathways were obtained by considering the correlated evolution of optoelectrical parameters. They constitute characteristic footprints of the underlying processes and allow to directly compare simulated and experimental degradation pathways. As a result, compatible mechanisms can be proposed, and others excluded when pathways differ, directly tackling the causality between performance losses and degradation mechanisms.

This approach has been applied in a first step to experimental measurements reported in literature. Obtained results could be compared to authors analyses and demonstrated the validity of the approach. Also, aging experiments performed at IPVF were investigated, with a first set of samples prepared with four variations in the deposition method of the perovskite layer. Results showed that the perovskite could be excluded as a cause for degradation in most cases, except for a specific method, also having the least stable samples. A second set, containing devices having different hole and electron transport layers was investigated through coupled current-voltage and photoluminescence measurements. Interestingly, hole transport layer degradation could be attributed to several samples, and a protective role of the electron transport layer could be envisaged. Also, coupling characterization techniques helped to distinguish pathways through new complementary perspectives.

Finally, the last part of this work took advantage of the numerous simulations performed to investigate degradation. It aimed at simplifying the design of drift diffusion simulations, first through meta-parameters. Principal components analyses were also employed on subsets selected according to solar cells performances, to point out the most important parameters or provide new simple phenomenological models. This supports the understanding of the role of the material parameters and their impact on performances.

The work presented here shows how coupling of characterization and modelling can support experimental development of stable perovskite solar cells. Insights on the causes of degradation of various samples have been proposed, based on classical experimental measurements that could be investigated more thoroughly. Finally, this also demonstrates that statistical approaches can support the solar cell modeling research field, by being less dependent on the knowledge of given parameters.

Key points:

- Coupled optical and electrical simulations are employed to compute the solar cell behavior and reproduce current voltage characteristics and photoluminescence spectra.
- Simulations require numerous input parameters. Some values are not confidently known for a given sample and a highly dimensional input parameters space could be to explore.
- A genetic algorithm has been developed to reproduce closely the optoelectrical performances of a given solar cells.
- Unitary degradation mechanisms are considered by simulating the response to a variation of a given material parameters.
- Degradation pathways are obtained by considering the evolution of the correlation of solar cells optoelectrical parameters. Their position is independent from time and therefore any speed of reaction: it constitutes a characteristic footprint of the underlying process.
- Combining characterization techniques allows further distinction of degradation pathways.
- Experimental measurements reported in literature have been investigated and provide a proof of concept of the methodology exposed here.
- Several degradation sequences over time can be analyzed to consider multiple successive degradation mechanisms.
- The approach employed here directly tackles the cause of optoelectrical performance losses. Conducting complementary characterization demonstrates concomitance with material evolutions.
- For both studies of samples characterized at IPVF, insights on the responsible degrading layer were obtained. The perovskite layer might have remained stable in most cases of the deposition method study (except for one). Degradation of the HTLs have been reported for the second set, with a potential protective effect by SnO_2.
- Results obtained here constitute guidelines for further improvements of perovskite solar cell stability.

Limits of the work

In order to evaluate the reliability of the results obtained in this work, it is crucial to consider the limits of the developed methods.

First, modelling methods and numerical solvers have a given finite accuracy. This can especially impact results when simulating strongly atypical cases, at the end of simulated degradation mechanism.

Also, the modelling scheme employed does not couple ionic migrations and electron-hole transport. Therefore, distinction of forward and reverse current-voltage (JV) characteristics can't be considered, and the impact on charge carrier transport of both configurations is not resolved. Furthermore, simulations are done under one dimension, making not possible to consider spatially resolved processes. However, such aspects would need to be compared to spatially resolved characterization techniques.

Slopes at open circuit and short circuit were extracted from JV characteristics, instead of proper series and shunt resistances. Considered parameters are rather indicators of the fitness of the curve. In fact, it would have been necessary to fit a model such as a single diode to have access to resistances. This would have added complexity and uncertainty, while being more time consuming.

Importantly, the methods exposed here have been designed to exclusively consider aging studies under constant conditions. Investigating studies under outdoor or cycling conditions would necessitate further models. However, a simple solution can be to consider the set of results obtained periodically under the same condition, at the same moment in the cycle.

Also, the experimental data investigated here had only a low sample statistic. Reliable conclusions on stability of given materials in given structures would necessitate more samples. Furthermore, average behavior of several samples could be considered if close enough, which would reduce measurement noise.

When simulating the impact of degradation mechanisms, the average response over inputs sets selected by the genetic algorithm was computed. In fact, selected sets must not necessarily respond similarly. If this occurs, the average value cannot properly reflect responses, but the wider 95 % confidence interval can still provide insights on its reliability.

Importantly, degradation mechanisms investigated in this work are unitary: they are characterized by the change of a single material parameter. Therefore, combined evolutions cannot be excluded. In fact, considering such combination would introduce degrees of freedom on parameters relative speeds of variation, needing a large number of supplementary simulations.

A very important aspect of the analysis of degradation pathways is that it only demonstrates the compatibility of a mechanism with experiment. Even with perfect superposition there could be another mechanism being the actual cause. However, when pathways are distinct, it is the proof that the processes were distinct.

Finally, it is to keep in mind that phenomenological results of statistical approaches, such as correlations or PCA, are only valid for configurations covered by the database.

Moreover, the available entries stem from the degradation studies degradation, even if a uniformly distributed subset has been extracted, it would be useful to explore larger distributions of some parameters in order to avoid boundary effects.

This could have an impact on principal components analyses performed on subsets of fixed output value. The link between the first component composition and the output has been demonstrated in a simple case, however, when outputs follow a more complex law towards inputs with higher dimensions, the impact of boundaries could be larger.

Finally, in the case of analyses performed on subsets with a varying output, the covered domain is very limited, due to the fixed values of both other outputs. Therefore, the domain of validity of obtained expressions is very restricted. As a result, these expressions might be only useful for specific device optimizations for instance.

Perspectives

Here, perspectives to overcome the limitations mentioned in previous section, or to go beyond are proposed.

The first aspect has already been mentioned several times: further characterization techniques can be simulated. For instance, capacitance spectroscopy measurements would provide knowledge on interface properties. External quantum efficiency would allow to reproduce the optical behavior of the solar cells more precisely. Even time resolved measurements (such as time resolved photoluminescence) could be useful, but numerical tools would need to be adapted. Also, spatial inhomogeneities are a significant aspect of perovskite solar cells degradation that could be investigated through the approach developed here, provided the suitable characterizations and modelling tools are employed.

Also any other materials and solar cell technology than perovskites could be investigated. The plausible degradation processes and the number of variable unknown input parameters might be restricted, leading to an even simpler problem.

It has been mentioned that larger sample statistics are necessary to provide reliable conclusions. In fact, greater numbers of samples could be investigated through parallel computing, from which very large improvements of computation speed are expected. The simulations performed here (at least at each step of the genetic algorithm) do not need the results of other ones, and therefore could almost run all at once in parallel.

Also, the genetic algorithm employed here has been developed specifically for this work, but more elaborate and efficient implementations do exist. Computation time would be also improved here, along with the precision of reproduction of the solar cell performances.

Furthermore, diverging responses of selected sets to simulated degradation mechanisms could be treated by clustering methods (a type of machine learning algorithm). These would find families of similar responses, providing several plausible simulated pathways for a given mechanism. This work is in fact under progress, through the supervision of an internship at IPVF.

Interestingly, it could have been possible to go back to kinetics considerations, once a dominant mechanism is considered. By associating the experimental time evolution to the simulated parameter degradation, its variation speed would have been obtained. One could even think to thermal activation studies: the work presented here would then be useful to verify that the same process is being recorded at each temperature, and to access its reaction speed.

Combining the unitary degradation mechanisms investigated in this work would be time consuming, but the number of necessary simulations is limited to a certain extend. For instance, for the combination of two mechanisms, the number of possible states by which the solar cell can go through is only defined by the matrix of possible couples for both parameters. Then, the relative speeds make the solar cell travel across

these possible states (matrix element) in potentially numerous ways. However, only the fixed number of matrix element need to be simulated.

Furthermore, the number of mechanisms combinations could be restricted to physically realistic processes, with combinations per layer for instance. However, comparison of the numerous simulated pathways and experiment would need to be rationalized, by computing their distance to each other for instance.

Finally, perovskite solar cells are also prone to reversible degradation under cycling or outdoor conditions. In a first step, recovery processes have been investigated by considering simulated "healing mechanisms" (for instance decrease of interface defect densities). Again, this has been done through the supervision of an internship at IPVF.

Importantly, understanding the behavior of perovskite solar cells under outdoor conditions is crucial for the community. Such results could be investigated by employing models to correct measured performances from their dependency on conditions. The obtained evolution, attributable to degradation, could then be analyzed with the methods exposed here.

Also, degradation pathways could be considered through more elaborate quantities than optoelectrical parameters. For instance, the slopes of the actual pathways, especially at the beginning of the degradation seem to be distinctive between mechanisms. Therefore, it could be useful to display these slopes (the derivatives of the parameters with respect to each other) that instead of starting from the same point, would lie in different potentially distinctive areas.

As a result, some of the limitations of the present work could be overtaken by complementary studies, exposed here. Finally, these perspectives show how more elaborate methods could be based on those presented here and be helpful to the research community to investigate perovskite solar cells stability.

Appendix A : Résumé en Français

Les cellules solaires à pérovskite ont attiré beaucoup d'attention ces dernières années, en raison de leur rendement élevé et de leur faible coût de fabrication. Les propriétés des matériaux et interfaces de ces dispositifs ont été intensément étudiées, permettant d'améliorer leurs performances. Cependant, leur durée de vie reste courte en raison de nombreux potentiel mécanismes de dégradation, déclenchés par divers facteurs environnementaux.

Ce travail a pour but d'aider à la compréhension de ces mécanismes et de soutenir le développement de cellules solaires pérovskites stables. Des méthodes de modélisation ont été développées pour distinguer et identifier les mécanismes responsables de la dégradation des performances dans le cadre d'expériences de vieillissement.

Afin d'étudier le comportement photovoltaïque des cellules solaires pérovskites, des modèles optiques (matrices de transfert) et électriques (dérive diffusion) ont été couplés. Une approche statistique a été développée en raison de certains paramètres mal connus. Un algorithme génétique a été conçu pour fournir des ensembles d'inputs compatibles avec un échantillon. Ces ensembles sont la base pour simuler l'impact de divers hypothétiques mécanismes.

Les chemins de dégradation sont obtenus en considérant l'évolution corrélée de paramètres optoélectroniques. Ils constituent des empreintes caractéristiques des processus de dégradation et les chemins simulés et expérimentaux peuvent directement être comparés. Des mécanismes compatibles peuvent donc être proposés et d'autres exclus lorsque les chemins diffèrent. La causalité entre les pertes de performance et les mécanismes de dégradation est ici directement considérée.

Après avoir appliqué cette approche à des mesures expérimentales rapportées dans la littérature, permettant de comparer les résultats aux analyses des auteurs et de démontrer la validité de l'approche, des expériences de vieillissement réalisées à l'IPVF ont été étudiées. Une première série d'échantillons a été préparée avec quatre variations de la méthode de dépôt de la couche pérovskite. Les résultats ont montré que celle-ci pouvait être exclue comme cause de dégradation dans la plupart des cas, à l'exception d'une méthode spécifique, ayant également les échantillons les moins stables.

Un deuxième jeu, contenant des dispositifs ayant différentes couches de transport des électrons et trous, a été étudié par des mesures couplés courant-tension et photoluminescence. La dégradation de la couche de transport des trous a pu être attribuée à plusieurs échantillons et un rôle protecteur de la couche de transport des

électrons peut être envisagé. En outre, le couplage des techniques de caractérisation a permis de distinguer les chemins de dégradation à travers de nouveaux plans complémentaires.

Enfin, la dernière partie de ce travail a tiré parti des nombreuses simulations de dégradation réalisées. Elle visait à simplifier la conception des simulations de dérive diffusion en réduisant le nombre de paramètres d'entrée nécessaires, et en identifiant les plus importants. Des méta-paramètres candidats ont été proposés en considérant un modèle analytique, et leur validité évaluée par leur corrélation avec les paramètres optoélectroniques. En outre, des analyses en composantes principales ont été employées sur des sous-ensembles sélectionnés en fonction des performances des cellules solaires, afin de mettre en évidence les paramètres les plus importants ou de fournir de nouveaux modèles phénoménologiques simples.

Ce travail montre comment la modélisation peut aider au développement expérimental de cellules solaires pérovskites stables. En particulier, des indications sur les causes de la dégradation de divers échantillons ont été proposées. Enfin, ce travail démontre également que les approches statistiques peuvent soutenir le domaine de la recherche sur la modélisation des cellules solaires, en étant moins dépendants de la connaissance de paramètres donnés.

Appendix B: Processing of experimental measurements

In this appendix are supplementary figures to illustrate the work reported in Chapter 2.

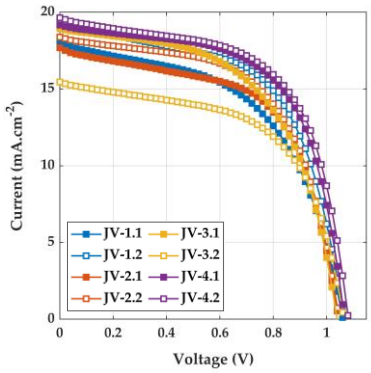

Figure B1. *Initial JV characteristics of the eight devices characterized through periodic JV measurements. Four techniques were employed to prepare the perovskite solution: the day of deposition or one day before, and with a pre-heating step of the solution or not.*

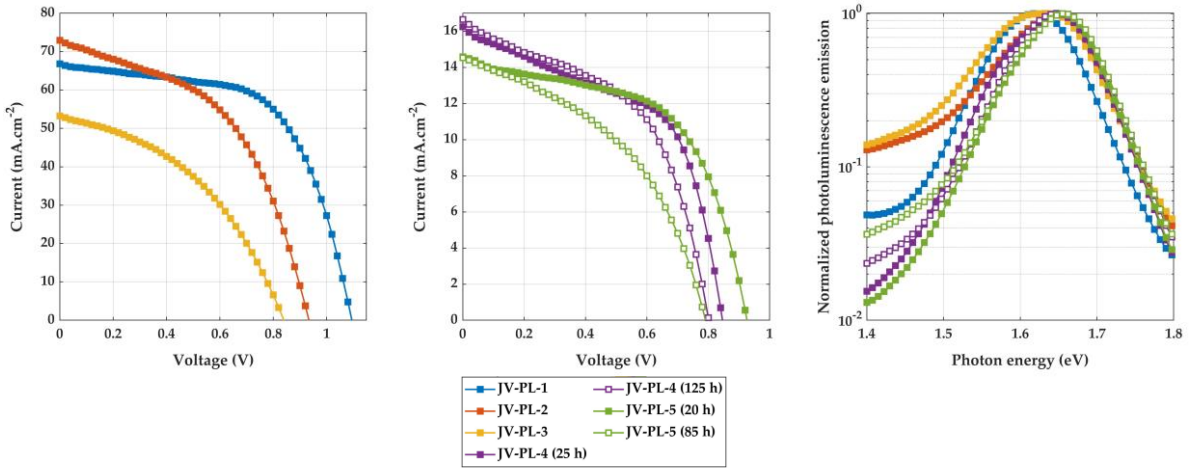

Figure B2. *Initial JV characteristics and PL spectra of the five devices characterized through periodic JV and PL measurements. They were fabricated with the same perovskite material, but combinations of two ETL and HTL materials were employed: TiO_2 / PTAA for JV-PL-1, 2 and 3, SnO_2 / PTAA for JV-PL-4, and TiO_2 / Spiro-MeOTAD for JV-PL-5. Importantly, JV characteristics were recorded under laser illumination, explaining the high Jsc values for JV-PL-1 to 3.*

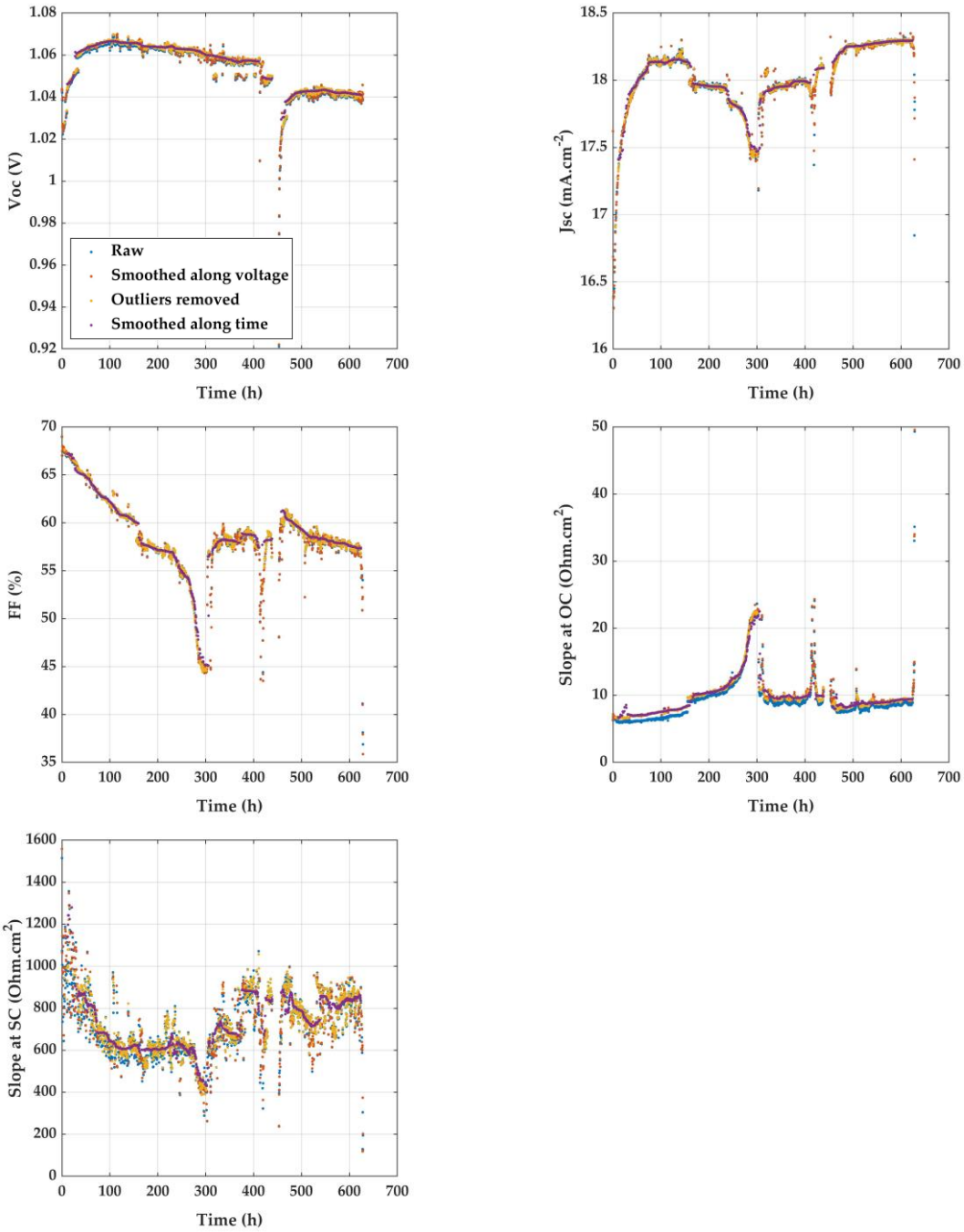

Figure B3. *Degradation over time of device JV-1.1 for reverse measurements. The parameters are extracted from the JV characteristics at each step of the pre-treatment.*

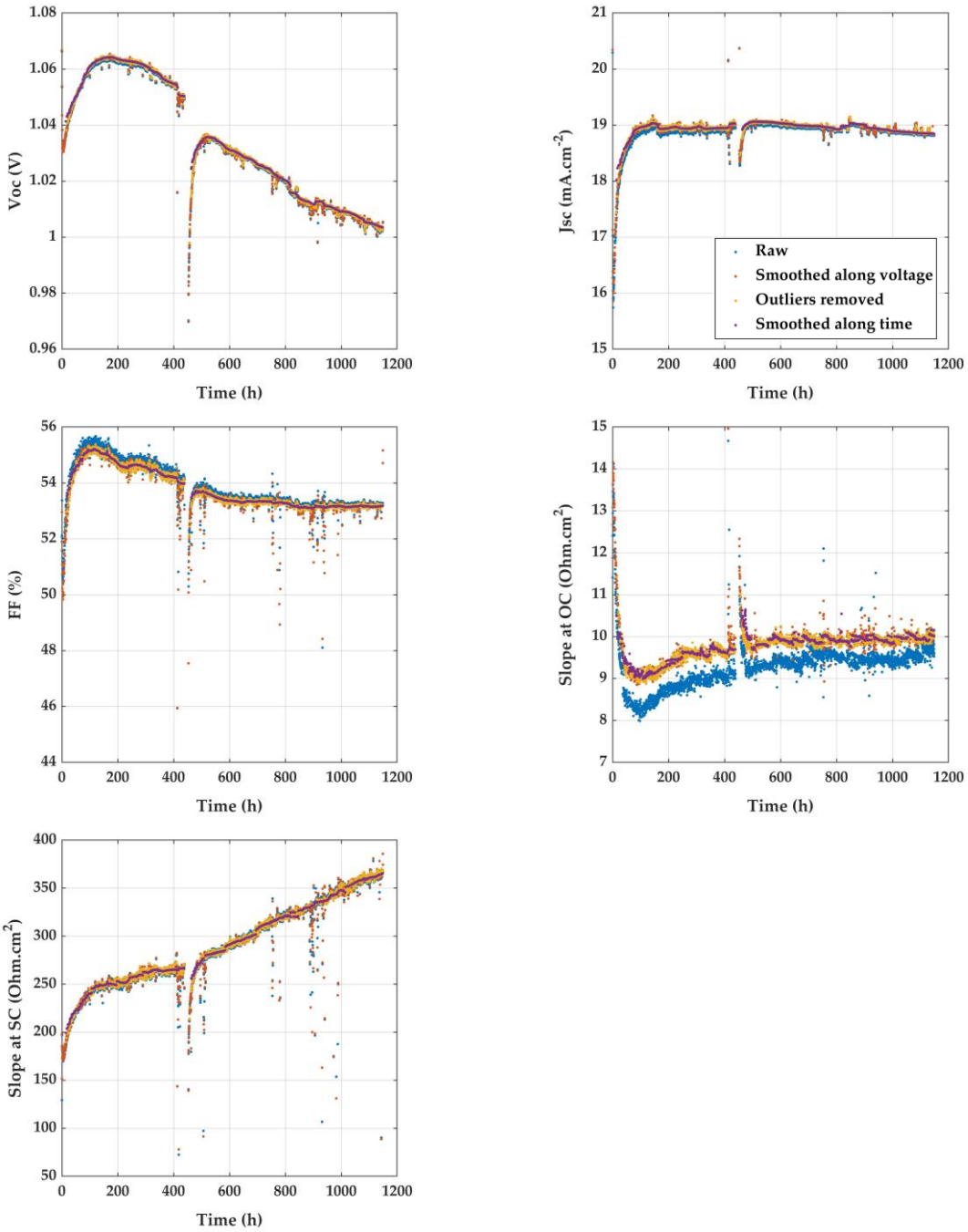

Figure B4. *Degradation over time of device JV-3.1 for forward measurements. The parameters are extracted from the JV characteristics at each step of the pre-treatment.*

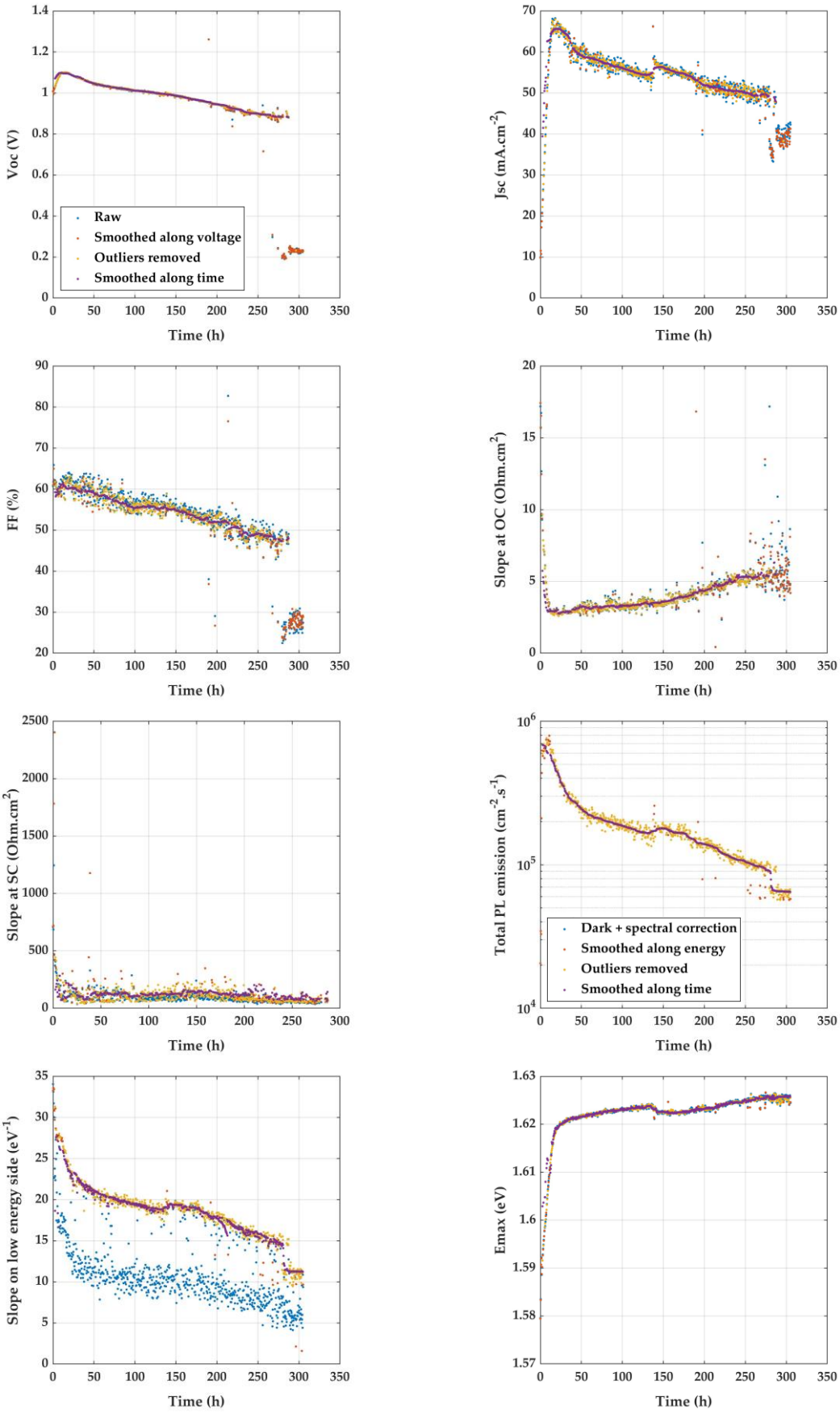

Figure B5. *Degradation over time of device JV-PL-1 (reverse JV measurements). The parameters are extracted from the JV characteristics and PL spectra at each step of the pre-treatment.*

Appendix C: Reproduction of initial performances of investigated devices

In this appendix are supplementary figures to illustrate the work reported in Chapter 3.

Peng *et al.*

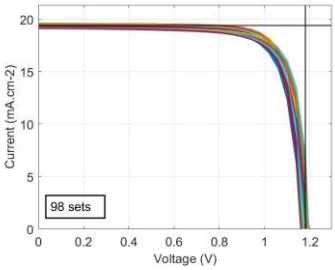

Li *et al.* (MPP)

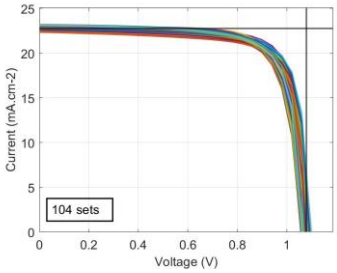

Li *et al.* (Voc)

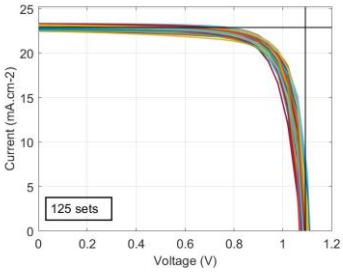

Chen *et al.*

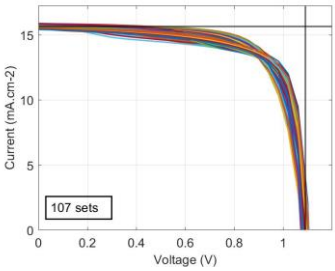

Lim *et al.* – 40 °C

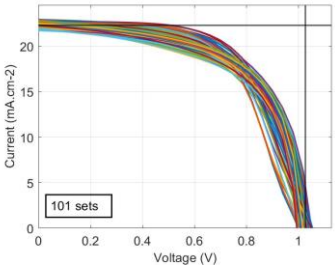

Lim *et al.* – 55 °C

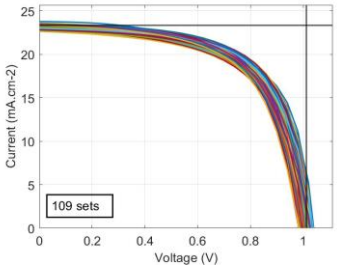

Lim *et al.* – 70 °C

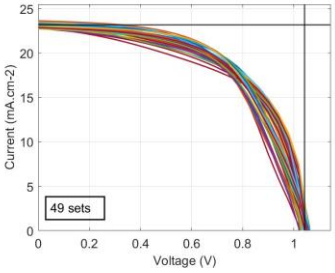

Peng *et al.* (P3HT:CuPc HTL)

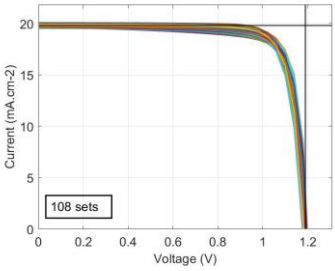

Lim *et al.* (from x h) – 40 °C

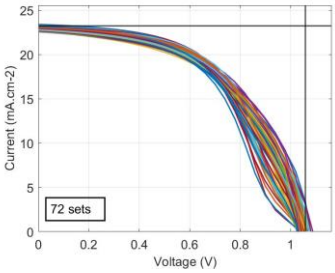

Lim *et al.* (from x h) – 55 °C

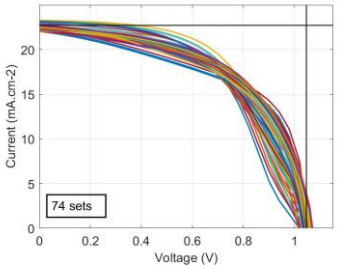

Lim *et al.* (from x h) – 70 °C

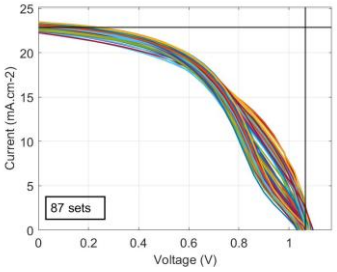

Figure C1. *Simulated JV characteristics selected to reproduce the initial performances of devices extracted from literature. Vertical and horizontal lines show experimental Voc and Jsc, respectively.*

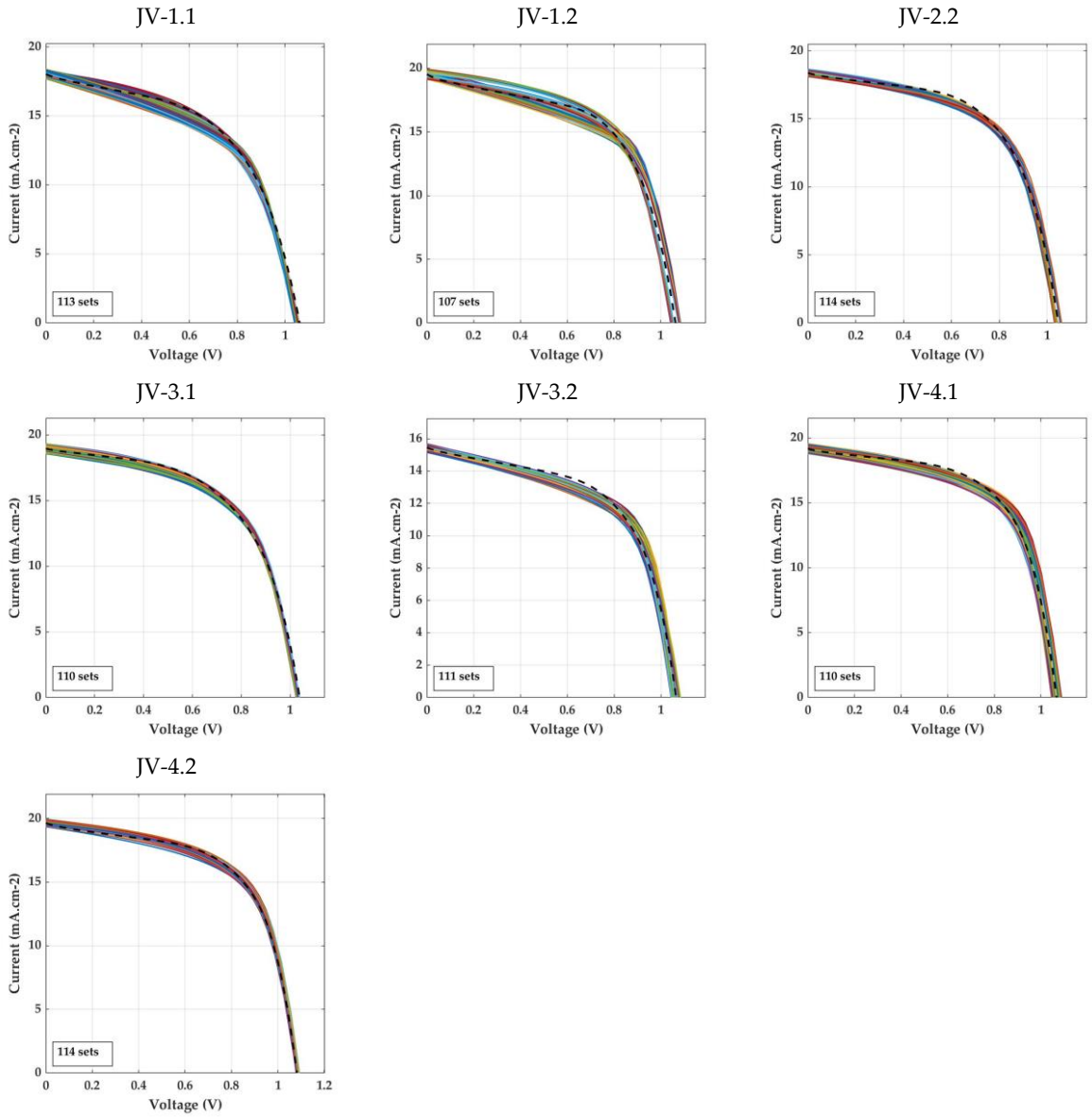

Figure C2. *Simulated JV characteristics selected to reproduce the initial performances of devices JV-1.1 to JV-4.2. Dotted lines show the experimental JV characteristic.*

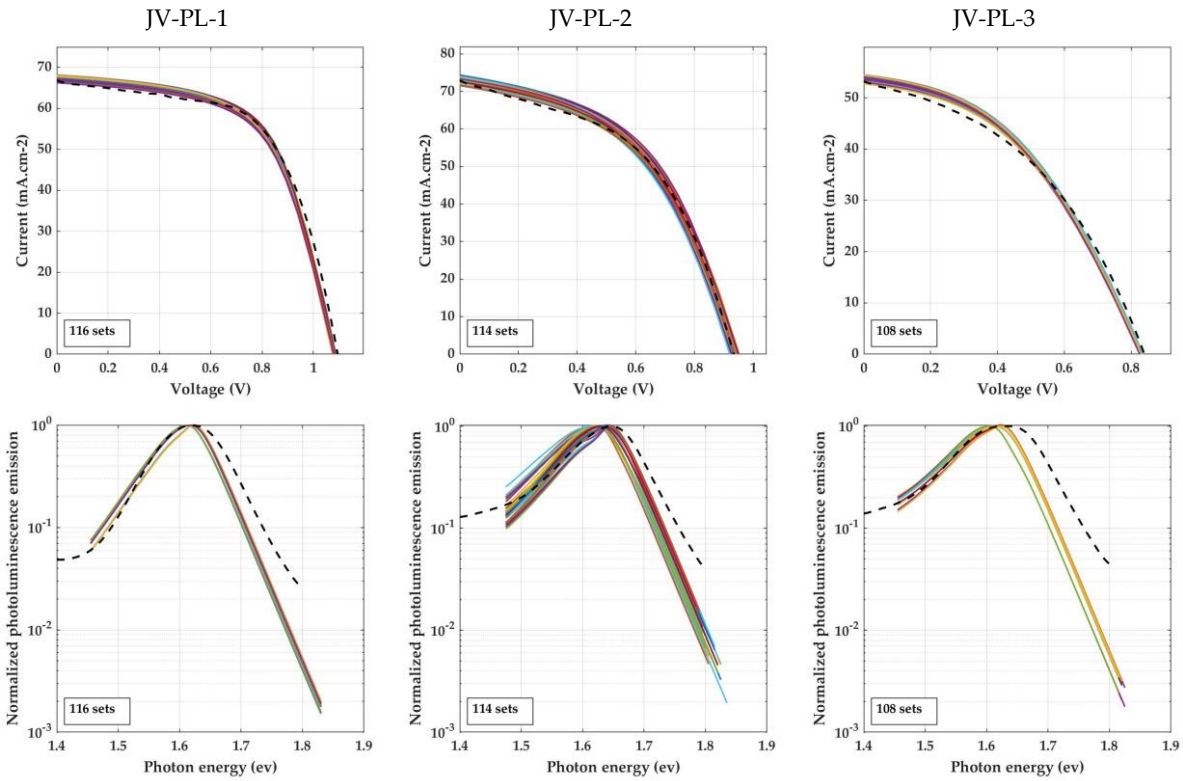

Figure C3. *Simulated JV characteristics and PL spectra selected to reproduce the initial performances of devices JV-PL-1 to JV-PL-3. Dotted lines show experimental measurements.*

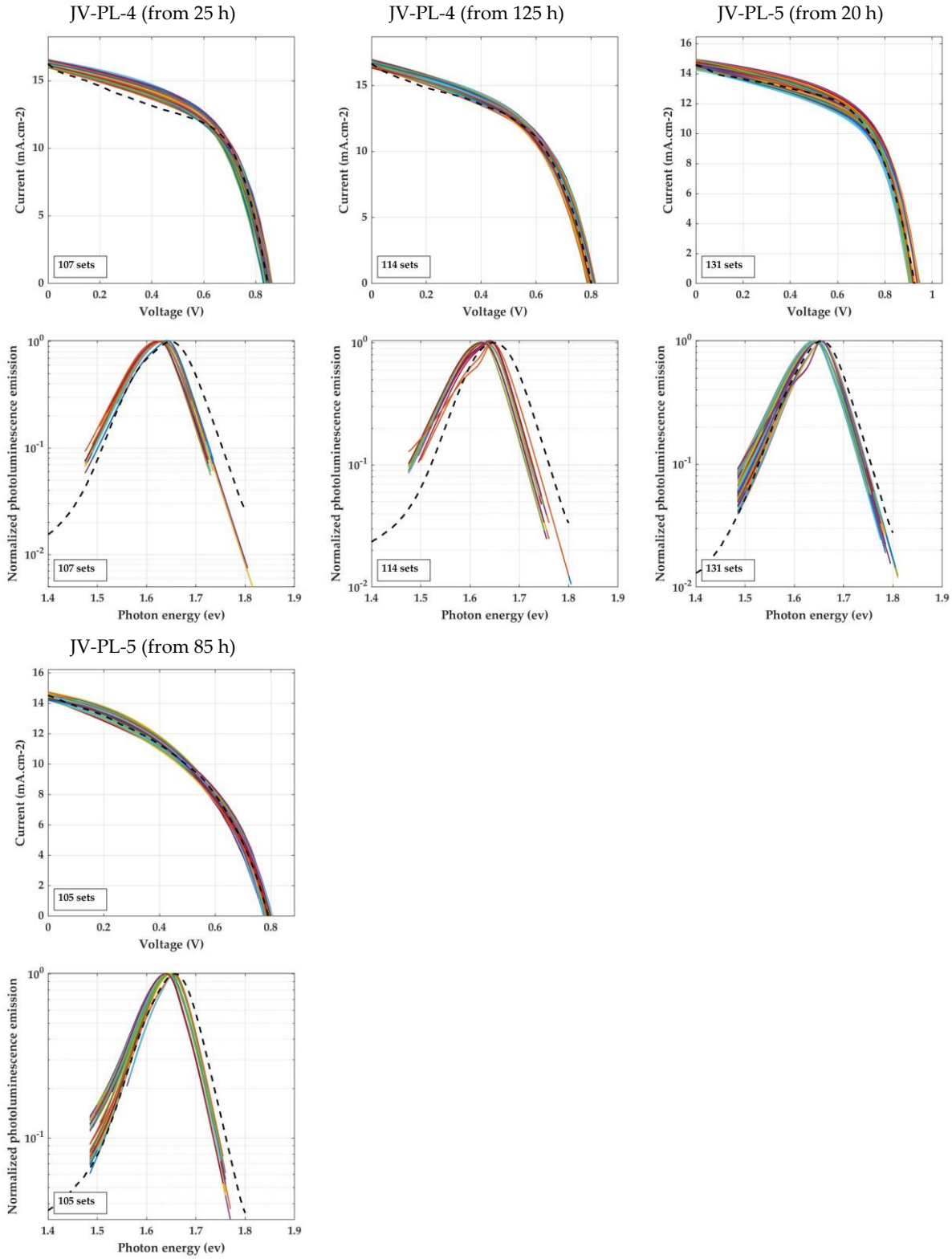

Figure C4. *Simulated JV characteristics and PL spectra selected to reproduce the initial performances of devices JV-PL-4 and JV-PL-5. Dotted lines show experimental measurements. For each device, two starting points of the degradation are envisaged.*

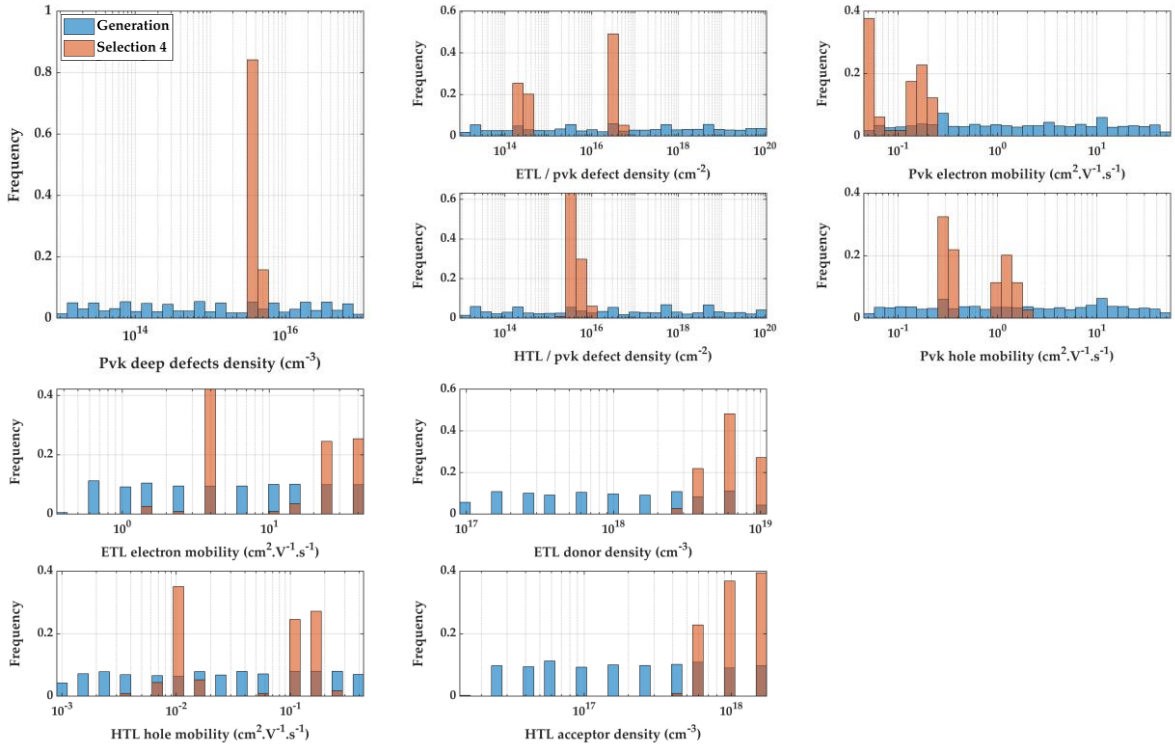

Figure C5. *Frequency distribution of material parameters in the initial generation and after the final selection step of the genetic algorithm for the device JV-4.2. The number of counts per bin in the histogram is normalized by the total number of sets.*

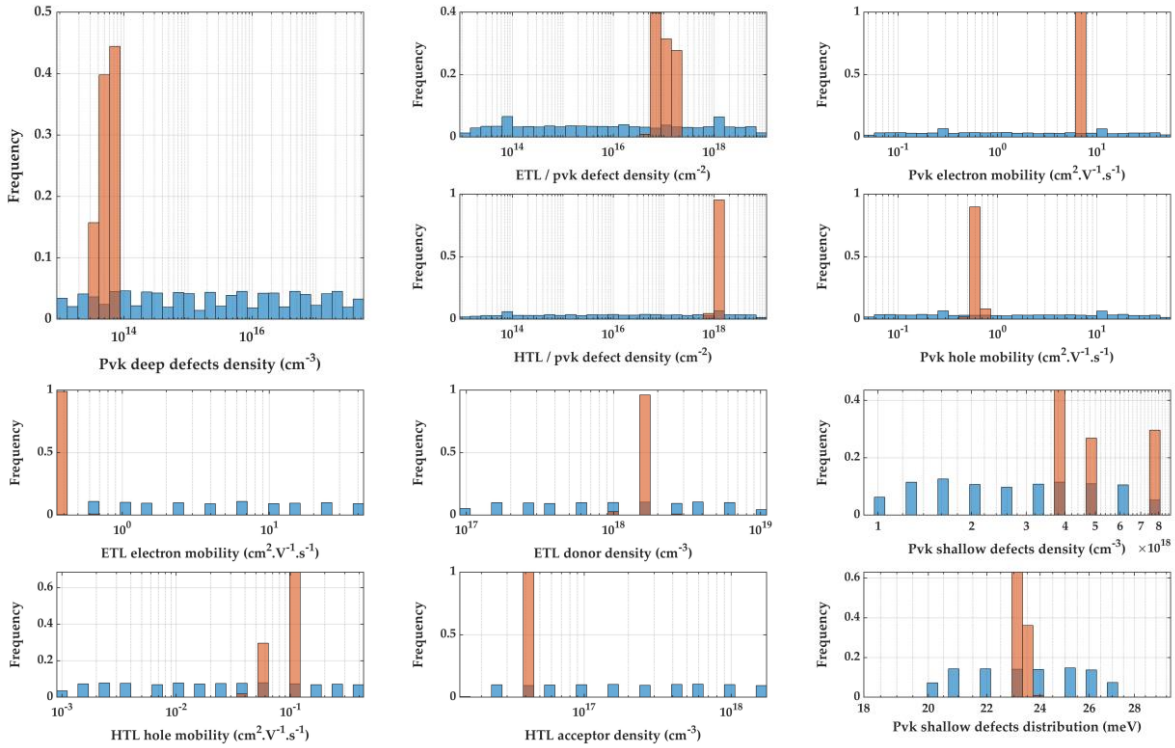

Figure C6. *Frequency distribution of material parameters in the initial generation and after the final selection step of the genetic algorithm for the device JV-PL-3. The number of counts per bin in the histogram is normalized by the total number of sets.*

Appendix D: Additional details on investigation of degradation pathways

In this appendix are supplementary figures to illustrate the work reported in Chapter 4.

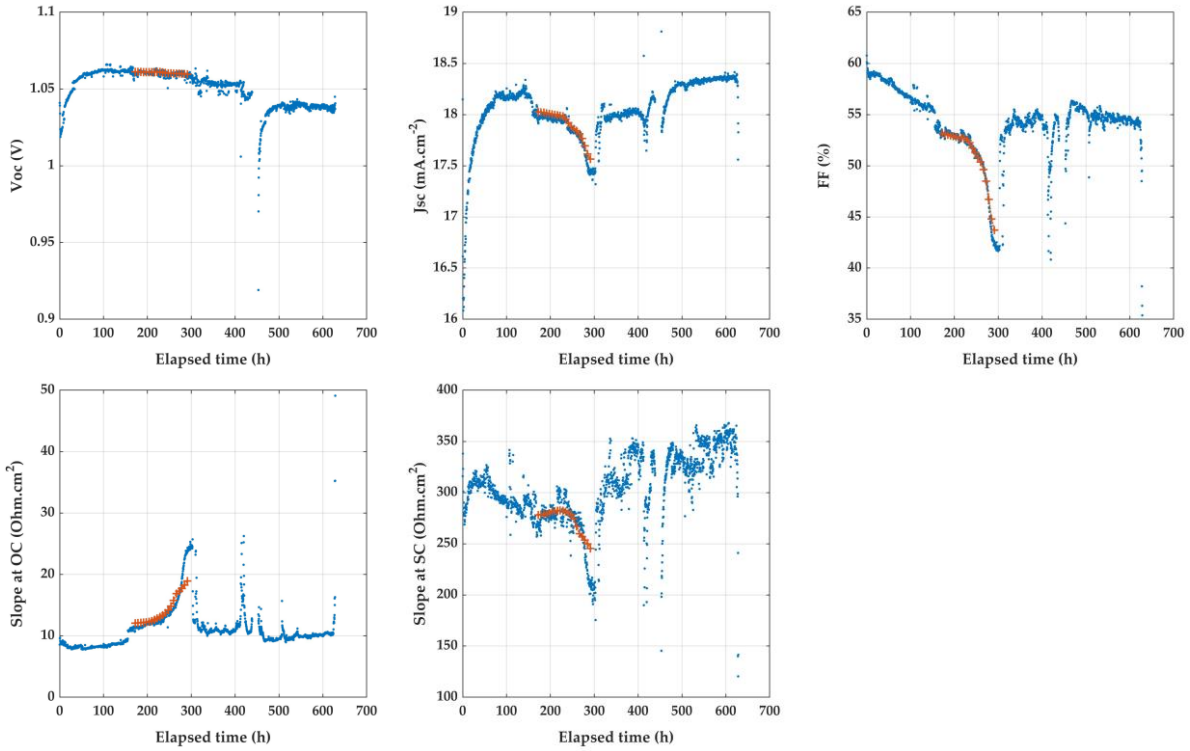

Figure D1. *Degradation over time of the device JV-1.1. Only part of the recorded degradation is extracted to be investigated, from 170 to 290 h of aging.*

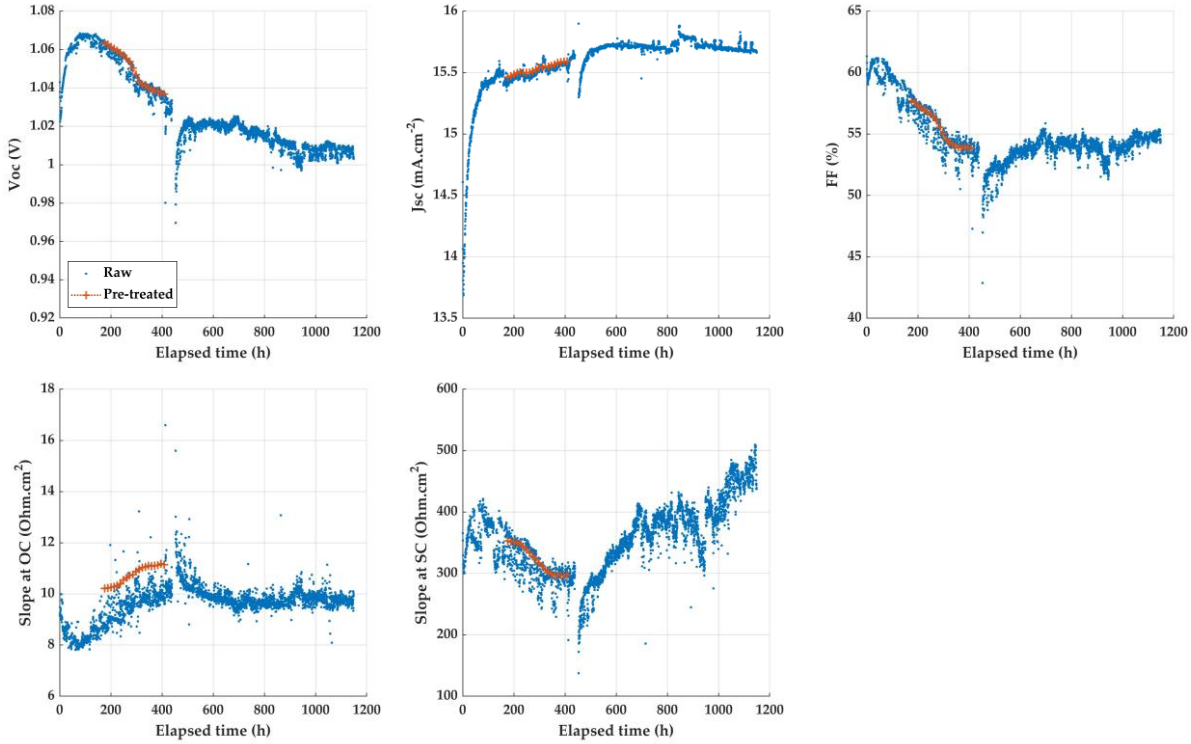

Figure D2. *Degradation over time of the device JV-3.2. Only part of the recorded degradation is extracted to be investigated, from 175 to 410 h of aging.*

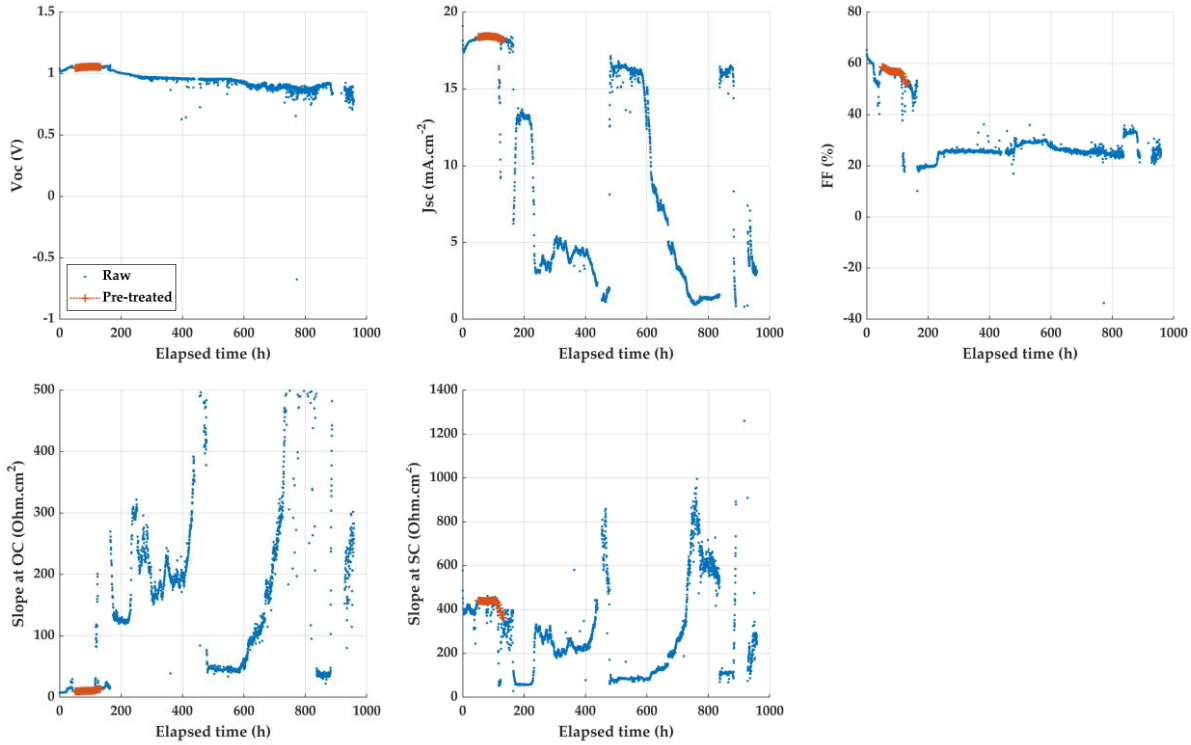

Figure D3. *Degradation over time of the device JV-2.2. Only part of the recorded degradation is extracted to be investigated, from 50 to 160 h of aging.*

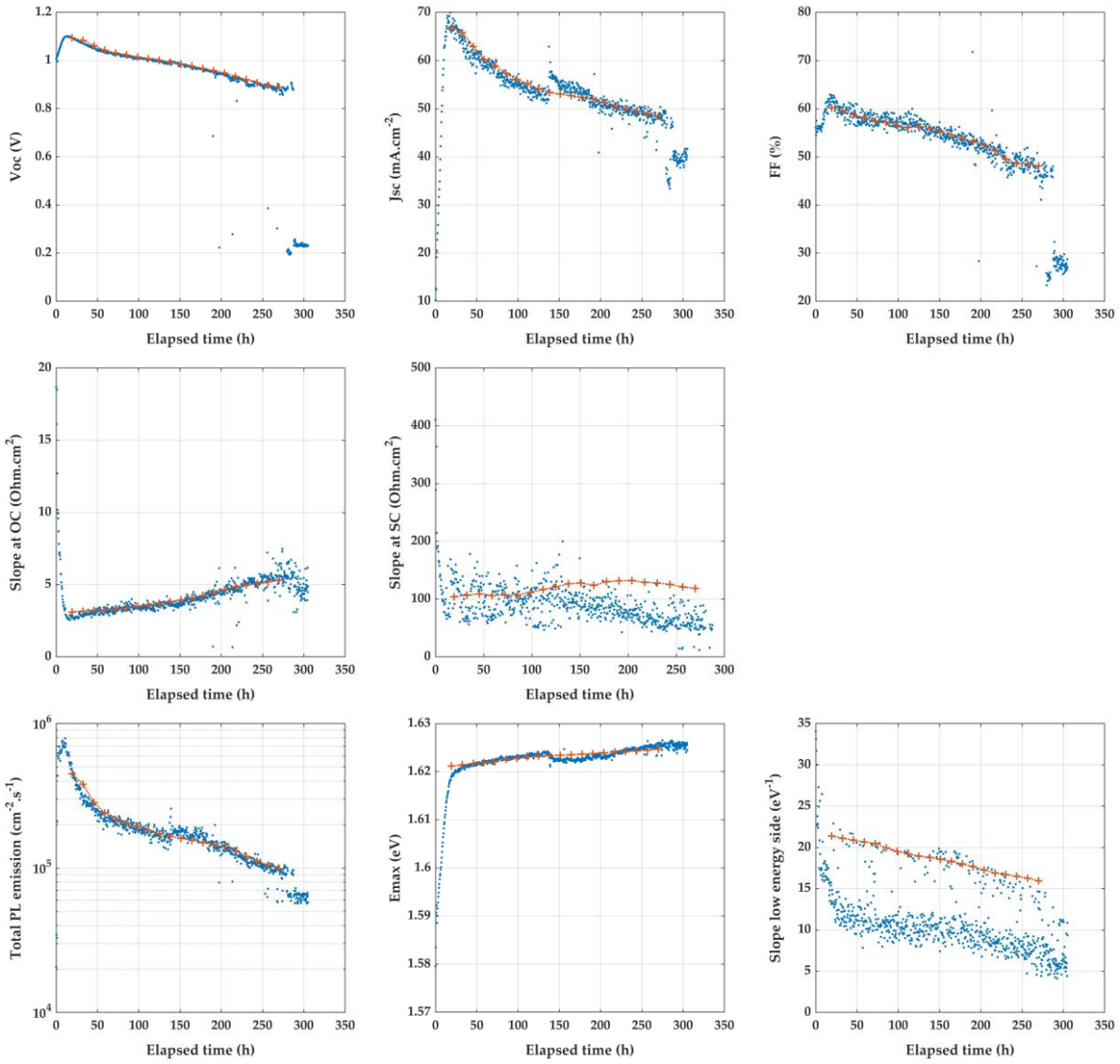

Figure D4. *Degradation over time of the device JV-PL-1. Only part of the recorded degradation is extracted to be investigated, from 20 to 272 h of aging.*

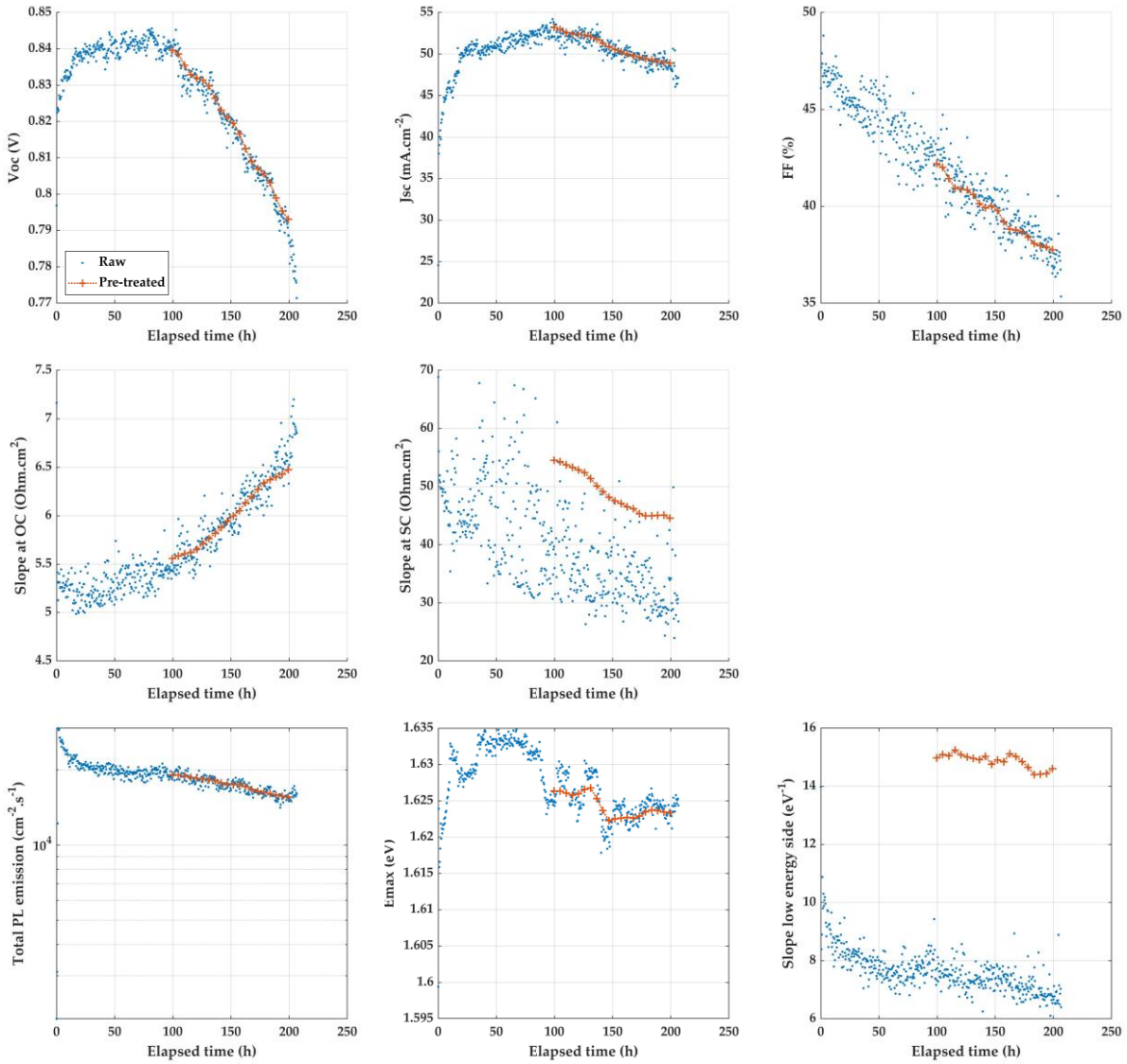

Figure D5. *Degradation over time of the device JV-PL-3. Only part of the recorded degradation is extracted to be investigated, from 100 to 200 h of aging.*

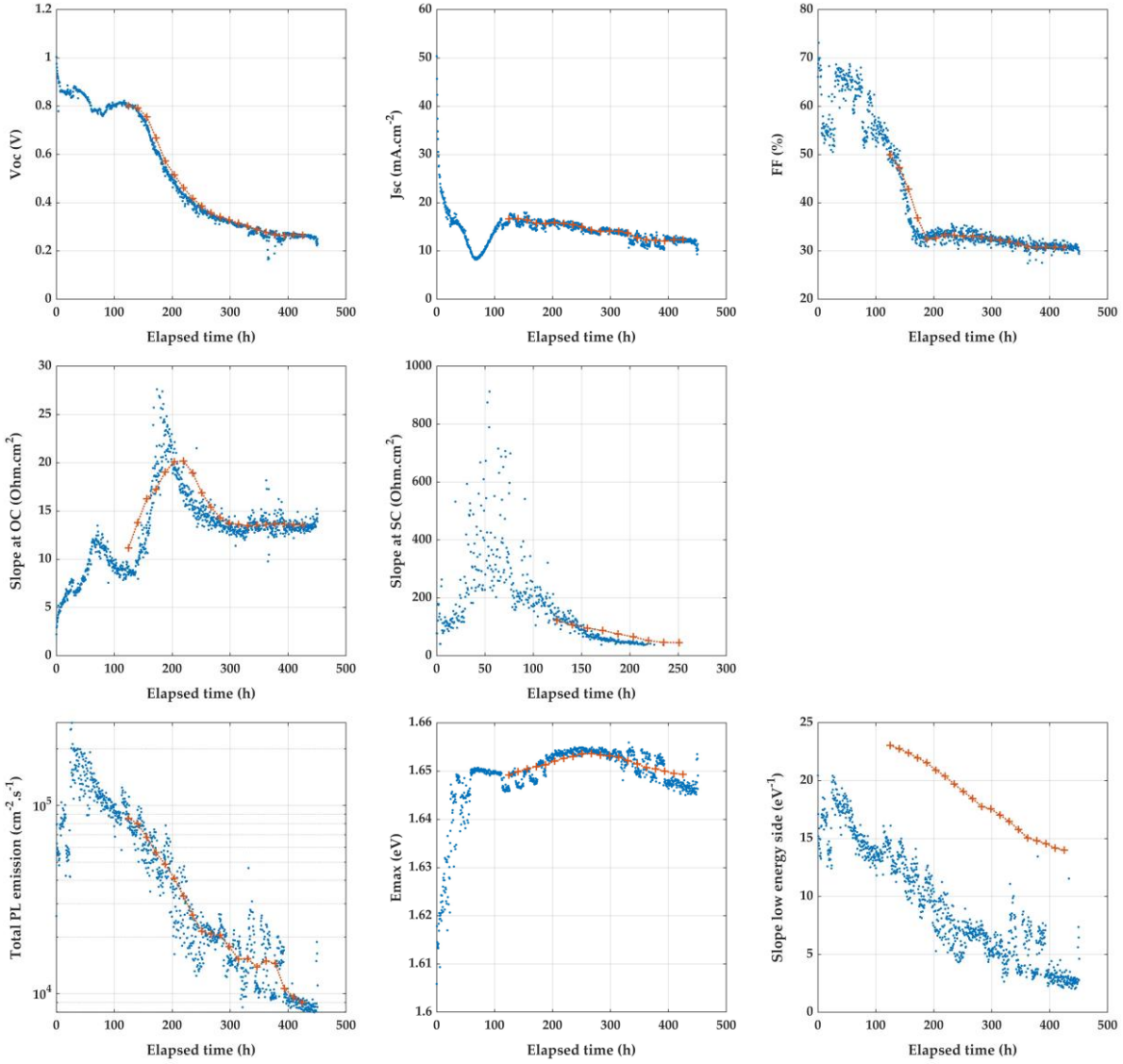

Figure D6. *Degradation over time of the device JV-PL-4. Only part of the recorded degradation is extracted to be investigated, from 125 to 425 h of aging.*

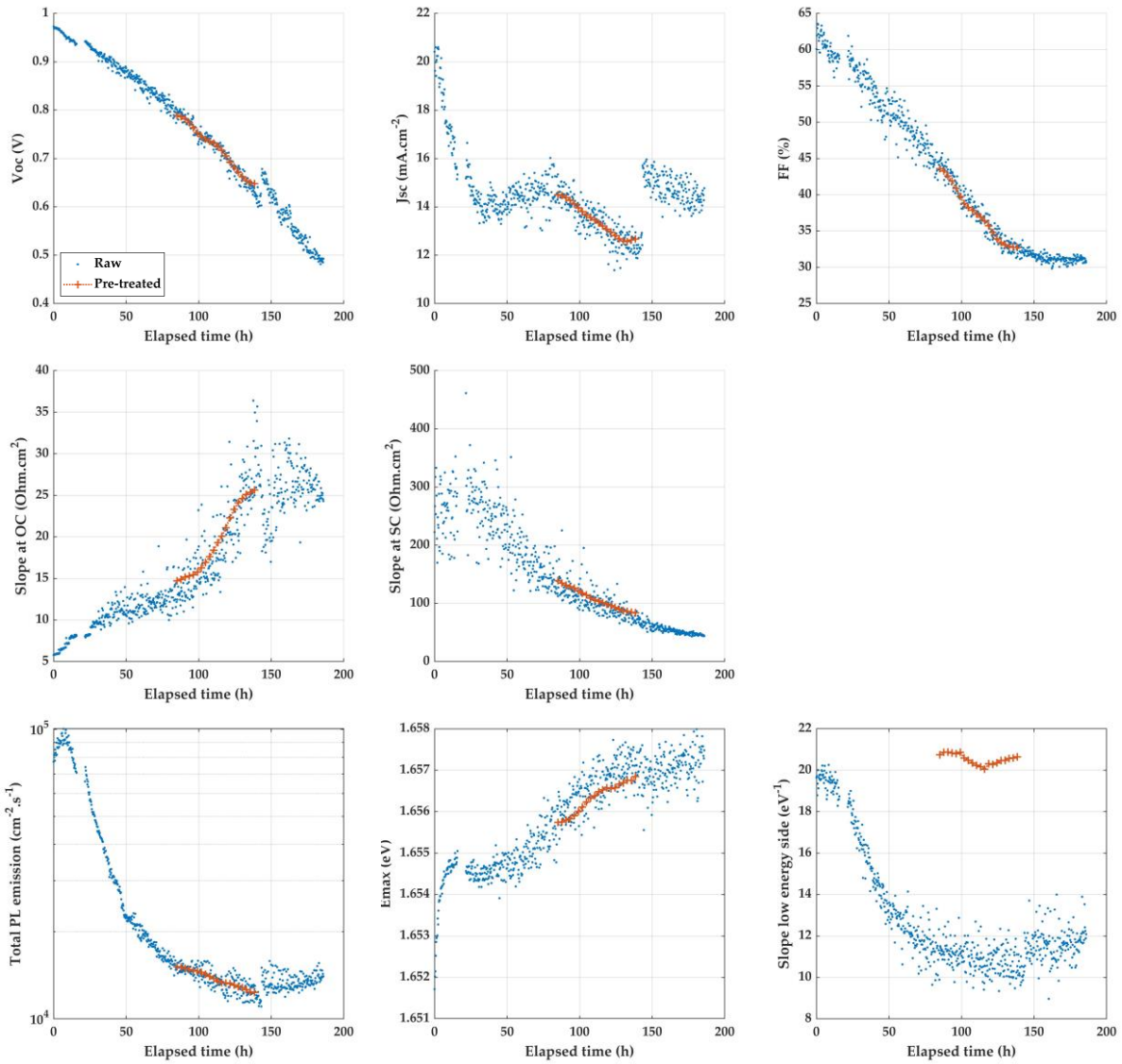

Figure D7. *Degradation over time of the device JV-PL-5. Only part of the recorded degradation is extracted to be investigated, and to cases are considered: from 20 to 140 h of aging, or only starting at 85 h.*

Table D1. *Input parameters for the analytical model of a pn junction. Four hypothetical devices with varying defect densities and carrier mobilities are considered.*

Parameter		High defect density	Low hole mobility	Low electron mobility
ϕ		AM1.5g – 1000 W.m-2		
α		Experimental – IPVF triple cations perovskite		
Illumination side		n-doped layer		
T		293.15 K		
E_G		1.62 eV		
ϵ		30		
N_C, N_V		10^{19} cm^{-3}, 10^{19} cm^{-3}		
B		10^{-10} cm^3.s^{-1}		
σ		10^{-15} cm^2		
v_{th}		10^7 cm.s^{-1}		
Front layer	W_n	50 nm		
	N_D	10^{18} cm^{-3}		
	μ_p	10 cm^2.V^{-1}.s^{-1}	0.01 cm^2.V^{-1}.s^{-1}	10 cm^2.V^{-1}.s^{-1}
	$N_{t-front}$	10^{12} cm^{-2}		
SCR	N_t	10^{17} cm^{-3}	10^{14} cm^{-3}	10^{14} cm^{-3}
Back layer	W_p	450 nm		
	N_A	10^{16} cm^{-3}		
	μ_n	10 cm^2.V^{-1}.s^{-1}	10 cm^2.V^{-1}.s^{-1}	0.01 cm^2.V^{-1}.s^{-1}
	N_{t-back}	10^{12} cm^{-2}		
External Rs		1 Ohm.cm^2		
External Rsh		10 000 Ohm.cm^2		

Table D2. *Input parameters for the drift diffusion model of a perovskite solar cell. Four hypothetical devices with varying defect densities and carrier mobilities are considered.*

Simulation parameter		**Good device**	**High defect density**	**Low electron mobility**	**Low hole mobility**
ϕ		AM1.5g – 1000 W.m-2			
T		293.15 K			
Illumination side		ETL side			
External Rs		1 Ohm.cm^2			
External Rsh		10000 Ohm.cm^2			
Hole transporting material	W	100 nm			
	E_G	3 eV			
	α	Experimental			
	χ	2.42 eV			
	ϵ	10			
	N_C, N_V	10^{19} cm^{-3}, 10^{19} cm^{-3}			
	μ_n	0.5 cm^2.V^{-1}.s^{-1}			
	μ_p	0.5 cm^2.V^{-1}.s^{-1}			
	N_A	10^{19} cm^{-3}			
HTL / pvk interface	$N_{t-HTL/pvk}$	10^{12} cm^{-2}			
Perovskite	W	500 nm			
	E_G	1.62 eV			
	α	Experimental – IPVF triple cations perovskite			
	χ	3.9 eV			
	ϵ	10			
	N_C, N_V	10^{19} cm^{-3}, 10^{19} cm^{-3}			
	μ_n	10 cm^2.V^{-1}.s^{-1}	10 cm^2.V^{-1}.s^{-1}	0.01 cm^2.V^{-1}.s^{-1}	10 cm^2.V^{-1}.s^{-1}
	μ_p	10 cm^2.V^{-1}.s^{-1}	10 cm^2.V^{-1}.s^{-1}	10 cm^2.V^{-1}.s^{-1}	0.01 cm^2.V^{-1}.s^{-1}
	N_{t-deep}	10^{14} cm^{-3}	10^{17} cm^{-3}	10^{14} cm^{-3}	10^{14} cm^{-3}
	$N_{t-shallow}$	7.8.10^{18} cm^{-3}			
	$E_{U-shallow}$	22 meV			
ETL / pvk interface	$N_{t-ETL/pvk}$	10^{12} cm^{-2}			
Electron transporting material	W	100 nm			
	E_G	3 eV			
	α	Experimental			
	χ	4 eV			

ϵ	10
N_C, N_V	10^{19} cm^{-3}, 10^{19} cm^{-3}
μ_n	0.5 cm^2.V^{-1}.s^{-1}
μ_p	0.5 cm^2.V^{-1}.s^{-1}
N_D	10^{19} cm^{-3}

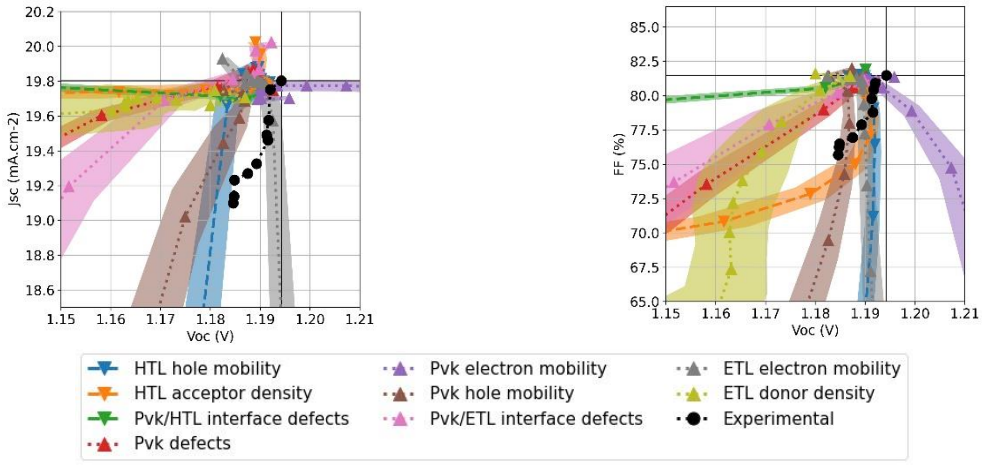

Figure D8. *Experimental degradation pathway of devices studied by Peng et al. with P3HT:CuPc HTL and associated simulated pathways.*

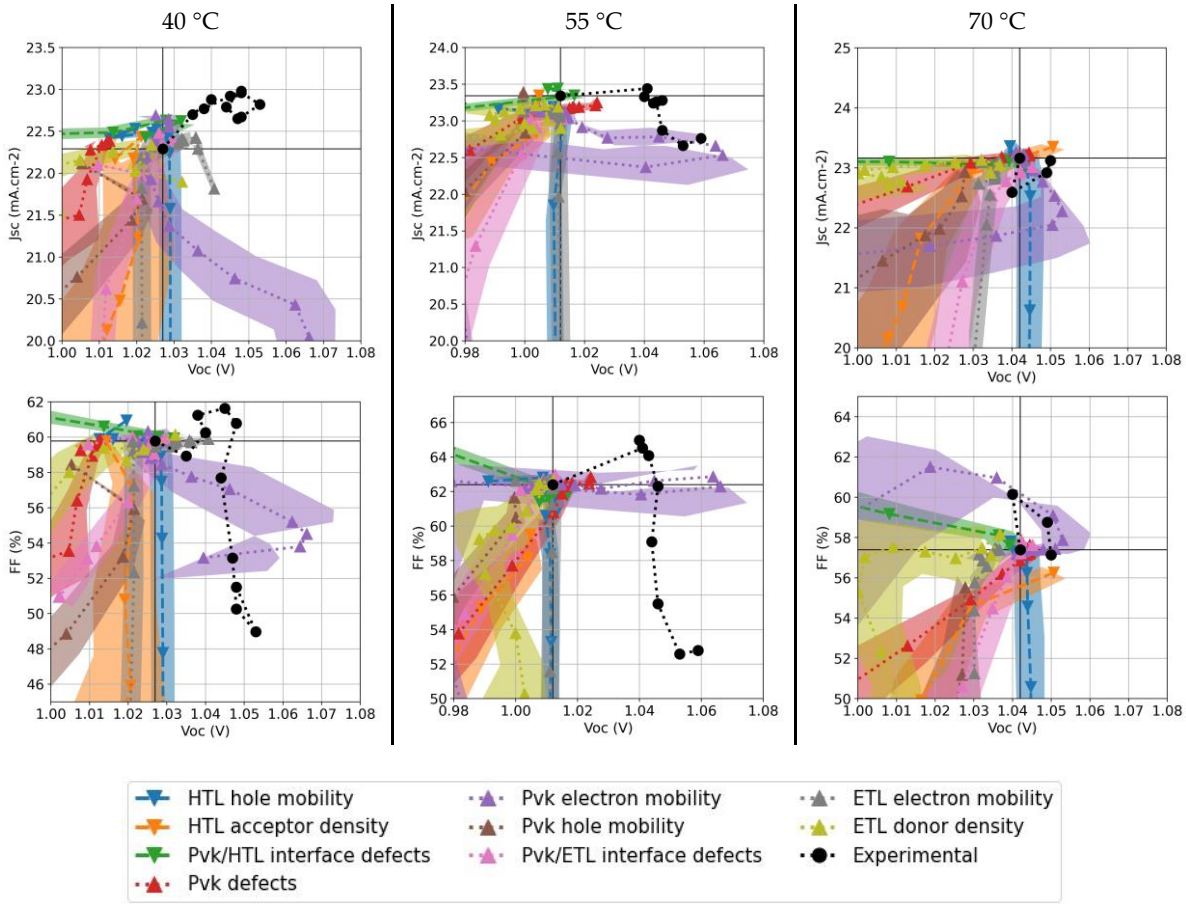

Figure D9. *Experimental degradation pathways from results published by Lim et al.: perovskite devices were aged under one sun, air and at 40, 55 or 70 °C (left, middle, and right respectively). Associated simulated pathways are superposed (down triangles and dashed lines for causes identified by authors, up triangles and dotted lines for others). Only the first part of the experimental degradation is extracted until respectively 475, 175 and 10 minutes.*

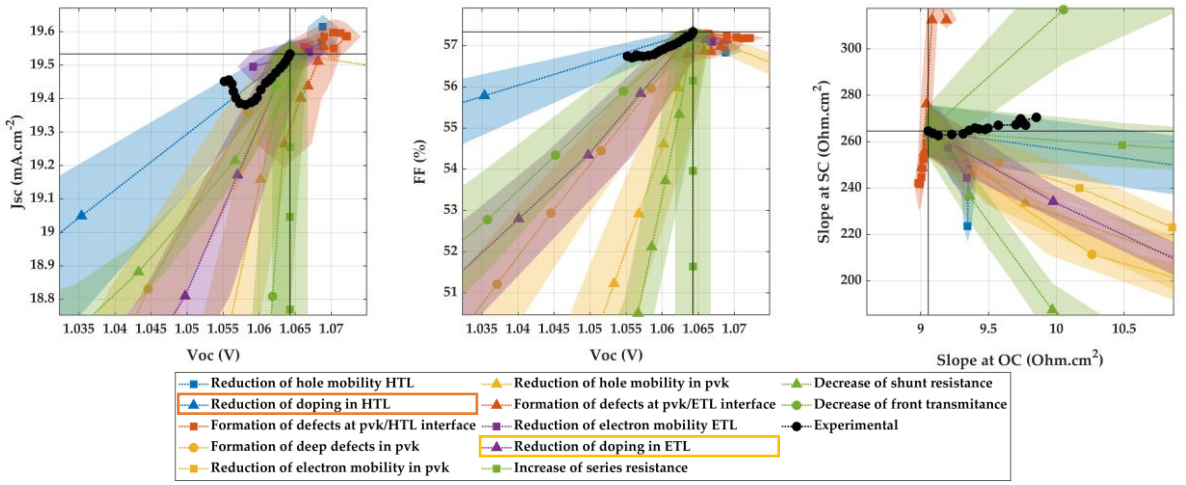

Figure D10. *Experimental degradation pathway of device JV-1.2 and associated simulated mechanisms. The reduction of HTL doping (blue triangles) is the most compatible, but loss of ETL doping (purple triangles) can't be excluded.*

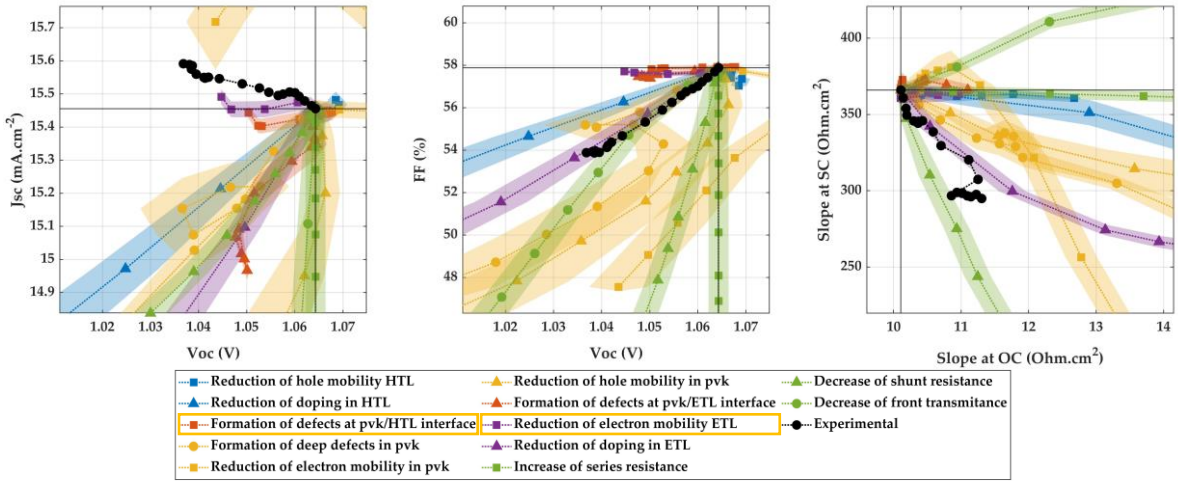

Figure D11. *Experimental degradation pathway of device JV-3.2 and associated simulated mechanisms. No simulated mechanism explain the increase of Jsc. Reduction of electron mobility (purple squares) or formation of defects at pvk – HTL interface (red squares) could still be compatible with experiment.*

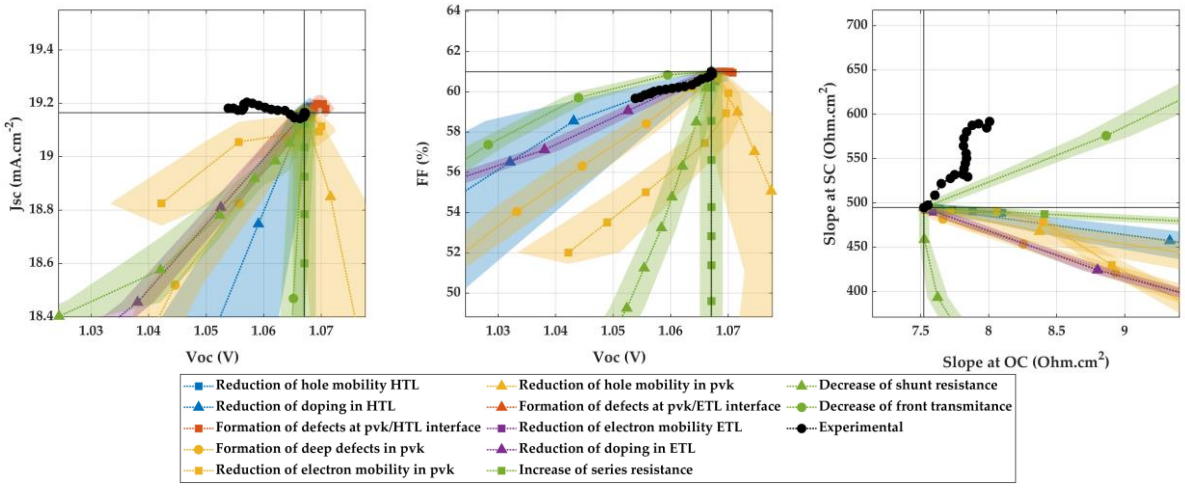

Figure D12. *Experimental degradation pathway of device JV-4.1 and associated simulated mechanisms. No simulated mechanism explains the stable Jsc or the rise of slope at SC.*

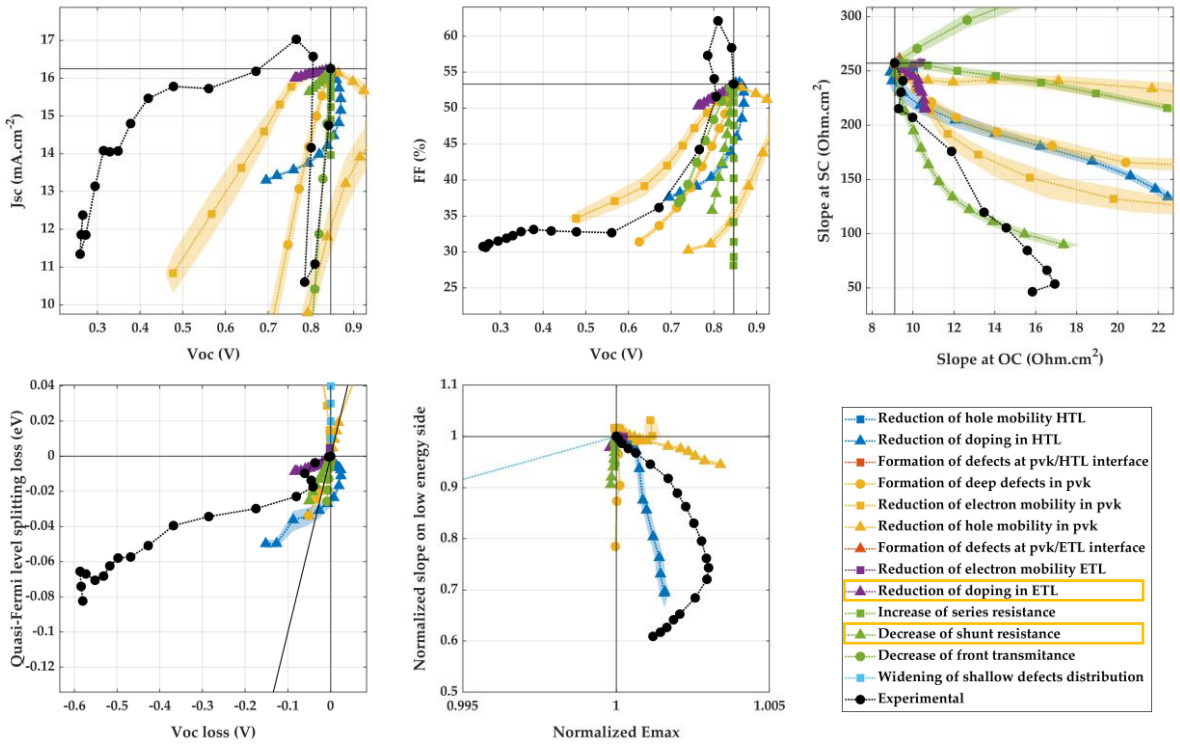

Figure D13. *Experimental degradation pathway of device JV-PL-4 (starting at 25 h) and associated simulated mechanisms. Reduction of ETL doping (purple triangles) or shunt resistance (green triangles) are compatible mechanisms with the beginning of degradation.*

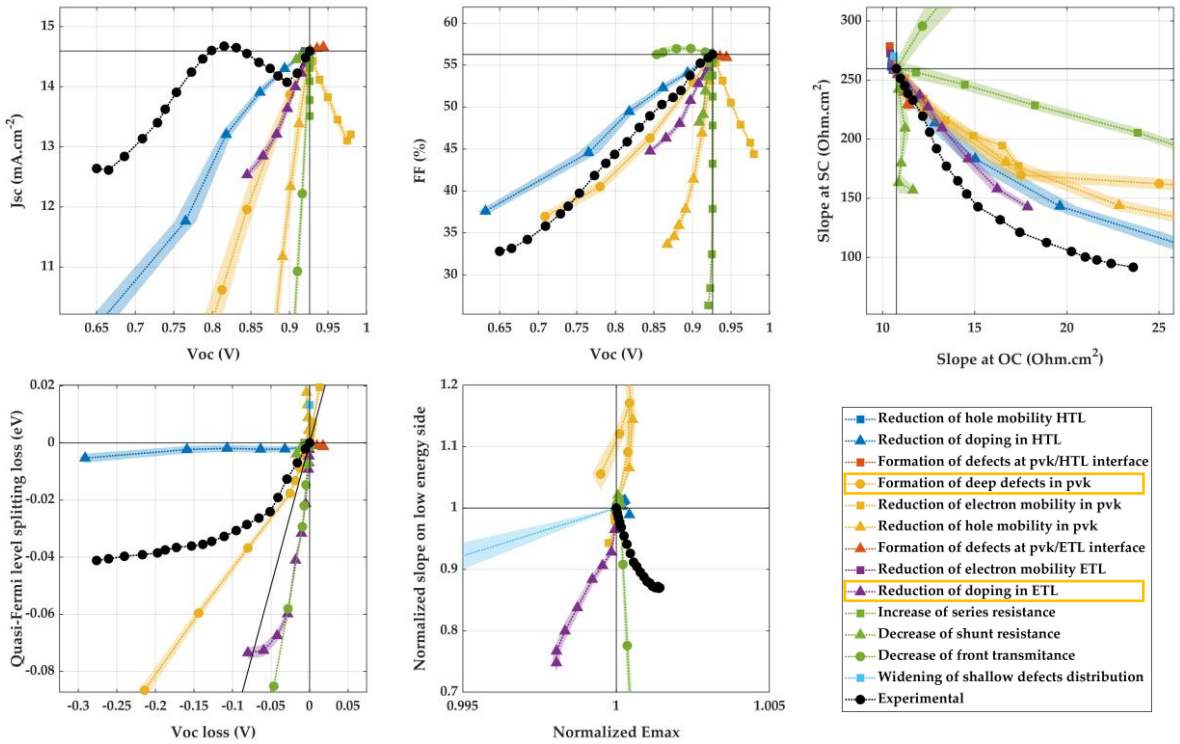

Figure D14. *Experimental degradation pathway of device JV-PL-5 (starting at 20 h) and associated simulated mechanisms. Reduction of doping in ETL (purple triangles) and formation of defects in the perovskite layer (yellow circles) can be compatible with the first experimental points.*

Appendix E : Complements on Principal Components Analyses

In this appendix are supplementary figures to illustrate the work reported in Chapter 5.

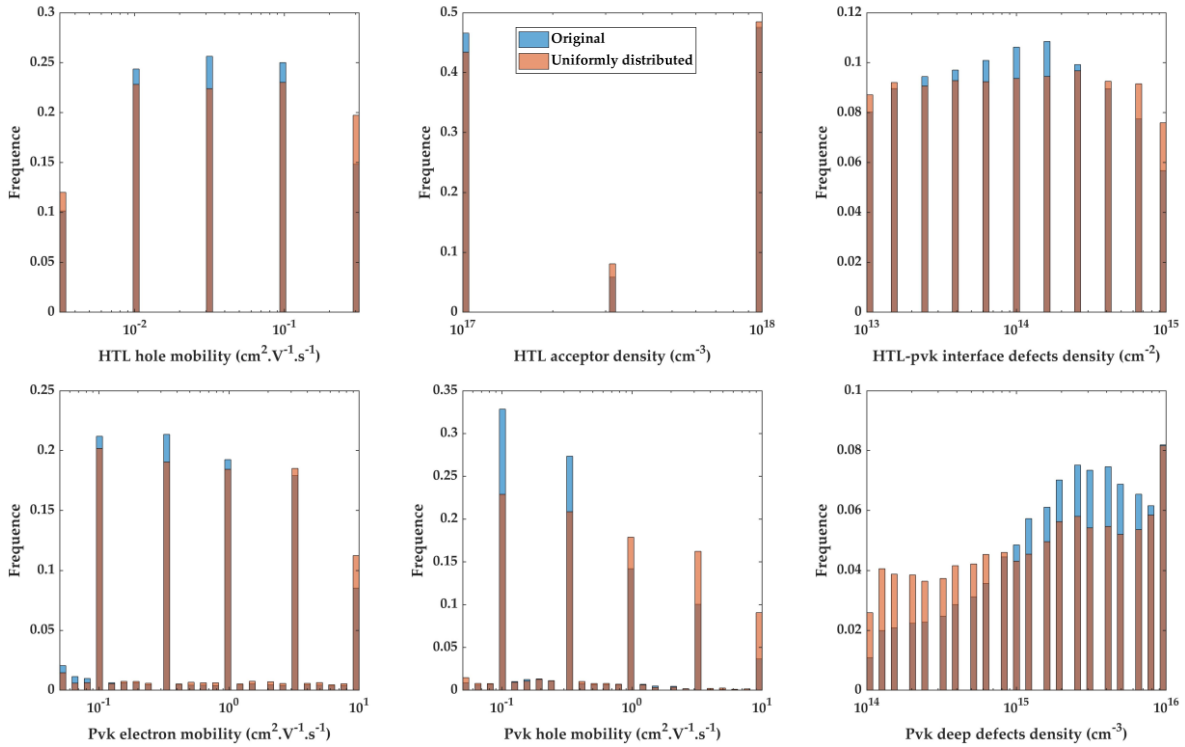

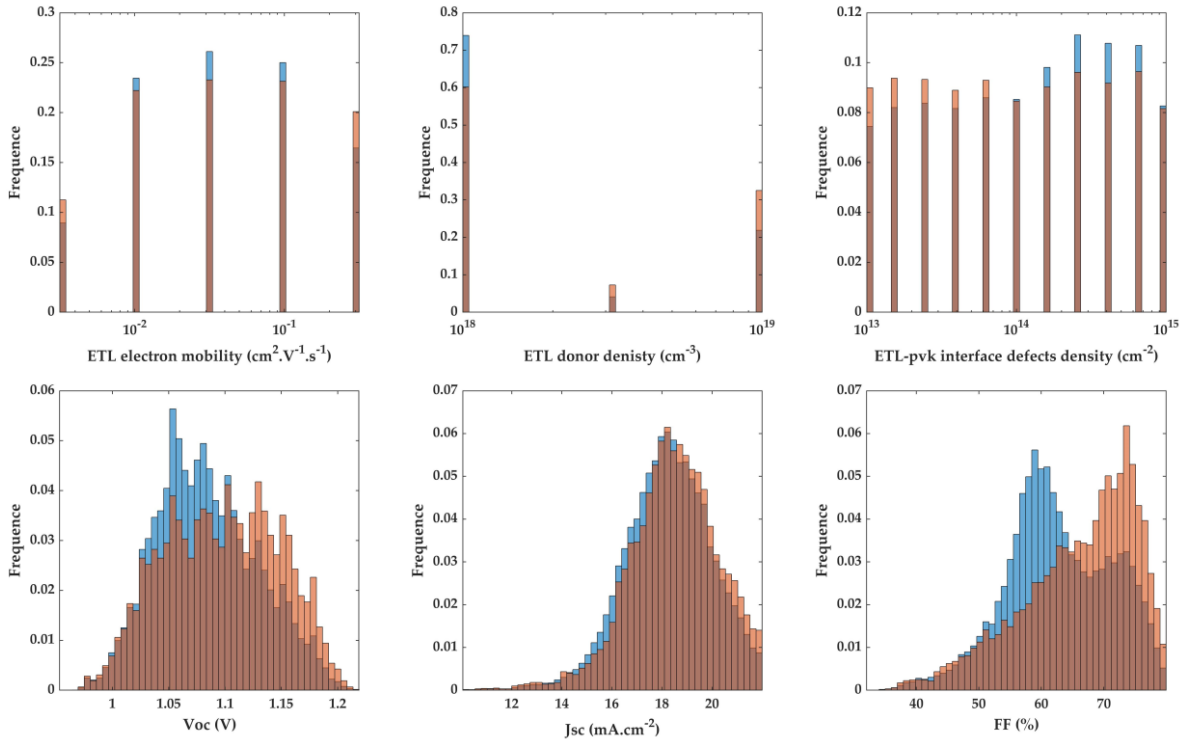

Figure E1. *Distribution of parameters in the global dataset employed to do principal components analyses. Original dataset contains 51 053 entries and 27 472 are picked uniformly.*

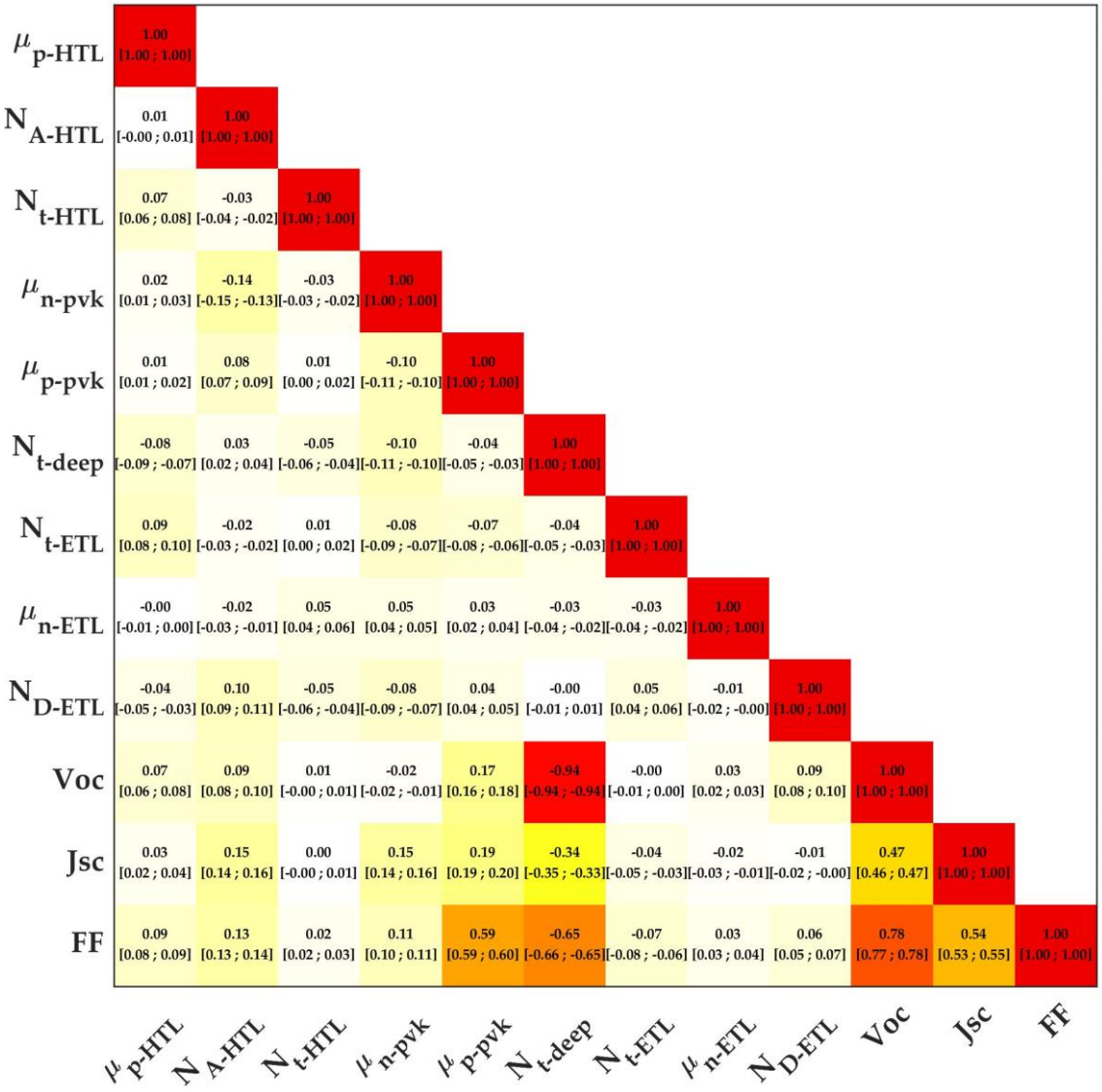

Figure E2. *Covariance matrix of the full available dataset (51 053 entries before extracting uniformly distributed subset) for all variables. Associated 95 % confidence interval is in brackets.*

Mathematical relationship between first component and ouput parameter in a simplified case

Here, the case investigated in Section 5.5.1 is considered, where one optoelectrical parameter is fixed to a given value. The associated subset is therefore constituted of all available input configurations compatible with the considered output value.

In order to express the relashionship between the first component and the output, a simplified case is considered, with three inputs (A, B and C) and one output (Y):

$$Y = ln\left(A^{\alpha} \cdot B^{\beta} \cdot C^{\delta}\right)$$

α, β and γ are fixed parameters, and their relation to the PCA results is exposed.

The principal component analysis is performed over a database of (A, B, C) triplets, all associated to the same Y value.

The normalized values, as exposed in Section 5.4.2, are expressed as follows:

$$\tilde{A} = \frac{ln\, A - \overline{ln\, A}}{\sigma_{ln\, A}}$$

In the associated space, the first component is associated to the direction containing in which data varies the most, described by the vector:

$$\begin{pmatrix} q_{A,1} \\ q_{B,1} \\ q_{C,1} \end{pmatrix}$$

This vector defines the following orthogonal hyperplane:

$$\left\{ \begin{pmatrix} \tilde{A} \\ \tilde{B} \\ \tilde{C} \end{pmatrix} \in \mathbb{R}^3 \mid \begin{pmatrix} \tilde{A} \\ \tilde{B} \\ \tilde{C} \end{pmatrix} \cdot \begin{pmatrix} q_{A,1} \\ q_{B,1} \\ q_{C,1} \end{pmatrix} = C_1 \right\}$$

C_1 is a constant that depends on Y. Therefore, there exist an unknown function, f such as:

$$C_1 = f\left(ln\left(A^{\alpha} \cdot B^{\beta} \cdot C^{\delta}\right)\right)$$

The expression of the scalar product defining the hyperplane is:

$$\begin{aligned} \tilde{A} q_{A,1} + \tilde{B} q_{B,1} + \tilde{C} q_{C,1} &= C_1 \\ ln\left(A^{\frac{q_{A,1}}{\sigma_{ln\, A}}} \cdot B^{\frac{q_{B,1}}{\sigma_{ln\, B}}} \cdot C^{\frac{q_{C,1}}{\sigma_{ln\, C}}}\right) + C_2 &= f(Y) \end{aligned}$$

C_2 is a constant, containing the term $\sum_i q_{i,j} \frac{\overline{ln\, X_i}}{\sigma_{ln\, X_i}}$, *see Section 5.4.2.*

From now, the following notations are employed:

$$\begin{aligned} \alpha_1 &= \frac{q_{A,1}}{\sigma_{ln\,A}} \\ \beta_1 &= \frac{q_{B,1}}{\sigma_{ln\,B}} \\ \gamma_1 &= \frac{q_{C,1}}{\sigma_{ln\,C}} \end{aligned}$$

The previous expression becomes:

$$ln\left(A^{\alpha_1} \cdot B^{\beta_1} \cdot C^{\gamma_1}\right) + C_2 = f\left(ln\left(A^{\alpha} \cdot B^{\beta} \cdot C^{\gamma}\right)\right)$$

Both sides are derived against A:
Left side:

$$\begin{aligned} \frac{\partial\, ln\left(A^{\alpha_1} \cdot B^{\beta_1} \cdot C^{\gamma_1}\right) + C_2}{\partial A} &= \frac{1}{A^{\alpha_1} \cdot B^{\beta_1} \cdot C^{\gamma_1}} \cdot \alpha_1 A^{\alpha_1 - 1} \cdot B^{\beta_1} \cdot C^{\gamma_1} \\ &= \alpha_1 A^{\alpha_1 - 2} \end{aligned}$$

Right side:

$$\begin{aligned} \frac{\partial f\left(ln\left(A^{\alpha} \cdot B^{\beta} \cdot C^{\gamma}\right)\right)}{\partial A} &= \frac{\partial f\left(ln\left(A^{\alpha} \cdot B^{\beta} \cdot C^{\gamma}\right)\right)}{\partial\, ln(A^{\alpha} \cdot B^{\beta} \cdot C^{\gamma})} \cdot \frac{1}{A^{\alpha} \cdot B^{\beta} \cdot C^{\gamma}} \cdot \alpha A^{\alpha-1} \cdot B^{\beta} \cdot C^{\gamma} \\ &= \frac{\partial f\left(ln\left(A^{\alpha} \cdot B^{\beta} \cdot C^{\gamma}\right)\right)}{\partial\, ln(A^{\alpha} \cdot B^{\beta} \cdot C^{\gamma})} \cdot \alpha A^{\alpha-2} \\ &= \frac{\partial f(Y)}{\partial Y} \cdot \alpha A^{\alpha-2} \end{aligned}$$

Finally, the following system is obtained by employing the same method for each variable, A, B and C:

$$\begin{cases} \alpha_1 A^{\alpha_1 - 2} = \frac{\partial f(Y)}{\partial Y} \cdot \alpha A^{\alpha-2} \\ \beta_1 B^{\beta_1 - 2} = \frac{\partial f(Y)}{\partial Y} \cdot \beta B^{\beta-2} \\ \gamma_1 C^{\gamma_1 - 2} = \frac{\partial f(Y)}{\partial Y} \cdot \gamma C^{\gamma-2} \end{cases}$$

It is important to note here, that α_1, β_1, and γ_1 exponents are defined to a common multiplicative constant. For instance, if they are all multiplied by a factor λ the following would hold:

$$\frac{1}{\lambda} ln\left(A^{\lambda\alpha_1} \cdot B^{\lambda\beta_1} \cdot C^{\lambda\gamma_1}\right) + C_2 = f(Y)$$

Which could be associated to another unknown function g, instead of f:

$$ln\left(A^{\lambda\alpha_1} \cdot B^{\lambda\beta_1} \cdot C^{\lambda\gamma_1}\right) + C_2 = g(Y)$$

Therefore, the system in equation (X) becomes:

$$\begin{cases} \lambda\alpha_1 A^{\lambda\alpha_1-2} &= \dfrac{\partial g(Y)}{\partial Y} \cdot \alpha A^{\alpha-2} \\ \lambda\beta_1 B^{\lambda\beta_1-2} &= \dfrac{\partial g(Y)}{\partial Y} \cdot \beta B^{\beta-2} \\ \lambda\gamma_1 C^{\lambda\gamma_1-2} &= \dfrac{\partial g(Y)}{\partial Y} \cdot \gamma C^{\gamma-2} \end{cases}$$

The two first equations of the system allow to express:

$$\begin{aligned} \frac{\lambda\alpha_1 A^{\lambda\alpha_1-2}}{\alpha A^{\alpha-2}} &= \frac{\lambda\beta_1 B^{\lambda\beta_1-2}}{\beta B^{\beta-2}} \\ \frac{\lambda\alpha_1}{\alpha} A^{\lambda\alpha_1-\alpha} &= \frac{\lambda\beta_1}{\beta} B^{\lambda\beta_1-\beta} \end{aligned}$$

In fact, A and B are two independent variables. It is therefore necessary that both sides are equal to a constant, to keep the equality true. This implies that exponents on A and B are equal to zero, therefore:

$$\begin{aligned} \lambda\alpha_1 &= \alpha \\ \lambda\beta_1 &= \beta \end{aligned}$$

Finally, this expresses the important result employed to interpret the PCA results in Section 5.5.1:

$$\frac{\alpha_1}{\alpha} = \frac{\beta_1}{\beta} = \frac{\gamma_1}{\gamma}$$

This demonstrates that the exponents obtained from PCA (α_1, β_1, and γ_1) on a set defined by a fixed value of the output are all proportional to the original composition of the output (α, β and γ).

Importantly, a simplified and favorable case was considered here. Therefore, this is not a demonstration for the analysis of the drift diffusion results in Section 5.5.1. For this reason, interpretations remain mostly qualitative, on the respective balance between inputs weight.

Illustration of the relationship between first component and ouput parameter in a simplified case

Here several examples are numericaly computed to illustrate the validity of the exporessions derived above. Several values of α, β and γ are considered, as well as several explored spaces for A, B and C. In each example, the analysis is performed over the range of available values of Y, similarly to Section 5.5.1.

Example 1:

$$Y = ln(A^2 \cdot B^{0.5} \cdot C^{0.1})$$

$A \in [5,100]$, $B \in [5,100]$, $C \in [5,100]$ and each input parameter is log-uniformly distributed over 200 points.

First, two examples of subsets are represented in Figure E3, for two fixed values of the output. Importantly, a projection of the three dimensional space on the plane A - B is represented. The three components are represented through their vector, displayed in plain lines originating at the middle of the subset. It appears clearly how the first component extracts the main tendency of the subset.

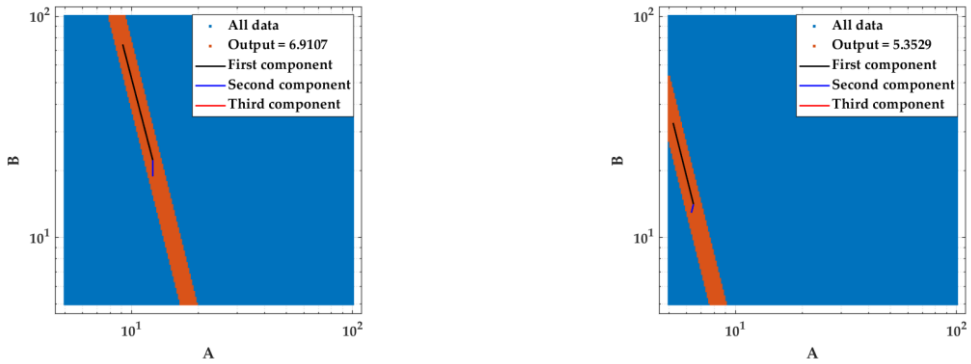

Figure E3. *Total explored input parameters space projected on A - B plane. Selected inputs for a fixed output value are represented in red, and first component (black line) follows the major trend. Two examples of output value are displayed (left and right) demonstrating the dependence of the hyperplane on the output.*

Results in Figure E4 also illustrate well the computations exposed above. First, the definition to a multiplicative constant of the exponent (left) appear clearly, as for one case, exponents are multiplied by -1 with respect to others.

This is avoided when plotting the ratios of exponents (middle). Here the relationship between PCA exponents and original values is almost perfectly verified for a range of output values between 6 and 10 (plain lines display the expected values):

$$\frac{\alpha_1}{\beta_1} = \frac{\alpha}{\beta}$$
$$\frac{\alpha_1}{\gamma_1} = \frac{\alpha}{\gamma}$$
$$\frac{\beta_1}{\gamma_1} = \frac{\beta}{\gamma}$$

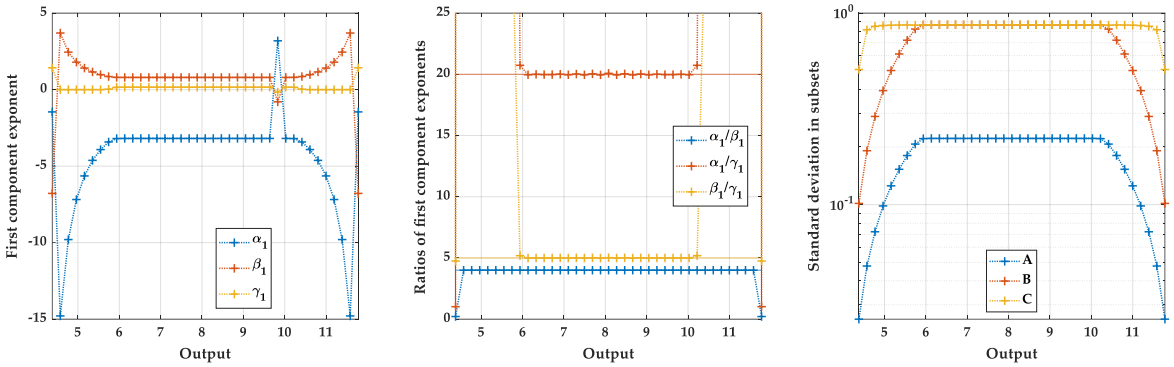

Figure E4. *Left: exponents of the first component from PCA performed over the range of fixed output values. Middle: ratios of first component exponents. Plain lines display the expected values. Right, standard deviation of each input parameter subsets over the range of fixed output values.*

Also, the distribution of available values for the inputs is also important. Here it appears that outside the output range 6 to 10, unbalanced distributions of available parameters perturb the results. This is in fact linked to the selected sets displayed in Figure E3. It appears on right side that available space is truncated when output value is set to approx. 5.4. Importantly, the standard deviation in Figure E4, right, is an indicator of this effect, as it is artificially lowered near the edges of the input space.

Example 2:

$$Y = ln(A^4 \cdot B^{0.5} \cdot C^{0.1})$$

$A \in [5,100]$, $B \in [5,100]$, $C \in [5,100]$ and each input parameter is log-uniformly distributed over 200 points.

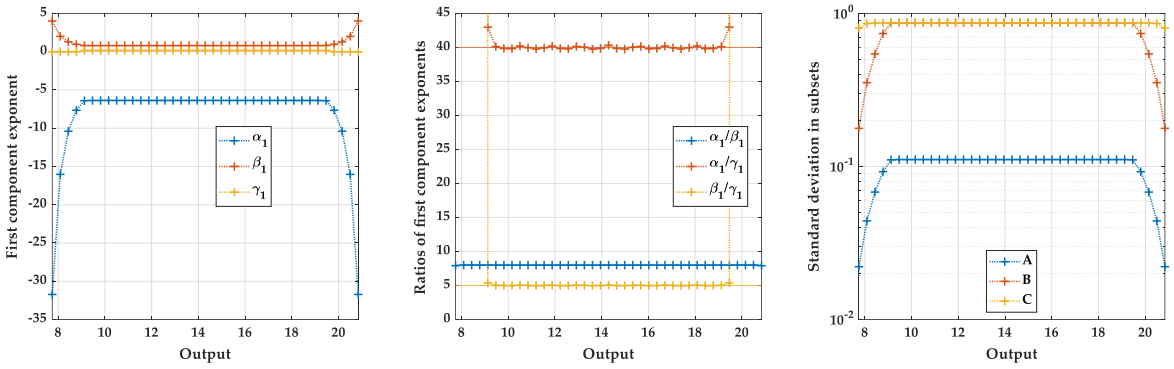

Figure E5. *Left: exponents of the first component from PCA performed over the range of fixed output values. Middle: ratios of first component exponents. Plain lines display the expected values. Right, standard deviation of each input parameter subsets over the range of fixed output values.*

Example 3:

$$Y = ln(A^2 \cdot B^{0.5} \cdot C^{0.1})$$

$A \in [5,10]$, $B \in [5,10]$, $C \in [5,1000]$ and each input parameter is log-uniformly distributed over 200 points.

Here the parameters distribution is highly unfavorable because C, the least important input varies over two more orders of magnitude than A and B.

Results show that ratios still follow the expected values at the center of the distribution, but boundaries effects are more prominent.

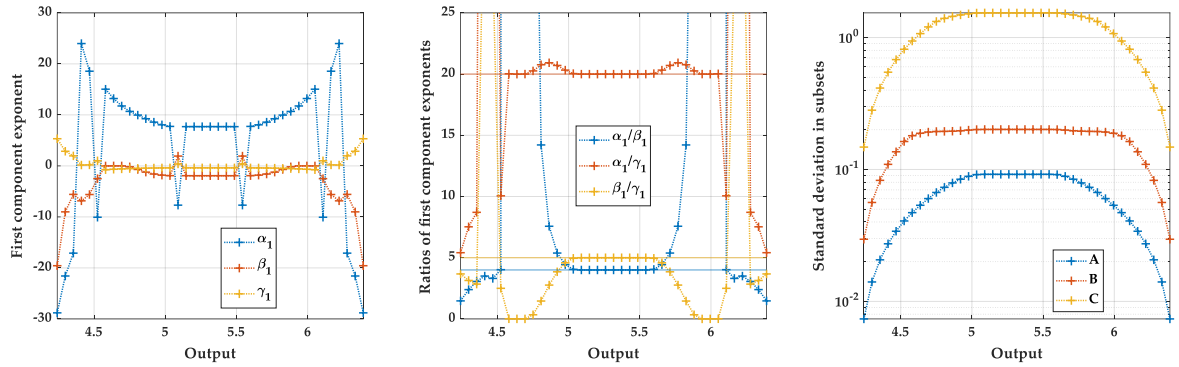

Figure E6. *Left: exponents of the first component from PCA performed over the range of fixed output values. Middle: ratios of first component exponents. Plain lines display the expected values. Right, standard deviation of each input parameter subsets over the range of fixed output values.*

Example 4:

$$Y = ln(A^2 \cdot B^{0.5} \cdot C^{0.1})$$

$A \in [5,1000]$, $B \in [5,10]$, $C \in [5,10]$ and each input parameter is log-uniformly distributed over 200 points.

The boundary conditions are not impacting significantly, and the expected values of the ratios are perfectly reproduced.

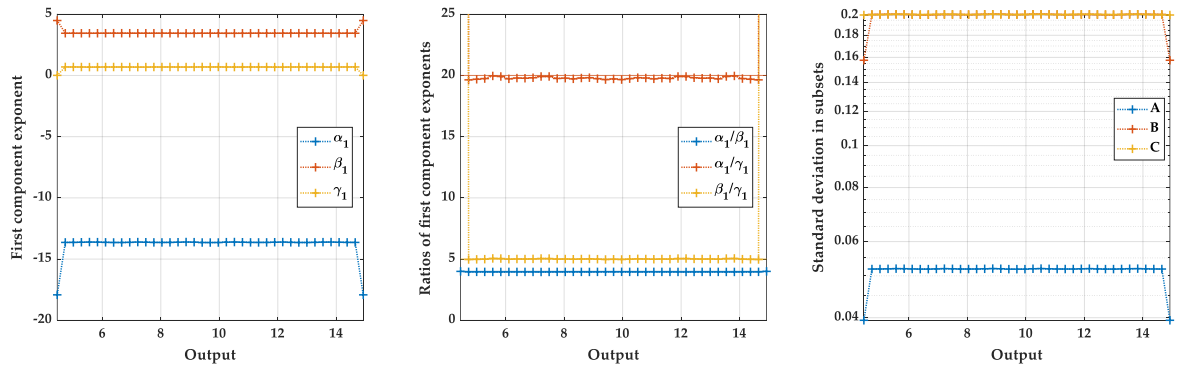

Figure E7. *Left: exponents of the first component from PCA performed over the range of fixed output values. Middle: ratios of first component exponents. Plain lines display the expected values. Right, standard deviation of each input parameter subsets over the range of fixed output values.*

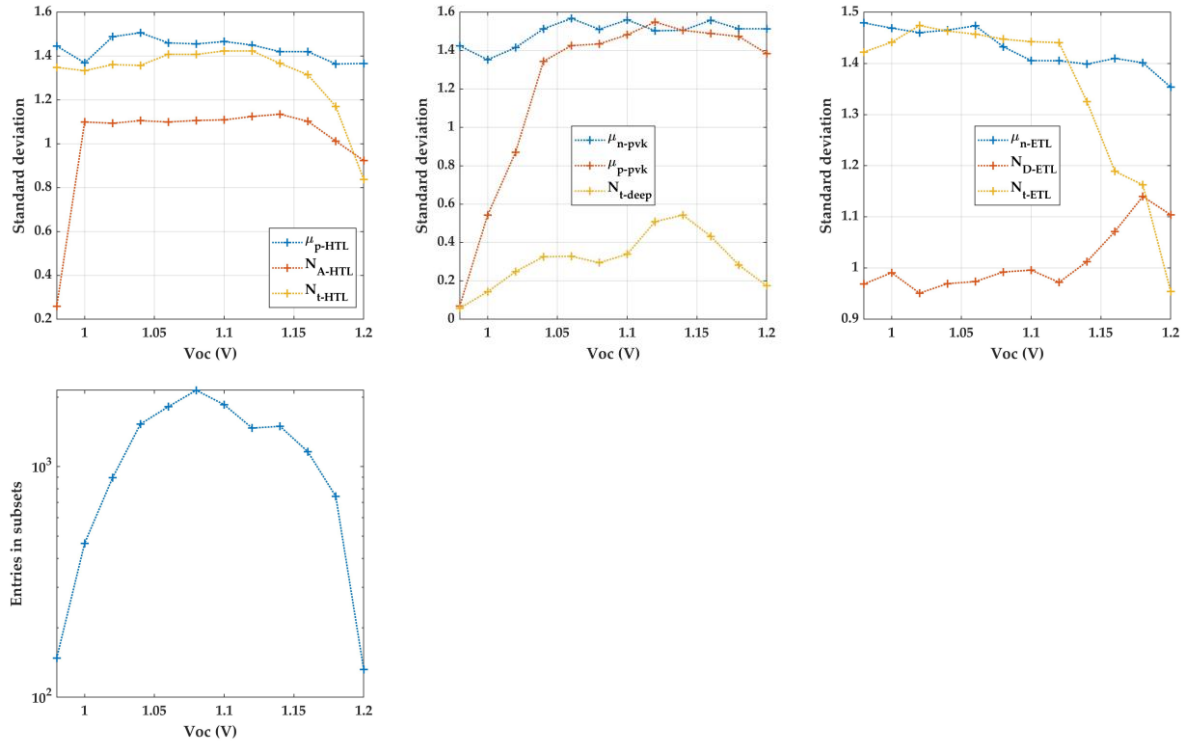

Figure E8. *Top: standard deviation of each input parameter subsets over the range of fixed Voc values. Bottom: total number of entries in each subset.*

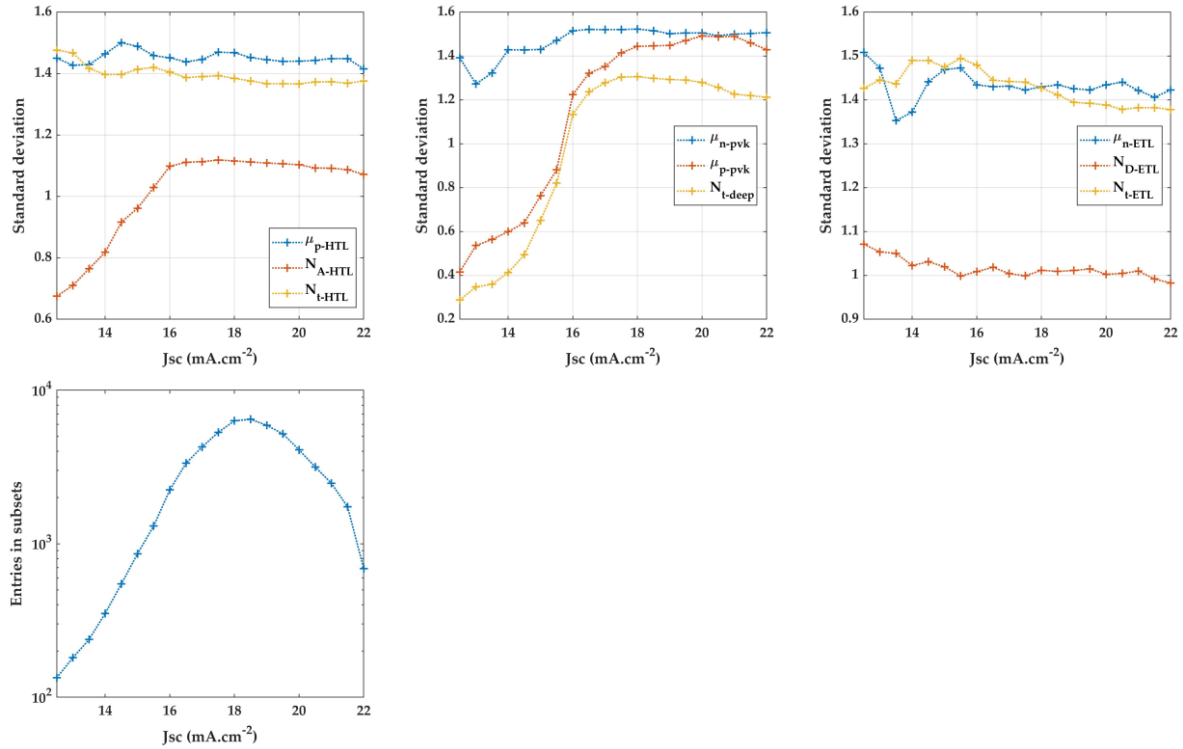

Figure E9. *Top: standard deviation of each input parameter subsets over the range of fixed Jsc values. Bottom: total number of entries in each subset.*

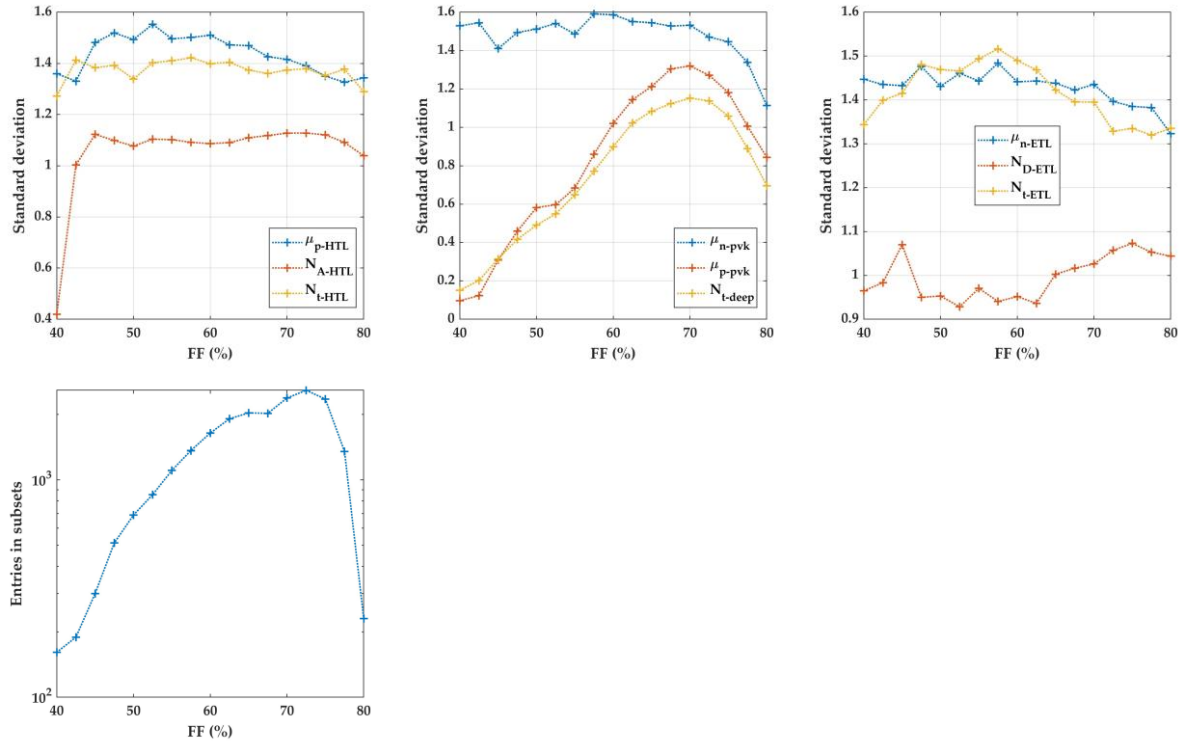

Figure E10. *Top: standard deviation of each input parameter subsets over the range of fixed FF values. Bottom: total number of entries in each subset.*

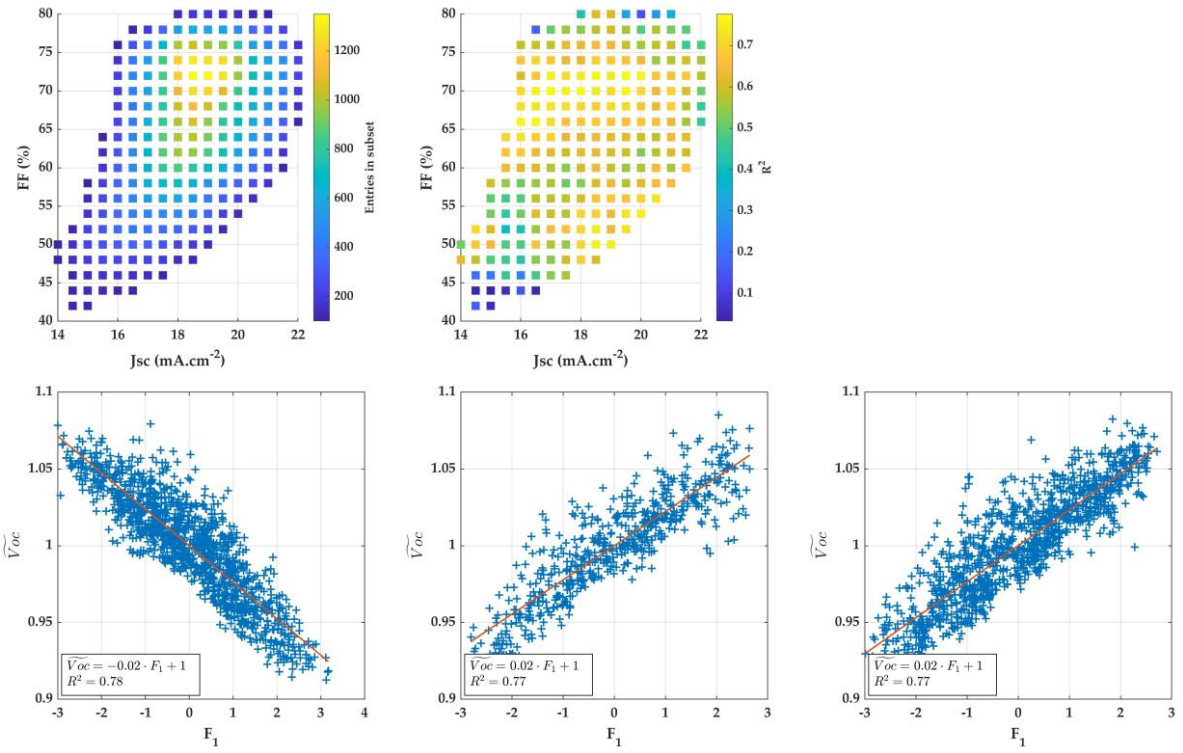

Figure E11. *Top: size of selected subsets for considered Jsc-FF couples and associated R^2 values for the linear regression of Voc with the first component. Bottom: correlation plot of first component with variable output parameter, in the three best cases of R^2 value.*

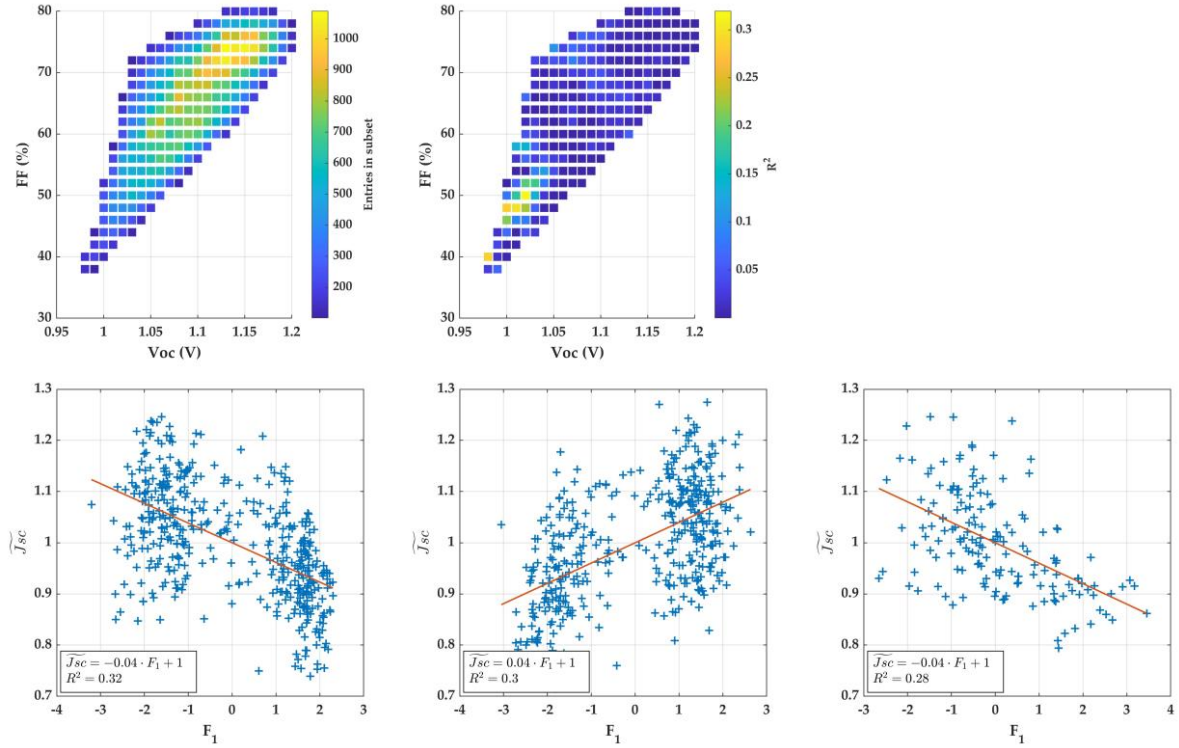

Figure E12. *Top: size of selected subsets for considered Voc-FF couples and associated R² values for the linear regression of Jsc with the first component. Bottom: correlation plot of first component with variable output parameter, in the three best cases of R² value.*

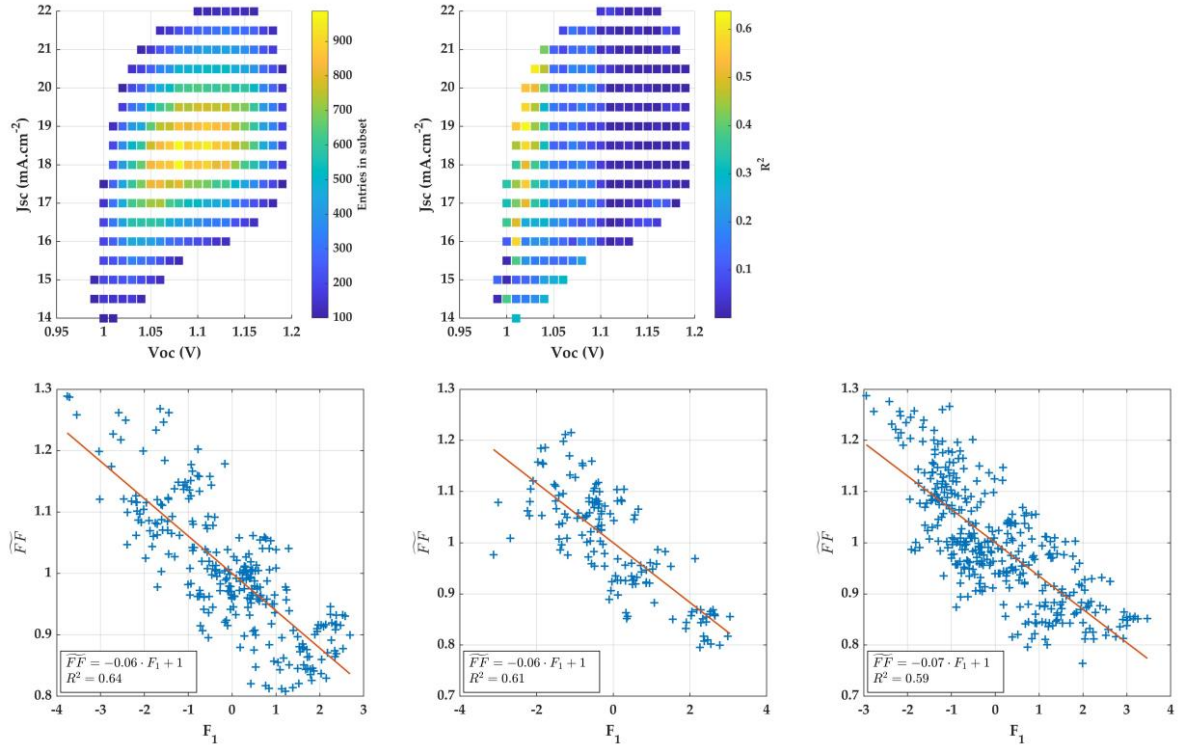

Figure E13. *Top: size of selected subsets for considered Voc-Jsc couples and associated R² values for the linear regression of FF with the first component. Bottom: correlation plot of first component with variable output parameter, in the three best cases of R² value.*